Search for the neutrinoless double beta decay of ^{100}Mo with the NEMO3 detector and calorimeter research and development for the SuperNEMO experiment

Anastasia Basharina-Freshville

Thesis submitted for the degree of

Doctor of Philosophy

of

UCL

Department of Physics and Astronomy

University College London

15th September 2011

I, Anastasia Basharina-Freshville, confirm that the work presented in this thesis is my own. Where information has been derived from other sources, I confirm that this has been indicated in the thesis.

Acknowledgements

I would like to give the biggest thanks to my supervisor, Ruben Saakyan, who originally inspired me to do particle physics with his brilliant undergraduate lectures and has made me become increasingly fascinated with the subject ever since. Thank you for all of your guidance and support throughout these years.

Thank you to all the NEMOs out there from the NEMO3 and SuperNEMO collaborations for the endless amounts of help and good times (I will always stay a proud member of "Team Barbotage"!). In particular I would like to thank Derek Attree and Brian Anderson for their help in the laboratory, Stefano Torre and Vladimir Vasiliev for their software expertise, Bobby Flack for giving me the courage to go after what I wanted, Manu Chauveau for showing me what true laboratory work really means - working until 6 am with the help of a cheeky pizza and some wine, and Benton Pahlka and Karol Lang for taking me under their wing in Texas.

Thank you to everyone at UCL HEP for your help and guidance, especially to Jon Butterworth and Mark Lancaster for being great HEP group leaders. To the guys in my office - you will not ever win the AirCon wars!

I would like to give special thanks to my dad, who has always brought out the physics part in me - this work is for you as much as it is for me. Thank you to the members of Adela Avenue - my incredible sister Dasha and good friend Alex for showing extreme amounts of patience and support, and for being able to put up with me during the finishing process. Thank you to Oliver and to all my amazing friends and family for your endless encouragement.

Mame

(For my mother)

Abstract

The world's most precise half-life measurement of $T^{2\nu}_{1/2} = [7.02 \pm 0.01(stat) \pm 0.46(syst)] \times 10^{18}$ years has been made for the $2\nu\beta\beta$ decay of ^{100}Mo using data from 6.9kg collected with the NEMO3 detector over 1471 days. The 2ν nuclear matrix element has been extracted using $T^{2\nu}_{1/2}$ and is $M^{2\nu}$ = 0.126 $\pm$ 0.004. The $0\nu\beta\beta$ search yielded a limit on the half-life of $T^{0\nu}_{1/2} > 1.1 \times 10^{24}$ years at the 90% CL, corresponding to a limit on the effective Majorona mass of $\langle m_{\nu e} \rangle <$ 0.3 - 1.0eV, one of the most stringent constraints on $\langle m_{\nu e} \rangle$ in the world. Limits on the right-handed currents and Majoron $0\nu\beta\beta$ modes have also been set. The world's most stringent bound has been set on the Majoron to neutrino coupling constant of $\langle g_{\chi^0} \rangle < (0.2 - 0.7) \times 10^{-4}$.

SuperNEMO is a next generation $\beta\beta$ decay experiment, based on the design and experience of NEMO3. Due to start demonstrator operation in 2013, SuperNEMO aims to achieve a sensitivity of 10^{26} years, corresponding to $\langle m_{\nu e} \rangle <$ 50-100meV using ^{82}Se. An alternative to the baseline calorimeter design was considered, using 2m x 10cm x 2.54cm scintillator bars. An energy resolution of 10% FWHM at 1 MeV and a time resolution of $\sim$ 450ps was achieved for the alternative design. This is an unprecedented energy resolution for a scintillator of this size.

Contents

List of Figures

List of Tables

Chapter 1

Introduction

The Standard Model (SM) of particle physics has been largely validated by experimental particle physics in recent years. However, fundamental and as yet unanswered questions remain about the neutrino sector of the SM, which postulates zero mass neutrinos. Recent observations of neutrino oscillations and flavour mixing imply a non-zero mass of the neutrino, which leads to questions about the absolute neutrino mass, the mass hierarchy and the nature of the neutrino - whether it is a Dirac or a Majorana particle. As neutrinos are neutral particles the theory of weak interactions presents the possibility that the neutrino is its own anti-particle (implying lepton number violation), rather than a Dirac particle, in which case the neutrino would have its own distinct anti-neutrino partner. The SM postulates that all fundamental particles are of a Dirac nature, therefore observing a neutrino of a Majorana nature would provide direct evidence of physics beyond the SM.

Neutrinoless double beta decay ($0\nu\beta\beta$) is a lepton number violating process forbidden in the SM, which occurs via the exchange of a virtual neutrino. It is one of the most sensitive processes to determine the nature and the absolute mass of the neutrino and has access to the neutrino mass hierarchy. If observed it will have extremely large significance for the fields of particle physics, nuclear physics, cosmology and astrophysics. It has an experimental signature of two electrons coming from a common vertex with an energy sum equal to the $Q_{\beta\beta}$ value of the measured isotope. Any $0\nu\beta\beta$ decay isotope also undergoes the SM allowed process of double beta decay ($2\nu\beta\beta$). A greater knowledge and understanding of $2\nu\beta\beta$ decay provides insight into the nuclear models used to calculate the nuclear matrix elements for $0\nu\beta\beta$ decay, which are required to extract the physics parameters, such as the absolute neutrino mass, from

the $0\nu\beta\beta$ decay search. Therefore it is important to continue studying $2\nu\beta\beta$ decay as well as carry out searches for $0\nu\beta\beta$ decay. The main aim of the NEMO3 experiment, which collected data from 2003 to 2011, is to search for $0\nu\beta\beta$ decay and to carry out in depth studies of $2\nu\beta\beta$ decay. The SuperNEMO experiment (which has recently started constructing the "demonstrator" module) is a next generation $0\nu\beta\beta$ experiment, which will employ the successful tracker-calorimeter technique used in NEMO3.

1.1 NEMO3

The main goals of the NEMO3 detector (located in the Laboratoire Souterrain de Modane, with 4850 metres water equivalent of rock overburden) are to study $0\nu\beta\beta$ decay to a half-life limit of 10^{24} years, corresponding to a sensitivity of 0.3 - 1.0eV for the effective neutrino mass and to carry out extensive studies of $2\nu\beta\beta$ decay. NEMO3 consists of 10kg of source foils, containing seven isotopes for the study of double beta decay (^{100}Mo, ^{82}Se, ^{116}Cd, ^{130}Te, ^{150}Nd, ^{96}Zr and ^{48}Ca, with $Q_{\beta\beta}$ values ranging between 2.5 and 4.3MeV) and two for background measurements (Cu and ^{nat}Te). The detector combines the techniques of a tracking wire chamber for particle identification with a calorimeter for energy and time measurements of the particles.

It is important to carry out $2\nu\beta\beta$ decay studies due to the importance of its input into nuclear models used to calculate the $0\nu\beta\beta$ decay nuclear matrix elements and because it is an irreducible background to the $0\nu\beta\beta$ decay search, with the two processes having the same event topologies. Therefore a precise measurement of the $2\nu\beta\beta$ decay half-life must precede the search for $0\nu\beta\beta$ decay.

In this thesis the measurement of the $2\nu\beta\beta$ decay half-life of ^{100}Mo (which is the main isotope used in NEMO3 with a mass of 6.9kg) is presented, followed by a search for $0\nu\beta\beta$ decay. Using 1471 days of data collected with the NEMO3 detector, the half-life of ^{100}Mo $2\nu\beta\beta$ decay is $T^{2\nu}_{1/2} = [7.02 \pm 0.01(stat) \pm 0.46(syst)] \times 10^{18}$ years and the corresponding nuclear matrix element is $M^{2\nu} = 0.126 \pm 0.004$. This is the world's most precise measurement of the ^{100}Mo $T^{2\nu}_{1/2}$ and $M^{2\nu}$.

No excess of events is observed in the $0\nu\beta\beta$ energy region ($\sim$ 3MeV), therefore a 90% CL (confidence level) limit was set on the $0\nu\beta\beta$ search for the neutrino mass mechanism, right-handed currents and Majoron particle emission modes. The half-life limit for the mass mechanism is $T^{0\nu}_{1/2} > 1.1 \times 10^{24}$ years corresponding to a limit on

the effective Majorona mass of $\langle m_{\nu e} \rangle < 0.3$ - 1.0 eV [1], which is the design sensitivity of NEMO3. This is one of the world's most stringent constraints on the effective Majorana neutrino mass. A half-life limit of $T^{0\nu\lambda}_{1/2} > 5.5 \times 10^{23}$ years is set for the right-handed currents $0\nu\beta\beta$ decay mode, corresponding to one of the world's most stringent results of the right-handed currents admixture parameter, $\langle \lambda \rangle < 1.4 \times 10^{-6}$. A half-life limit of $T^{0\nu\chi^0}_{1/2} > 5.3 \times 10^{22}$ years is set for the main Majoron particle emission mode, corresponding to the world's most stringent bound on the Majoron coupling constant, $\langle g_{\chi^0} \rangle < (0.2 - 0.7) \times 10^{-4}$.

1.2 SuperNEMO

SuperNEMO is based on the technology and experience of the NEMO3 experiment, using a tracker-calorimeter detection technique for particle identification. The detector will hold $\sim$ 100kg of double beta decay source isotopes (^{82}Se is the "baseline" design isotope, with ^{150}Nd and ^{48}Ca being considered depending on enrichment possibilities) to reach a projected sensitivity of 10^{26} years (at 90% CL), corresponding to an effective neutrino mass of 50 - 100meV. One of the main focuses of the SuperNEMO R&D was to obtain a previously unprecedented energy resolution of 4% FWHM at 3MeV (the $Q_{\beta\beta}$ value of ^{82}Se) for the baseline design, which uses calorimeter blocks based on the design of NEMO3. An alternative calorimeter design, known as the "bar" design was considered for the SuperNEMO experiment, using 2m x 10cm x 2.54cm scintillator bars to create multi-layered SuperNEMO modules. The main advantages of the bar design come from the reduction in the number and mass of photomultiplier tubes (PMTs) used ($\sim 11,000$ 8" PMTs for the baseline design and $\sim 5,000 - 7,000$ 3" smaller and lighter PMTs for the bar design), decreasing the background contribution from the PMTs and the cost of the experiment.

In this thesis the R&D of the bar design is presented, focusing on the energy and time resolution test bench measurements of the calorimeter bar unit, with different scintillator, PMT and other parameters considered. An energy resolution of 10% FWHM at 1 MeV and a time resolution of 450ps has been obtained with the calorimeter bar unit. The energy resolution achieved for this size of scintillator is the world's best.

[1] The range in this and other $0\nu\beta\beta$ decay physics parameters is introduced by the uncertainty in the nuclear matrix elements used to extract them, discussed later.

In February 2010 the SuperNEMO collaboration reached the decision to use the block design for the SuperNEMO demonstrator module, which is currently under construction, with the advantages of the block design outweighing those of the bar design. This decision could not have been made informatively without the detailed study of the bar design presented here.

1.3 Author's Contributions

1.3.1 NEMO3 Contributions

- Software development for the main analysis package (correct implementation of the laser time corrections, implementation of laser energy corrections, comparison of results with different versions of reconstructions used for the data and the MC)

- Analysis of ^{100}Mo $2\nu\beta\beta$ decay: half-life measurement of the $2\nu\beta\beta$ decay half-life and extraction of the $2\nu\beta\beta$ nuclear matrix element

- Analysis of ^{100}Mo $0\nu\beta\beta$ decay: search for $0\nu\beta\beta$ decay, half-life limit bounds on the mass mechanism, right-handed currents and Majoron emission $0\nu\beta\beta$ decay modes and the extraction of the corresponding physics parameters

  Not presented in this thesis:

- Study of possible Pauli Exclusion Principle violation

  The plastic scintillators used in NEMO3 contain ^{12}C - a stable nucleus which has fully occupied shells. Using NEMO3 data a search can be carried out to look for transitions of ^{12}C to non-Paulian states and a half-life limit on PEP violation can be extracted. The limit obtained, at 90% CL, is $T_{1/2} > 8.9 \times 10^{25}$ years, an order of magnitude higher than the limit obtained with the NEMO2 experiment [1]. However, the analysis was abandonned due to the Borexino experiment having a superior sensitivity to the process (published in 2010 [2]) because of the larger mass of ^{12}C contained in the detector.

- Data acquisition and calibration shifts for NEMO3

- Reporting results at collaboration meetings

1.3.2 SuperNEMO Contributions

- Bar calorimeter R&D test bench and data acquisition setup
- Validation of the analysis package with simulations
- Characterisation of photomultipliers
- Precision energy and time resolution measurements of various configurations of the scintillator bar unit

  Not presented in this thesis:

- Efficiency simulations for the SuperNEMO tracker Geiger cell geometry
- Physics and efficiency simulations for the SuperNEMO calorimeter bar design, in particular investigating the effect of a magnetic field
- Reporting block and bar calorimeter development results at collaboration meetings and the CALOR 2010 conference

Chapter 2

Neutrino Physics Phenomenology

2.1 The History of the Neutrino

In early nuclear beta decay experiments it was thought that a nucleus A transformed into a lighter nucleus B accompanied by an electron emission ($A \rightarrow B + e^-$). However, the electron was observed to have a spectrum of energies rather than be monochromatic. To explain this phenomenon, in 1930 Wolfgang Pauli proposed the neutrino [3] - an electrically neutral particle emitted alongside the electron that carries off the "missing" energy. In 1933 Enrico Fermi postulated the correct theory for beta (β) decay, which incorporated the neutrino [4]. In the mid-fifties Clyde Cowan and Frederick Reines detected the neutrino at the Savannah River nuclear reactor whilst studying inverse beta decay, confirming the existence of the neutrino [5, 6].

In the 1950s, the Goldhaber-Grodzins-Sunyar experiment [7] at the Brookhaven National Laboratory used circular polarisation and resonant scattering of γ rays following orbital electron capture of ^{152m}Eu to measure the helicity of the neutrino. The findings of the experiment showed the neutrino to be "left-handed" (i.e. emitted with left helicity). As neutrinos are always found to be emitted with left helicity the Standard Model (SM) of particle physics assumes the particle to be massless. In 1957, Bruno Pontecorvo suggested that if neutrinos have non-zero mass then they could oscillate between a neutrino and anti-neutrino (by analogy with the Kaon sector) [8], [9]. This idea was developed into neutrino oscillations between flavour eigenstates by Ziro Maki, Masami Nakagawa and Shoichi Sakata in 1962 [10].

A confirmation of the existence of more than one flavour of neutrinos was made by discovery of the muon neutrino in 1962 by Leon Lederman, Melvin Schwartz and Jack

Streinberger at the Brookhaven National Laboratory [11]. The third neutrino flavour, the tau neutrino, was discovered in 2000 by the DONUT (Direct Observation of NU Tau) experiment at Fermilab [12].

In 1968 Ray Davis used the Homestake mine in South Dakota to observe solar neutrinos [13]. A deficit was seen in the number of neutrinos detected compared to the number expected from theory - only a third of the expected neutrinos was found, implying neutrino oscillations. This deficit became known as the "solar neutrino problem". In 2001 the SNO (Sudbury Neutrino Observatory) experiment, based in Canada, discovered the first compelling evidence of solar neutrino oscillations [14], providing the solution to the solar neutrino problem. The Super-Kamiokande experiment, located in Japan, discovered the first evidence for atmospheric neutrino oscillations in 1998 [15].

The first long baseline accelerator experiment to study neutrino oscillations produced by a controlled artificial source was the K2K (KEK to Kamioka) [16] experiment, which started running in 1999. Accelerator experiments are able to produce neutrino beams of a controlled flavour, energy and flux, allowing the neutrinos' disappearance to be accurately monitored from the point of injection (the KEK accelerator for K2K) to the point of detection (the Super-K detector based in the Kamioka mine for K2K). K2K was the first experiment to confirm ν_μ disappearance, leading to a measurement of the Δm^2_{23} and θ_{23} oscillation parameters. ν_μ disappearance has also been observed by the successful MINOS (Main Injector Neutrino Oscillation Search) experiment [17] (which started running in 2005, using the NuMI (Neutrinos at the Main Injector) main injector at Fermilab to produce a beam of mostly ν_μ, which then travels a distance of 735km to be detected at the Soudan Mine in Minnesota), leading to the world's best results of Δm^2_{23}.

Compelling evidence has been collected to show that the neutrino has mass and undergoes flavour oscillations and mixing.

2.2 Neutrino Mixing and Oscillations

Neutrino mixing is analogous to the Cabibbo-Kobyashi-Masakawa (CKM) mixing in the quark sector and is expressed with the three neutrino flavours (ν_e, ν_μ and ν_τ) as a superposition of the three neutrino mass eigenstates (ν_1, ν_2 and ν_3) via the Pontecorvo-

Maki-Nagawa-Sakate (PMNS) unitary matrix,

$$|\nu_\alpha\rangle = \sum iU_{\alpha i}|\nu_i\rangle, \tag{2.2.1}$$

where ν_α are the neutrino flavour eigenstates, ν_i are the neutrino mass eigenstates and U is the PMNS matrix, represented as

$$\begin{pmatrix} c_{12}c_{13} & s_{12}c_{13} & s_{13}e^{-i\delta} \\ -s_{12}c_{23} - c_{12}s_{23}s_{13}e^{i\delta} & c_{12}c_{23} - s_{12}s_{23}s_{13}e^{i\delta} & s_{23}c_{13} \\ s_{12}s_{23} - c_{12}c_{23}s_{13}e^{i\delta} & -c_{12}s_{23} - s_{12}c_{23}s_{13}e^{i\delta} & c_{23}c_{13} \end{pmatrix} \cdot D_M, \tag{2.2.2}$$

where s_{ij} and c_{ij} are the sine and cosine of the three mixing angles θ_{ij}, δ is the Dirac CP violating phase and D_M is the diagonal Majorana phase matrix,

$$D_M = \begin{pmatrix} 1 & 0 & 0 \\ 0 & e^{i\phi_2} & 0 \\ 0 & 0 & e^{i\phi_3} \end{pmatrix}, \tag{2.2.3}$$

where ϕ_2 and ϕ_3 are the Majorana CP violating phases and only apply to Majorana neutrinos.

For neutrino oscillations, the probability for a neutrino of flavour α to change into flavour β, in vacuum is

$$P(\nu_\alpha \to \nu_\beta) = \left| \sum iU^*_{\alpha i}U_{\beta i}e^{-i\frac{m_i^2 L}{2E}} \right|^2, \tag{2.2.4}$$

where m_i are the neutrino mass eigenstates, $U_{\alpha,\beta}$ are the unitary PMNS matrices, L is the propagation length of the mass eigenstates and E is the neutrino energy. In the simplified two neutrino case the experimental appearance (Equation 2.2.5) and disappearance (Equation 2.2.6) oscillation probabilities become

$$P(\nu_\alpha \to \nu_\beta) = \sin^2 2\theta_{ij} \sin^2 \left(\Delta m^2_{ij}(\text{eV}^2) \frac{1.27L(\text{km})}{E(\text{GeV})} \right) \tag{2.2.5}$$

and

$$P(\nu_\alpha \to \nu_\alpha) = 1 - \sin^2 2\theta_{ij} \sin^2 \left(\Delta m^2_{ij}(\text{eV}^2) \frac{1.27L(\text{km})}{E(\text{GeV})} \right), \tag{2.2.6}$$

Parameter	Value	Neutrino Source	Experiment	Ref.
$sin^2\theta_{12}$	$0.312^{+0.017}_{-0.015}$	solar, reactor	SNO, KamLAND	[23, 28]
$sin^2\theta_{23}$	0.52 ± 0.06	atm., accel.	Super-K, MINOS	[29, 30]
$sin^2\theta_{13}$	$0.013^{+0.007}_{-0.005}$	accel.	T2K, MINOS	[31, 32]
θ_{13}	$< 11^\circ$ at 90% CL	atm., reactor	CHOOZ	[22]
Δm^2_{21}	$(7.59 \pm 0.21) \times 10^{-5}$ eV^2	solar, reactor	SNO, KamLAND	[23, 28]
$\lvert\Delta m^2_{23}\rvert$	$(2.43 \pm 0.13) \times 10^{-3}$ eV^2	atm., accel.	Super-K, MINOS	[29, 30]

Table 2.1: Current best measured neutrino oscillation parameters, with the best global fits to neutrino oscillations found in [33], where an indication of non-zero θ_{13} is based on the global fit of several experiments [33] and a limit on θ_{13} is obtained with the CHOOZ experiment [22].

where $\Delta m^2 = m_i^2 - m_j^2$ and θ and Δm^2 can be extracted from experimental data. So far oscillation parameters have only been measured with neutrino disappearance from solar (with the SNO [18, 19] and Super-Kamiokande [20, 21] experiments), atmospheric (with the Super-Kamiokande [20, 21] experiment), reactor (with the CHOOZ [22] and KamLAND [23, 24] experiments) and accelerator (the K2K [25, 26] and MINOS [27] experiments) neutrino sources. A summary of the current measured parameters can be seen in Table 2.1.

Oscillation parameters will be measured more precisely by the next generation of oscillation experiments. The T2K [34] and NOνA [35] experiments will measure θ_{23} and Δm^2_{23} more precisely. Experiments such as Daya-Bay [36], Double CHOOZ [37], T2K and NOνA will strive to obtain precision measurements of θ_{13}. In June 2011, the T2K (Tokai-to-Kamioka) experiment, which searches for $\nu_\mu \rightarrow \nu_e$ appearance to improve the sensitivity to θ_{13} using an off-axis neutrino beam, reported the first indication of ν_e appearance in data collected before March 2011, when data taking was interrupted by the Japan earthquake [31]. Six ν_e appearance events were observed indicating a non-zero sin$^2 2\theta_{13}$. T2K will aim to resume data collection by the end of 2011 and will be able to provide more insight into this recent finding once more data has been obtained. T2K will also study $\overline{\nu_\mu} \rightarrow \overline{\nu_e}$ appearance. Shortly after the T2K results, the MINOS experiment also reported its $\nu_\mu \rightarrow \nu_e$ appearance results with 62 electron-like events observed with an expected background of 49 events [32]. A global fit to

the data obtained with both MINOS and T2K has a significance of 3σ for a non-zero θ_{13} [38]. CP violation searches with the current generation of oscillation accelerator experiments are limited by hadron production uncertainty. However, if θ_{13} is found to be at the order of $\sim 10^{\circ}$ then future off-axis super beam experiments such as NOνA will start having access to the CP violation phases. CP violation searches will also be made accessible with the next generation of oscillation experiments, which will include neutrino factories providing a neutrino beam of a highly pure flavour, allowing neutrino CP violation effects and mass hierarchy of the neutrino to be studied via matter effects.

2.3 Neutrino Mass

The neutrino mass can be constructed using Dirac or Majorana terms in the electroweak Lagrangian. Combining the two Lagrangians leads to the see-saw mechanism (Section 2.3.3), which justifies the smallness of the neutrino mass compared to that of the other fermions in the SM. The see-saw mechanism assumes very heavy Majorana neutrinos ($\sim 10^{15}$GeV), which may help to explain the matter/anti-matter asymmetry we observe in the Universe today.

2.3.1 The Dirac Mass Term

The SM Higgs-lepton Yukawa coupling with a chirally right-handed singlet field under the SM symmetries generates a Dirac neutrino mass [39]. The field introduced is a singlet, which therefore leads to a "sterile" neutrino. The introduction of only one neutrino singlet field is referred to as the minimally extended SM. However, to represent each lepton generation (e, μ and τ) three chirally right-handed singlet fields are introduced into the Lagrangian, which is written as

$$\mathcal{L}^{D}_{mass} = \overline{\nu_R} M_D \nu_L + H.C., \tag{2.3.1}$$

where M_D is the non-diagonal Dirac mass matrix, $H.C.$ is the Hermitian conjugate, and ν_R and ν_L are the chirally right-handed and left-handed neutrino flavour fields

$$\nu_R = \begin{pmatrix} \nu_{eR} \\ \nu_{\mu R} \\ \nu_{\tau R} \end{pmatrix}, \nu_L = \begin{pmatrix} \nu_{eL} \\ \nu_{\mu L} \\ \nu_{\tau L} \end{pmatrix}. \tag{2.3.2}$$

The Dirac mass construction therefore requires four independent components (ν_L, $\overline{\nu_L}$, ν_R, $\overline{\nu_R}$). The difficulty with the Dirac mass term is the requirement of a sterile neutrino, which cannot be detected. The theory also fails to explain the smallness of the Higgs-neutrino Yukawa coupling relative to the other fermions in the SM.

2.3.2 The Majorana Mass Term

Another approach to constructing the neutrino mass is to construct a massive Majorana neutrino, as first proposed by Ettore Majorana in 1937 [40], which only requires two independent components and can be constructed entirely out of the left-handed (or right-handed) neutrino field. The Lagrangian for a massive Majorana neutrino is

$$\mathcal{L}_{mass}^{M_L} = -\frac{1}{2}\overline{\nu_L^c} M_{M_L} \nu_L + H.C., \tag{2.3.3}$$

where M_{M_L} is the left-handed symmetric Majorana mass matrix and $H.C.$ is the Hermitian conjugate. ν_L^c and ν_L are not independent of each other, therefore a factor of 1/2 is introduced to avoid double counting. ν_L^c is the charge conjugate of ν_L, which satisfies the condition

$$\nu_L^c = C\overline{\nu_L}^{\,T} \quad [39], \tag{2.3.4}$$

where C is the charge conjugation matrix and T indicates a transposed matrix. Another property of this field is that

$$\nu_L^c = P_R \nu^c, \tag{2.3.5}$$

where P_R is the right-handed projection operator, making ν_L^c a right-handed field.

Only two independent components (ν_L^c and ν_L) are required to construct the Majorana neutrino mass compared to the four required for the Dirac mass, making the Majorana mass a simpler theoretical model. The charge conjugate of the field is unchanged, which leads to the neutrino being its own anti-particle. This is only allowed for the neutrino among the other fermions in the SM as it is an electrically neutral particle.

2.3.3 The See-Saw Mechanism

The see-saw mechanism justifies the smallness of the neutrino mass by combining both the Dirac and the Majorana mass terms in the Lagrangian.

$$\begin{aligned}\mathcal{L}_{see-saw} &= \mathcal{L}_D + \mathcal{L}_{M_R}, \\ &= \overline{\nu_R} M_D \nu_L - \frac{1}{2}\overline{\nu_R^c} M_{M_R} \nu_R + H.C., \\ &= -\frac{1}{2}\left(\overline{\nu_L^c}, \nu_R\right) \mathcal{M}_\nu \begin{pmatrix} \nu_L \\ \nu_R^c \end{pmatrix} + H.C.,\end{aligned} \tag{2.3.6}$$

where $\mathcal{M}_\nu$ is the neutrino mass matrix,

$$\mathcal{M}_\nu = \begin{pmatrix} 0 & m_D \\ m_D & m_{M_R} \end{pmatrix}. \tag{2.3.7}$$

$\mathcal{M}_\nu$ is diagonalised to obtain the eigenvalues

$$M_{1,2} = \frac{1}{2} m_{M_R} \pm \sqrt{m_{M_R}^2 + 4m_D^2}\,. \tag{2.3.8}$$

If the Dirac mass, m_D, is of the same order of magnitude as the fermions in the SM and the right-handed Majorana neutrino mass, m_{M_R}, is much heavier than the Dirac neutrino mass term ($m_{M_R} \gg m_D$), then the first approximation of the eigenvalues is

$$M_1 \approx \frac{m_D^2}{m_{M_R}} \tag{2.3.9}$$

and

$$M_2 \approx m_{M_R}. \tag{2.3.10}$$

The see-saw mechanism therefore predicts a left-handed neutrino of a small mass and a heavy right-handed Majorana neutrino partner. Assuming the heavy Majorana neutrino to be at the mass of the Grand Unified Theory (GUT) scale ($\sim 10^{15}$GeV) leads to a light neutrino mass of the order of meV. This theory therefore explains the smallness of the observed light left-handed neutrino compared to that of the other fermions in the SM. The see-saw mechanism could also play a significant role in leptogenesis - the heavy Majorana neutrinos produced at the GUT scale could have decayed in a

CP violating way leading to the matter/anti-matter asymmetry we see today. The see-saw mechanism assumes the nature of the neutrino to be that of a Majorana particle as the Majorana mass term appears in both eigenvalues, implying total lepton number violation (physics beyond the SM).

2.4 Constraints on Neutrino Mass

There are a number of techniques to set the limit on the absolute neutrino mass, which include tritium β decay, cosmological constraints and $0\nu\beta\beta$ decay. Oscillation experiments can also provide constraints on some neutrino mass eigenstates.

2.4.1 Recent Experimental Constraints

A number of independent techniques have been used to set the limit on the absolute neutrino mass. A summary of the current best limits obtained on neutrino mass is shown in Table 2.2.

- Δm^2_{23} (also known as $\Delta m^2_{atmospheric}$) obtained from neutrino oscillation experiments (Table 2.1) implies that at least one of the neutrinos involved in the oscillation must have non-zero mass. This gives a lower bound on the heaviest mass eigenstate of the neutrino to be > 0.05eV ($\sqrt{\Delta m^2_{23}}$).
- Tritium (^{3}H) beta decay,

$$^3\text{H} \rightarrow ^3\text{He} + e^- + \overline{\nu_e}, \tag{2.4.1}$$

produces a β decay energy spectrum. If the neutrino is massless then the tritium decay spectrum would look identical to that of an electron. However, if the neutrino has mass then it will carry off some of the energy available in the decay, decreasing the Q_β value of the spectrum. Measuring the difference between the spectrum produced if $\langle m_\nu \rangle = 0$ and the spectrum produced in tritium decay if $\langle m_\nu \rangle \neq 0$ by looking at the distortion at the end of the β spectrum gives a constraint on the neutrino mass (as demonstrated in Figure 2.1). The spectrum being measured is defined as

$$\frac{dN}{dt} = N(E) = CFp_eE(E_0 - E)^2\sqrt{1 - \frac{m^2_{\overline{\nu_e}}c^4}{(E_0 - E)^2}}, \tag{2.4.2}$$

where C is a constant, F is the Fermi function, p_e is the momentum of the electron, E_0 is the energy of the endpoint of tritium decay and E is the energy of the electron.

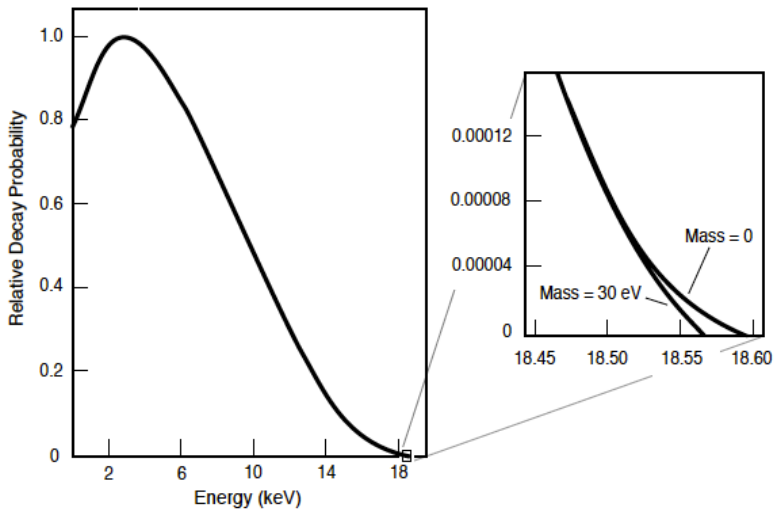

Figure 2.1: Tritium β decay spectra for determining neutrino mass.

To extract the neutrino mass from tritium β-decay a knowledge of the neutrino flavour mixing angles is required, however it is not dependent on the Dirac and Majorana CP violation phases. The neutrino mass is extracted with

$$\langle m_\nu \rangle^2 = \sum i|U_{\alpha i}|^2 m_i^2 = c_{12}^2 c_{13}^2 m_1^2 + s_{12}^2 c_{13}^2 m_2^2 + s_{13}^2 m_3^2 \ [41]. \tag{2.4.3}$$

Measurement of the end point of tritium decay has provided a limit of $\langle m_\nu \rangle < 2.0$eV (at 95% CL), obtained by combining two independent measurements from the Mainz and Troitsk experiments [41, 42]. The main advantage of extracting a limit on the absolute neutrino mass with tritium decay is that it is model independent. However, to measure the spectrum distortion of tritium β decay the counting rate at the end of the spectrum needs to be high, whilst the density of the source needs to be as low as possible. The sensitivity to the mass is dependent on the square root of the size of the vessel used to contain the source. Therefore the size of the vessel used is the limiting factor in the mass sensitivity. It is not expected for tritium decay experiments to reach a neutrino mass limit below 0.3eV.

• Cosmological data can be used to place a limit on the sum of the neutrino masses (Σm_i). Neutrinos are near relativistic and hence place a limit on the size of cosmological structures, such as galaxies (due to the streaming effect). With this information a limit on Σm_i is extracted. From a combination of data sources a limit of $\Sigma m_i < 2$eV (at 95% CL) [43, 44] is obtained. The limits obtained are model dependent. For this result

Parameter	Limit	CL	Reference
Oscillations	> 0.05eV	68%	Heaviest mass eigenstate [20, 27]
$\langle m_\nu \rangle$	< 2.0eV	95%	Tritium decay [42, 41]
Σm_i	< 2eV	95%	Cosmology [43, 44]
$\langle m_{\nu_e} \rangle$	< 0.30eV	90%	$0\nu\beta\beta$ [45]

Table 2.2: Current limits obtained on neutrino mass from oscillation data, tritium β decay, cosmological constraints and $0\nu\beta\beta$ decay.

a flat, isotropic, homogeneous universe made up of ordinary matter, dark matter, dark energy and radiation is assumed. The measurement of Σ also gives access to the neutrino mass hierarchy (Section 2.4.2). If the hierarchy is degenerate ($m_{\nu_1} \approx m_{\nu_2} \approx m_{\nu_3}$) an observable signature in the Cosmic Microwave Background power spectrum would be seen.

The advantage of cosmological neutrino mass measurements is that an extremely large amount of data are available to study, increasing the sensitivity to the mass limit. However, the calculations of the mass limit are heavily model dependent.

- The effective mass obtained from $0\nu\beta\beta$ decay is extracted with

$$\langle m_{\nu_e} \rangle = \left| \sum i U_{\alpha i}^2 m_i \right| = \left| c_{12}^2 c_{13}^2 m_1 + s_{12}^2 c_{13}^2 m_2 e^{2i\phi_2} + s_{13}^2 m_3 e^{2i(\phi_3+\delta)} \right| . \quad (2.4.4)$$

Currently, the best upper bound limit on neutrino mass from double beta decay experiments is $\langle m_{\nu_e} \rangle < 0.30$eV at 90% CL (considering one specific nuclear matrix element chosen by the author) [45] obtained by combining data from the IGEX and the Heidelberg-Moscow experiments (Section 4.2.1). A fraction of the Heidelberg-Moscow experiment published a claim of observing a $0\nu\beta\beta$ signal, discussed in Section 4.2.1.

The advantage of using $0\nu\beta\beta$ decay to extract neutrino mass is that it can reach sensitivities of $\sim$ 50meV with next generation experiments. However, $0\nu\beta\beta$ is dependent on the neutrino being of a Majorana nature. If the neutrino is found to be a Dirac particle then no neutrino mass can be extracted using $0\nu\beta\beta$ decay experiments.

2.4.2 Future Experimental Constraints

The understanding of the neutrino mass can be improved by further study with next generation oscillation, tritium β decay and $0\nu\beta\beta$ decay experiments. Oscillation experiments provide access to the neutrino mixing parameters, the neutrino mass hierarchy and possibly CP violation (for example, via access to θ_{13} with off-axis super beam experiments and neutrino factories).

KATRIN (Karlsruhe Tritium Neutrino Experiment) [46] is a next generation spectrometer tritium β decay experiment, which is about to begin data taking. It scales up the size, precision and intensity of the tritium β decay source used by an order of magnitude compared to previous experiments to reach a neutrino mass sensitivity of $<$ 0.3eV. This is the best sensitivity that can be expected from this type of experiment.

$0\nu\beta\beta$ decay is the only practical experimental approach that gives access to determining the Dirac or Majorana nature of the neutrino. Neutrino parameters such as the CP violating phases and the scale of the absolute neutrino mass are also accessible with $0\nu\beta\beta$ decay. It is a possibility, although an unlikely one, that the neutrino Majorana phases could cancel out to give an effective neutrino mass of zero, in which case no $0\nu\beta\beta$ decay could be observed. $0\nu\beta\beta$ decay can also be a sensitive probe to the absolute neutrino mass eigenstate hierarchy, complimentary to oscillation experiments. Currently we do not know whether the mass hierarchy is "normal" (with $m_{\nu_3} > m_{\nu_2}$ and m_{ν_1}), "inverted" (with $m_{\nu_3} < m_{\nu_2}$ and m_{ν_1}) or "degenerate" (with $m_{\nu_1} \approx m_{\nu_2} \approx m_{\nu_3}$), as shown in Figure 2.2. Figure 2.3 shows the probing of the hierarchy with $0\nu\beta\beta$ decay, where discrimination between hierarchies is shown as a function of the effective neutrino mass obtained from experimental data. A degenerate hierarchy is suggested by Klapdor's claim of observing $0\nu\beta\beta$ decay (Section 4.2.1) [47]. The next generation of $0\nu\beta\beta$ decay experiments will be able to fully probe the degenerate hierarchy, however not all of the inverted hierarchy.

It is crucial to consider information on neutrino mass gathered from all possible sources. A combination of findings from oscillation and $0\nu\beta\beta$ experiments can give some vital answers about the neutrino sector even if no signal is observed. As a hypothetical example, the next generation oscillation N0νA experiment might see that neutrinos have an inverted hierarchy. If a next generation $0\nu\beta\beta$ decay experiment which can reach a sensitivity of 20meV (at which we expect to see the inverted hierarchy) runs

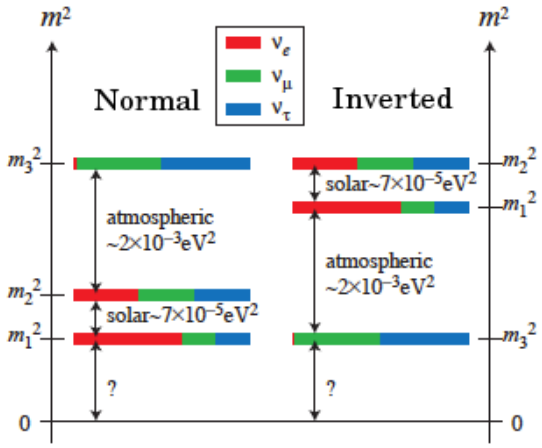

Figure 2.2: The "normal" and "inverted" hierarchies of absolute neutrino mass eigenstates.

Characteristic	Oscillations	β-decay	$0\nu\beta\beta$ decay
Neutrino nature			✓
Absolute mass		✓	✓
Mass hierarchy	✓		✓
Mixing parameters	✓		
Dirac CP violating phase	✓		
Majorana CP violating phase			✓

Table 2.3: Neutrino characteristics and the experimental techniques used to measure them.

but does not see an inverted hierarchy this would lead to the conclusion that neutrinos are not of a Majorana nature.

Table 2.3 summaries the characteristics of the neutrino and which experimental technique they are accessible with.

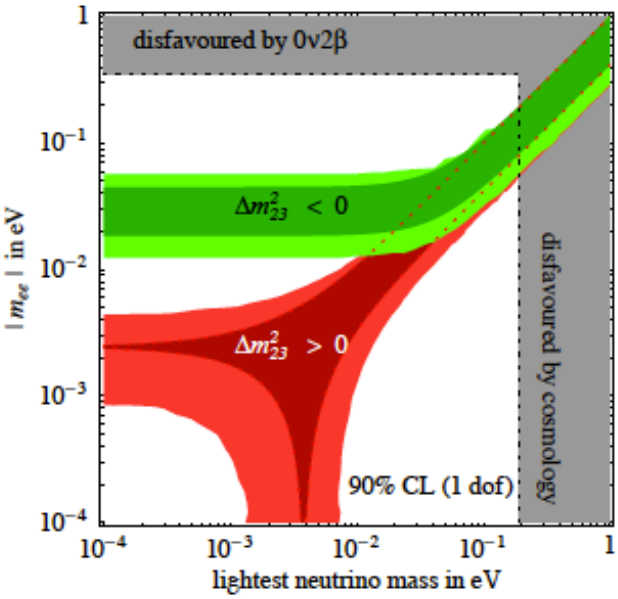

Figure 2.3: The use of $0\nu\beta\beta$ decay for the probing of the neutrino mass eigenstate hierarchy, with the effective electron neutrino mass shown as a function of the lightest mass eigenstate [48].

Chapter 3

Double Beta Decay

3.1 Beta Decay

Single beta (β) decay can occur via three modes, involving electron emission (β^- decay), positron emission (β^+ decay) and electron capture (EC). In β^- decay,

$$n \rightarrow p + e^- + \overline{\nu_e}, \tag{3.1.1}$$

a neutron decays to a proton, causing the emission of an electron and an anti-neutrino. In β^+ decay,

$$p \rightarrow n + e^+ + \nu_e, \tag{3.1.2}$$

a proton decays to a neutron, causing the emission of a positron and an electron neutrino. The process of EC,

$$p + e^- \rightarrow n + \nu_e, \tag{3.1.3}$$

occurs when the nucleus does not contain enough energy to emit a positron. Instead, an electron (usually from the K-shell) is captured by the nucleus, causing the proton to change into a neutron alongside an electron neutrino emission. The captured electron leaves a "hole" in the atomic shell, causing electrons from higher levels to cascade down to fill it. This process is therefore accompanied by X-rays and/or Auger electrons.

These β-decay processes can only occur if the mass of the parent atom is greater than the summed mass of the daughter atom and the particles emitted in the process,

$$Z_i m_p + (A_i - Z_i)m_n + N_i m_e - E_i^B > Z_f m_p + (A_f - Z_f)m_n + N_f m_e - E_f^B, \quad (3.1.4)$$

where m_p, m_n and m_e are the mass of the proton, neutron and electron respectively, E^B is the nuclear binding energy and subscripts i and f denote the initial and final states.

The atomic mass M is calculated with the Semi-Empirical Mass Formula (SEMF) [49] as a function of its mass number A and atomic number Z. The SEMF also provides predictions for allowed and forbidden decay modes and the transition energies involved. The SEMF has six terms - the first is an approximation of the summed mass of all protons and neutrons and the remaining five are corrections to the first approximated term and are the volume, surface, Coulomb, asymmetry and pairing terms. The pairing term maximises the binding energy of even-even nuclei and minimises the binding energy of the odd-odd nuclei as a function of Z, as shown in Figure 3.1. Thus double beta decay can only occur for even-even nuclei. It can occur by going from the ground state (0^+) of the parent nucleus to the ground state (0^+) of the daughter nucleus and, where energetically possible, the excited states (0^+, 2^+) of the daughter nucleus.

3.2 Two Neutrino Double Beta Decay

Two neutrino double beta decay ($2\nu\beta\beta$), proposed by Maria Goeppert-Mayer in 1935 [50], is a process which occurs when single β decay is not energetically favourable (as shown in Figure 3.1). It is a second order process, which conserves electric charge and lepton number and is allowed under the standard electroweak model. In $2\nu\beta\beta$ decay,

$$(A, Z) \rightarrow (A, Z + 2) + 2e^- + 2\overline{\nu_e}, \quad (3.2.1)$$

two neutrons spontaneously decay to two protons, emitting two electrons and two anti-neutrinos (Figure 3.2). $2\nu\beta\beta$ decay occurs in even-even nuclei (which contain an even number of protons and neutrons). The nuclear transition energy of the decay, $Q_{\beta\beta}$, is defined as

$$Q_{\beta\beta} = M(A, Z) - M(A, Z + 2), \quad (3.2.2)$$

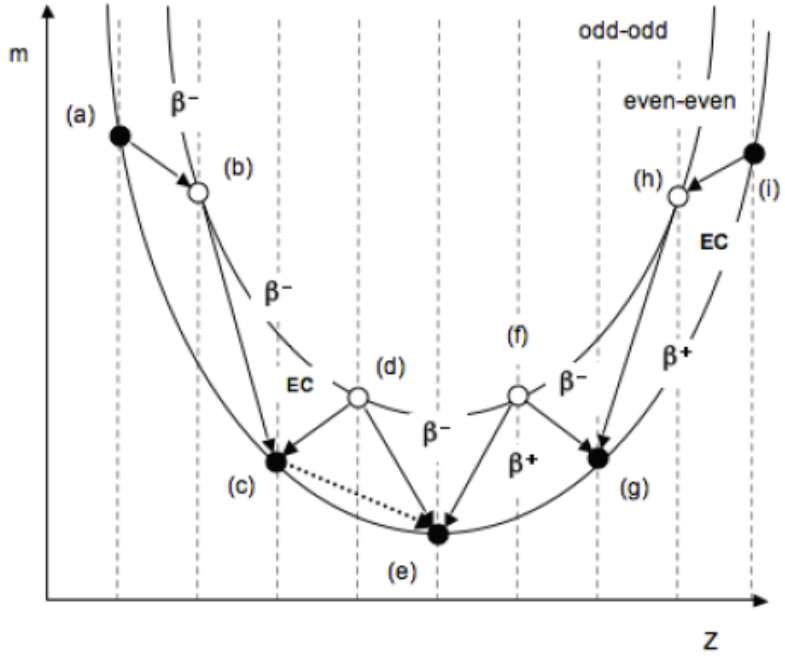

Figure 3.1: The two parabolas showing energetically allowed beta and double-beta decays for an arbitrary decay chain, where (e) is stable with the lowest mass, the transition (c) → (d) is energetically forbidden as the mass of (d) is greater than that of (c) and double beta decay allows the transition of (c) → (e).

where $M(A, Z)$ and $M(A, Z+2)$ is the mass of the initial and final atom respectively.

The half-life of $2\nu\beta\beta$ decay is given by

$$[T^{2\nu}_{1/2}]^{-1} = G^{2\nu} \left| M^{2\nu} \right|^2 , \tag{3.2.3}$$

where $G^{2\nu}$ is the precisely calculable phase space, obtained by taking the integral over momenta and angles of all possible final state particles emitted in the decay, and $M^{2\nu}$ is the the $2\nu\beta\beta$ nuclear matrix element (NME), which is the theoretically calculated transition probability between the initial and final nuclear states of the decay. $M^{2\nu}$ calculations are model dependent, therefore comparison of theoretically calculated and experimentally extracted values is crucial to tune the $M^{2\nu}$ calculation. NME models are further discussed in Section 3.4.

The experimental signature of $2\nu\beta\beta$ decay is a continuous spectrum of energies from the two final state electrons (originating from the same vertex) in the decay, with the end point of the spectrum equal to the $Q_{\beta\beta}$ value of the isotope.

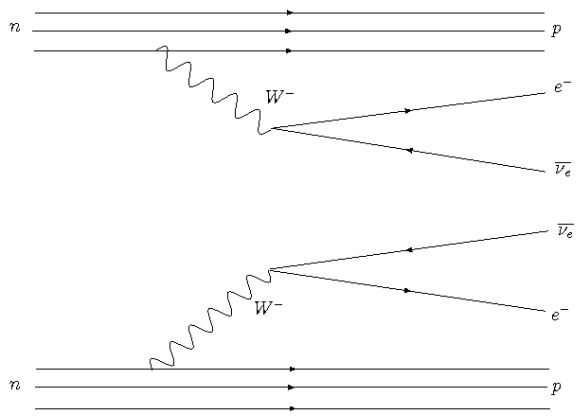

Figure 3.2: Feynman diagram of two neutrino double beta ($2\nu\beta\beta$) decay - a process which conserves electric and leptonic charge and is allowed in the Standard Model.

3.3 Neutrinoless Double Beta Decay

Guilio Racah [51] first proposed neutrinoless double beta ($0\nu\beta\beta$) decay in 1937 to test Majorana's theory of neutrinos being Majorana particles. By 1939 Wendell Furry calculated the transition probabilities for $0\nu\beta\beta$ decay [52]. In $0\nu\beta\beta$ decay,

$$(A, Z) \rightarrow (A, Z + 2) + 2e^{-}, \tag{3.3.1}$$

only two electrons are emitted during the process, with no neutrinos in the final state (Figure 3.3). This process therefore violates total lepton number conservation and is forbidden in the SM. During the decay a virtual right-handed Majorana neutrino (comparable to a Dirac anti-neutrino) is emitted from one vertex and absorbed at the the other as a virtual left-handed Majorana neutrino. In order for this to happen the right-handed Majorana neutrino has to flip helicity to turn into a left-handed Majorana neutrino in order to conserve angular momentum. This can only be done by selecting a frame of reference that is moving faster than the neutrino, requiring the Majorana neutrino to have mass. The probability of the second vertex being in a frame of reference for this to happen is proportional to the squared mass of the neutrino. Therefore, for $0\nu\beta\beta$ decay to occur the neutrino must have mass and must be of a Majorana nature ($\nu_e = \overline{\nu_e}$).

The half-life of $0\nu\beta\beta$ decay is given by

$$[T^{0\nu}_{1/2}]^{-1} = G^{0\nu} \left| M^{0\nu} \right|^2 \eta^2_{LV}, \tag{3.3.2}$$

where $G^{0\nu}$ is the precisely calculable phase space, $M^{0\nu}$ is the the $0\nu\beta\beta$ NME and η_{LV}

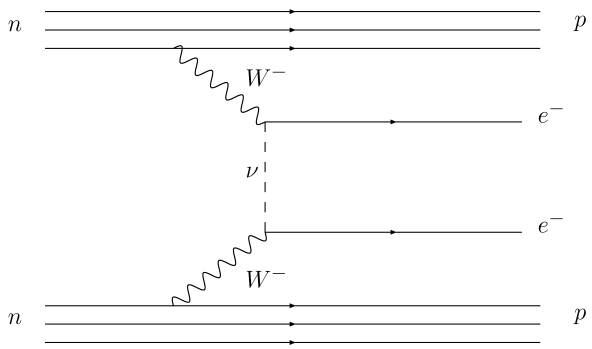

Figure 3.3: Feynman diagram of neutrinoless double beta ($0\nu\beta\beta$) decay - a process which violates total lepton number conservation and is forbidden in the Standard Model. There is a factor of $U_{\alpha i}$ (Equation 2.4.4) at each $W^{-}\nu e^{-}$ vertex of the diagram.

is the lepton number violating parameter, which takes on a different form depending on which $0\nu\beta\beta$ decay mechanism is behind it and is $\langle m_{\nu_e} \rangle$ for the mass mechanism (Section 3.3.1), $\langle \lambda \rangle$ and $\langle \eta \rangle$ for the right-handed currents (Section 3.3.2) and $\langle g_{\chi^o} \rangle$ for Majoron emission (Section 3.3.3). Measurements of the $\langle m_{\nu_e} \rangle$, $\langle \lambda \rangle$ and $\langle g_{\chi^o} \rangle$ lepton violating physics parameters are presented in this thesis.

Other more exotic modes of $0\nu\beta\beta$ decay also exist, such as doubly charged Higgs [53], R-parity violating SUSY [54] and leptoquarks.

The experimental signature of $0\nu\beta\beta$ decay (for all modes except Majoron particle emission, Section 3.3.3) is that of two electrons originating at a common vertex with the energy sum equal to the $Q_{\beta\beta}$ value of the isotope being looked at, resulting in a peak seen in the distribution, the width of which is determined by the energy resolution of the experiment.

3.3.1 The Neutrino Mass Mechanism

The neutrino mass mechanism, where the right-handed Majorana neutrino must flip helicity to become a left-handed Majorana neutrino which requires the neutrino to have mass, is the most discussed scenario for the production of $0\nu\beta\beta$ decay as it requires the fewest modifications to the SM. The half-life of the $0\nu\beta\beta$ mass mechanism is expressed as

$$[T^{0\nu}_{1/2}]^{-1} = G^{0\nu} \left| M^{0\nu} \right|^2 \left(\frac{\langle m_{\nu_e} \rangle}{m_e} \right)^2, \tag{3.3.3}$$

where $G^{0\nu}$ is the precisely calculable phase space, $M^{0\nu}$ is the $0\nu\beta\beta$ NME, $\langle m_{\nu_e} \rangle$ is the

effective Majorana neutrino mass and m_e is the electron rest mass. $G^{0\nu}$ is proportional to $Q^5_{\beta\beta}$ and the atomic number Z [55], therefore $0\nu\beta\beta$ rates are higher for isotopes with high $Q_{\beta\beta}$ values. $G^{0\nu}$ is limited by the kinematics of the virtual neutrino exchanged in the decay and is much lower than the phase space available for $2\nu\beta\beta$ decay, which is proportional to $Q^{11}_{\beta\beta}$. There is much uncertainty in the value of $M^{0\nu}$, which is required to extract $\langle m_{\nu_e} \rangle$ from experiments. This is further discussed in Section 3.4.

3.3.2 Right-Handed Currents

Another proposed $0\nu\beta\beta$ decay mechanism, which leads to two electrons in the final state, is known as the right-handed currents mechanism. The electroweak Lagrangian of the SM contains only left-handed chiral states (due to the V-A structure found in nature). Theories beyond the SM predict the existence of pure right-handed W bosons (W_R) or W bosons which are a mix of right-handed and left-handed W bosons ($W = W_R + W_L$) [56] by adding a small admixture of V+A currents (i.e. right-handed chiral states) into the Lagrangian. If W_R exists and the neutrino is a Majorana particle, then the neutrino can interact at the second vertex of Figure 3.3 without the need for a helicity flip. Two new physics parameters are introduced with the right-handed currents mechanism - $\langle \lambda \rangle$, the right chiral state coupling of the right-handed quarks to the right-handed leptons (related to the ratio of W_R and W_L), and $\langle \eta \rangle$, the coupling of the right-handed quarks to the left-handed leptons (related to the mixing angle between W_R and W_L).

The $\langle \lambda \rangle$ parameter is extracted in the analysis presented in this thesis. This is because only monte carlo simulations generated with the $\langle \lambda \rangle$ admixture parameter are available in the GENBB generator used for NEMO3. In this case the $\langle \eta \rangle$ parameter is set to zero and $\langle \lambda \rangle$ is extracted using

$$[T^{0\nu\lambda}_{1/2}]^{-1} = G^{0\nu\lambda} |M^{0\nu\lambda}|^2 \langle \lambda \rangle^2. \tag{3.3.4}$$

3.3.3 Majoron Particle Emission

Some extensions to the SM exist in which global Baryon-Lepton (B-L) symmetry is spontaneously broken, leading to a prediction of a massless Goldstone boson which couples to the neutrino, known as the "Majoron" [57]. Single, doublet and triplet models were postulated [58] but the doublet and triplet models were excluded with the

measurement of the Z boson width at LEP [59]. The singlet and dominantly singlet Majoron models remain, predicting a coupling of a Majoron to a neutrino. The singlet models require severe fine tuning as the coupling strength,

$$g = (m_{\nu_L}/M_{B-L}) \text{ [60]}, \tag{3.3.5}$$

where m_{ν_L} is the mass of the light neutrino and M_{B-L} is the symmetry-breaking scale, is at the symmetry-breaking scale, which is higher than the electro-weak scale at $\sim$ 90GeV. New Majoron models have been constructed, where the term "Majoron" has been redefined to mean a light or massless boson which weakly couples to the neutrino. There is no constraint on this Majoron being a Goldstone boson.

The existing Majoron models are referred to by their spectral index (n), which shows the phase space dependence on the energy realeased in the decay by

$$G^{0\nu} \propto (Q_{\beta\beta} - E_{sum})^n, \tag{3.3.6}$$

where E_{sum} is the sum of the kinetic energies of the two electrons emitted in the decay. Spectral index $n = 1$ refers to the models which involve one Majoron emission [58, 61], $n = 2$ refers to models which involve the "bulk" Majoron (in the context of the "brane-bulk" scenario) [62], $n = 3$ refers to models which involve the emission of one or two massless lepton number carrying Majorons [58, 63, 64] and $n = 7$ refers to models where two light Majorons are emitted [58, 63, 64]. The energy of the final state electrons of these models forms four distinguishable distributions, shown in Figure 3.4.

The half-life of $0\nu\beta\beta$ Majoron emission mechanism is given by

$$[T^{0\nu\chi^0}_{1/2}]^{-1} = G^{0\nu\chi^0}|M^{0\nu}|^2\langle g_{\chi^0}\rangle^2, \tag{3.3.7}$$

where $\langle g_{\chi^0}\rangle$ is the Majoron to neutrino coupling.

The extraction of the g_{χ^0} parameter for the $n = 1$ Majoron emission mode only is presented in this thesis as it is the only mode for which the relevant NMEs have been calculated.

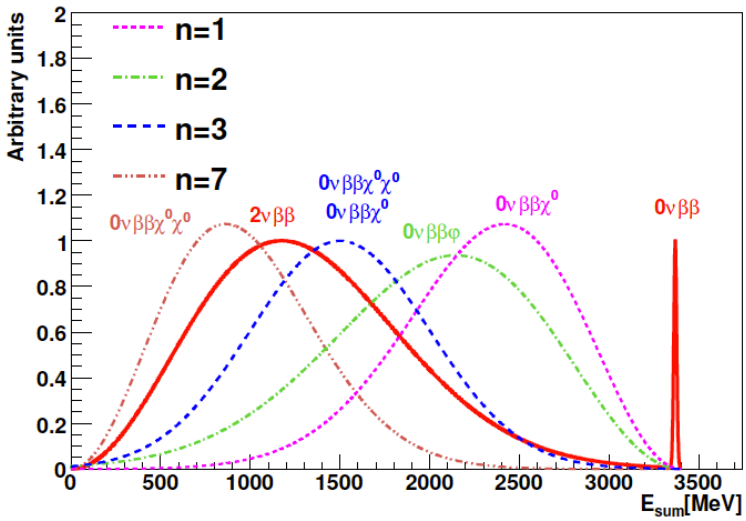

Figure 3.4: Energy spectra for $2\nu\beta\beta$, $0\nu\beta\beta$ neutrino mass mechanism and $0\nu\beta\beta$ Majoron emission mode (for spectral index n = 1, 2, 3 and 7) decay [65].

3.4 Nuclear Matrix Elements

The precision with which $\langle m_{\nu_e} \rangle$ (and other $0\nu\beta\beta$ decay physics parameters) can be experimentally extracted from Equation 3.3.2 depends on the half-life measurement of $0\nu\beta\beta$ decay and the precision of the NME. The largest uncertainty comes from the calculation of the NME, which is model dependent. NME calculations are carried out by solving the many-body Schrodinger equation and accounting for the dynamics of each nucleon-nucleon interaction given the total initial and final state nuclear wavefunctions, which there are a great number of for $\beta\beta$ decay. The intermediate state interactions must also be taken into consideration. Various approximations of the nucleon-nucleon interactions and neglecting of second order effects such as the spin quantum number are used as solutions to the complicated calculations.

Although there is no one-to-one correspondance between the $2\nu\beta\beta$ matrix element, $M^{2\nu}$, and $M^{0\nu}$, calculations of $M^{0\nu}$ can be informed by $M^{2\nu}$, which can be experimentally extracted.

Some of the successful models to date include the nuclear shell model (NSM), the quasiparticle random approximation (QRPA), the projected Hartree-Fock-Bogoluibov (PHFB) and the microscopic interacting boson (IBM-2) models.

3.4.1 The Nuclear Shell Model

The NSM postulates few single-particle orbitals (which the calculations are performed on) around a relatively large inert core and includes arbitarily complex corrections. The NSM is a useful model for calculating single particle states close to the Fermi level and has difficulty for calculations of deformed nuclei (such as ^{150}Nd) and heavy isotopes. The NSM is considered to be more reliable for light nuclei, such as ^{48}Ca, ^{76}Ge and ^{82}Se.

3.4.2 The Quasiparticle Random Phase Approximation

The QRPA is the reverse of the NSM, with many single-particle orbitals around a relatively small inert core and includes fewer corrections, reducing the complexity of the model. The QRPA model calculates the $0\nu\beta\beta$ NME by connecting initial and final states of $0\nu\beta\beta$ decay with the intermediate virtual excitation states. The NME is calculated using

$$M^{0\nu} = M_{GT} - \frac{M_F}{g_A^2} + M_T, \tag{3.4.1}$$

where M_{GT}, M_F and M_T are the contributions from the Gamow-Teller, Fermi and tensor matrix elemets respectively and g_A is the effective axial coupling usually set to $g_A = 1.25$. Parameters for the particle-particle (g_{pp}), which is correlated to the proton-proton interaction, and particle-hole (g_{ph}), which is correlated to the proton-neutron interaction, pairing interactions must also be introduced into the calculation. The value of g_{ph} is generally set to $g_{ph} \approx 1$ to reproduce the experimentally measured excitation energy of the Gamow-Teller giant resonance. The value of g_{pp} is either left as a free parameter, making the calculations of $M^{0\nu}$ unstable, or set to the experimentally measured rate of $2\nu\beta\beta$ decay (or the intermediate rate of β decay), greatly reducing the uncertainty associated with variations in the QRPA model [66]. The QRPA model has more success for the heavier isotopes compared to the NSM. The QRPA model is unstable against the increase of proton-neutron correlations. Model extensions have been proposed to stabilise the solutions, discussed in [67, 68, 69].

The NSM and QRPA models are complimentary to each other and after the inclusion of short-range correlations in the NSM in 2007 [70, 71] the consistency between the NSM and QRPA models improved, as shown in Figure 3.5.

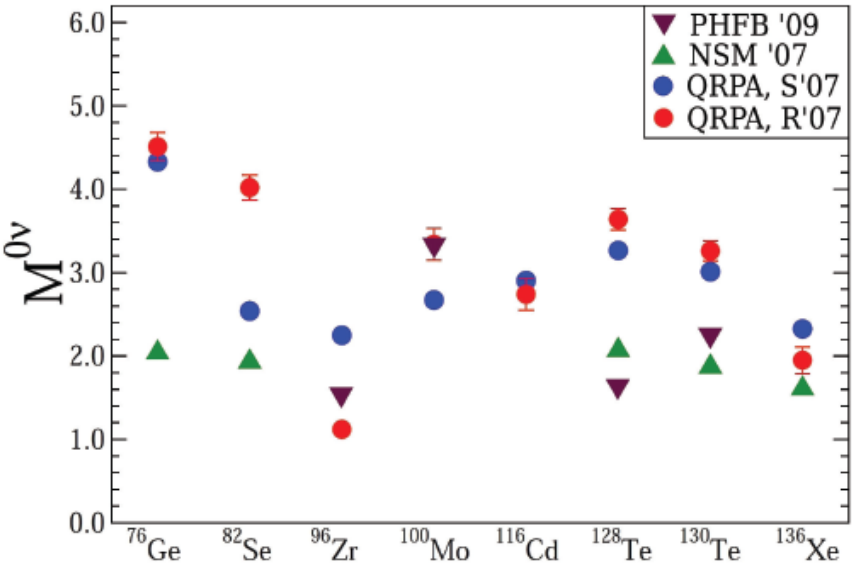

Figure 3.5: Nuclear matrix element calculations with the NSM [71], the QRPA model calculations by Rodin *et al.* [66] and Suhonen *et al.* [72] and the PHFB model [73].

3.4.3 The Projected Hartree-Fock-Bogoliubov Model

In the PHFB model $M^{2\nu}$ and $M^{0\nu}$ are calculated with fewer model dependent parameters and it is therefore advantageous. The model includes nuclear deformation degrees of freedom, which has a significant effect on the quenching of $M^{2\nu}$ [73, 74]. The PHFB model only allows neutron pairs with angular momenta 0^+, 2^+, 4^+ etc. to be transformed into two protons in the $0\nu\beta\beta$ decay process. The pairs that are different to 0^+ are strongly suppressed compared to the LSM and QRPA models. NMEs obtained with the PHFB model can be seen in Figure 3.5, compared to those obtained with the NSM and QRPA models.

3.4.4 The Microscopic Interacting Boson Model

The IBM-2 model is quite restrictive and only allows neutron pairs with angular momenta 0^+ and 2^+ to be transformed into two protons in $0\nu\beta\beta$ decay. The model aims to use realistic wavefunctions of initial and final nuclei which accurately describe the known properties of the nuclei the NME is being calculated for. Good agreement is found between the QRPA and IBM-2 models, as shown in Figure 3.6.

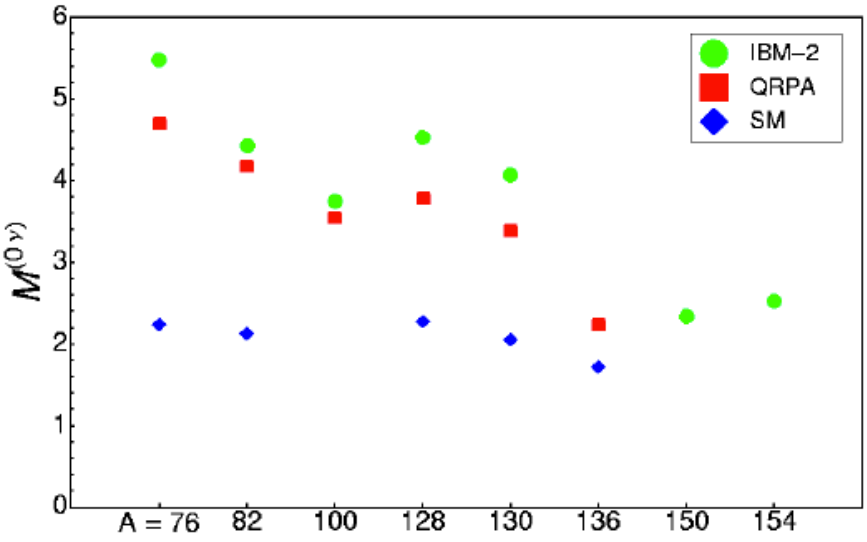

Figure 3.6: Nuclear matrix element calculations with the NSM [75], QRPA [76] and IBM-2 [77] models.

Chapter 4

Double Beta Decay Experimental Techniques and Status

4.1 Half-life Sensitivity

The challenge of double beta decay experiments is to search for the $0\nu\beta\beta$ peak in the summed electron energy distribution within the continuum of the $2\nu\beta\beta$ decay and natural radioactive backgrounds. The half-life sensitivity (in years) for $0\nu\beta\beta$, in terms of experimentally accessible quantities, is given by

$$T_{1/2}^{0\nu} > \frac{ln2 \cdot N_A \cdot a}{W} \frac{\eta}{\kappa_{CL}} Mt \tag{4.1.1}$$

for the case where there is zero background to the experiment and

$$T_{1/2}^{0\nu} > \frac{ln2 \cdot N_A \cdot a}{W} \frac{\eta}{\kappa_{CL}} \sqrt{\frac{Mt}{N_{bkg}\Delta E}}, \tag{4.1.2}$$

for the case where there is non-zero background to the experiment, where N_A is Avogadro's number, a is the isotopic abundance, W is the molar mass of the source, M is the total mass of the source, η is the detection efficiency (after passing all event selection criteria), t is the exposure time and κ_{CL} is the number of standard deviations corresponding to a given confidence level (usually 1.64σ for a 90% CL for the case of non-zero background experiments and 2.3 for a 90% CL for the case of zero background experiments). ΔE is defined as the energy window of the $0\nu\beta\beta$ decay at the $Q_{\beta\beta}$ value and can be approximated by the energy resolution of the detector in keV. N_{bkg} is the number of background events (for the case with non-zero background) in

$\text{kg}^{-1}\text{keV}^{-1}\text{yr}^{-1}$. The total number of background events, N_B, after accounting for the detector acceptance of background events, for a time interval t is then given by

$$N_B = N_{bkg} M t \Delta E \tag{4.1.3}$$

If an experimental condition of zero background can be achieved (Equation 4.1.1) then the sensitivity grows linearly with the mass M of the source and the exposure time t. For the case of non-zero background experiments (Equation 4.1.2) the sensitivity grows as a square root with the mass M of the source and exposure time t, and the number of background events N_{bkg} per unit mass and energy per year and the energy resolution ΔE of the experiment play an important part in the sensitivity. In particular, the product of $N_{bkg}\Delta E$ is one of the dominant factors that defines the experiment's sensitivity to $0\nu\beta\beta$ decay.

One of the main focuses of experimental techniques used to search for $0\nu\beta\beta$ decay is therefore background suppression, with typical $0\nu\beta\beta$ half-lives being $> 10^{25}$ years and natural radioactivity half-lives being $\sim 10^{10}$ years. Background suppression and other factors that contribute to the sensitivity of $0\nu\beta\beta$ decay experiments are the following, based on Equation 4.1.2:

- Mt: To reach an effective Majorana neutrino mass of 50meV $\sim$ 100kg of enriched isotope is required. Future experiments hoping to reach a sensitivity of $\sim$ few meV require $>$ 1 ton of isotope. To increase the product of Mt a long exposure time and/or a large isotope mass are required.

- N_{bkg}:

  - One of the largest concerns for $0\nu\beta\beta$ decay searches in the region of $0\nu\beta\beta$ decay are ^{208}Tl ($Q_\beta = 4.99$MeV) and ^{214}Bi ($Q_\beta = 3.27$MeV) originating from the natural radioactivity chains of ^{232}Th and ^{238}U respectively. To suppress natural radioactivity background source isotopes with $Q_{\beta\beta} > 2.6$MeV are preferable, which is the energy of the highest γ-line occurring in the natural radioactivity decay chains (from ^{208}Tl) and reduces the level of background by $\sim$ an order of magnitude. The isotope and detector components themselves must also have high radiopurity ($<$ mBq/kg) to suppress natu-

ral radioactivity. Future experiments hoping to reach a sensitivity of $\sim$ few meV require a radiopurity of well below μBq/kg.

- Experiments must be located underground or underneath a large overburden of rock (typically $>$ 2500 metre water equivalent) to suppress backgrounds from cosmic muons.
- Experiments must have additional shielding to suppress external backgrounds originating from the surrounding environment. The backgrounds originate from γs coming from the surrounding rock and neutrons coming from spontaneous fission of Uranium in the surrounding rocks and (α,n) reactions on light elements.
- Event reconstruction, particle identification and event topologies are required for background suppression.

- a: Isotopes with a large $Q_{\beta\beta}$ value ($>$ 2.6MeV) are desirable to separate the $0\nu\beta\beta$ decay region of interest from the lower energy backgrounds (as described above) and to increase the phase space available for the decay, which is proportional to $|\eta_{LV}|^2$ (where η_{LV} is the lepton number violating parameter, Equation 3.3.2). The isotopes should have as high a natural abundance as possible or the means for the isotope to be enriched. Table 4.1 shows a summary of the main isotopes used for $0\nu\beta\beta$ decay experiments and their enrichment possibilities with the techniques of gas centrifugation, laser enrichment and electromagnetic separation. The reliability of NME calculations are essential for extraction of the effective Majorana neutrino mass and other $0\nu\beta\beta$ physics parameters.

- ΔE: $2\nu\beta\beta$ decay is an irreducible background to searches for $0\nu\beta\beta$ therefore a good energy resolution is required to provide separation between the $2\nu\beta\beta$ tail and the $0\nu\beta\beta$ peak and to suppress other radioactive backgrounds. The product of the background events observed and the energy resolution of the experiment is one of the most important factors contributing to the sensitivity of an experiment. Some experiments (such as ^{76}Ge based semiconductor experiments, Section 4.2.1) focus on the ΔE, whilst others focus more on background suppression. For example, the Heidelberg-Moscow (H-M) ^{76}Ge (Section 4.2.1) ex-

Isotope	$Q_{\beta\beta}$ (keV)	NA (%)	Enrichment Possibilities
^{48}Ca $\rightarrow$ ^{48}Ti	4272	0.19	EMS is currently the only option, with LE being looked at.
^{76}Ge $\rightarrow$ ^{76}Se	2039	7.8	GC is well established.
^{82}Se $\rightarrow$ ^{82}Kr	2996	9.2	GC is well established.
^{96}Zr $\rightarrow$ ^{96}Mo	3350	2.8	EMS is currently the only option, with LE being looked at.
^{100}Mo $\rightarrow$ ^{100}Ru	3034	9.6	GC is well established.
^{116}Cd $\rightarrow$ ^{116}Sn	2805	7.5	GC is well established.
^{130}Te $\rightarrow$ ^{130}Xe	2529	33.8	GC is well established but not necessary due to high NA.
^{136}Xe $\rightarrow$ ^{136}Ba	2459	8.9	GC is well established and cheapest for ^{136}Xe as it is already a gas.
^{150}Nd $\rightarrow$ ^{150}Sm	3367	5.6	EMS is currently the only option, with LE and GC being looked at.

Table 4.1: Isotopes used in $0\nu\beta\beta$ decay with the transition of the isotope, the $Q_{\beta\beta}$ value (in keV), the natural abundance (NA, in %) and the enrichment possibilities of the isotope, where GC is gas centrifugation, LE is laser enrichment and EMS is electromagnetic separation (only possible for small quantities of isotope).

periment has a N_{bkg} of 0.2kg^{-1}keV^{-1}yr^{-1} and a ΔE of 0.2% at 2039keV (corresponding to 4.1keV) therefore $N_{bkg}\Delta E$ = 0.8. In comparison, the NEMO3 tracker calorimeter experiment (Section 4.3.2), which uses a range of isotopes, has a N_{bkg} of $\sim$ 0.0007kg^{-1}keV^{-1}yr^{-1} and a ΔE of $\sim$ 8% at 3000keV (corresponding to 240keV) therefore $N_{bkg}\Delta E$ = 0.2. Whilst the H-M has a much better ΔE NEMO-3 has a much lower N_{bkg} counting rate, but when taking the product of the two into consideration the sensitivity of the experiments is comparable.

- η: Experiments must have as high a detection efficiency for double beta decay as possible.

Double beta decay experiments are divided into two main categories: homogeneous experiments (where the source itself is the detector) and heterogeneous experiments (where the source and the detector are distinct). Homogeneous experiments (discussed in Section 4.2) generally give very good energy resolution, whereas heterogeneous experiments (discussed in Section 4.3) include tracking detectors providing better particle identification.

The most precise $2\nu\beta\beta$ decay half-life measurements obtained with recent experiments are summarised in Table 4.2. Recently past $0\nu\beta\beta$ decay experiments and the limits they have reached on the effective Majorana neutrino mass are summarised in Table 4.3. Next generation and future planned experiments and their projected sensitivities for the effective neutrino mass are summarised in Table 4.4. The references for the experiments mentioned below can be found in the fore mentioned tables.

4.2 Homogeneous Design Experiments

The main advantages of a homogeneous design experiment are a high energy resolution, good detection efficiency and a relatively compact design and therefore good radiopurity. The main disadvantages of this design are poor event reconstruction and particle identification. Homogeneous systems include semiconductor detectors, bolometers and scintillator detectors.

4.2.1 Semiconductor Experiments

Semiconductor germanium (Ge) detectors are among the most popular $0\nu\beta\beta$ decay experiments due to the high energy resolution that they can achieve. An established

Experiment	Isotope	$T^{2\nu}_{1/2}$(yr)	Ref.
NEMO3	^{48}Ca	$(4.4 \pm 0.6) \times 10^{19}$	[78]
H-M	^{76}Ge	$(1.5 \pm 0.1) \times 10^{21}$	[79]
NEMO3	^{82}Se	$(9.6 \pm 1.0) \times 10^{19}$	[80]
NEMO3	^{96}Zr	$(2.35 \pm 0.21) \times 10^{19}$	[81]
NEMO3	^{100}Mo	$(7.02 \pm 0.46) \times 10^{18}$	This Work
NEMO3	^{116}Cd	$(2.88 \pm 0.17) \times 10^{19}$	[78]
NEMO3	^{130}Te	$(7.0 \pm 1.4) \times 10^{20}$	[82]
NEMO3	^{150}Nd	$(9.11 \pm 0.68) \times 10^{18}$	[83]
EXO-200	^{136}Xe	$(2.1 \pm 0.2) \times 10^{21}$	[84]

Table 4.2: A summary of the best $2\nu\beta\beta$ half-life measurements obtained with recent $\beta\beta$ decay experiments. The ^{100}Mo $2\nu\beta\beta$ half-life is the result of the analysis presented in this thesis.

Experiment	Isotope	Mass	kg·yr	$T^{0\nu}_{1/2}$(yr)	$\langle m_{\nu_e} \rangle$(eV)	Ref.
ELEGANT VI	^{48}Ca	7.6g	0.025	$> 5.8 \times 10^{22}$	$< 3.5 - 22$	[85]
H-M	^{76}Ge	11kg	71.7	1.19×10^{25}	0.44	[47]
IGEX	^{76}Ge	8.4kg	10.1	1.6×10^{25}	$0.33 - 1.35$	[86]
NEMO3	^{82}Se	932g	4.19	$> 3.2 \times 10^{23}$	$< 0.94 - 2.6$	[87]
NEMO3	^{96}Zr	9.4g	0.031	$> 9.2 \times 10^{21}$	$< 7.2 - 19.5$	[81]
NEMO3	^{100}Mo	6.9kg	27.8	$> 1.1 \times 10^{24}$	$< 0.3 - 1.0$	This Work
CUORICINO	^{130}Te	11kg	19.75	$> 2.8 \times 10^{24}$	$< 0.30 - 0.71$	[88]
NEMO3	^{150}Nd	37g	0.094	$> 1.8 \times 10^{22}$	$< 4.0 - 6.3$	[83]

Table 4.3: A summary of the best limits on effective Majorana neutrino mass (at 90% CL) obtained with recent $0\nu\beta\beta$ decay experiments, including the measurement presented in this thesis. The $\langle m_{\nu_e} \rangle$ limits have been quoted from the references specified, where the authors have chosen a range of or one NME for the calculations.

Experiment	Isotope	Mass (kg)	Type	$\langle m_{\nu_e} \rangle$(meV)	Ref.
GERDA-I	^{76}Ge	18	Semiconductor	600	[89]
GERDA-II	^{76}Ge	40	Semiconductor	100	[89]
MAJORANA	^{76}Ge	30-60	Semiconductor	70 - 200	[90]
CUORE	^{130}Te	200	Bolometer	40 - 90	[91]
CANDLES III	^{48}Ca	0.2	Scintillator	500	[92]
SNO+	^{150}Nd	56	Liquid Scint.	100	[93]
KamLAND-Zen	^{136}Xe	400	Liquid Scint.	40-80	[94]
EXO-200	^{136}Xe	200	Liquid Xe TPC	100-200	[95]
SuperNEMO	^{82}Se	100	Tracker-Calor.	50-100	[96]
1ton Ge	^{76}Ge	1000	Semiconductor	10-40	[89, 90]
COBRA	^{116}Cd	140	Semiconductor	45	[97]
CANDLES	^{48}Ca	3	Scintillator	100	[98]
EXO	^{136}Xe	1000	Liquid Xe TPC	30-60	[99]
NEXT-100	^{136}Xe	100	Gas HPTPC	100-140	[100]
DCBA:MTD-1	^{150}Nd	32	TPC	100	[101]
DCBA:MTD-50	^{150}Nd	600	TPC	30	[101]
MOON-I	^{100}Mo	30	TPC	160	[102]
MOON-II	^{100}Mo	120	TPC	100	[102]
MOON-III	^{100}Mo	480	TPC	45	[102]

Table 4.4: A summary of effective Majorana neutrino mass limits for next generation $0\nu\beta\beta$ experiments currently under construction and which are due to start/have started data taking (top) and future planned/in the R&D phase (bottom). The $\langle m_{\nu_e} \rangle$ limits have been quoted from the references specified, where the authors have chosen a range of or one NME for the calculations.

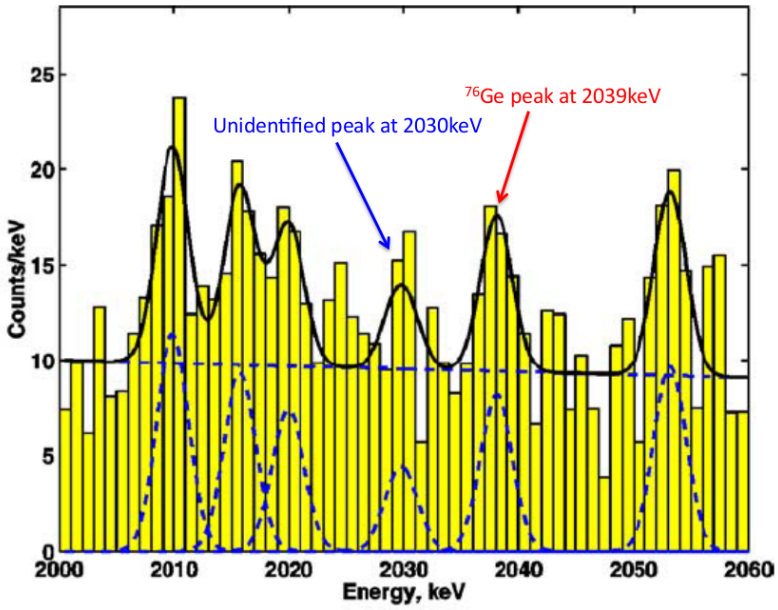

Figure 4.1: The claim for a $0\nu\beta\beta$ signal of ^{76}Ge seen at 2039keV by a subset of the Heidelberg-Moscow collaboration [47]. An identified peak is seen at 2030keV and the ^{214}Bi peaks are seen at 2011, 2017, 2022 and 2053keV.

enrichment process for large quantities is available for ^{76}Ge. The isotope also has good efficiency and its NME is considered reliable. The Heidelberg-Moscow (H-M) and IGEX (International Germanium EXperiment) experiments have obtained some of the most stringent limits on $\langle m_{\nu_e} \rangle$, as shown in Table 4.3.

The Heidelberg-Moscow experiment ran from 1990 to 2003, with 11.5kg of ^{76}Ge (enriched to 86%). In 2001 a claim for discovery of a $0\nu\beta\beta$ decay signal was made by a subset of the collaboration (Figure 4.1) [47]. For 71.7 kg·yr of data a half-life of $T^{0\nu}_{1/2} = 1.19^{+2.99}_{-0.50} \times 10^{25}$ years (3σ) was claimed, corresponding to $\langle m_{\nu_e} \rangle = 0.44^{+0.14}_{-0.20}$eV ($3\sigma$) using the NME found in [103]. This claim has received criticism due to an unidentified peak seen at 2030 keV and incorrect relative strengths of the ^{214}Bi peaks at 2011, 2017, 2022 and 2053keV. It is also believed that the background and systematic uncertainty of the experiment are underestimated. The IGEX experiment [104] used a similar technique to the Heidelberg-Moscow experiment and did not see evidence of a $0\nu\beta\beta$ signal and instead excluded it with a limit on the half-life of $T^{0\nu}_{1/2} > 1.6 \times 10^{25}$ years (at 90% CL). However the claim has not been fully excluded due to insufficient sensitivity of current experiments and uncertainty in NME calculations. One of the main tasks of the next generation experiments will be to investigate this claim.

Two next generation experiments are being designed to investigate the Heidelberg-Moscow claim, both using ^{76}Ge (enriched to 86%). The GERDA (GERmanium Detector Array) experiment has evolved from the H-M experiment and will implement the concept of using Ge diodes immersed in a liquid argon bath for background suppression. GERDA uses the ^{76}Ge from the Heidelberg-Moscow and IGEX experiments ($\sim$ 18kg) for the first phase of its running (GERDA-I), which has recently started data taking. For the second phase of running (GERDA-II) another $\sim$ 25kg of the isotope will be added to reach a half-life sensitivity of $\sim 1.4 \times 10^{26}$ years, corresponding to $\langle m_{\nu_e} \rangle$ $\sim$100meV. The MAJORANA experiment is an evolution of the IGEX experiment, which aims to investigate the feasibility and cost of constructing and operating a 1 ton Ge detector. The demonstrator module of MAJORANA will use $\sim$30-60kg of ^{76}Ge to reach a sensitivity of $\langle m_{\nu_e} \rangle$ $\sim$70-200meV. Depending ont the findings of GERDA and MAJORANA future plans for a 1 ton Ge experiment may be considered by combining the GERDA and MAJORANA experiments.

The COBRA (Cadmium telluride 0-neutrino Beta decay Research Apparatus) experiment proposes to use semiconducting CdZnTe (CZT) crystals arranged in a large array to carry out a search for $0\nu\beta\beta$ decay for several isotopes and decay mechanisms, using ^{67}Zn, ^{106}Cd, ^{108}Cd, ^{120}Te and ^{116}Cd, with ^{116}Cd being the main isotope. $\beta^+\beta^+$, β^+EC and EC EC decay processes will be studied. COBRA is currently in its R&D phase and is developing the use of pixelised CdZnTe detectors, which are unique in $0\nu\beta\beta$ decay physics and have the potential to reduce the experimental background by several orders of magnitude using their tracking capabilities. COBRA plans to use a total of 140kg of isotope to reach a sensitivity of $\langle m_{\nu_e} \rangle \sim$ 45meV.

4.2.2 Bolometer Experiments

Bolometer $0\nu\beta\beta$ decay experiments use bolometers containing double beta decay isotopes to measure the increase in temperature when double beta decay occurs as a function of the energy deposited in the crystal. According to Debye's law the heat capacity of a single crystal is proportional to $(T/T_D)^3$, where T_D is the Debye temperature of the crystal. The change in the temperature of the crystal per unit energy deposited is inversely proportional to the specific heat of the crystal, therefore extremely low temperatures of $\sim$ 10mK are required to measure a noticeable rise in temperature in the

required energy region.

MI-BETA [105, 106] was the first experiment to utilise the bolometric technique with a large array of ^{130}Te crystal bolometers to search for $0\nu\beta\beta$ decay. The CUORICINO experiment then followed, with a total mass of 41kg of TeO_2 (with a natural abundance of ^{130}Te of 33.8% corresponding to 11kg of ^{130}Te) crystals operating at 10mK ($\sim$0.2 mK/MeV). The experiment obtained a $0\nu\beta\beta$ decay limit of $T^{0\nu}_{1/2} > 2.8\times10^{24}$ years corresponding to $\langle m_{\nu_e}\rangle <$ 0.3-0.7eV, which is competitive with the world's best limits and comparable to the limit presented in this thesis ($\langle m_{\nu_e}\rangle <$ 0.3-1.0eV). The next generation experiment CUORE (Cryogenic Underground Observatory of Rare Events) will utilise the successful bolometer technique to study 750kg of $Te0_2$ crystals (corresponding to 203kg of ^{130}Te) to a projected half-life sensitivity of $T^{0\nu}_{1/2} > 1.1\times10^{26}$ corresponding to $\langle m_{\nu_e}\rangle \sim$ 40 - 90meV. The energy resolution of the experiment reaches 5keV at 2500keV and has an expected background level of $\sim 10^{-2} - 10^{-3}$ counts kg^{-1}keV^{-1}yr^{-1}. CUORE has currently started construction in the Gran Sasso laboratory and is expected to start running in 2013.

4.2.3 Scintillator Experiments

The advantage of scintillator experiments is that they are generally less technically complicated than the semiconductor or bolometer types. Both solid and liquid scintillators can be used. The ELEGANT VI experiment used solid CaF_2 crystal scintillators and obtained a limit of $T^{0\nu}_{1/2} > 5.8\times10^{22}$ years on $0\nu\beta\beta$ decay of ^{48}Ca corresponding to $\langle m_{\nu_e}\rangle <$3.5 - 22eV. ^{48}Ca has a large $Q_{\beta\beta}$ value of 4.27MeV and is therefore a good $0\nu\beta\beta$ decay candidate as a lot of the natural radioactivity background is below the region of interest for its $0\nu\beta\beta$ decay. However it has an extremely low natural abundance of 0.19% and is currently very difficult to enrich to large amounts, with electromagnetic separation possible but only for small amounts of ^{48}Ca and with laser enrichment currently being looked into. Currently only small amounts of ^{48}Ca can be produced. The CANDLES (CAlcium fluoride for studies of Neutrinos and Dark matter by Low Energy Spectroscopy) experiment is a next generation double beta decay experiment based on the success of ELEGANT VI and currently holds 200kg of CaF_2 scintillator corresponding to a mass of $\sim$ 0.2kg of ^{48}Ca (known as CANDLES III), reaching a sensitivity of $\langle m_{\nu_e}\rangle \sim$ 500meV. The experiment will be expanded to contain 3 tons of

CaF_2 ($\sim$ 3kg of ^{48}Ca) to reach a sensitivity of $\langle m_{\nu_e} \rangle \sim$ 100meV.

The SNO+ (Sudbury Neutrino Observatory +) and KamLAND-Zen (KAMioka Liquid scintillator Anti-Neutrino Detector-Zen) experiments are the proposed next generation experiments to utilise liquid scintillator. The SNO+ experiment plans to search for $0\nu\beta\beta$ decay with ^{150}Nd, with solar and geo-neutrinos still a focus of the programme. The experiment plans to use most of the SNO experiment (the experiment that confirmed solar neutrino oscillations) infrastructure and shielding, replacing the heavy water with 1000 tons of scintillator loaded with natural Nd. A Nd-loading of 0.1% would correspond to 56kg of ^{150}Nd and a $\langle m_{\nu_e} \rangle \sim$ 100meV. If ^{150}Nd can be enriched then the expreiment may reach a sensitiviy of $<$ 100meV, however Nd purification and energy resolution issues will need to be considered. The KamLAND experiment is a one thousand ton liquid scintillator detector designed to search for ν_e appearance with neutrino oscillations, based in the Kamioka mine in Japan. Whilst reactor and geo neutrino measurements will continue a 400kg balloon loaded with liquid ^{136}Xe will be suspended in the KamLAND detector to search for $0\nu\beta\beta$ decay with a projected sensitivity of $\langle m_{\nu_e} \rangle$ $\sim$40-80meV. Phase I of the experiment is due to start data taking next year. Phase II of the experiment will see an increase of mass to 1000kg of liquid ^{136}Xe with plans to improve the energy resolution of the detector. The experiment plans to run for 5 years reaching a total sensitivity of $\langle m_{\nu_e} \rangle \sim$ 20meV.

The EXO (Enriched Xenon Observatory) experiment is a time projection chamber (TPC, Section 4.3.1, which can also be of a heterogeneous design) which will use 1-10 tons of liquid xenon enriched to 80% ^{136}Xe. The deposited energy is measured via particle interaction reconstruction and charge collection, achieved by placing a high voltage cathode wire at the centre of the detector surrounded by anode wires along the detector's circumference. Liquid xenon is an efficient scintillator, therefore using both the collected charge and scintillator light leads to an improved energy resolution of the detector. The first phase of the experiment (known as EXO-200) uses 200kg of xenon enriched to 80% ^{136}Xe corresponding to a sensitivity of $\langle m_{\nu_e} \rangle \sim$ 100-200meV and is currently running. In August 2011 EXO-200 reported the first observation of $2\nu\beta\beta$ decay with ^{136}Xe with a half-life of $T^{2\nu}_{1/2} = (2.1 \pm 0.2) \times 10^{21}$ years [84]. Depending on the background level findings of EXO-200 and the feasibility of Ba-tagging the second phase of the EXO experiment may run by trapping and identifying the daughter

isotope of ^{136}Xe - ^{136}Ba - with the use of laser spectroscopy, significantly reducing the radioactive background with Ba-tagging. The NEXT (Neutrino Experiment with a Xenon TPC) experiment is a high pressure TPC filled with xenon gas, which allows capabilities for tracking and calorimetry (with a planned energy resolution of 26keV at the $Q_{\beta\beta}$ value of ^{136}Xe) and hence topological background suppression. The NEXT experiment is currently in its R&D phase. NEXT's first phase will run with 100kg of xenon enriched to 80% ^{136}Xe to reach a sensitivity of $\langle m_{\nu_e} \rangle \sim$ 100-140meV. Plans for a ton-scale upgrade to the experiment are being considered.

4.3 Heterogeneous Design Experiments

The main advantage of a heterogeneous design experiment is good background suppression, using particle identification and event topology. Heterogeneous experiment designs include time projection chambers (TPCs), where the ionising liquid or gas is loaded with a double beta decay isotope (or the double beta decay source is housed in a foil within the TPC), and tracker-calorimeter detectors, where the double beta decay isotope is housed in a source foil located in the middle of the detector.

4.3.1 Time Projection Chambers

TPCs employ the technique of using an electric field to drift ionisation electrons created by an event to a charge collection device (usually a drift-cell). An image of electroluminescence can be produced with the use of a CCD or a multi-pixel photomultiplier tube. The amount of ionisation in the chamber is proportional to the energy deposited in the gas, allowing the energy of a double beta decay event to be measured. The density of the gas and geometry of the chamber are therefore generally chosen to allow double beta decay events to deposit all of their energy in the ionising gas. TPCs allow event vertex reconstruction, which is important for background suppression.

The DCBA (Drift Chamber Beta Analyser) experiment is a TPC which will use source plates to house ^{150}Nd. The TPC will have a 2 kGauss magnetic field running through it so that the momentum of the particles can be extracted from the curvature of the track. The main experiment, DCBA-T3 (now known as MTD - Magnetic Tracking Detector [101]), will use Nd_2O_3 enriched to 60% ^{150}Nd and contains two detectors - a single module detector (MTD-1) and a modular detector (MTD-50) comprising of 50

modules. MTD-1 will hold 32kg of ^{150}Nd corresponding to a $\langle m_{\nu_e} \rangle \sim$ 100meV after one year of running. MTD-50 will contain 50 MTD-1 like modules, holding 600kg of ^{150}Nd with a projected sensitivity of $\langle m_{\nu_e} \rangle \sim$ 30meV.

The ELEGANT V detector used a TPC containing a helium gas mixture, surrounded by arrays of scintillator and PMT counters with ^{100}Mo and ^{116}Cd isotopes contained in source foils. The next generation MOON (Molybdenum Observatory Of Neutrinos) experiment is based on the techniques used in ELEGANT V and will search for $0\nu\beta\beta$ decay of ^{100}Mo as well as study solar neutrinos. Three phases of the experiment are planned - MOON-I, MOON-II and MOON-III. MOON-I will contain 30kg of ^{100}Mo corresponding to $\langle m_{\nu_e} \rangle \sim$ 160meV, MOON-II will increase the ^{100}Mo to 120kg with a projected sensitivity of $\langle m_{\nu_e} \rangle \sim$ 100meV and MOON-III will hold a total of $\sim$ 480kg of ^{100}Mo corresponding to $\langle m_{\nu_e} \rangle \sim$ 45meV.

4.3.2 Tracker-Calorimeter Experiments

Tracker-calorimeter experiments are advantageous due to their powerful particle and event topology identification, which are useful tools in background suppression, and their ability to disentangle different $0\nu\beta\beta$ decay physics mechanisms. This type of experiment also allows for several isotopes to be studied at once. The NEMO3 (Neutrino Ettore Majorana Observatory, Chapter 5) and NEMO2 experiments were the first type of this experiment to run. NEMO3, which ran from 2003 to 2011, housed seven different double beta decay isotopes. The main isotope studied is ^{100}Mo with a mass of 6.9kg, corresponding to a sensitivity of $\langle m_{\nu_e} \rangle <$ 0.3 - 1.0eV. Analyses are currently underway to study all of the obtained data.

SuperNEMO (Chapter 9) is a next generation $0\nu\beta\beta$ decay experiment based on the successful tracker-calorimeter technique of the NEMO3 experiment. It will contain 100kg of ^{82}Se corresponding to a projected sensitivity of $\langle m_{\nu_e} \rangle \sim$ 50 - 100meV. Following a 3 year R&D programme the techniques used in NEMO3 have been further improved and new technology has been implemented to improve the energy resolution of the calorimeter, the tracking efficiency and the $0\nu\beta\beta$ decay detection efficiency.

Chapter 5

The NEMO3 Experiment and Detector

The main goals of the Neutrino Ettore Majorana Observatory (NEMO3) detector (Figure 5.1) are to study $0\nu\beta\beta$ decay to a sensitivity of 10^{24} years, corresponding to an effective neutrino mass of $0.3 - 1.0$ eV, and to carry out in depth studies of $2\nu\beta\beta$. The experiment ran from February 2003 to January 2011.

NEMO3 consists of 10kg of source foils (Section 5.3), containing seven double beta decay isotopes with $Q_{\beta\beta}$ values ranging between 2.5 and 4.3 MeV and two source foils for background measurement (Cu and ^{nat}Te). The geometry of the detector is cylindrical with a height of 3m and a diameter of 5m (excluding the passive shielding of the detector (Section 5.8)). It is split into twenty equal sectors (Figure 5.2), each containing seven strips of source foils. The foils, arranged in a ring, are vertically suspended and surrounded by the vertical wires of the drift-cell tracking chamber, used for particle identification (Section 5.1), and internal and external calorimeter walls and petals, providing energy and time measurements (Section 5.2). The detector is located in the Laboratoire Souterrain de Modane (LSM) in the Fréjus tunnel connecting France and Italy and is covered by an overburden of 4800 metres water equivalent (MWE) to reduce the incoming cosmic muon flux.

The summary of the main detector features and components can be seen in Table 5.3 at the end of this chapter.

5.1 Tracker

The NEMO3 tracker provides three dimensional tracking of charged particles and consists of 6180 vertically aligned, octagonal drift cells, which operate in Geiger mode. Each Geiger cell has a 3.0cm diameter and is 2.7m long, containing a central stainless

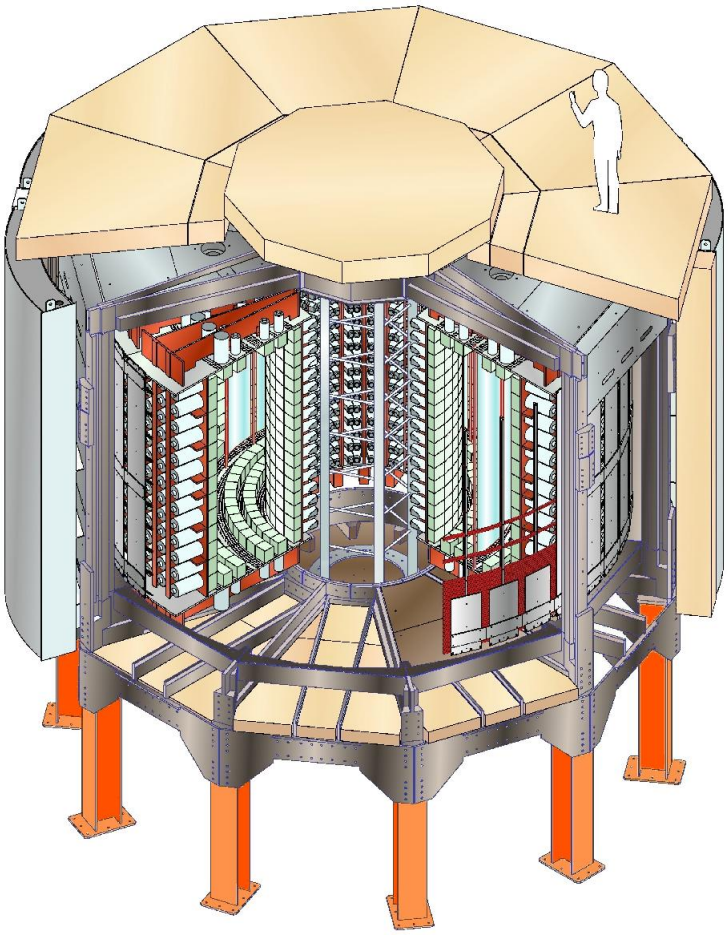

Figure 5.1: A cutaway view of the NEMO3 detector.

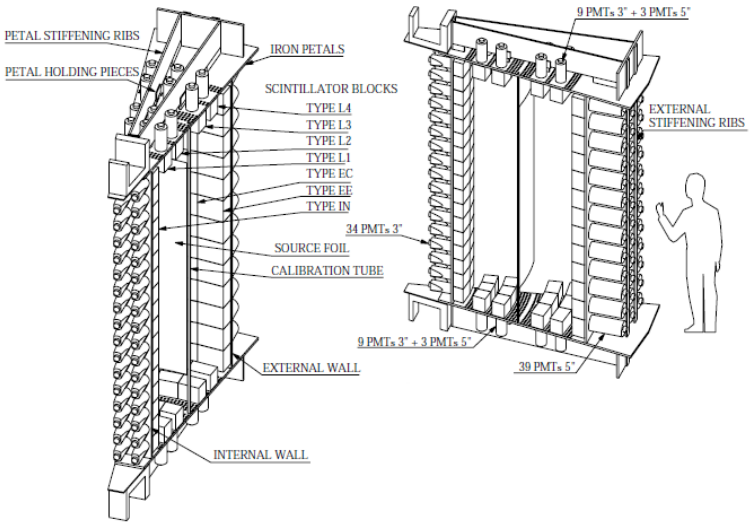

Figure 5.2: A NEMO3 sector showing the source foils and the calorimeter walls. The Geiger cells (not shown) are located between the internal and external walls.

steel anode wire (of a 50μm diameter) surrounded by eight ground wires (with an extra ground wire placed between layers of Geiger cells to avoid electrostatic cross-talk). The eight ground wires are shared amongst adjacent cells in order to minimise the amount of wire material used, which in turn minimises the scattering of electrons off the wires and the radioactivity originating from the wires. A cathode ring (of a 2.3cm diameter and 3cm length) is positioned around the anode wire at the end of each cell, with the ground wires supported just outside of the ring. The characteristic operating voltage of the anode wire is ~ 1600V.

On each side of the source foil the Geiger cells are organised in a $4-2-3$ layer configuration (Figure 5.3), with four cells of layers closest to the source foil (in order to maximise the vertex resolution, which ensures the event originated in the source foil), followed by two layers of cells in the middle block and three layers next to the internal or external calorimeter walls. There is a total of 309 Geiger cells in each sector. The gaps between the layers are used to position the calorimeter counters on the top and bottom of the detector (known as 'petals').

The tracking volume is filled with a gas mixture, consisting of 95% helium, 4% ethyl alcohol and 1% argon at 10mbar above atmospheric pressure. The use of helium, which is light and has a low atomic number (Z), allows good transparency of the wire chamber by minimising multiple scattering (electrons lose ~ 30keV in the gas). The ethyl alcohol in the gas acts as a quencher to limit the photoinosation process of the fired cell by absorbing UV photons and also reduces the probability of neighbouring cells being triggered. The argon is used to make the plasma propagation more stable as it has a lower ionisation potential than helium.

When a charged particle passes through the gas in the chamber an ionisation of an average of 6 electrons/cm is produced. These electrons travel to the closest anode, accelerating (due to the increase in the electric field near the wire) from ~ 1cm/μs to ~ 2.3cm/μs. The time t_A elapsed before reaching the anode is used to calculate the distance d of the track from the wire ($d = k\sqrt{t_A}$, where k is a constant), giving the transverse position of the particle in the cell. In the Geiger regime this anode pulse has a fast rise time of ~ 10ns and can be used as a reference for TDC measurements. An avalanche is formed close to the anode wire, producing a Geiger plasma which propagates along the anode wire at a speed of $6-7$cm/μs and is detected by the cathode

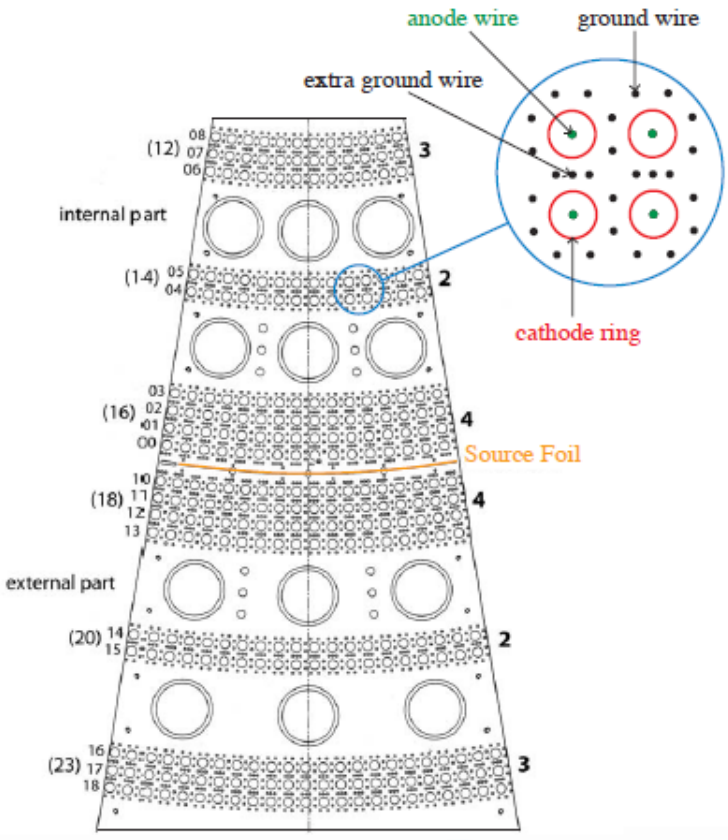

Figure 5.3: A top view of one NEMO3 sector showing the $4-2-3$ Geiger configuration. The large circles in the diagram show the positions of the calorimeter counters on the petals of the sector.

rings at either end of the cell. The two cathode times, t_{top} and t_{bottom} are used to calculate the longitudinal position (y) of the particle, according to:

$$z = -\frac{L_{eff}}{2}\frac{t_{top}-t_{bottom}}{t_{top}+t_{bottom}}\left[1-0.505\times10^{-4}\frac{L_{eff}}{2}\left(1-\frac{t_{top}-t_{bottom}}{t_{top}+t_{bottom}}\right)\right] \quad (5.1.1)$$

where L_{eff} is the effective length of the cell.

The average hit resolution of each Geiger cell is ~ 0.5mm in the transverse direction and ~ 0.8cm in the longitudinal direction, but varies with the angle of incidence of the track to the wire [107].

5.2 Calorimeter

The NEMO3 calorimeter provides energy measurements (up to 12MeV) of the deposited particles and time of flight (ToF) information, whilst also acting as a trigger.

There are 1940 calorimeter units, each made up of a scintillator, two light guides and a $3"$ or $5"$ photomultiplier tube (PMT), depending on their position in the detector. The units cover the cylindrical internal and external walls surrounding the tracking volume as well as partially the top and bottom of the detector.

There are 480 petal scintillators and 1460 wall scintillators, with the shape and size differing slightly according to their location in the detector (in order to fit the cylindrical geometry of the detector). Typical dimensions of a block are 10cm $\times$ 20cm $\times$ 20cm. The scintillator thickness was chosen to increase γ-ray detection efficiency (50% at 500keV [108]). The scintillator is made of polystyrene (PST), chosen for its low Z value which reduces back-scattering of low energy electrons. PST is also easy to mass produce, has good uniformity and is radio-pure. The PST scintillators are doped with a solid solution of scintillation agent, p-Terphenyl (p-TP) and a wavelength shifter, 1.4-bis(5-phenyloxazol-2-yl) benzene (POPOP). Petal scintillators consist of 98.75% PST, 1.2% p-TP and 0.5% POPOP, whilst wall scintillators consist of 98.49% PST, 1.5% p-TP and 0.01% POPOP. To increase light collection the four lateral sides of the scintillator are wrapped in 350μm (or five layers) of polytetrafluoroethylene (Teflon) for diffusive reflection. Five faces of the scintillator (excluding the light guide coupling face) are then further wrapped in 12μm thick aluminised Mylar for specular reflection and to protect the scintillators from the UV photons produced by excitation inside the tracker, which can cause scintillation.

The light guides that couple the scintillator to the PMT are made from polymethyl-methacrylate (PMMA). Whilst the scintillator blocks are placed within the helium gas mixture of the tracking chamber in order to minimise energy losses, PMTs can age rapidly when in contact with helium. The PMTs are also a lot more radio-polluted ($\sim$ 60 to 340 times more than the scintillators) so it is important to keep them out of the active volume of detector. The light guides also serve the purpose of isolating the PMTs from the helium/detector volume.

The PMTs used are $3"$ (R6091) and $5"$ (R6594) Hamamatsu types made from low radioactivity glass and other components, with a fast signal rise time and good linearity. The $3"$ PMTs, found on the internal wall and the inside petals, have 12 dynodes and a flat photo-cathode. The $5"$ PMTs, found on the external walls and the outer petals, have 10 dynodes and a hemispherical photo-cathode for structural integrity and need a

second interface guide to match the PMT and the light guide. Each PMT has a μ-metal shield to protect it from NEMO3's magnetic field.

All calorimeter counters have been tested and information such as gain, dark noise and linearity can be found in a database. Deviation from linearity begins at $\sim$ 4MeV, satisfying the detector requirement of having good linearity up to the $Q_{\beta\beta}$ value of the source foil isotopes studied (Section 5.3). The energy threshold of the counters is 30keV. The calorimeter energy resolution is $\frac{14.1-17.6\%}{\sqrt{E(MeV)}}$ (quoted as a range due to the spread of energy resolution measured over the 1940 calorimeter blocks) and the time resolution is 250ps (σ at 1MeV). A schematic of a calorimeter unit is shown in Figure 5.4.

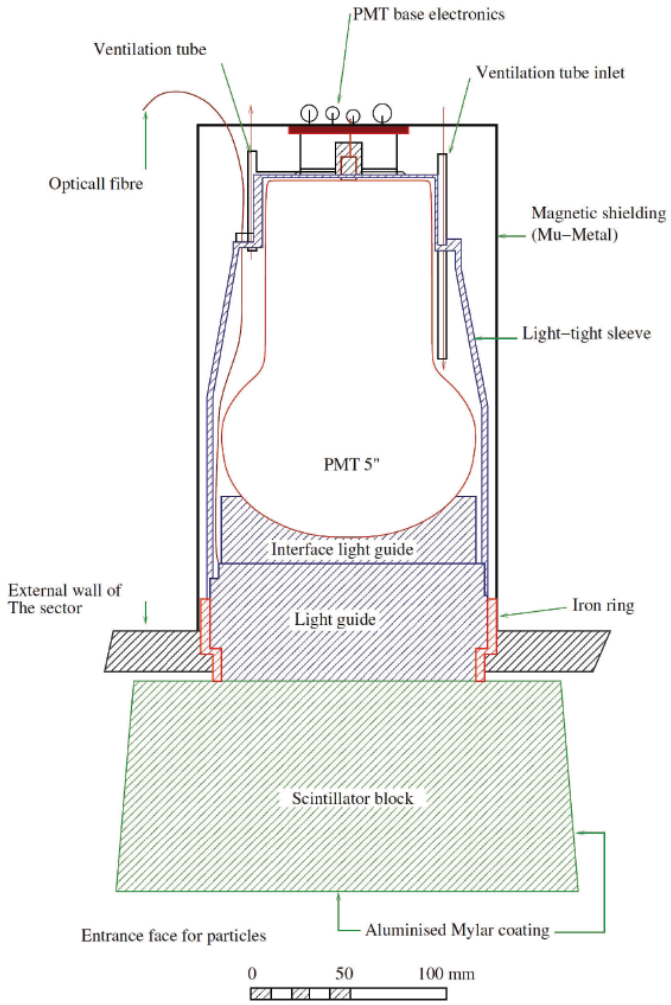

Figure 5.4: Schematic of a NEMO3 calorimeter unit showing the coupling of the scintillator to light guides and a $5''$ PMT, and magnetic μ-metal shielding.

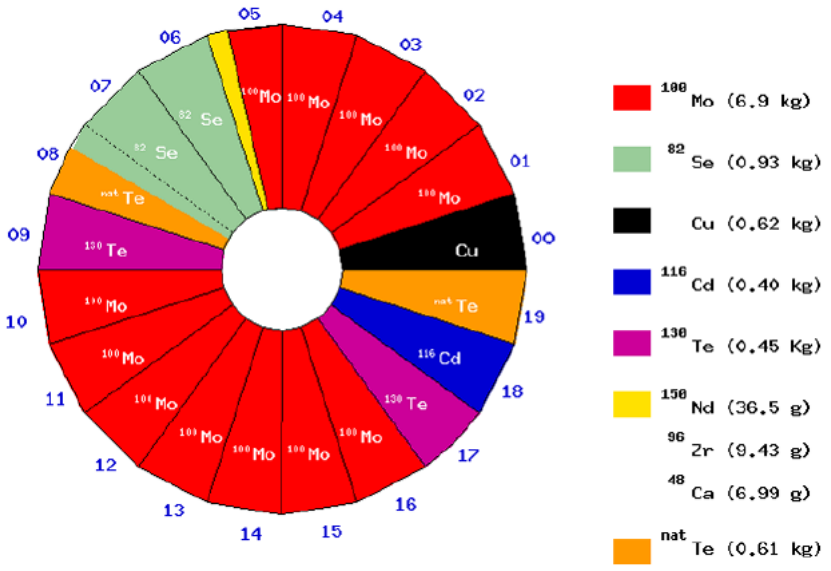

Figure 5.5: Distribution of sources in the NEMO3 detector.

5.3 Source Foils

As NEMO3 is of a heterogeneous design (Section 4.3), meaning that the source and the detector are independent, several double beta decay isotopes can be studied by the detector. NEMO3 contains 8.8kg of seven double beta decay isotopes (^{100}Mo, ^{82}Se, ^{116}Cd, ^{130}Te, ^{150}Nd, ^{48}Ca and ^{96}Zr) distributed throughout the detector as shown in Figure 5.5. There are also two sectors in NEMO3 that contain ultra-pure copper and ^{nat}Te, which provide sectors of high radiopurity largely free from internal backgrounds and aid the understanding of the external background model.

The isotopes studied by NEMO3 were chosen according to the following parameters:

- The $Q_{\beta\beta}$ value of the isotope, which should be relatively high to suppress background contributions in the $0\nu\beta\beta$ region coming from the ^{208}Tl and ^{214}Bi decay chains which have high Q_{β} values of 4.99MeV and 3.27MeV respectively. A γ transition of 2.615MeV coming from ^{208}Tl is particularly troublesome, therefore isotopes with $Q_{\beta\beta} > 2.6$MeV are preferred. A larger $Q_{\beta\beta}$ value also increases the phase-space factors, $G^{0\nu}$ and $G^{2\nu}$, for $0\nu\beta\beta$ and $2\nu\beta\beta$ decay.

- The possibility of obtaining high radio-purity of the source.

- The natural isotropic abundance of the isotope (typically, it should be $\geq 2\%$).

Transition	$Q_{\beta\beta}$ (keV)	Natural Abundance (%)	Mass (kg) in NEMO3	$G^{2\nu}$ (yr^{-1})	$G^{0\nu}$ (yr^{-1})
^{100}Mo $\rightarrow$ ^{100}Ru	3034.8 $\pm$ 6.3	9.6	6.914	8.9 $\times 10^{-18}$	4.6 $\times 10^{-14}$
^{82}Se $\rightarrow$ ^{82}Kr	2995.2 $\pm$ 3.3	9.2	0.932	4.3 $\times 10^{-18}$	2.7 $\times 10^{-14}$
^{130}Te $\rightarrow$ ^{130}Xe	2528.8 $\pm$ 2.1	33.8	0.614	4.8 $\times 10^{-18}$	4.1 $\times 10^{-14}$
^{116}Cd $\rightarrow$ ^{116}Sn	2804.7 $\pm$ 4.2	7.5	0.405	7.4 $\times 10^{-18}$	4.7 $\times 10^{-14}$
^{150}Nd $\rightarrow$ ^{150}Sm	3367.1 $\pm$ 4.9	5.6	0.037	1.2 $\times 10^{-16}$	1.9 $\times 10^{-13}$
^{48}Ca $\rightarrow$ ^{48}Ti	4272.0 $\pm$ 4.1	0.187	0.007	4.0 $\times 10^{-17}$	6.4 $\times 10^{-14}$
^{96}Zr $\rightarrow$ ^{96}Mo	3350.0 $\pm$ 3.5	2.8	0.0094	1.8 $\times 10^{-17}$	5.7 $\times 10^{-14}$

Table 5.1: Double beta decay isotopes used in NEMO3. All isotopes have a $Q_{\beta\beta}$ value $>$ the 2.6MeV γ-ray transition from ^{208}Tl (except ^{130}Te) and a natural abundance $> 2\%$ (except for ^{48}Ca). Phase-space values are published in Reference [67] for all isotopes, other than for $G^{0\nu}$ of ^{100}Mo, which is published in [111].

- A suggested large nuclear matrix element for both the $0\nu\beta\beta$ and $2\nu\beta\beta$ decay. There are currently many uncertainties in the calculations of nuclear matrix elements, therefore those that are favourable by theory to be large should be considered.

^{100}Mo, ^{82}Se, ^{116}Cd, ^{96}Zr and ^{150}Nd were chosen as they have a natural abundance $> 2\%$ and a $Q_{\beta\beta}$ value > 2.615MeV. ^{48}Ca was included due to its large $Q_{\beta\beta}$ value of 4.27MeV and ^{130}Te was included in order to obtain a direct measurement of its $2\nu\beta\beta$ half-life and to solve the dispute between a number of inconsistent geochemically measured $2\nu\beta\beta$ half-lives [109, 110]. Table 5.1 summarises the seven isotopes studied by NEMO3, their $Q_{\beta\beta}$ values, natural abundances, mass in NEMO3 and phase-spaces.

The detector holds 140 strips of source foil. Each sector of the detector has a source frame on which seven strips of source foil are mounted. Each strip has a mean length of 2480mm and a width of 63mm (if they are on the edges of the frame) or 65mm (for the five strips in the middle of the frame). The thickness of the foil is a compromise between the need for large source mass and the necessity to limit worsening of energy resolution due to loss of electron energy inside the foil. The area density of the foil

is $30 - 60$mg/cm^2, corresponding to a thickness of $\sim 60\mu$m for metallic foils (^{116}Cd, a fraction of ^{100}Mo and Cu) or $\sim 300\mu$m for composite foils, which are a mixture of isotope source powder and organic glue (^{82}Se, ^{130}Te, ^{96}Zr, ^{150}Nd, ^{48}Ca and 64% of ^{100}Mo).

5.3.1 Characteristics of the ^{100}Mo Source Foils

The isotropic abundance of ^{100}Mo in ^{nat}Mo is 9.6%. The enrichment process, carried out in Russia, involved the production of MoF_6 gas from ^{nat}Mo, which was then centrifuged to isolate heavy isotopes, such as ^{100}Mo. The enriched MoF_6 then underwent an oxidation-reduction reaction to produce a metalic ^{100}Mo powder from $^{100}MoO_3$. A total mass of 10kg was obtained, with enrichment levels of $95.14 \pm 0.05\%$ to $98.95 \pm 0.05\%$. When measured for radioactivity the samples were found to be too radio-polluted and had to undergo further purification, using two different methods - physical purification (to produce metallic ^{100}Mo) and chemical purifaction (to produce composite ^{100}Mo).

5.3.2 Physical Purification of the Enriched ^{100}Mo Powder for Metallic ^{100}Mo Production

The ^{100}Mo powder was first pressed to obtain a solid ^{100}Mo sample and then melted with an electron beam in a vacuum to extract a mono crystal from the liquid. The impurities contained within the sample are more soluble at the temperature the liquid was melted to than ^{100}Mo and so were attracted to the extremities of the crystal. The impure skin was then cut off from the crystal and the process repeated until an ultra-pure mono crystal was obtained. Metallic strips ($44 - 63\mu$m thick, $64 - 1445$mm long and $63 - 65$mm wide) were then fabricated from the crystal by heating and rolling it in a vacuum. Three to five short strips were then attached together with Araldite AW106/Hardener HV953U glue to create a source strip ~ 2480mm in length. Sector 02, 03 and 04 are fully occupied by metallic ^{100}Mo. Sector 01 contains five strips of metallic ^{100}Mo and sector 05 contains a further two. The total mass of metallic ^{100}Mo contained in NEMO3 is 2478.94 ± 5g.

Table 5.2 shows radioactivity measurements of metallic ^{100}Mo after purification carried out with high purity germanium (HPGe) detectors.

				^{238}U chain		^{232}Th chain	
Isotope	Mass (g)	^{40}K	^{235}U	^{234}Th	^{214}Bi	^{228}Ac	^{208}Tl
Metallic ^{100}Mo	2479 ± 5	< 5	1.5 ± 0.3	< 15	< 0.39	< 0.5	< 0.11
Composite ^{100}Mo	4435 ± 22	< 6	< 0.3	< 15	< 0.34	< 0.3	< 0.10

Table 5.2: Radioactivity measurements (in mBq/kg) for ^{100}Mo carried out with HPGe detectors [107].

5.3.3 Chemical Purification of the Enriched ^{100}Mo Powder for Composite ^{100}Mo Production

A solution containing the enriched ^{100}Mo powder, ultra-pure H_2O, quartz distilled HNO_3 and $Ba(NO_3)_2$ (an almost radon free salt) was heated to dissolve the ^{100}Mo. The solution was then further heated to increase the acidity and reduce the volume until the ^{100}Mo precipitated as MoO_3. The MoO_3 precipitate then underwent vacuum assisted filtration to separate it from impurities in the sample, most of which are acid soluble. The resulting compound was then rinsed, dried and heated in a quartz lined tube furnace to further dry the powder and to reduce the MoO_3 to a purified metal powder, typically containing $< 2\%$ O_2.

The resulting powder was then sieved to select grains $< 45\mu$m in diameter so that a good bond between the powder and the Mylar foils used to hold the powder could be achieved. It was then mixed with water and PVA glue and inserted into a syringe, which was heated with ultra sound to obtain a paste. The paste was then spread between two sheets of $18 - 19\mu$m thick Mylar, left to dry for 10 hours and then cut into source foil strips of required size (2480mm long with a surface density < 60mg/cm^2). Sectors 01, 05 and 10-16 contain composite ^{100}Mo in various combinations, with a total mass of 4434.61 ± 22g.

Table 5.2 shows radioactivity measurements of composite ^{100}Mo after purification carried out with HPGe detectors.

5.4 Electronics, DAQ and Trigger

The NEMO3 detector has an independent tracker and calorimeter, which allows individual or interdependent triggering and data readout systems. This gives the flexibility

to change the triggering for calibration and testing purposes of the detector, as well as for acquiring $\beta\beta$ data.

5.4.1 Calorimeter Electronics

The high voltage (HV) for the PMTs is provided by three CAEN power supplies, which each contain ten modules with 24 HV channels (providing 240 HV channels per power supply). The HV is transferred to a sector through nine distribution boards, each containing four channels. Each of the channels is split into three outputs, supplying HV for twelve PMTs. The typical HV is positive 1800V for the $3"$ PMTs and positive 1350V for the $5"$ PMTs.

Each sector contains 97 PMTs, which are divided into two sections by the source foil - an internal (containing 46 PMTs) and external (containing 51 PMTs) section. Each section has a motherboard, which contains either 46 or 51 dedicated signal processing daughter cards for each PMT channel. There are 40 motherboards in total housed in three Versa Module Europa (VME) crates.

The calorimeter DAQ electronic boards have a low and high threshold leading edge discriminator. When a PMT signal exceeds the low level threshold (7mV, corresponding to 23keV) a TTL (Transistor Transistor Logic) 'start' command is sent to the TDC (Time to Digital Converter). This opens the charge integration gate for 80ns. The high level threshold is set to 48mV (corresponding to 150keV) and if the required multiplicity of active PMTs is achieved (usually one PMT) the first level trigger (T1) is activated. The trigger logic then sends a 'stop' signal to the TDC, activating the ADC (Analogue to Digital Converter). The relevant data are then read out and saved.

The TDCs have a time resolution of ~ 53ps/channel for 12 bits for a total time of ~ 200ns. The ADCs have a charge resolution of 0.36pC/channel (corresponding to ~ 3keV/channel) for 12 bits and get saturated at ~ 12MeV.

5.4.2 Tracker Electronics

The HV for the tracker is supplied by two CAEN power supplies, each containing 16 HV channels. The tracker is made up of 18 concentric layers of Geiger cells, with each layer requiring a slightly different HV to avoid electrostatic effects. The internal nine layers are each powered by one HV channel, and the external nine layers are each powered by two HV channels to supply a greater current. The HV is delivered to the

tracker by distribution boards, which are also used to receive the analogue signals from the anode and cathode rings. Each sector contains eight boards, which each contain 15 daughter boards with eight channels. Five of the daughter boards are used for the anode signal, five for the top cathode ring and five for the bottom cathode ring. The typical HV on the anode wires is $1620 - 1650$V.

The tracker acquisition boards amplify and discriminate the signal before initialising the TDCs for the anode (tdc$_A$), the top cathode ring (tdc$_{top}$) and the bottom cathode ring (tdc$_{bottom}$). When running acquisition for $\beta\beta$ events the T1 trigger from the calorimeter starts the tdc$_A$ measurement. The anode signal then sends a 'stop' signal to tdc$_A$ and a 'start' signal to tdc$_{top}$ and tdc$_{bottom}$, which are then 'stopped' by the signals arriving at the cathode rings. The time difference between the tdc$_A$ 'start' and 'stop' is used to obtain the drift time from the point of ionisation, t_A. The time differences between the tdc$_{top}$ and tdc$_{bottom}$ 'starts' and 'stops' are used to obtain the longitudinal plasma propogation times, t_{top} and t_{bottom} (see Section 5.1).

In the case of a $\beta\beta$ event the 'stop' signal is sent $\sim 6.4\mu$s after the 'start' signal. However, the tracker has the ability to wait for up to 710μs after T1 to look for delayed Geiger hits produced by the troublesome ^{214}Bi background (see Section 7.1). ^{214}Po is the daughter isotope of ^{214}Bi and undergoes α decay with a half-life of 164μs, producing a short ionization track in the chamber. By keeping a time window of 710μs open most of these events can be identified.

5.4.3 NEMO3 Trigger

The NEMO3 detector trigger has three levels: T1, T2 and T3.

The first level trigger, T1, is applied by the calorimeter. It requires the desired mulitplicity of PMTs to be activated with energies > 150keV. For $\beta\beta$ acquisition only one PMT is required. However, this changes for some of the other runs, such as calibration with ^{60}Co, where two coincident PMT signals are required (see Section 5.5).

The T2 trigger is applied by the tracker. It allows the use of a rough track recognition programme, which is later refined by spatially connecting triggered Geiger cells and PMTs, by requiring specific patterns of triggered Geiger cells. A half-sector of NEMO3 contains nine Geiger layers and the T2 trigger requires Geiger hits in at least three of these layers. At least two of these hits must also be in one (and the same) of

the three groups of the $4-2-3$ Geiger cell configuration (layers $0-3$, $4-5$ or $6-8$, Section 5.1).

The T3 trigger is only used during calibration runs. It checks for possible coincidences between the Geiger hits in T2 and fired PMTs to select tracks coming from radioactive sources positioned in the calibration tubes.

5.5 Energy and Time Calibration

For absolute energy and time measurements NEMO3 relies on dedicated calibration runs with radioactive sources. Laser surveys are used for PMT gain fluctuation monitoring (for relative energy calibration).

The detector's 20 sectors are each equipped with a vertical copper calibration tube fixed on the same cylindrical radius as the source foil. Each tube has three pairs of windows, covered by 25μm thick kapton, one hole oriented towards the internal wall and the other towards the external wall of the detector. The vertical positions of the windows (z $= -90$, 0 and $+90$cm) have been chosen to optimise illumination uniformity of the scintillator blocks. Radioactive sources are introduced into the top of the tubes in long narrow Delrin rods. Each rod can support three source holders.

The absolute energy calibration of the PMTs is carried out monthly. The sources used for this are ^{207}Bi (Section 11.3.1) and, less frequently, ^{90}Sr. ^{207}Bi provides two calibration points from K-shell conversion electrons at 976keV and 482keV. ^{90}Sr decays to ^{90}Y via β-decay with a half-life of 2.67days, providing a higher energy calibration point at the endpoint of the β ^{90}Y spectrum (2.28MeV).

^{60}Co sources are used for the calorimeter time calibration. ^{60}Co emits two coincident γ-rays with energies of 1173keV and 1332keV. The relative time difference between the signal of the two γs is used for the calibration.

The gain stability of the PMTs is measured twice daily with a calibrated laser light injection system. A small sphere of scintillator wrapped in Teflon and aluminium shifts the wavelength of the laser beam to reproduce an ionisation signal. This signal is monitored by six reference PMTs fitted with ^{207}Bi and a pin diode, and is then transmitted to the PMTs via an optical fibre. The linearity (up to 12MeV) of the PMTs is measured on a yearly basis using a 75mm variable optical attenuator disk.

5.6 Radon Trapping Facility

One of the main backgrounds in NEMO3 (discussed in Section 7.1), and all low background experiments, is ^{222}Rn (radon), whose daughter ^{214}Bi has a Q_β value of 3.27MeV and is in the region of interest for $0\nu\beta\beta$. After one year of NEMO3 running it was discovered that radon from rock surrounding LSM was diffusing into the detector through the glued joints of the sectors, depositing $\sim$ an order of magnitude more ^{214}Bi on the surface of the source foils than ^{214}Bi coming from internal contamination.

A radon trapping facility was installed around NEMO3 to reduce the amount of radon present in the detector by an order of magnitude based on the design of the Super-Kamiokande air purification system [112]. The facility works by cooling fresh compressed air to $-50°$C and flushing it through activated charcoal, which is also cooled to the same temperature. The cooled radon is adsorbed (or 'trapped') by the porous charcoal, where it decays with a half-life, $T_{1/2}$, of 3.8 days. The radon free air is then flushed into an air-tight polyethylene tent surrounding the NEMO3 detector, which prevents any radon-infused air entering the detector. Air enters the trapping facility with an activity of ~ 15Bq/m^3 and leaves it with ~ 0.015Bq/m^3, achieving a reduction factor of 1000. This translates as a reduction from an average total of 700 ± 1mBq (or 37.7 ± 0.1mBq/m^3) to 140 ± 1mBq (or 6.46 ± 0.05mBq/m^3) [113] inside the tracking volume of the detector (the reduction factor within the detector is smaller due to outgassing of radon from detector components), providing an acceptable level of radon contamination.

NEMO3 data are split into two 'phases' according to the level of radon contamination within the detector. 'Phase I' includes data from the beginning of the experiment (February 2003) to September 2004, when the trapping facility was installed. 'Phase II' includes data collected after the installation of the facility, from October 2004 to January 2011.

5.7 Magnetic Field

There is a solenoidal coil surrounding the detector which produces a 25G ($= 2.5 \times 10^{-3}$T) magnetic field parallel to the z axis of the cylinder (i.e. the Geiger cells), created by passing $\sim$ 30A of current through 203 loops of copper rods connected by copper rings. The magnetic field allows charge identification using the curvature of the

tracks and is used to suppress some of the backgrounds that mimic $2e^-$ common vertex events, such as e^-- e^+ pairs (with 95% efficieny at 1 MeV [107]) and external electrons crossing the detector.

The magnetic field also allows a measurement of the particle's momentum. The radius of the track gives the momentum component orthogonal to the field and the helix pitch of the track gives the parallel component. However, the reconstruction of momentum from a track's curvature is less accurate than and not competitive with the energy measurement given by the calorimeter.

5.8 Passive Shielding

It is extremely important to suppress as much of the background originating from outside of the detector ('external' background) as possible as it can mimic $\beta\beta$ events by interacting within the detector (Section 7.4). To achieve this NEMO3 uses a set of passive shielding surrounding it, consisting of an iron shield and a neutron shield.

NEMO3 is shielded from cosmic rays by the overburden of mountain surrounding the LSM (4800mwe). The rock reduces the muon flux by a factor of one million at sea level to $5 \times 10^{-5}\text{m}^{-2}\text{s}^{-1}$ measured inside the LSM.

The iron shield is used to reduce the γ-ray flux coming from radioactive decays from the surrouding rock and neutron capture. It is made of low radioactivity iron plates (20cm thick) surrounding the detector in its entirety. It also acts as a flux return for the solenoidal coil of the detector.

Spontaneous fission from Uranium and Thorium in the surrounding rock of the LSM produces fast, thermal and epithermal neutrons. Once these neutrons are slowed down by the iron shield they can be captured by the materials inside of the NEMO3 detector to produce high energy photons. In order to suppress this background a shield made of 20cm of paraffin, 35cm of borated water (held in ten tanks attached to the cylindrical external walls of the detector) and 28cm of wood (surrounding the petals of the detector where borated water is inconvenient) is used. This structure surrounds the iron shield. Fast and epithermal neutrons are slowed down and thermalised on the hydrogen in the water. The thermal neutrons are then captured by the boron (which has a high thermal neutron cross-section) through an (n,γ) reaction, creating γs, which are shielded by the iron.

	The NEMO3 Experiment
Depth	4800m water equivalent
Running Time	February 2003− January 2011
Magnetic Field	25G ($= 2.5 \times 10^{-3}$T)
	Tracker
Gas	Helium gas (4% ethyl alcohol, 1% argon)
Pressure	10mbar above atmospheric pressure
Drift Cells	6180
Wire Thickness	50μm
Wire Length	2.7m
Single Hit Transverse Resolution	0.5mm [107]
Single Hit Longitudinal Resolution	0.8cm [107]
	Calorimeter
Blocks	1940
Block Size	$\sim 10 \times 20 \times 20\times$cm^3
Energy Threshold	30keV
Energy Resolution	$\frac{14.1-17.6\%}{\sqrt{E}(MeV)}$
PMT Size	3" and 5"
PMT Coincidence Time Resolution	250ps (σ at 1MeV)
	Foil
Diameter	3.1m
Height	2.5m
Thickness	$30 - 60$mg/cm^2
	Backgrounds
^{214}Bi	$\sim 300\mu$Bq/kg (for ^{100}Mo)
^{208}Tl	$\sim 20\mu$Bq/kg (for ^{100}Mo)
^{222}Rn in tracking volume	37.7 (Phase I) & 6.46 (Phase II) mBq/m^3[113]
	Shielding
Iron	20cm
Paraffin	20cm
Borated Water	35cm
Wood	28cm

Table 5.3: Summary of the NEMO3 detector features and components.

Chapter 6

NEMO3 General Analysis Technique

NEMO3 analysis consists of generating simulated events (Section 6.1), carrying these events through the detector description (Section 6.1), reconstructing the simulated and NEMO3 data events (Section 6.2) and preselection of all events (Section 6.6). Following this a statistical analysis is carried out for background estimation, a $2\nu\beta\beta$ half-life measurement and a search for $0\nu\beta\beta$ decay (Section 6.7).

6.1 Monte Carlo Simulation

The NEMO3 simulation package (NEMOS) uses the GENBB [114] event generator, which contains full kinematic and branching ratio descriptions of α, β and γ events for the required isotopes. Once generated, the events are propagated through a full geometrical detector description (including resolution and detector acceptance effects) created with GEANT-3.21 [115]. This structure is used to produce Monte Carlo (MC) simulations of the $2\nu\beta\beta$ and $0\nu\beta\beta$ modes and Majoron emission processes to ground and excited states for the source isotopes. The associated internal and external radioactive backgrounds in NEMO3 are also simulated. The simulated events are stored in the same format as the raw data collected by the experiment so that an identical reconstruction process can be carried out on both.

6.2 Reconstruction

In order to reproduce the same detector conditions for the reconstruction of the MC as for the data the NEMO3 reconstruction package (NEMOR) connects to the NEMO3 database. The database stores information such as PMT, scintillator and drift cell characteristics and calibration constants. The simulated MC events must correspond to the

detector status during the entire period of data being analysed and are therefore distributed among the data acquisition periods (known as 'runs') as a function of run time. The MC events are reweighted by the length of the data runs, so that the sample of events in each MC file is proportional to the distribution of the events in the data. The associated run status (a flag to identify the quality of a run e.g. run status $= 1$ corresponds to a good run and run status $= 6$ corresponds to a high radon run) is then applied to each corresponding acquisition period. This produces reconstructed MC with all intrinsic and running detector characteristics taken into account.

During the reconstruction the ADC and TDC signals collected in both data and MC are converted to energies and times, the particle tracks are reconstructed and associated to scintillator hits (in the case of electrons and positrons).

6.3 Particle Identification

Using NEMO3's ability to combine calorimetry and tracking the experiment can identify electrons, positrons, γ-rays and αs.

An electron is identified as an ionization track of negative curvature (due to the magnetic field) originating from the source foil and a deposit in a scintillator associated to that track. A positron is identified in the same way, but with a track of positive curvature.

As only charged particles produce an ionization in the Geiger chamber a γ does not leave a track and is identified as an 'isolated' single scintillator deposit (not surrounded by any other scintillator hits, as shown in Figure 6.1). The eγ and e$\gamma\gamma$ channels are used to ascertain background activities in NEMO3 (Chapter 7), therefore it is important to be able to distinguish them. Low energy γs can scatter and hit a neighbouring scintillator, producing two or more hits. When a situation arises where two scintillator hits next to each other have been fired, as in Figure 6.2, it is difficult to distinguish between an eγ event where the γ has scattered to a neighbouring scintillator and a genuine e$\gamma\gamma$ event. Low energy γ interactions are modelled less precisely in GEANT-3.21, therefore simulations do not reproduce scattering of low energy γs accurately for these events. The probability of a γ interaction with a single 10cm calorimeter block is $\sim 50\%$ for a 0.5MeV γ [108].

An α particle is identified as a short straight ionization track in the gas of the

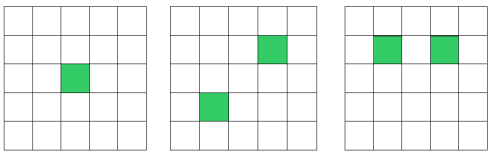

Figure 6.1: Three scenarios showing scintillator deposits that are considered to be 'isolated' (no two scintillator blocks next to each other are fired), with the grid representing a set of scintillator blocks and the γ hit to the scintillator block represented in green. These events are considered as suitable γ candidates.

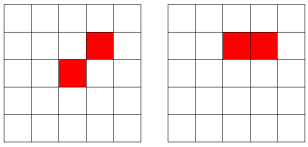

Figure 6.2: Two scenarios showing scintillator deposits that are considered to be 'non-isolated' (two scintillator blocks next to each other are fired), with the grid representing a set of scintillator blocks and the γ hit to the scintillator block represented in red. These events are not considered as suitable γ candidates.

tracking volume which does not leave a deposit in the calorimeter.

6.3.1 ^{214}Bi-^{214}Po Event Identification

A troublesome background for NEMO3 comes from ^{214}Bi (produced by ^{222}Rn decay, originating from the ^{238}U natural decay chain inside or outside of the detector), which decays to ^{214}Po with a Q_β value of 3.27MeV. It is important to be able to identify these events as background in order to distinguish them from $2\nu\beta\beta$ or $0\nu\beta\beta$ events. This can be done using Bismuth-Polonium (Bi-Po) delayed coincidence events, using electronics as described in Section 5.4.2. ^{214}Po decays to an α with a half-life of 164μs, therefore a Bi-Po event (Figure 6.3) consists of a β accompanied by a delayed α (within a 710μs time window), with a common event vertex in the source foil or inside the tracking volume. The α particle is identified as a straight short ionisation track (produced by one or more delayed hits) in the gas volume of the tracking detector, without depositing energy in the calorimeter. For events with only one accompanied delayed signal the delay is required to be $> 90\mu$s [113]. For grouped hits (one or more hits within 2.1μs of each other, correlated in space) a delay $> 30\mu$s is required [113]. These times were chosen to exclude background non-α events caused by refiring coincidences produced

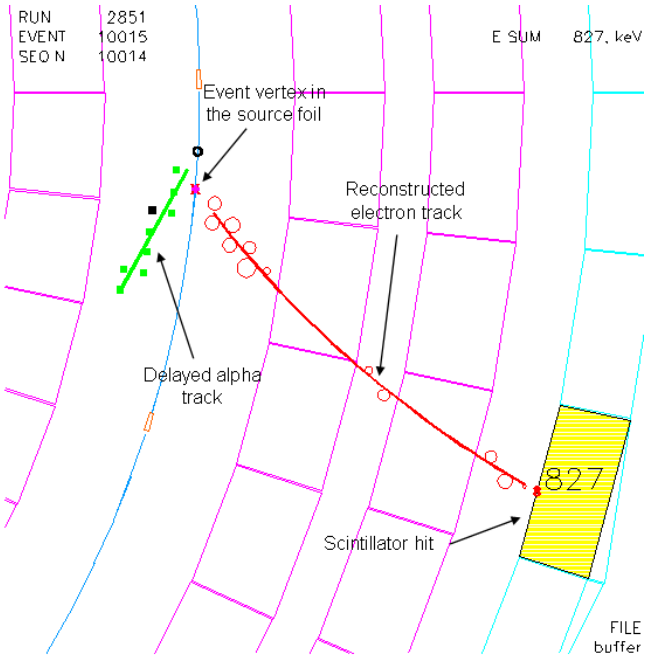

Figure 6.3: NEMO3 event display showing a transverse view of a ^{214}Bi-^{214}Po event, with one electron track (red) and a delayed α particle (green), with a common vertex in the source foil.

by the Geiger cells (caused by UV γs and cross-talk between the cells). The maximum range of a Bi-Po α in the helium gas of the Geiger chamber is $\sim$ 36cm, therefore the delayed hits are required to be within 35cm of each other. The distance between the reconstructed vertex of the β and α particles is required to be $<$ 15cm in space, with $|\Delta XY| = \sqrt{\Delta X^2 + \Delta Y^2} < 10$cm in the transverse $(x - y)$ plane and $|\Delta Z| < 15$cm in the longitudinal plane [116].

6.4 Time of Flight Criterion

Time of flight (ToF) information is used to distinguish between internal 2e$^-$ and $e^-\gamma$ events (originating in the source foils) and external events that mimic 2e$^-$ events and e$^-\gamma$ events (originating from γs outside of the source foils). These γs come from detector components and the rock surrounding LSM and can fake events used in the analysis in the following way:

- $e^-\gamma$ events (Figure 6.4): The external γ crosses the detector after leaving a deposit in a scintillator and Compton scatters in the foil to produce an electron, which leaves a second scintillator deposit. The ToF information is used to construct $e\gamma$ internal and external hypotheses (similar to the two electron vertex hy-

potheses described in Sections 6.4.1 and 6.4.2) in order to distinguish between genuine internal eγ events and fake external eγ events, which originate from a single external γ.

- $\beta\beta$ events (Figure 6.4): The external γ Compton scatters in the initial scintillator block and produces an electron that crosses the entire tracking volume via one of the source foils, leaving two associated scintillator deposits and what appears to be two tracks with an event vertex originating in the source foil.

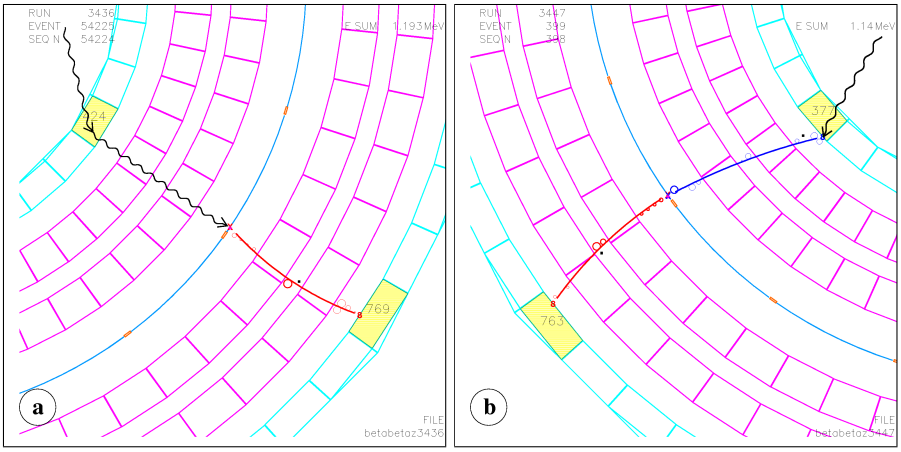

Figure 6.4: NEMO3 event display showing a transverse view of (a) eγ external (where an external γ leaves a deposit in the scintillator and Compton scatters inside the source foil to produce an electron, leaving a second scintillator deposit) and (b) crossing electron events (where an external γ leaves a deposit in the scintillator, then Compton scatters in that scintillator producing an electron that crosses the entire detector volume), with presumed γs (wavy black lines) superimposed onto the display.

These fake $\beta\beta$ events are known as 'crossing electron' events and are a background to the analysis. In order to distinguish between $\beta\beta$ events that originate inside the source foil (genuine events) and those that originate from external γs coming from outside of the detector (producing crossing electron events) two hypotheses are formed: the two electron internal vertex hypothesis and the crossing electron external vertex hypothesis. Each hypothesis, χ^2, takes the following form:

$$\chi^2 = \frac{(t_{exp} - t_{th})^2}{\sigma_{exp}^2 + \sigma_{th}^2}, \tag{6.4.1}$$

where t_{exp} is the experimentally measured time difference between the two scintillator hits, t_{th} is the theoretically calculated time difference, and σ_{exp} and σ_{th} are the uncertainties on the experimentally measured and theoretically calculated time differences respectively.

The TDC information, t_i^{tdc}, from the two PMTs ($i = 1, 2$) is used to calculate the probability of the event originating inside and outside of the source foil.

6.4.1 The Two Electron Internal Vertex Hypothesis (χ^2_{int})

The internal vertex hypothesis assumes that the two electrons are emitted from the source foil simultaneously. They then travel through the Geiger chamber and leave two energy deposits in the calorimeter associated to two different tracks. The particles have reconstructed track lengths L_i ($i = 1, 2$), a trigger time t_i^{tdc}, deposit an energy E_i in the calorimeter, and have a ToF, t_i^{tof}, obtained from the reconstruction, (in natural units) of

$$t_i^{tof} = \frac{L_i}{\beta_i}, \tag{6.4.2}$$

where E_i takes into consideration the energy loss in the gas of the tracking volume and includes corrections for the energy calibration, and β_i is defined as

$$\beta_i = \frac{\sqrt{E_i(E_i + 2m_e)}}{E_i + m_e,} \tag{6.4.3}$$

where m_e is the electron rest mass. The time of emission for each particle, assuming internal origin, t_i^{int}, is then

$$t_i^{int} = t_i^{tdc} - t_i^{tof} = t_i^{tdc} - \frac{L_i}{\beta_i} \tag{6.4.4}$$

and the internal χ^2_{int} ToF variable is written as

$$\chi^2_{int} = \frac{\left(\left(t_2^{tdc} - \frac{L_2}{\beta_2}\right) - \left(t_1^{tdc} - \frac{L_1}{\beta_1}\right)\right)^2}{\sigma^2_{t^{int}}}, \tag{6.4.5}$$

where $\sigma^2_{t^{int}}$ is the sum of errors on the time $\sigma_{t^{tdc}}$, energy σ_E and track length σ_L, which is defined as

$$\sigma^2_{t^{int}} = \sum_{i=1}^{2} \left(\frac{\partial t^{int}}{\partial t_i^{tdc}}\right)^2 \sigma^2_{t_i^{tdc}} + \left(\frac{\partial t^{int}}{\partial \beta_i}\right)^2 \sigma^2_{E_i} + \left(\frac{\partial t^{int}}{\partial L_i}\right)^2 \sigma^2_{L_i} \tag{6.4.6}$$

and has the more explicit form of

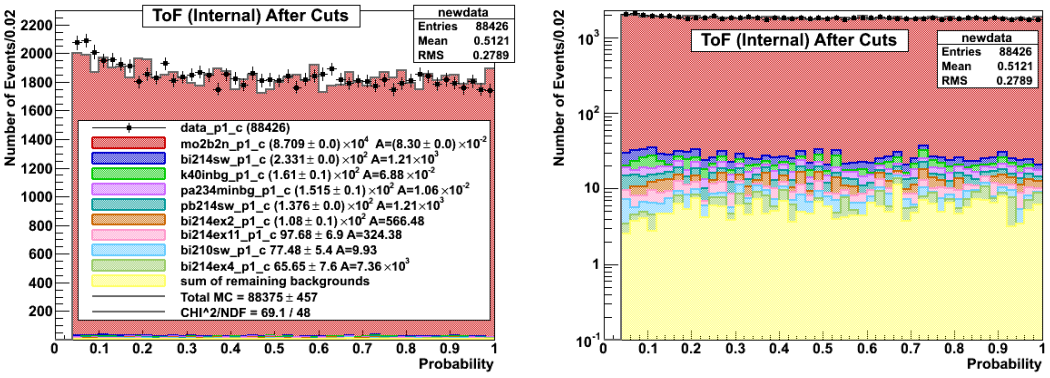

(a) linear scale (b) logarithmic scale

Figure 6.5: Distribution of the internal probability calculated from the time of flight for the Composite Phase I ^{100}Mo data set on a linear scale (a) and a logarithmic scale (b).

$$\sigma^2_{t^{int}} = \sum_{i=1}^{2} \sigma^2_{t_i^{tdc}} + \left(\frac{t_i^{tof} m_e^2}{E_i(E_i + m_e)(E_i + 2m_e)} \right) \sigma^2_{E_i} + \left(\frac{1}{\beta_i} \right) \sigma^2_{L_i}. \tag{6.4.7}$$

The probability that the event is internal $P(\chi^2_{int})$ is given by

$$P(\chi^2_{int}) = 1 - \frac{2}{\pi} \int_0^{\chi^2_{int}} e^{x^2}\, dx, \tag{6.4.8}$$

where

$$x = \frac{1}{1 + \sqrt{2\chi^2_{int}}}. \tag{6.4.9}$$

The internal probability built using this description is shown in Figure 6.5 for the Composite Phase I data sample (Section 6.5).

6.4.2 The Crossing Electron External Vertex Hypothesis (χ^2_{ext})

The external vertex hypothesis assumes that an external γ particle Compton scatters in a scintillator to produce an electron, which then crosses the entire tracking volume via a source foil and deposits energy in a second scintillator. Assuming that only one particle crosses the tracking volume, it has reconstructed track lengths L_i and deposits energies E_i in the calorimeter, and has a ToF, t^{tof}, obtained from the reconstruction, (in natural units) of

$$t^{tof} = \frac{L_1}{\beta_1} + \frac{L_1'}{\beta_1'}, \tag{6.4.10}$$

where β_1 and β_1' have the same form as β_i in Equation 6.4.3, but β_1' takes into consideration the energy loss of the particle as it traverses the source foil as well as through the tracking chamber. The external χ^2_{ext} ToF variable is then written as

$$\chi^2_{ext} = \frac{((t^{tdc}_{1'} - t^{tdc}_1) - t^{tof})^2}{\sigma^2_{t^{ext}}} \tag{6.4.11}$$

where $\sigma^2_{t^{ext}}$ has the explicit form of

$$\sigma^2_{t^{ext}} = \sum_{i=1'}^{1} \sigma^2_{t^{tdc}_i} + \left(\frac{t^{tof} m_e^2}{E_1(E_1+m_e)(E_1+2m_e)}\right)\sigma^2_{E_1} + \left(\frac{1}{\beta_1}\right)(\sigma^2_{L_{1'}} + \sigma^2_{L_1}). \tag{6.4.12}$$

The probability that the event is external $P(\chi^2_{ext})$ has the same form as in Equation 6.4.8.

6.5 Analysis Data Set

NEMO3 data are split into two phases (Section 5.6) according to the level of radon contamination present during the time of data acquisition. 'Phase I' (February 2003 - September 2004) contains higher level radon data and 'Phase II' (October 2004 - January 2011) contains lower level radon data (taken after the installation of the radon trapping facility). Phase II data collected up to December 2009 is presented in this analysis. As mentioned in Section 5.3 the ^{100}Mo source foils are split into two categories: composite and metal foils. The analysis presented is carried out in four subsets of data due to the individual background models required for each: ^{100}Mo composite foils Phase I, ^{100}Mo composite foils Phase II, ^{100}Mo metal foils Phase I and ^{100}Mo metal foils Phase II.

6.6 Event Preselection

In order to create a subset of a manageable size, yet one that is still flexible for cut studies, the data and MC undergo a 'slimming' process, where loose selection criteria cuts are applied. In order to select a $\beta\beta$ event the following criteria are required:

- Two negatively charged tracks (reconstructed from the direction of curvature) originating within the ^{100} Mo source foil with two scintillator deposits > 200keV associated to each track.

- The event vertex is defined as the distance between the position of the two reconstructed track vertices of intersection with the foil. As the source foils are 80μm thick the vertex cuts are determined by the resolution of the tracking detector (Section 6.6.1). In order to maximise the positional resolution of the event origin the distance between event vertices must be ΔXY < 4cm in the transverse plane and ΔZ < 8cm in the longitudinal direction as an initial selection. This criteria is further tightened during the final selection (Section 8.1).

- The sum of the two tracks must be > 60cm. This number is chosen in order to increase distinction between the internal and external hypothesis. Considering a 60cm minimum of the sum of the two tracks (or $\sim$ 30cm for each track) a relativistic internal electron will travel its minimum track length (per particle) in 1000ps. An external electron will hence take 2000ps, which is significantly larger than NEMO3's time resolution ($\sigma = 250$ ps at 1MeV).

- The event must be 'internal', hence the ToF probabilities are required to be $\chi^2_{int} > 1\%$ (Section 6.4.1) and $\chi^2_{ext} < 10\%$ (Section 6.4.2) for the initial selection. This criteria is further tightened during the final selection (Section 8.1).

An example of a typical $\beta\beta$ event that has passed the listed selection criteria can be seen in Figure 6.6.

6.6.1 The Two Electron Vertex Resolution

As the two electrons are required to originate in the same vertex to select $\beta\beta$ events it is important to understand the vertex resolution of NEMO3. The vertex selection requirements are determined by the resolution of the tracking detector and are taken as $\sim 5\sigma$ of the resolution. The transverse (ΔXY) and longitudinal (ΔZ) vertex distributions were studied with ^{207}Bi sources placed inside the calibration tubes of the detector (providing two simultaneous conversion electrons of a 2% relative intensity), giving a measurement of the vertex resolutions:

$$\sigma(\Delta\mathrm{XY}) = 0.6\mathrm{cm} \ \text{ and } \ \sigma(\Delta\mathrm{Z}) = 1.0\mathrm{cm}\,[107]. \tag{6.6.1}$$

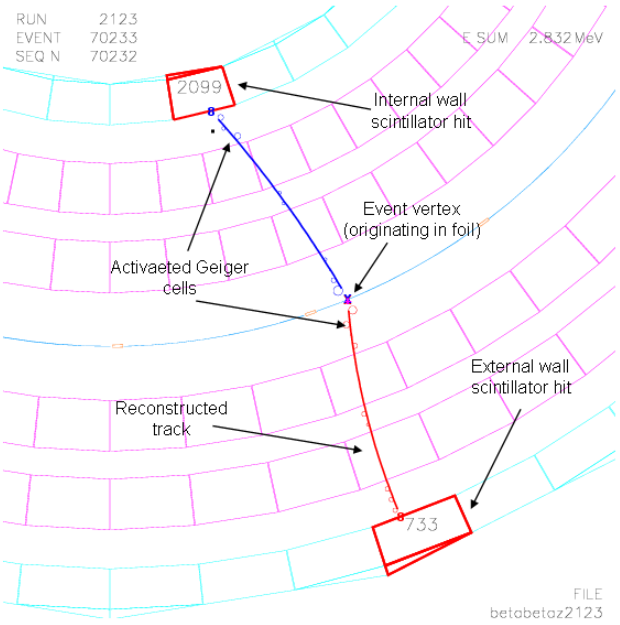

Figure 6.6: NEMO3 event display showing a transverse view of a typical $\beta\beta$ event, with two negatively charged electron tracks and two associated scintillator hits, with a common vertex in the source foil.

6.7 Statistical Analysis

ROOTANA, written in C/C++/ROOT, is a statistical analysis package used for in depth NEMO3 analysis. The software is used to optimise and apply further selection cuts (Section 8.1), to carry out likelihood fitting to determine the $2\nu\beta\beta$ half-life (Sections 6.7.1 and 6.7.2) and to search for $0\nu\beta\beta$ decay. If no $0\nu\beta\beta$ signal is found then an exclusion of the signal at a specific confidence level is performed (Section 6.7.3).

6.7.1 Likelihood Fitting of Monte Carlo to Data

In order to take into account the shape of the energy distribution ROOTANA uses a maximised binned log-likelihood function [117], where each bin is treated as an independent search channel. Assume that the number of events, d_i, in the i^{th} bin is predicted by the MC to be

$$d_i = s_i + b_i, \tag{6.7.1}$$

where s_i is the signal ($2\nu\beta\beta$) and b_i is all other backgrounds. Each bin follows a Poisson distribution, therefore the probability P_i to observe n_i events is given by

$$P_i = \frac{e^{-d_i} d_i^{n_i}}{n_i!} = \frac{e^{s_i+b_i}(s_i+b_i)^{n_i}}{n_i!}. \tag{6.7.2}$$

The likelihood (L) is defined as the product of the binned probabilities (for a total number of bins N) as

$$L = \prod_{i=0}^{N} P_i = \prod_{i=0}^{N} \frac{e^{s_i+b_i}(s_i+b_i)^{n_i}}{n_i!}. \tag{6.7.3}$$

As the function is monotonic a logarithm of the function can be taken

$$\ln(L) = \sum_{i=o}^{N} -(s_i+b_i) + n_i \ln(s_i+b_i) - \ln(n_i!). \tag{6.7.4}$$

The first derivative is then taken (with respect to the total signal (number of $2\nu\beta\beta$ events), S) to find the maximum for L:

$$\frac{\partial \ln(L)}{\partial S} = -1 + \sum_{i=o}^{N} \left(\frac{n_i}{s_i+b_i} \frac{\partial s_i}{\partial S} \right) = 0. \tag{6.7.5}$$

Equation 6.7.5 is solved numerically for S to find the number of $2\nu\beta\beta$ events in the experiment. The likelihood, L, follows a χ^2 distribution. Hence, to determine the one σ error, ΔS, on S one must find the interval where $\ln(L)$ (Equation 6.7.4) decreases by $^1/_2$ from its maximum value:

$$\ln(L(S)) - \ln(L(S \pm \Delta S)) = \frac{1}{2}. \tag{6.7.6}$$

Equation 6.7.6 is solved numerically for ΔS to find the error on the total number of signal events.

6.7.2 Calculating the Half-Life

Like other decays, the isotopes under study in NEMO3 obey the radioactive decay law:

$$N = N_0 e^{-\lambda t}, \tag{6.7.7}$$

where N_0 is the number of initial atoms in the sample, N is the number of atoms remaining in the sample after time t (the experimental run time) and $\lambda = \frac{1}{\tau} = \frac{\ln(2)}{T_{1/2}}$ (where τ is the average lifetime and $T_{1/2}$ is the half-life). As the half-lives involved are large (of the order of 10^{20} years or more), λ becomes small and a Taylor expansion of the exponential in Equation 6.7.7 can be taken, giving

$$e^{-\lambda t} \approx 1 - \lambda t, \tag{6.7.8}$$

which is substituted into Equation 6.7.7 to give

$$N_{decay} = N_0(1 - (1 - \lambda t)) = N_0 \lambda t = N_0 \frac{\ln(2)}{T_{1/2}} t, \tag{6.7.9}$$

where $N_{decay} = N_0 - N$ and is the number of observed decays. The efficiency of the detector, η, is not perfect and therefore N_{decay} must be corrected for

$$N_{decay} \rightarrow \frac{N_{decay}}{\eta} \tag{6.7.10}$$

and η introduced into Equation 6.7.9:

$$N_{decay} = \eta N_0 \lambda t, \tag{6.7.11}$$

where the initial number of atoms in the experiment, N_0, is expressed as $N_0 = \frac{N_A m}{M}$, N_A is Avogadro's number $= 6.022\text{x}10^{23}$ mol^{-1}, m is the isotope mass (in g) and M is the molar mass (in gmol^{-1}).

Solving for $T_{1/2}$ gives

$$T_{1/2} = \frac{N_A m}{M} \frac{\eta}{N_{decay}} \ln(2) t. \tag{6.7.12}$$

6.7.3 Limit Setting and Confidence Levels

The search for $0\nu\beta\beta$ involves looking for rare events with potentially high backgrounds. When the statistical significance of a signal is too low to claim a half-life measurement, the signal is excluded at a particular confidence level (CL). Using the binned distribution of data, background and signal (similar to the method described in Section 6.7.1) provides a more robust and reliable method for limit setting compared to simple counting experiments [118, 119].

The so called CL$_S$ method uses the log likelihood ratio (LLR) test statistic, which is an optimal one for searches involving small statistics [120, 121]. The LLR test checks for consistency between data and two hypotheses: the 'signal plus background, $S + B$' hypothesis, which takes into account indication of new physics and the background,

and the 'background only, B', hypothesis, which takes into account background only. This is defined as

$$Q = \frac{L(S+B)}{L(B)}, \tag{6.7.13}$$

where $L(S+B)$ and $L(B)$ are the Poisson likelihoods for the $S+B$ and B hypotheses respectively.

Substituting the $S+B$ (as defined in Equation 6.7.3) and B hypotheses into Equation 6.7.13 gives

$$Q = \prod_{i=0}^{N} \frac{e^{-(s_i+b_i)}(s_i+b_i)^{x_i}/x_i!}{e^{-b_i}b_i^{x_i}/x_i!}, \tag{6.7.14}$$

$$= \prod_{i=0}^{N} e^{-s_i} \left(\frac{s_i+b_i}{b_i}\right)^{x_i}, \tag{6.7.15}$$

where i is the i^{th} bin of the histogram, s_i is the number of expected signal ($0\nu\beta\beta$) events in bin i, b_i is the number of predicted background events and x_i is randomly obtained Poisson distributed pseudo-data given an expectation of $p = s_i + b_i$ events. The systematic uncertainties, σ_j, on the expectations, p^0, are assumed to follow a Gaussian distribution,

$$p = p^0 \left(1 + \sum_j g(\sigma_j)\right), \tag{6.7.16}$$

where g is a random number taken from a Gaussian distribution with a width of one and a mean of zero, and σ_j is the j^{th} fractional uncertainty on the rate of p^0.

The LLR statistic in Equation 6.7.15 is recast as a negative LLR (NLLR) and is written as

$$\chi \equiv NLLR = -2\ln(Q), \tag{6.7.17}$$

$$= -2\sum_{i=0}^{N} \left(s_i - x_i \ln(1 + \frac{s_i}{b_i})\right). \tag{6.7.18}$$

The generated x_i is substituted with observed data, d_i, to obtain the NLLR of the real data (χ_d). The confidence level (CL) in the $S+B$ hypothesis (CL_{S+B}) is given by

$$CL_{S+B} = P_{S+B}(\chi > \chi_d) = \int_{\chi_d}^{\infty} \frac{\partial P_{S+B}}{\partial \chi}\, d\chi, \tag{6.7.19}$$

where $P_{S+B}(\chi > \chi_d)$ is the probability to produce an outcome which is less like the $S+B$ hypothesis than the observed data and is found by integrating the expected NLLR distribution for the $S + B$ hypothesis. Similarly, the CL in the B hypothesis (CL_B) is found by integrating the expected NLLR distribution for the B hypothesis, and is given by

$$CL_B = P_B(\chi > \chi_d) = \int_{\chi_d}^{\infty} \frac{\partial P_B}{\partial \chi}\, d\chi. \tag{6.7.20}$$

An example of NLLR distributions for the $S + B$ and B hypotheses can be seen in Figure 6.7. The confidence level in the signal (CL_S, which gives its name to the CL_S method) is then defined as

$$CL_S = \frac{CL_{S+B}}{CL_B}, \tag{6.7.21}$$

where CL_{S+B} is divided by CL_B to take into account downward fluctuations of the background, which create inconsistencies between the expected background and observed data. The limit is found by scaling the signal until $CL_S = 0.1$ (or $1-CL_S = 0.9$, a 90% confidence level), which is the convention for $0\nu\beta\beta$ searches.

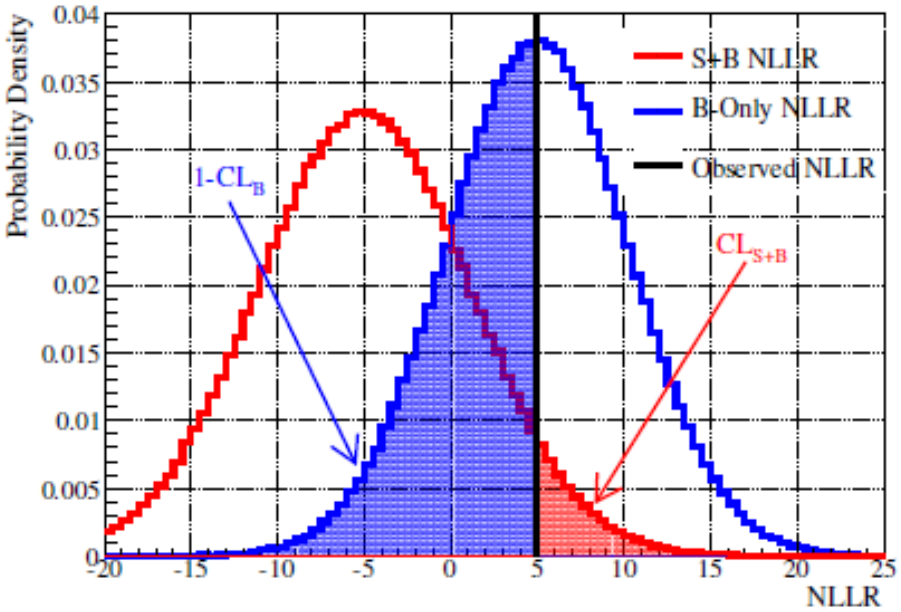

Figure 6.7: Example distributions of the NLLR (negative log likelihood) test statistic for the expectation in the $S + B$ hypothesis (red) and in the B hypothesis (blue) compared to observed data (black). The regions used for the integral to obtain $1 - CL_B$ and CL_{S+B} are shown [122].

Chapter 7

NEMO3 ^{100}Mo Background Model

NEMO3 is unique amongst $0\nu\beta\beta$ detectors as the only backgrounds to the experiment are those that mimic the signature of $2\nu\beta\beta$ and $0\nu\beta\beta$ events, producing two tracks with two scintillator deposits ($2e^-$-like events), with an energy sum in the region of $2\nu\beta\beta$ and the $Q_{\beta\beta}$ value of $0\nu\beta\beta$ decay ($2.5 - 4.3$MeV). Any other background events, such as α particles, which contribute to backgrounds in other $0\nu\beta\beta$ detectors, are rejected by NEMO3's event topology. In particular, NEMO3's sensitivity to $0\nu\beta\beta$ decay depends on the number of background events found in the $Q_{\beta\beta}$ region. It is important to be able to identify 2β-like background events that remain in the data after event selection and to statistically subtract them from the data to obtain the signal.

The NEMO3 backgrounds can be thought of in two categories - internal backgrounds (Section 7.3), originating from radioactive contaminants inside the double beta decay source foils, and external backgrounds (Section 7.4), originating outside of the source foils.

7.1 Natural Radioactivity

The are two isotopes from the ^{232}Th and ^{238}U natural radioactivity chains that are particularly dangerous to $0\nu\beta\beta$ searches in the region of 3MeV (the $Q_{\beta\beta}$ value of ^{100}Mo), whose decay schemes are shown in Figure 7.1. ^{208}Tl is part of the ^{232}Th chain, with a Q_β value of 4.99MeV and a half-life of 3.05 minutes (Figure 7.2). ^{214}Bi is part of the ^{238}U chain, with a Q_β value of 3.27MeV and a half-life of 19.9 minutes (Figure 7.3). Both of the isotopes decay via β emission and can mimic 2β events via certain mechanisms (described in Sections 7.3 and 7.4).

One of the focuses of the NEMO3 R&D was to suppress the amount of ^{208}Tl and

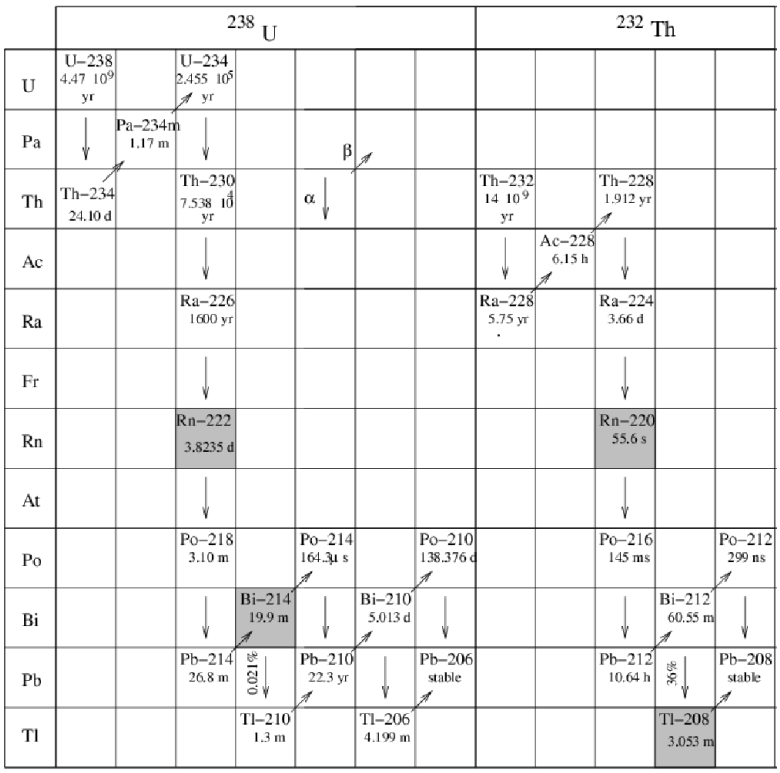

Figure 7.1: ^{238}U and ^{232}Th natural radioactivity chains, with the the ^{222}Rn $\rightarrow^{214}$Bi and ^{220}Rn $\rightarrow^{208}$Tl transitions highlighted.

^{214}Bi in the detector components to minimise contamination. Prior to installation into the detector the components were measured with HPGe detectors, the results of which can be seen in Table 7.1. However, both ^{208}Tl and ^{214}Bi are produced by ^{220}Rn and ^{222}Rn respectively, which enter the detector through diffusion from the surrounding rock. ^{220}Rn has a short half-life of 55.6 seconds and therefore does not pose as much of a problem as ^{222}Rn, which has a half-life of 3.82 days and has enough time to diffuse through the concrete walls of the laboratory into the detector.

7.2 ^{222}Radon

^{222}Radon is the most troublesome background for the experiment as it originates from the ^{238}U natural radioactivity decay chain and is therefore present within the detector components and the surroundings. It therefore contributes to both the internal and external backgrounds of NEMO3. It diffusely permeates into the detector, providing a steady supply of its daughter isotope, ^{214}Bi via two α decays and a β decay (Figure 7.1). Various steps have been taken to reduce the level of radon contamination in the

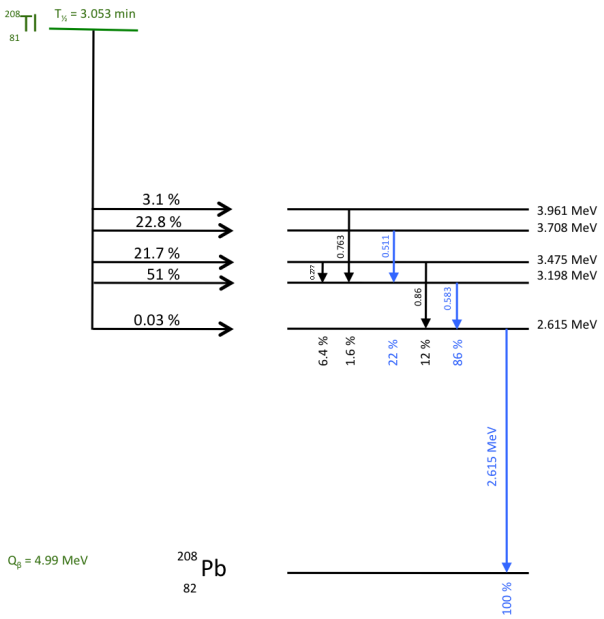

Figure 7.2: Heavily simplified ^{208}Tl decay scheme, with a harmful γ transition (in blue) at 2.62MeV with a $\sim 100\%$ intensity. β decays are represented by horizontal arrows and γ decays by vertical arrows.

		Activity (Bq)	
Detector Component	Mass (kg)	^{208}Tl	^{214}Bi
Copper Frame	25000	< 25	< 10
Iron Shield	180000	< 300	< 300
Steel Frame	10000	< 6	< 8
Tracker Wires	1.7	$< 10^{-3}$	$< 6 \times 10^{-4}$
Scintillator Blocks	5000	< 0.7	< 0.3
PMTs	600	< 302	< 17.8
μ-metal PMT Shields	2000	< 2	< 2.7

Table 7.1: Radioactivity measurements of ^{208}Tl and ^{214}Bi (in Bq) for the main detector components, carried out with HPGe detectors and extrapolated to the total mass of the component [108].

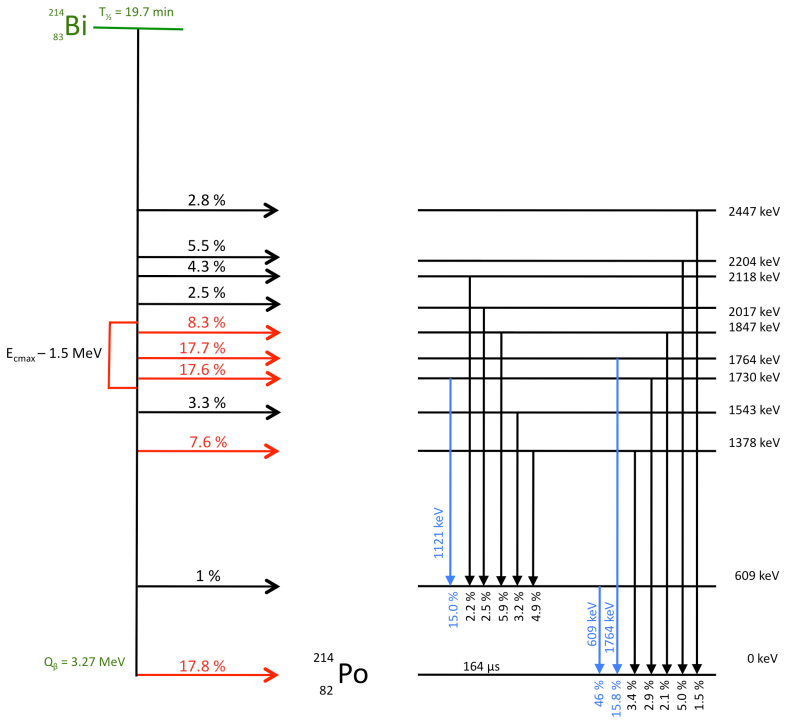

Figure 7.3: ^{214}Bi decay scheme, with harmful γ transitions (in blue) at 1.12MeV (with a 15.0% intensity) and at 1.76MeV (with a 15.8% intensity). β decays are represented by horizontal arrows and γ decays by vertical arrows.

experiment, such as purification of materials and the installation of the anti-radon factory in the LSM (Section 5.6). Bi-Po events (Section 6.3.1) are used to measure the level of ^{222}Rn background and to exclude these events from the $\beta\beta$ analysis, using the α decay of ^{214}Bi's daughter isotope, ^{214}Po, which has a half-life of 164μs. Keeping a time window open for 710μs allows the αs produced in the Bi-Po process to be tagged.

Phase I data (February 2003 - September 2004) has a total average radon contamination level of $\sim$ 700 $\pm$ 1mBq (or 37.7 $\pm$ 0.1mBq/m^3) inside the tracking volume of the detector [107]. NEMO3 data indicates that the α radon daughters are deposited on the surface of the source foils, the Geiger chamber cathode wires and the reflective wrapping around the scintillators [113]. This supports evidence that $\sim$ 87% of α-decay daughters are positively charged [123] and hence attracted to negative and grounded surfaces.

After the installation of the anti-radon factory, the total average radon contamination was reduced to 140 $\pm$ 1mBq (or 6.46 $\pm$ 0.05mBq/m^3) insinde the tracking volume of the detector for Phase II (October 2004 - present day) [107], as can be seen in Figure

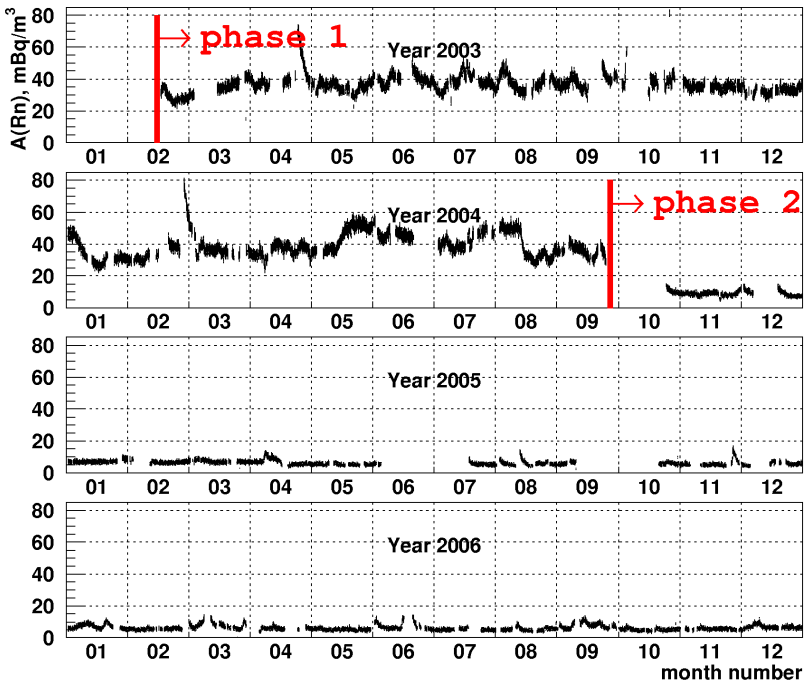

Figure 7.4: The ^{222}Rn activity (in mBq/m^3) inside the tracking chamber measured on an hourly basis for Phase I and part of Phase II (to the end of 2006) [113].

7.4.

7.3 Internal Backgrounds

Internal backgrounds are defined as those that come from isotopes decaying within the source foils.

7.3.1 The $2\nu\beta\beta$ Tail

An irreducible background for NEMO3 is the overlap of the $2\nu\beta\beta$ decay tail onto the $0\nu\beta\beta$ decay peak, as shown in Figure 7.5. The energy resolution of the calorimeter is key to discriminating between the 0ν and 2ν distributions as their topological signatures are identical. The thickness of the source foils was chosen so that the loss of energy effects in the foils would not be greater than the intrinsic resolution of the calorimeter. This is one of the dominant backgrounds to the search for $0\nu\beta\beta$ decay for NEMO3 and therefore must be extremely well measured and understood by the experiment in order to estimate the number of $2\nu\beta\beta$ events contributing to the $0\nu\beta\beta$ peak.

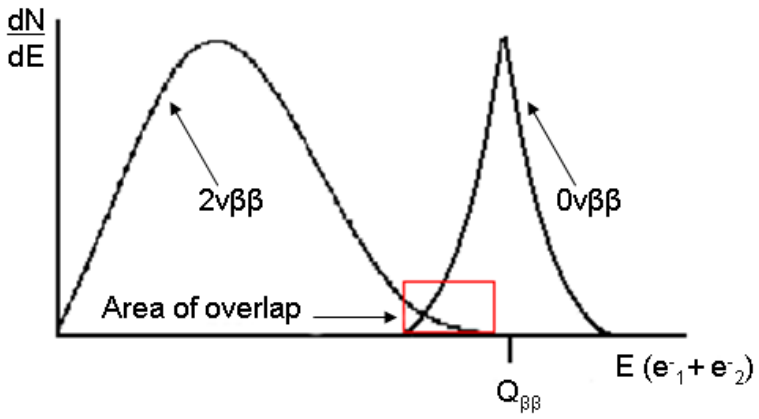

Figure 7.5: Overlap of the $2\nu\beta\beta$ tail onto the $0\nu\beta\beta$ peak, with indistinction between the two due to the calorimeter's non perfect energy resolution. The scale of the $0\nu\beta\beta$ decay peak is greatly exaggerated to emphasize the overlap.

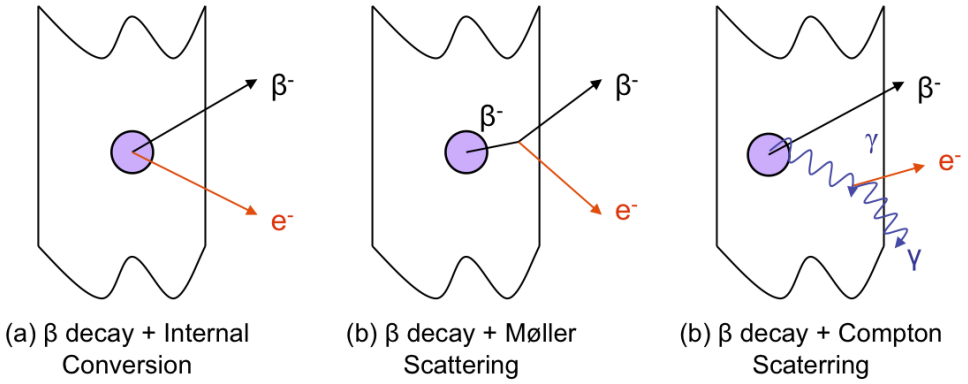

Figure 7.6: The three dominant internal background processes that mimic $\beta\beta$ events.

7.3.2 Internal β Emitters

β emitters, such as ^{208}Tl, ^{214}Bi and others, coming from radon and natural radioactivity are contaminants present inside the source foils. They decay via β emission, typically to an excited state, and can mimic $\beta\beta$ events via three mechanisms: β decay accompanied by an internal conversion (where the excitation energy of a daughter nucleus is transferred to an orbital electron which is then ejected from the nucleus), Møller scattering (where an emitted β particle scatters in the foil, ejecting a second electron) or Compton scattering (where a β particle emission is followed by a de-excitation photon, which scatters in the source foil to generate a Compton electron). These processes are illustrated in Figure 7.6).

7.4 External Backgrounds

External backgrounds are defined as those that come from isotopes which originate outside of the source foils, including the detector components and the laboratory and its surroundings. External background interactions are dominated by photon interactions, which originate from natural radioactivity of the detector components and the surroundings (Section 7.1) and neutrons (produced in the surrounding rocks and detector components by spontaneous fission and the (α,n) reaction). The contribution from cosmic muons is negligible due to the overburden of rock surrounding the laboratory.

7.4.1 Crossing Events

Crossing electron events (described in Section 6.4) are those produced by external photons Compton scattering in the detector components. The electrons produced can scatter in the foil to create an event with two tracks and two scintillator deposits. This background is reduced using ToF information and NEMO3's magnetic field, causing external crossing electron events to curve into the same direction on the two sides of the source foil as opposed to opposite directions for internal events.

7.4.2 γ-Ray Interaction with Source Foils

The external γs can interact with the source foil to mimic $\beta\beta$ events via five different mechanisms: pair creation, Compton scattering followed by Møller scattering, double Compton scattering, the photoelectric effect followed by Møller scattering and Compton scattering followed by the photoelectric effect. Pair production occurs when a high energy γ ($E_\gamma \geq 1.02$MeV) interacts with the source foil to produce an electron-positron pair. The positron can be misidentified as an electron in the reconstruction, mimicking a $\beta\beta$ event. NEMO3's 25G magnetic field is able to identify these events with a 95% efficiency at 1MeV [107]. The external background processes are illustrated in Figure 7.7.

7.4.3 External ^{208}Tl and ^{214}Bi

The ^{208}Tl and ^{214}Bi originating from ^{220}Rn (thoron) and ^{222}Rn (radon) (as described in Sections 7.1 and 7.2) outside of the source foils are considered to be part of the external background, contaminating the tracking chamber.

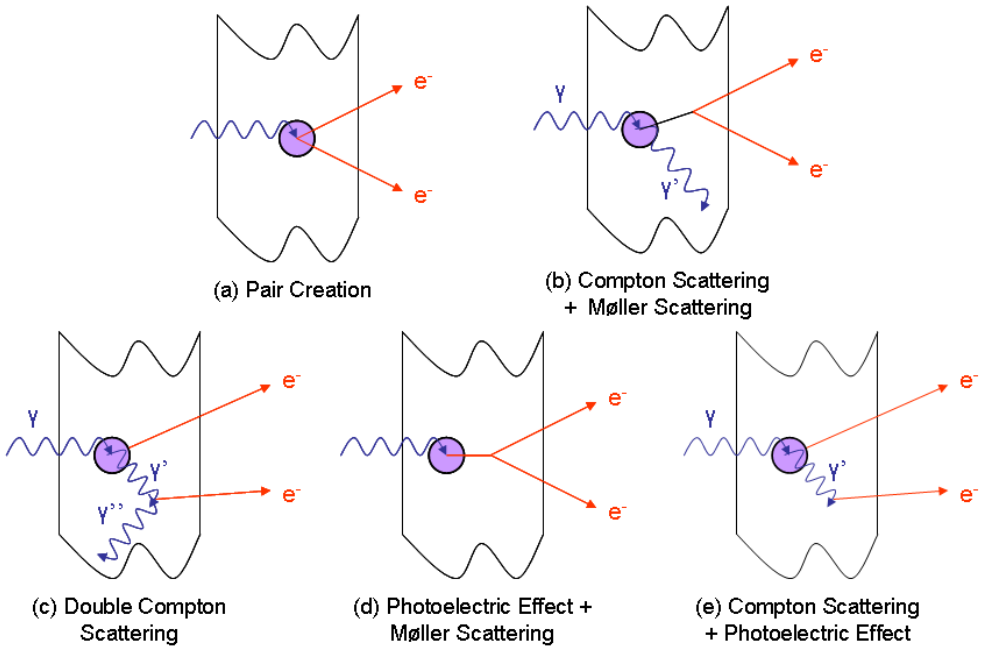

Figure 7.7: The five dominant external background processes that mimic $\beta\beta$ events.

7.5 ^{100}Mo Background Model

The ^{100}Mo internal and external radioactive background models used for the analysis presented are existing models developed by the NEMO3 collaboration. A summary of the ^{100}Mo background model is presented. An in depth description of the background model can be found in [113]. All backgrounds are identified using event topologies obtained with NEMO3's calorimeter-tracker technique.

7.5.1 ^{100}Mo Internal Background Model

The internal background varies for the metal and composite ^{100}Mo foils due to their different production techniques. ToF information cannot be used to reject internal background events. Instead, after topology event selection has been carried out to select $\beta\beta$ events, energy and angular distribution cuts are used. The components of the internal backgrounds are radon (^{222}Rn) and thoron (^{220}Rn) products deposited on the surface of the foils and β emitters originating in the source foil.

The internal radon background component is measured using Bi-Po events (Section 6.3.1). The analysis is carried out for each ^{100}Mo sector, studied for layer by layer of the Geiger tracking chamber in order to get an accurate description of the background near the source foils.

^{214}Bi Contamination on the Surface of the ^{100}Mo Source Foils

- The ^{100}Mo composite foils are held together by thin Mylar films, which are also considered to be a source of internal background. The activity for the Mylar was obtained with HPGe detector measurements, prior to and post foil fabrication. The ^{214}Bi activity originating in the ^{100}Mo composite Mylar films is set to the value obtained with the HPGe detectors (0.59mBq [113]). The ^{214}Bi contamination of the foil is estimated both inside the foil and on the surface of the foil, using statistical models based on electron distributions and MC simulations to distinguish between the two. An electron coming from inside of the source foil loses more energy (through interactions inside the foil) and therefore stops earlier and has a distorted distribution compared to that of an electron coming from the surface of the foil.

- The ^{100}Mo metallic foils were produced from a ^{100}Mo powder (without the need for any Mylar to hold them together). The ^{214}Bi contamination of the foil is estimated both inside and on the surface of the foil, as described above for the composite foil.

The ^{208}Tl contamination is measured with the e$\gamma\gamma$ and e$\gamma\gamma\gamma$ channels. The β decay of ^{208}Tl (its daughter isotope) is accompanied by a 2.62MeV γ from the first excited state of ^{208}Pb [124] in $\sim 100\%$ of cases. It is accompanied by a second γ (of 583 or 860keV) with a branching ratio of $\sim 100\%$. There is a 35% chance for a third γ to be emitted during the decay. This places a selection requirement of the highest energy γ to have $E_\gamma > 1.7$MeV and the energy of the electron to be $E_e > (4.2 - \Sigma E_\gamma)$MeV, with an event vertex in the source foil [113].

At lower energies other isotopes, such as ^{40}K (originating from the surrounding rock), ^{228}Ac, ^{212}Bi (both from the ^{232}Th chain), ^{234m}Pa and ^{210}Pb (both from the ^{238}U chain), contribute to the background in the $2\nu\beta\beta$ spectrum. The 1e and eγ channels are used to study these backgrounds, requiring a track associated to a scintillator deposit with energy > 500keV, with the event vertex in the ^{100}Mo foils. An estimate of the ^{40}K activity was made with HPGe detectors and used as part of the internal model [125].

Figure 7.8 [126] shows the internal backgrounds for the 1e channel for composite and metallic foils for Phase I data. The internal backgrounds shown include ^{228}Ac,

^{212}Bi and ^{208}Tl collectively (labelled as ^{228}Ra - backgrounds that originate from the ^{232}Th chain), ^{214}Bi and ^{214}Pb collectively (labelled as ^{226}Ra - backgrounds that originate from the ^{238}U chain), ^{234m}Pa and ^{40}K. ^{214}Bi is also shown as an individual component (labelled as Radon, originating from ^{222}Rn). The metallic foils also have a contamination contribution from ^{211}Pb and ^{207}Tl (labelled as ^{235}U, originating from the ^{235}U natural decay chain) due to the different production mechanisms for the composite and metallic foils. The internal background model is summarised in Table 7.2.

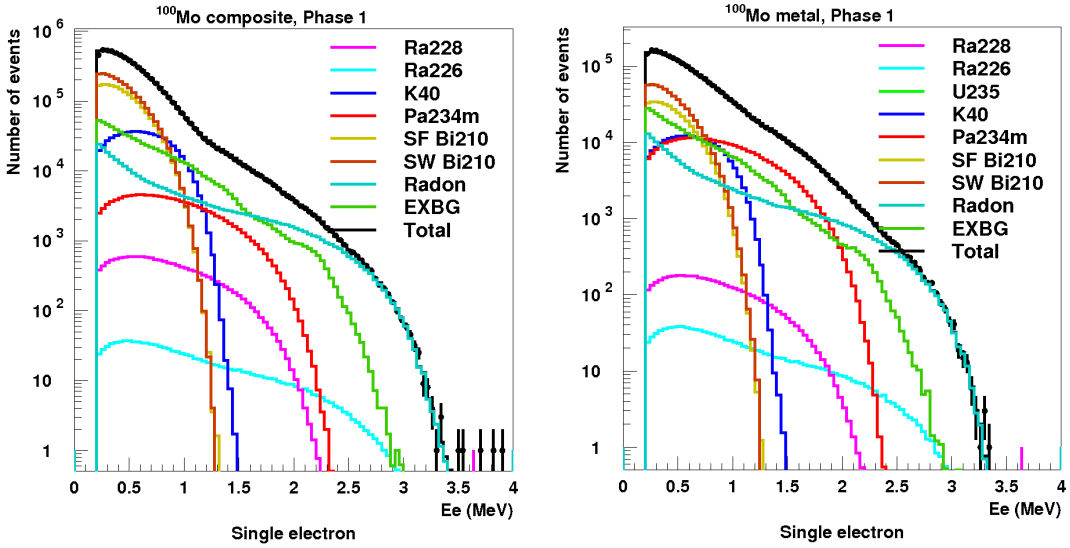

Figure 7.8: Energy spectrum of the ^{100}Mo internal backgrounds (for composite (left) and metallic (right) foils) in the 1e channel. The sum of external backgrounds and backgrounds originating on the surface of the foil and the wires are also shown [126].

7.5.2 ^{100}Mo External Background Model

The external background varies for Phase I and Phase II, due to the higher flux of radon during Phase I running. The external background is divided into two categories: background events due to radioactivity inside the tracking chamber and background events that originate outside of the tracking chamber (such as the calorimeter, the detector shielding and the laboratory surroundings).

External Background Inside the Tracking Chamber

The main components that comprise the background inside the tracking chamber are radon (^{222}Rn), thoron (^{220}Rn) and ^{210}Bi (on the Geiger wires of the tracker). The external background component originating from radon in the tracking chamber is measured

Isotope	Composite Foil Activity (mBq)	Metallic Foil Activity (mBq)
^{228}Ac	1.86	0.79
^{212}Bi	1.86	0.79
^{208}Tl	0.70	0.28
^{214}Bi	0.25	0.26
^{214}Pb	0.25	0.26
^{234m}Pa	10.59	11.82
^{40}K	68.82	12.94
^{211}Pb	0	17.97
^{207}Tl	0	17.97
^{214}Bi in Mylar	0.59	0
^{214}Pb in Mylar	0.59	0

Table 7.2: Summary of the main components of the NEMO3 internal background model (in mBq) measured with the eα, e$\gamma\gamma$, e$\gamma\gamma\gamma$ and 1e channels [113, 126].

using Bi-Po events (Section 6.3.1). The analysis is carried out sector by sector and layer by layer of the tracking chamber to have an accurate description of the background near the source foils. A cross check to measure this background can be carried out using the eγ channel as a large fraction of ^{214}Bi events is accompanied by a high energy γ-ray. The eγ channel provides a measurement of the systematic uncertainty of ^{222}Rn activity within the Geiger chamber to within 10%. The 20 sector average of ^{214}Bi contamination in the tracker is 700 ± 1mBq for Phase I and 140 ± 1mBq for Phase II [113].

The thoron contamination is measured with the e$\gamma\gamma$ and e$\gamma\gamma\gamma$ channels with selection criteria similar to that described in Section 7.5.1, with the event vertex required to originate on a Geiger wire. The average of ^{208}Tl contamination in the tracker is 3.5 ± 0.4mBq for Phase I and 2.9 ± 0.4mBq for Phase II [113].

Another source of contamination in the tracking chamber comes from the β-decay of ^{210}Bi from ^{210}Pb, originating in the ^{238}U natural radioactivity chain, with a half-life of 22.3 years and a Q_β value of 1.16MeV. This does not pose a threat to the search for $0\nu\beta\beta$ but must be considered as a background to the $2\nu\beta\beta$ spectrum. The ^{210}Bi and

	Activity (Bq)						
Detector Component	^{40}K	^{208}Tl	^{214}Bi	^{214}Pb	^{228}Ac	^{60}Co	^{210}Bi
Copper Frame	0	0	0	0	6.09	0	0
Iron Shield	0	484	7360	0	1350	0	0
Steel Frame	100	3.07	9.12	0	8.54	6.09	0
Tracker Wires	0	0	0.198	0.198	0	0	12.6
Scintillator Blocks	21.5	0	0.38	0.38	0	0	30.4
PMTs	1080	27.0	324	0	72.7	0	0
μ-metal PMT Shields	0	0	0	0	0	14.6	0

Table 7.3: Summary of the main components of the NEMO3 external background model (in Bq), according to detector components [113].

^{214}Bi coming from ^{222}Rn are not in equilibrium, with levels of ^{210}Bi being much higher than that of ^{214}Bi. This is speculated to be due to ^{210}Pb being deposited on the wires of the tracking chamber during construction of the detector. The 1e channel is used to estimate this background, with the event selection criteria requiring one electron track with an energy deposit > 600keV with the vertex associated to a Geiger cell. Levels between 2.11Bq and 18.37Bq are measured for different sectors of the detector [113].

External Background Outside of the Tracking Chamber

The external γ flux that originates outside of the tracking chamber is measured using eγ-external and crossing electron events (Section 6.4). Out of the possible sources of external γ events the natural radioactivity in the detector components is the dominant source of contamination, with half of the contribution coming from the cathode glass of the PMTs. A summary of the external background model (including background originating in the tracking chamber) can be seen in Table 7.3.

The model has been verified using the ultra radiopure OFHC (oxygen-free high conductivity) copper foils which occupy sector 0 of the 20 NEMO3 sectors. The eγ-internal (coming from the copper foils) and $2e$ channels were used for the study. Figure 7.9 shows the fit of the background model to the copper data for Phase I and Phase II. A detailed study of the NEMO3 external background model is presented in [113].

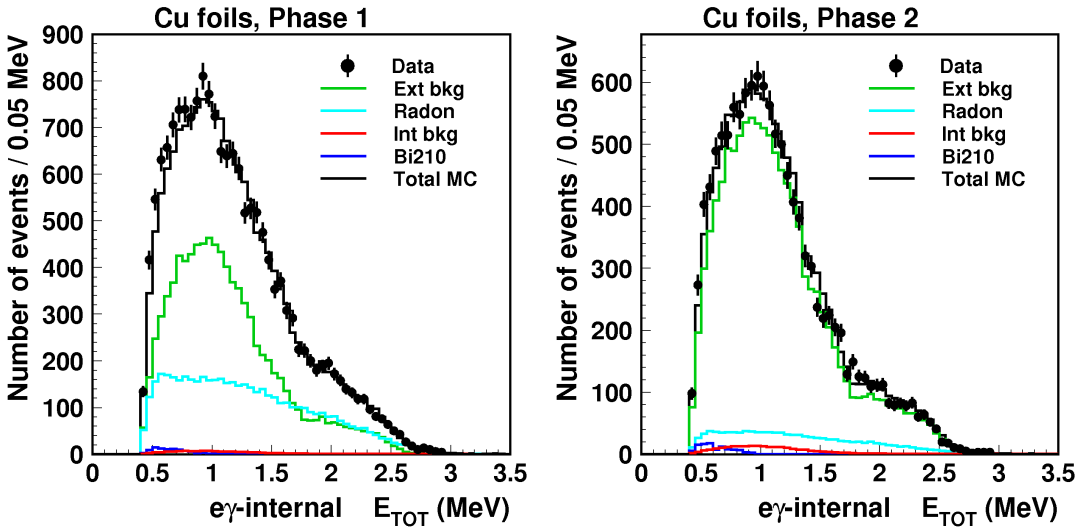

Figure 7.9: Validation of the external background model with Cu foil events, showing the distribution of the energy sum of the e^- and the γ for Phase I and Phase II data [113].

Chapter 8

^{100}Mo Double Beta Decay Analysis

The analysis presented in this thesis focuses on the search for the $0\nu\beta\beta$ decay of ^{100}Mo. Existing NEMO3 collaboration models for the internal and external radioactive backgrounds are used (as described in Chapter 7). Based on these models a $2\nu\beta\beta$ half-life measurement, which is an irreducible background to the $0\nu\beta\beta$ signal, is made. A search for $0\nu\beta\beta$ decay is then carried out.

The double beta decay analysis of ^{100}Mo is carried out as described in Chapter 6. The $2\nu\beta\beta$ background, radioactive backgrounds and the $0\nu\beta\beta$ signal MC events are simulated and propagated through a full detector description (Section 6.1). The MC and data are then both reconstructed, taking into account the status of the detector at the time of acquisition (Section 6.2) and undergo event preselection (Section 6.6). Following this the event selection is further refined (Section 8.1) and the fitting of the signal to data (including full internal and external background descriptions) is done using the log-likelihood method (Section 6.7.1).

8.1 Final Selection Cuts

Standard selection criteria have already been applied to the data and MC samples (as described in Section 6.6). To select $\beta\beta$ events further cuts must be applied. The validity of the cut is tested using the signal-to-background (S/B) ratio of the total of $2\nu\beta\beta$ events selected after cuts to the total number of background events.

The $2\nu\beta\beta$ signal (S) was obtained by running an MC simulation of $2\nu\beta\beta$ events originating from the ^{100}Mo source foils, and was then propagated through the NEMO3 detector description and normalised on a previously measured half-life of ^{100}Mo (using Phase I NEMO3 ^{100}Mo data [80]).

The background (B) to the signal was obtained by using control channels where the signal contribution is negligible, selected using event topology (such as the eα, eγ and e$\gamma\gamma$ channels, discussed in Chapter 7), to obtain the background activity. An MC simulation was then run to select 2β-decay like events normalised to the activity of the background measured in those control decay channels.

Standardly, the parameter used for cut optimisation is S/σ_B, where σ_B is the uncertainty on the background B. However, as the background for the ^{100}Mo analysis is very small compared to the signal the fluctuation in σ_B is very small and S/B becomes a more informative variable. The cut study has also been carried out using the S/σ_B parameter, which lead to the same optimisation of cuts as using the S/B parameter.

Each cut was applied in turn to ensure the improvement of the S/B ratio obtained for each successive cut (Figure 8.4). The selection criteria applied are:

- Require isolated scintillator deposits to exclude events where an e$^-$ or a γ has hit the centre of two scintillators or scattered into a nearby scintillator to avoid false energy readings (Section 6.3). This cut is MC driven.

- Require for any scintillator hits that are in the 'petals' (the top and bottom rings of scintillators) to have a hit to the face of the scintillator (any hits to the side give an inaccurate energy reading to due non uniformity in the light collection). This cut is data driven by observation of poor energy readings in data.

- Require the track to be 'internal', with $\chi^2_{int} > 4\%$ and $\chi^2_{ext} < 1\%$. These values were chosen to discard a large fraction of background events. Data are used to determine $\sigma^2_{t^{int}}$ (the error associated with the two electron internal vertex hypothesis (Section 6.4.1) and $\sigma^2_{t^{ext}}$ (the error associated with the crossing electron external vertex hypothesis, Section 6.4.2). These errors are then used as input to the MC simulations.

- Require less than two fast Geiger hits (Geiger hits not associated to a track) on the opposite side of the source foil with the reconstructed tracks within 15cm of the event vertex. This suppresses false $\beta\beta$ events where electrons originate from the wires of the tracker and interact with the source foil. Data are used to measure the level of ^{222}Rn inside the Geiger chamber. This measurement is then

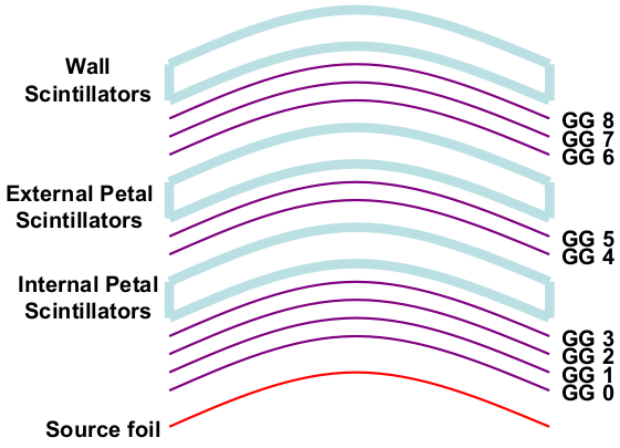

Figure 8.1: Geiger cell layout with respect to scintillators.

extrapolated to $2e^-$ events using MC simulations.

- Require the two tracks to cross one of the first two Geiger layers, ensuring the track originates in the source foil. This cut is driven by observation of Geiger cell efficiencies in the data.

- Require the two tracks to cross one of the last two Geiger layers, ensuring the track ends near a scintillator. This cut was investigated in depth to determine which group of scintillators the tracks should pass near to obtain the best S/B ratio. The possibility of excluding events that end up with scintillator hits in the petals was investigated as these events have poor timing, making it difficult to distinguish between internal and external events [127]. This is because the electrons have a shorter distance to travel to the petal scintillators than to the wall scintillators, making the internal/external distinction more difficult.

  As shown in Figure 5.3 there are nine Geiger layers on each side of the foil, in a $4-2-3$ layer configuration. Geiger layers 0 and 1 are near the source foil, 2 and 3 are near the 'internal petals' (the petal scintillators that are nearest to the source foils), 4 and 5 are near the 'external petals' (the petal scintillators that are furthest from the source foil) and 7 and 8 are near the scintillator walls, as illustrated in Figure 8.1. Three distinct possibilities of Geiger layer cuts were considered:

  - Request that the two tracks cross Geiger layer 7 or 8. This will accept tracks that mostly end near the wall scintillators. However, it does not explicitly

reject all events that end up in the petal scintillators, as can be seen in Figure 8.3, which shows the distribution of scintillator hits after applying the cut. It is possible for some of the events to scatter after interacting with the Geiger wires, with some of the scintillator hits ending up in the petals. This is known as 'Scenario 1' (Figure 8.2(a)).

- Request that the two tracks cross near any scintillator hit (if the scintillator hit is on a wall request layer 7 or 8, if the scintillator hit is on an internal petal request layer 2 or 3 and if the scintillator hit is on an external petal request layer 4 or 5). This accepts any scintillator hit events (Figure 8.3). This is known as 'Scenario 2' (Figure 8.2(b)).
- Request that the two tracks cross layer 7 or 8 if the scintillator hit is on a wall, layer 4 or 5 if the scintillator hit is on an external petal and explicitly reject any events that end up with hits in the internal petals. This accepts scintillator hits in the wall scintillators and the external petals (Figure 8.3). Internal petals are the closest layer of scintillators to the source foil, therefore decreasing the distance of the track from the foil to the scintillator even more than for external petals. Another reason to potentially exclude internal petal events is the identification of the curvature of the track, which is done in the transverse plane (from a top view). When going to a petal hit the track would only have four points in the Geiger layers for the curvature reconstruction, which could be easily misreconstructed. This is known as 'Scenario 3' (Figure 8.2(c)).

The three different possibilities were also looked at as part of the S/B study (Figure 8.4), obtaining the ratio for the three different scenarios and thereafter. Scenario 1 was found to give the highest S/B ratio and hence chosen as the cut to apply. For this cut, data are used to measure the time resolution of the petal and main calorimeter blocks. The resolution is then input into MC simulations to optimise the significance of the measurement.

- Reject any delayed α events, using Bi-Po events (Section 6.3.1). Data is used to measure the level of ^{222}Rn present in the active volume of the detector using control channels (such as the eα, eγ and e$\gamma\gamma$ channels, discussed in Chapter

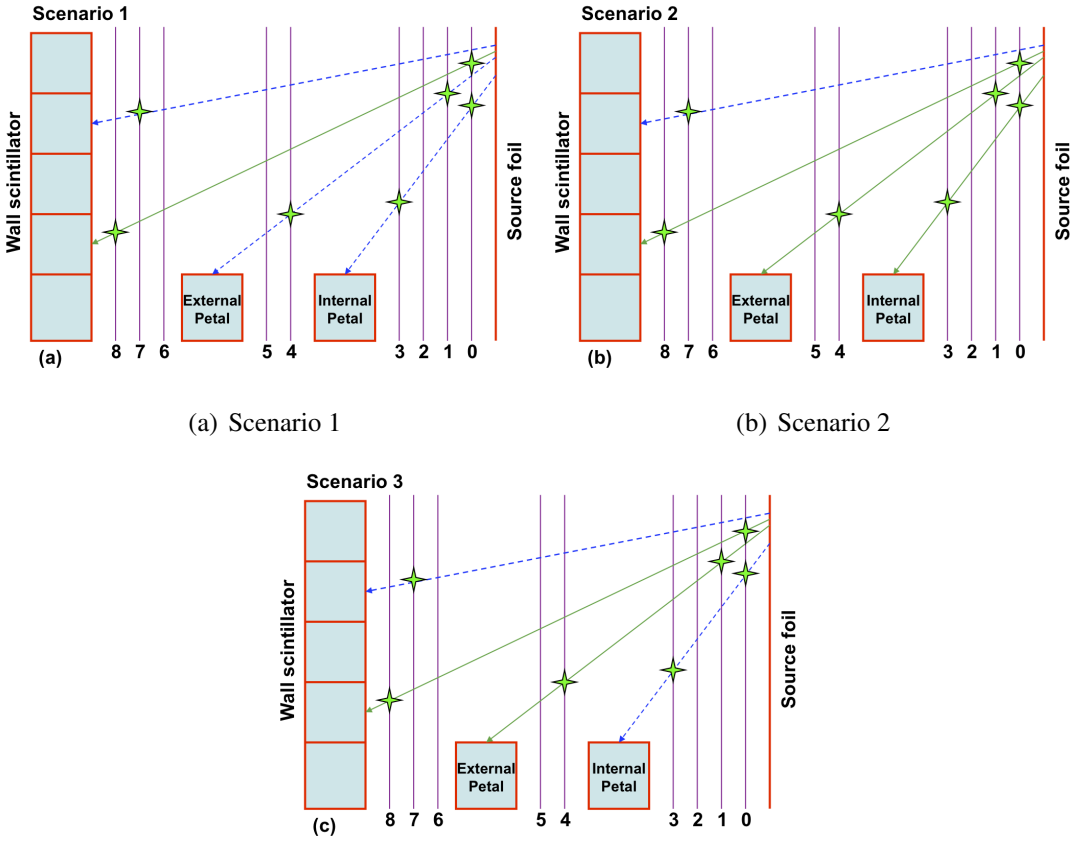

(a) Scenario 1

(b) Scenario 2

(c) Scenario 3

Figure 8.2: Geiger layer requirement scenarios: (a) Scenario 1, (b) Scenario 2 and (c) Scenario 3. The green star markers indicate a triggered Geiger layer, the green solid arrows represent accepted events and the blue dashed arrows represent rejected events. See text for details.

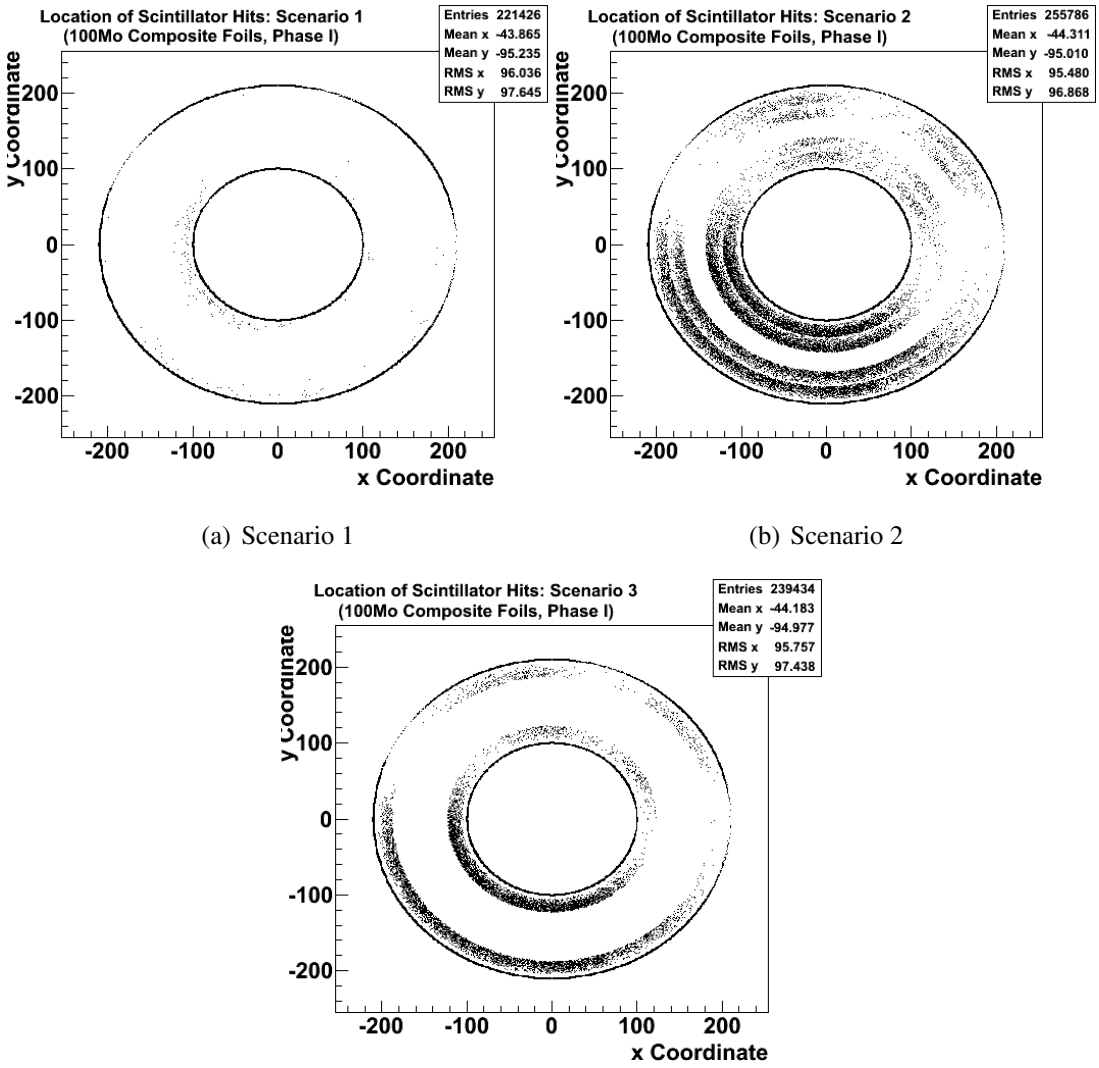

(a) Scenario 1

(b) Scenario 2

(c) Scenario 3

Figure 8.3: Scintillator hit distribution for three different Geiger layer requirement scenarios: (a) Scenario 1, (b) Scenario 2 and (c) Scenario 3. These examples are for the ^{100}Mo Composite Foils and Phase I data. See text for details.

7). The measured activity is then input into MC simulations, which are used to extrapolate to $2e^-$ events and to optimise the S/B ratio.

- Require a tight event vertex to maximise the positional resolution of the event origin within the ^{100}Mo source foils, with the distance between event vertices: ΔXY $<$ 2cm in the transverse plane and ΔZ $<$ 4cm in the longitudinal plane. Special calibration runs in the collected NEMO3 data are used to measure the spatial resolution of the tracker detector, which is then input into MC simulations, used for the S/B optimisation.

- Require events to originate within $\pm$120cm of the source foil in the longitudinal plane ($|Z| < 120$cm). This suppresses extra ^{214}Bi events found near the extremities of the source foils, most likely originating in the foil holders and/or the scintillator faces, as discussed in [113]. This cut is data driven.

Figure 8.4 shows the S/B study (where S = $2\nu\beta\beta$ MC events selected and B = expected number of background events) cut by cut, for the four different parts of the analysis (^{100}Mo Composite Phase I (Figure 8.4(b)) and Phase II (Figure 8.4(c)), and ^{100}Mo Metallic Phase I (Figure 8.4(d)) and Phase II (Figure 8.4(e))). The fractional error on S/B, $\sigma_{S/B}$, is determined by the normalisation of the signal to the previously measured half-life. The S/B ratio increases with each cut, showing that each cut is a valid requirement for selecting $2\nu\beta\beta$ events. The breakdown of the above cuts applied to the $2\nu\beta\beta$ signal and expected background (for Scenario 1) can be seen in Table 8.1.

8.2 The $2e^-$ Angular Distribution Correction

Using NEMO3's topological information it is possible to look at the angular distribution between the two selected electron tracks. The angular distribution can be used to verify the background model and as a discriminator between different $0\nu\beta\beta$ mechanisms [128]. A $(1-\cos\theta)$ distribution is expected due to the kinematics of $2\nu\beta\beta$ decay (with back-to-back events being the most probable), however due to the detector geometry and acceptance an altered distribution with an access of events at $\cos\theta = 0.6-0.8$ is seen. As can be seen in Figure 8.5 (showing the ^{100}Mo Composite Phase I sample) the fit of the total MC to the data are not perfect (with a χ^2 of 126.6/25), with an access of data events over MC at smaller $\cos\theta$ (< -0.7) and a depletion of events at

Cut Applied	Number of $2\nu\beta\beta$ signal events (S)	Number of expected background events (B)
Events generated	2.5 $\times 10^6$	2.5$\times 10^{11}$
1: Preselection	129363 $\pm$ 367	3179 $\pm$ 51
2: Isolated hits	123588 $\pm$ 359	2974 $\pm$ 50
3: No side hits to petal	117285 $\pm$ 350	2757 $\pm$ 49
4: Time of flight	113806 $\pm$ 344	2581 $\pm$ 49
5: Non-associated fast hits	113430 $\pm$ 343	2443 $\pm$ 48
6: GG layers near foil (0/1)	111507 $\pm$ 340	2305 $\pm$ 47
7: GG layers near wall (7/8)	95708 $\pm$ 316	1919 $\pm$ 45
10: No delayed αs	95534 $\pm$ 315	1685 $\pm$ 45
11: Δxy $<$ 2cm, Δz $<$ 4cm	87612 $\pm$ 302	1349 $\pm$ 43
12: Z $\pm$120 cm	87086 $\pm$ 298	1290 $\pm$ 26

Table 8.1: Cut breakdown applied to the $2\nu\beta\beta$ signal (S) and expected background (B) for Scenario 1 for the ^{100}Mo Composite Foils Phase I sample.

1: Preselection
2: Isolated hits
3: No side hits to petals
4: ToF
5: Non-associated fast hits
6: GG layers near foil (0/1)

7: GG layers near wall (7/8)
10: No delayed αs
11: Δxy < 2cm, Δz < 4cm
12. Z: ±120cm

7: If hit on wall, GG 7/8
8: If hit on int petal, GG 2/3
9: If hit on ext petal, GG 4/5
10: No delayed αs
11: Δxy < 2cm, Δz < 4cm
12. Z: ±120cm

7: If hit on wall, GG 7/8
8: If hit on ext petal, GG 4/5
9: Reject all int petal events
10: No delayed αs
11: Δxy < 2cm, Δz < 4cm
12. Z: ±120cm

(a) Cut Breakdown

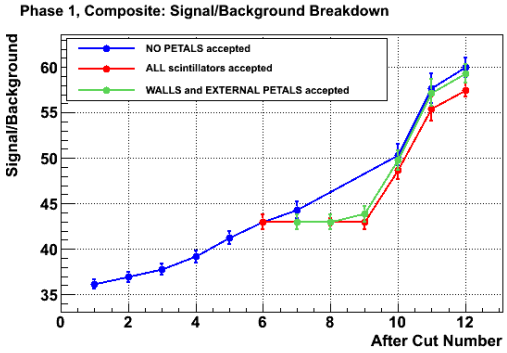

(b) ^{100}Mo Composite Phase I

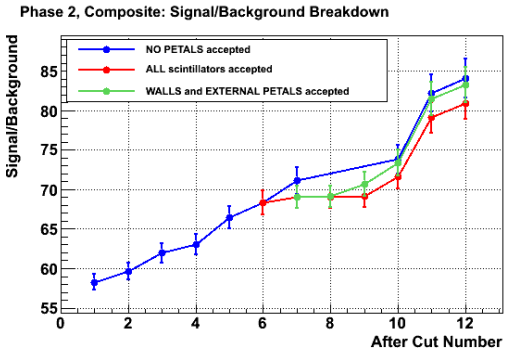

(c) ^{100}Mo Composite Phase II

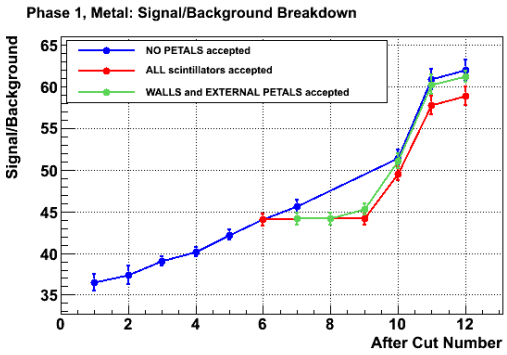

(d) ^{100}Mo Metal Phase I

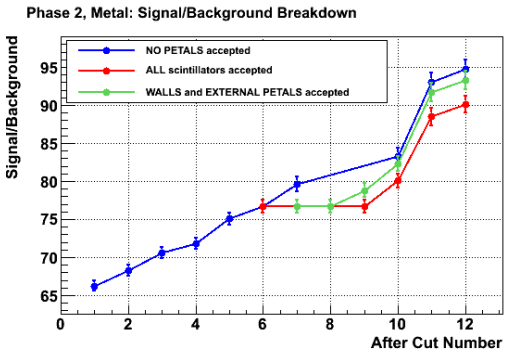

(e) ^{100}Mo Metal Phase II

Figure 8.4: S/B (signal-to-background) cut studies for ^{100}Mo Composite Phase I (a) and II (b) and Metallic Phase I (c) and II (d), calculated after each cut is applied. The three different Geiger layer scenarios are included in the study. The breakdown of cuts is shown in (a).

$0 < \cos\theta < 0.6$. Observing this result has led to a tuning of the MC using NEMO3 data (rather than trying to alter the detector description using GEANT-3.21).

NEMO3 calibration runs are carried out with ^{207}Bi sources (Section 5.5) on a roughly bi-weekly basis, providing two conversion electrons at 482 and 976keV. The acquired ^{207}Bi data are processed in an identical way to the $\beta\beta$ data (as described at the beginning of the section) and the distributions for the real calibration data and MC are obtained. The discrepancy between the ^{207}Bi data and MC is present, as it is in $\beta\beta$ events, therefore taking the ratio of the ^{207}Bi data and MC and applying this ratio to the $\beta\beta$ data provides an angular distribution correction (or a scaling) of the $\beta\beta$ distribution. The result of the corrected $2e^-$ angular distribution (for the ^{100}Mo Composite Phase I sample) can be seen in Figure 8.5, giving a factor of 2 improvement of the χ^2 to 63.5/25.

The speculative reasons for the physics behind this discrepancy are the following. The first and the main reason is due to the imperfect modelling of electron multiple scattering in the foils. This, in turn, is due to an inaccurate description of the foils themselves. For example, the ^{100}Mo composite foils were glued together with water based PVA therefore at the time of installation there was water present in the foils. This water could have evaporated over the running time of the experiment, causing the description of the foils to be altered. In order to rectify this problem after dismantling the NEMO3 experiment (the dismantling is currently underway) the foils will be carefully measured again in order to improve their description. The second reason is due to the imperfect modelling of the response of the Geiger tracker cells, effecting the hit reconstruction efficiency and hence the reconstruction of the tracks.

8.3 Laser Energy Corrections

As discussed in Section 5.5 a laser light injection system is used to monitor the gain stability of the PMTs on a bi-daily basis. Laser Energy Corrections (LECs) are calculated from these runs, used to correct the ADC energy distributions of the collected data for the PMT gain variations (this work is currently being carried out by the collaboration and is yet unavailable) and to flag unstable PMTs. For the analysis presented in this thesis the LECs were used to flag and remove "bad" PMTs from the data and MC samples. The LECs are calculated separately for each period between absolute energy calibrations carried out with ^{207}Bi (Section 5.5), with a run in the middle of the absolute

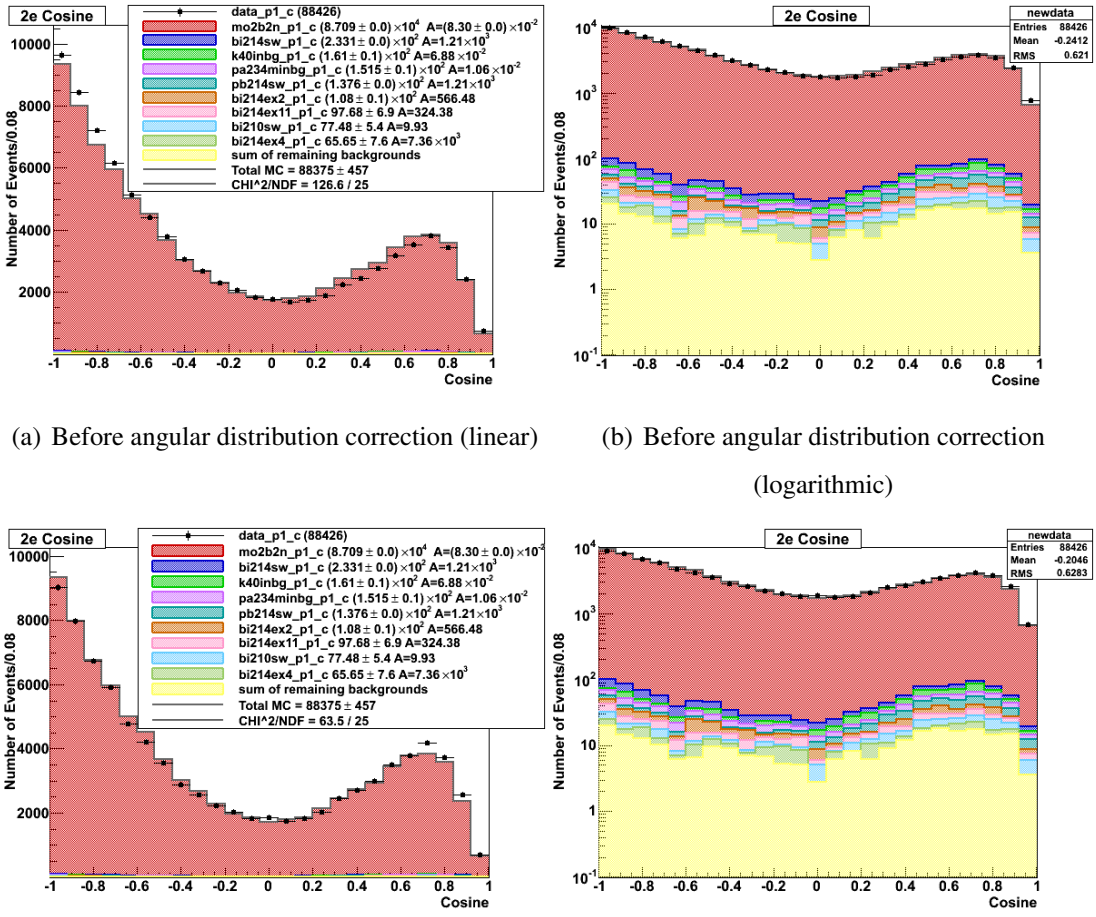

(a) Before angular distribution correction (linear)

(b) Before angular distribution correction (logarithmic)

(c) After angular distribution correction (linear)

(d) After angular distribution correction (logarithmic)

Figure 8.5: Distributions of the cosine of the angle between the two electrons before (a and b) and after (c and d) applying the angular distribution correction obtained from ^{207}Bi calibration data on linear and logarithmic scales respectively. This example is for the ^{100}Mo Composite Phase I data sample.

calibration chosen as a reference run. The energy, E, of the laser signal is calculated for each PMT in each of the laser runs. A ratio, R, of the laser energy of a current run E_i to the laser energy of the chosen reference run E_R is obtained:

$$R = \frac{E_i}{E_R}. \tag{8.3.1}$$

The variation of the laser energy, V, is then estimated using the mean overall energies of all the PMTs (carried out separately for 3" and 5" PMTs):

$$V = \frac{< E_i >}{< E_R >}. \tag{8.3.2}$$

The laser energy correction coefficient, C_i, is then:

$$C_i = \frac{R}{V}. \tag{8.3.3}$$

The values of the correction coefficient, C_i, are then analysed to define stability flags for the PMT:

- Flag 0: stable PMT
- Flag 2: A distribution of the PMT response to the laser light is plotted as a function of time to determine whether the gain drift of a PMT is continuous with time or shows erratic behaviour. If a linear fit obtained has a $\chi^2 > 10$ the PMT is flagged.
- Flag 4: the variation of C_i between two successive laser runs is $> 5\%$
- Flag 8: the PMT is unstable during the absolute calibration causing the correction amplitude to be $> 5\%$

Flags > 2 are considered to be suspicious and only PMTs with flags ≤ 2 are used in the analysis presented in this thesis. At present moment the LECs are available for data up to the end of 2009, which has determined the Phase II data set used for this analysis (October 2004 - December 2009). Using the LECs reduces the $2\nu\beta\beta$ efficiency for ^{100}Mo from 3.6% to 3.3%.

8.4 $2\nu\beta\beta$ Results

The $2\nu\beta\beta$ ^{100}Mo simulations used for the analysis presented here are for the single state dominance (SSD) hypothesis [129, 130] which NEMO3 data favours over the higher order state dominance (HSD) hypothesis. The four ^{100}Mo data samples (Composite Phase I, Composite Phase II, Metal Phase I and Metal Phase II) are evaluated individually using the log-likelihood method (Section 6.7.1) and are then combined to give a half-life for the entire ^{100}Mo data set.

The final cuts lead to the distributions seen in Figures 8.6 - 8.9, where Figure 8.6 shows the Composite Phase I ('CPI') distributions, 8.7 shows the Composite Phase II ('CPII') distributions, Figure 8.8 shows the Metal Phase I ('MPI') distributions and Figure 8.9 shows the Metal Phase II ('MPII') distributions. The figures show the $2\nu\beta\beta$ signal described by the two electron energy sum, the angular distribution of the two electrons and the single electron energy, which are useful for verifying the background model and for discriminating between different modes of $0\nu\beta\beta$ decay. The results for each of the data sets are summarised in Table 8.2, showing the total run time, the number of data events, the number of expected background events, the number of signal events, the detection efficiency and the obtained half-life. The errors on the number of expected background events, σ_B, and on the signal events, σ_S ($\sigma_S = \sqrt{\sigma_D^2 + \sigma_B^2}$, where σ_D is the error on the number of data events), are determined by the statistical error on the large background MC simulation samples scaled down according to the activity measured for those backgrounds and by the error on the measurement of the background activities in the control channels. Due to the scaling down of the MC sample σ_B and σ_S may have an error smaller than the square root of B and S.

The average S/B obtained is 68 for Phase I data and 96 for Phase II data.

8.4.1 Combining Half-Lives

In order to extract the $2\nu\beta\beta$ half-life for the combined data sample the backgrounds for each of the four individual samples are all treated as independent background channels, with an activity specified for each channel (extracted from the four individual data set analyses). The data and signal ($2\nu\beta\beta$ and different $0\nu\beta\beta$ decay modes) are slimmed and booked into one combined data set (containing Phase I, Phase II, metal and composite ^{100}Mo). The log-likelihood method is then used to extract the combined half-life

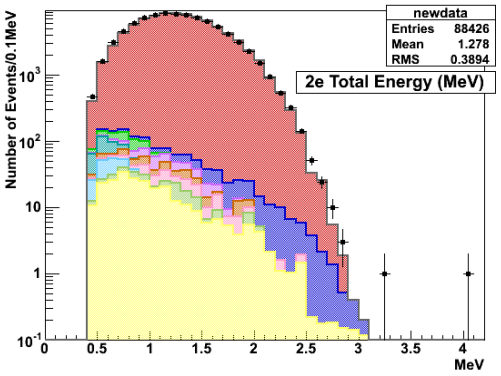

(a) 2 electron energy sum

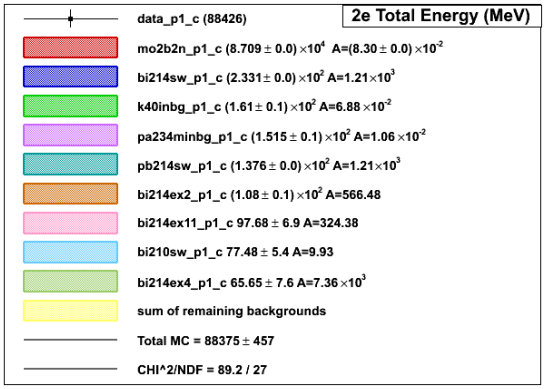

(b) 2 electron energy sum legend

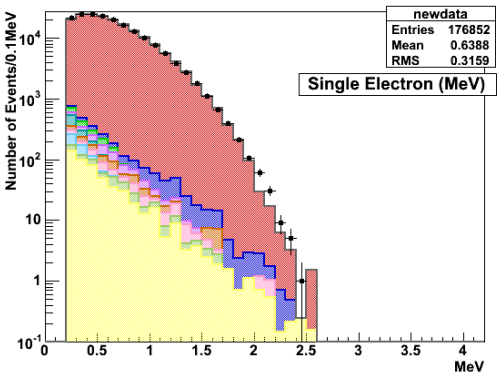

(c) single electron energy

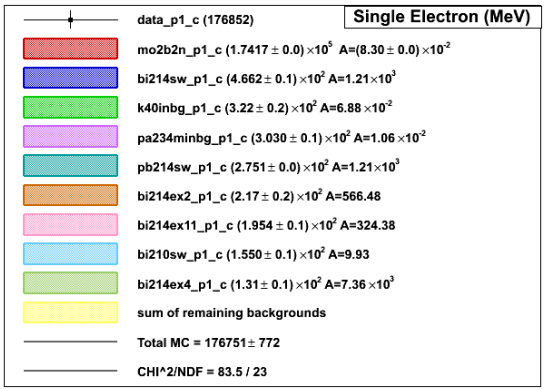

(d) single electron energy legend

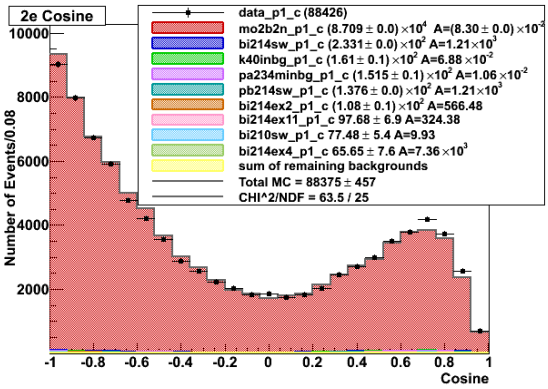

(e) angle between 2 electrons (linear)

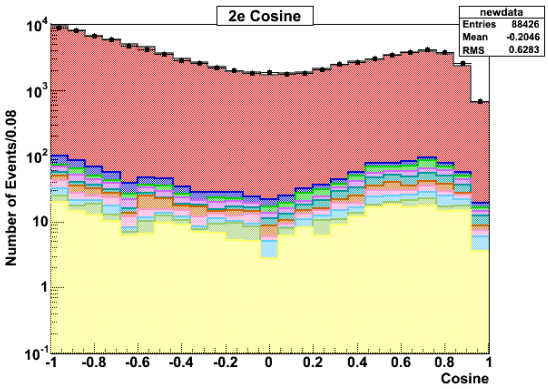

(f) angle between 2 electrons (logarithmic)

Figure 8.6: Distributions of (a) the two electron energy sum, $E_1 + E_2$, and (b) legend, (c) the single electron energy, E_e, and (d) legend and the cosine of the angle between the two electrons on (e) a linear and (f) logarithmic scale respectively for the ^{100}Mo Composite Phase I data set, showing the top 8 contributing expected backgrounds (and the sum of the rest) and the $2\nu\beta\beta$ signal. A S/B of 68 is obtained for the CPI data set.

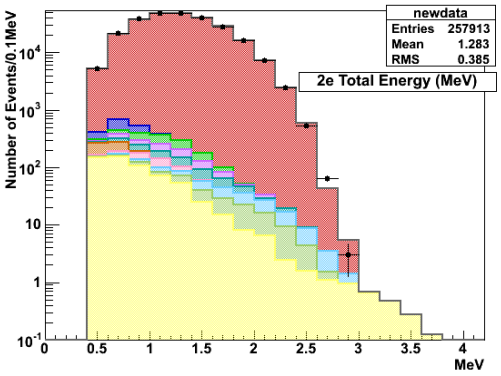

(a) 2 electron energy sum

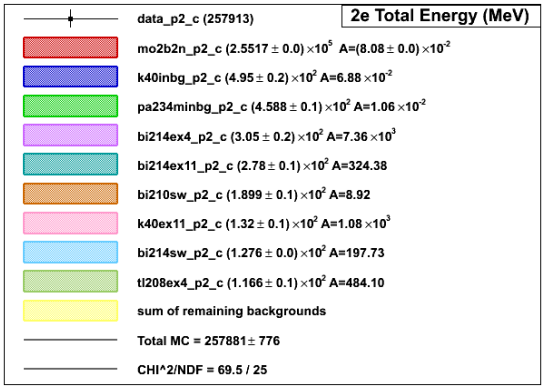

(b) 2 electron energy sum legend

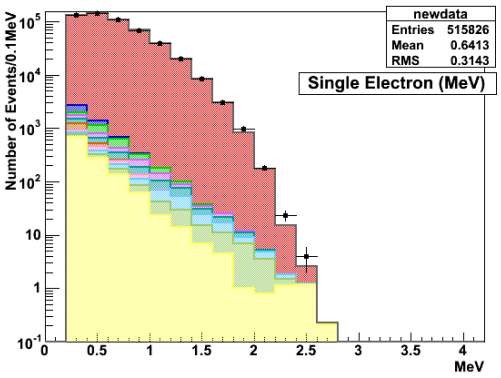

(c) single electron energy

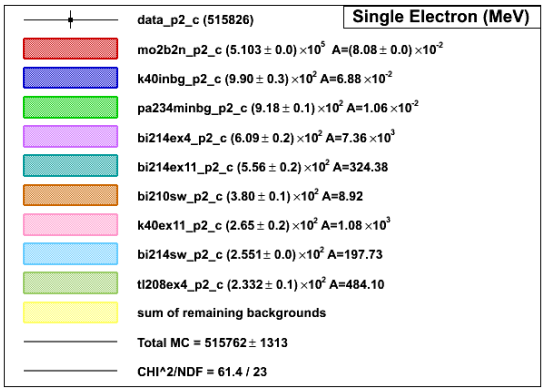

(d) single electron energy legend

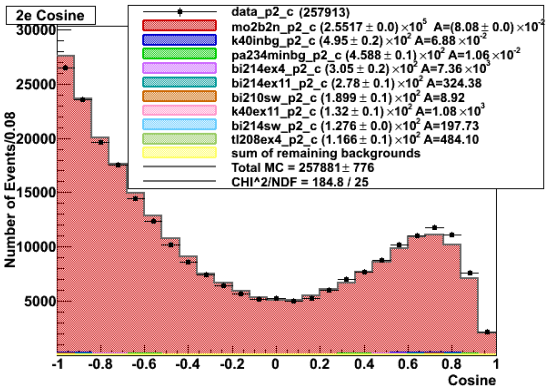

(e) angle between 2 electrons (linear)

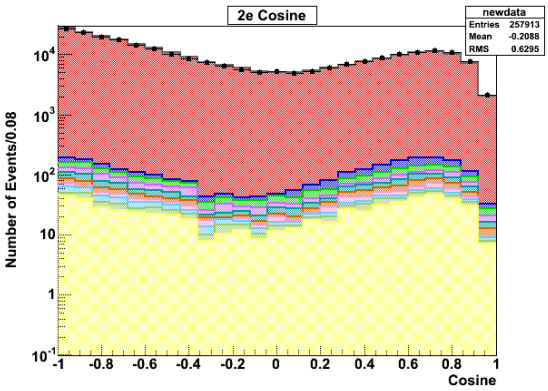

(f) angle between 2 electrons (logarithmic)

Figure 8.7: Distributions of (a) the two electron energy sum, $E_1 + E_2$, and (b) legend, (c) the single electron energy, E_e, and (d) legend and the cosine of the angle between the two electrons on (e) a linear and (f) logarithmic scale respectively for the ^{100}Mo Composite Phase II data set, showing the top 8 contributing expected backgrounds (and the sum of the rest) and the $2\nu\beta\beta$ signal. A S/B of 94 is obtained for the CPII data set.

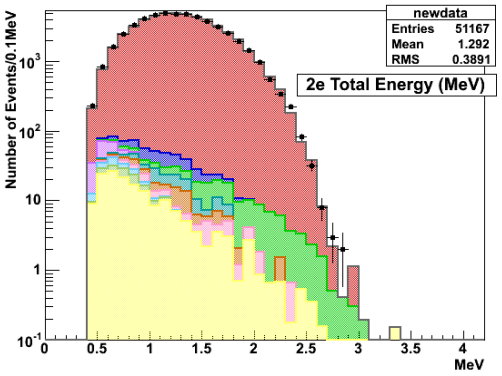

(a) 2 electron energy sum

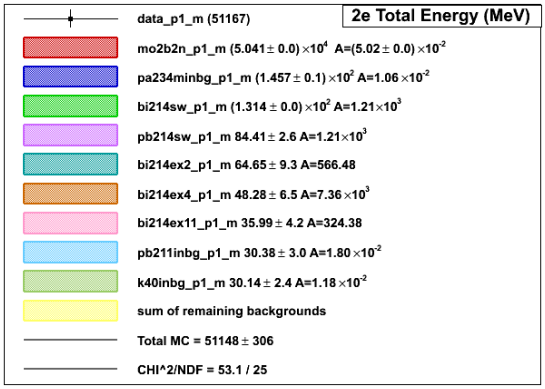

(b) 2 electron energy sum legend

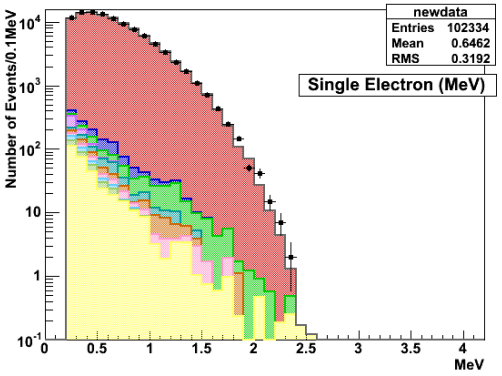

(c) single electron energy

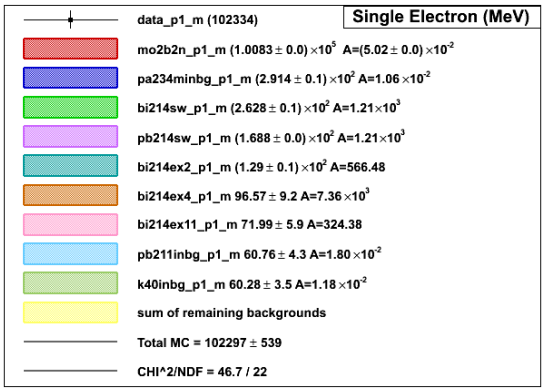

(d) single electron energy legend

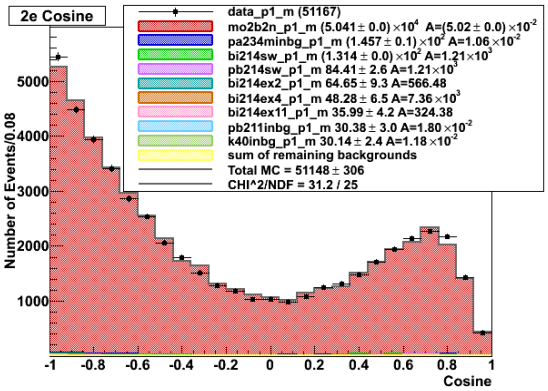

(e) angle between 2 electrons (linear)

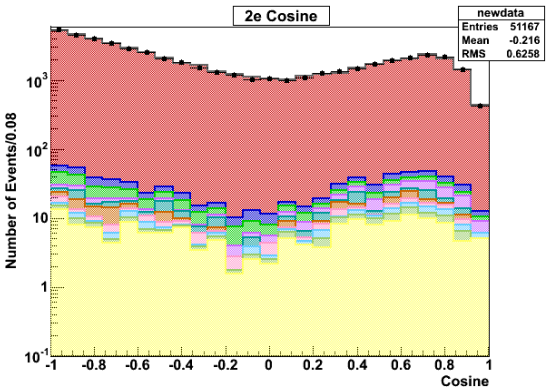

(f) angle between 2 electrons (logarithmic)

Figure 8.8: Distributions of (a) the two electron energy sum, $E_1 + E_2$, and (b) legend, (c) the single electron energy, E_e, and (d) legend and the cosine of the angle between the two electrons on (e) a linear and (f) logarithmic scale respectively for the ^{100}Mo Metal Phase I data set, showing the top 8 contributing expected backgrounds (and the sum of the rest) and the $2\nu\beta\beta$ signal. A S/B of 69 is obtained for the MPI data set.

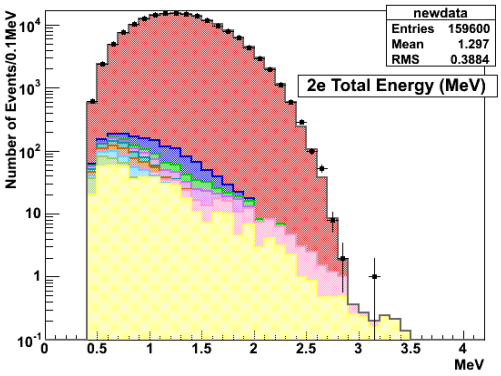

(a) 2 electron energy sum

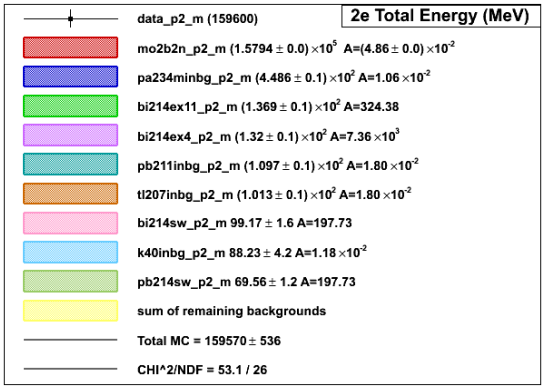

(b) 2 electron energy sum legend

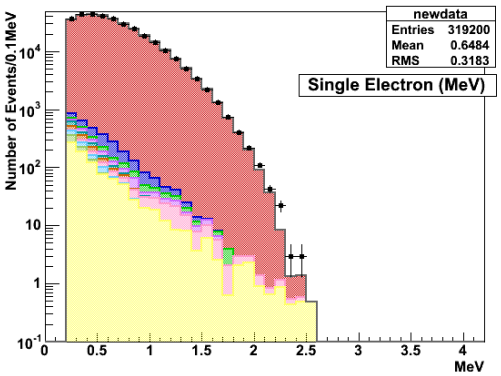

(c) single electron energy

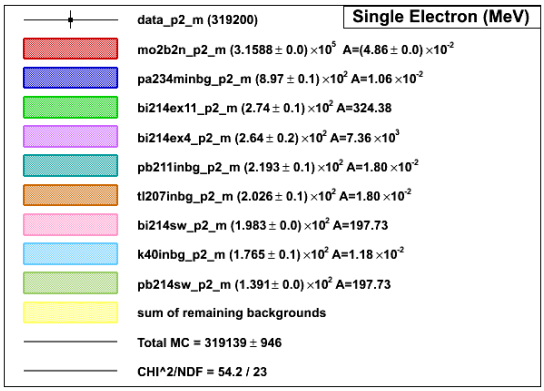

(d) single electron energy legend

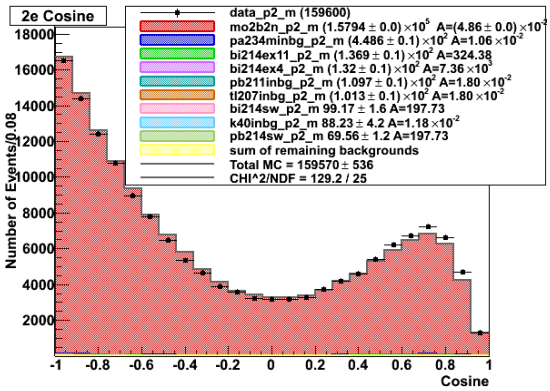

(e) angle between 2 electrons (linear)

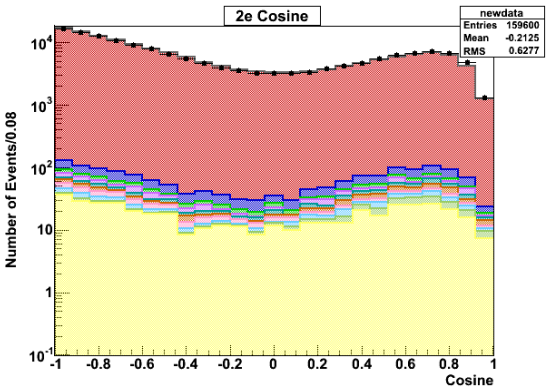

(f) angle between 2 electrons (logarithmic)

Figure 8.9: Distributions of (1) the two electron energy sum, $E_1 + E_2$, and (b) legend, (c) the single electron energy, E_e, and (d) legend and the cosine of the angle between the two electrons on (e) a linear and (f) logarithmic scale respectively for the ^{100}Mo Metal Phase II data set, showing the top 8 contributing expected backgrounds (and the sum of the rest) and the $2\nu\beta\beta$ signal. A S/B of 97 is obtained for the MPII data set.

Set	Run Time	Data	Bkg	Signal	η	Half-Life $\times 10^{18}$
CPI	341	88426 ± 297	1290 ± 26	87086 ± 298	3.6%	7.08 ± 0.02
CPII	1130	257913 ± 508	2708 ± 39	255173 ± 509	3.2%	7.27 ± 0.01
MPI	341	51167 ± 226	734 ± 17	50415 ± 227	3.4%	6.54 ± 0.03
MPII	1130	159600 ± 399	1630 ± 23	157939 ± 400	3.3%	6.75 ± 0.02

Table 8.2: Summary of the half-lives obtained for the $2\nu\beta\beta$ decay of ^{100}Mo for the four data samples, using the the log-likelihood method (i.e. not simply data - background). The run time (in days), number of data, expected background and signal events, the efficiency (η) and the half-life (in years) with the statistical error are shown.

(shown in Figure 8.10).

8.4.2 Systematic Error Discussion

The following uncertainties contribute to the systematic error of the $2\nu\beta\beta$ analysis:

- The largest contributing factor comes from the geometrical acceptance of the detector and the reconstruction algorithm [107]. The imperfect detector description with GEANT-3.21 introduces a systematic error into the analysis. The reconstruction algorithm tightens the vertex resolution between two tracks, also introducing a systematic error. The combined error is estimated by placing the ^{207}Bi calibration sources of known activities inside the detector. This data then undergoes a $\beta\beta$ analysis and the number of expected events calculated from the activity is compared to the number of observed events. The error contributes $\pm 5\%$ to the systematic error.

- There is a $\pm 1\%$ error on the precision of energy calibration in the calorimeter, which contributes $\pm 1\%$ to the systematic error of the half-life (studied by fluctuating the gain of the PMTs by $\pm 1\%$).

- There is a $\pm 0.54\%$ uncertainty on the mass of the ^{100}Mo foils [107].

- The external background model is determined with a precision of 10% [113]. The effect on the $2\nu\beta\beta$ half-life is observed by fluctuating the external back-

ground model by $\pm 10\%$ and is found to be negligible due to the large S/B for the measurement.

- The internal background model is determined with a precision of 5% [113]. The effect on the $2\nu\beta\beta$ half-life is observed by fluctuating the internal background model by $\pm 5\%$ and is found to be negligible due to the large S/B for the measurement.

- A systematic uncertainty is introduced by the imperfect modelling of the geometry of the ^{100}Mo source foils and how they vary with time (in particular the composite foils) and of electrons passing through those different source foils. To estimate the systematic uncerainty contribution from the source foils the analysis is carried out on four different samples in order to study each type of source foil and phase of running individually. The root mean square (RMS) value of a histogram of the individual sample measured half-lives weighted by their statistical errors then gives the error due to source foil composition. The error from these factors contributes $\sim \pm 4.0\%$ to the systematic error.

A summary of the systematic error elements can be seen in Table 8.3. The total systematic error contributing to the analysis is $\pm 6.5\%$, obtained by adding the individual independent components in quadrature.

Description	Syst. Error ($\%$)	
Acceptance and reconstruction	± 5.0	[107]
Energy calibration precision	± 1.0	
The mass of ^{100}Mo	± 0.54	[107]
$\pm 10\%$ external background precision	negligible	[113]
$\pm 5\%$ internal background precision	negligible	[113]
Source foil composition	$\pm 4.0\%$	
Total Systematic Error	$\pm 6.5\%$	

Table 8.3: Summary of the systematic error components for the $2\nu\beta\beta$ analysis of ^{100}Mo.

The final combined result (Figure 8.10) for the $2\nu\beta\beta$ half-life of ^{100}Mo for 1471 days of data taking, with 557191 $\pm$ 746 data events and 6362 $\pm$ 54 background events

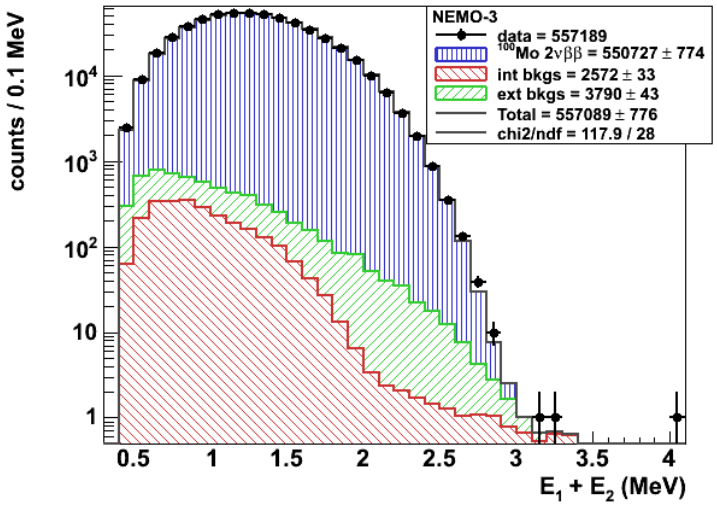

Figure 8.10: Two electron energy sum, $E_1 + E_2$, distribution for the combined ^{100}Mo data set, showing the data described by the sum of the expected external and internal backgrounds and the $2\nu\beta\beta$ signal.

selected, and 550727 $\pm$ 774 signal events predicted (with an S/B of 87) with an efficiency of 3.3%, including statistical and systematic ($\pm$6.5% as described in Table 8.3) errors is

$$T^{2\nu}_{1/2} = [7.02 \pm 0.01(stat) \pm 0.46(syst)] \times 10^{18}\text{years}. \quad (8.4.1)$$

This is the world's most precise measurement of $T^{2\nu}_{1/2}$ for ^{100}Mo and can be compared to the previous direct measurement of $T^{2\nu}_{1/2} = [7.11 \pm 0.02(stat) \pm 0.54(syst)] \times 10^{18}$ years obtained with the NEMO3 detector for Phase I data only [80] and $T^{2\nu}_{1/2} = [7.2 \pm 0.9(stat) \pm 1.8(syst)] \times 10^{18}$ years obtained with a liquid argon ionisation chamber [131].

8.5 $0\nu\beta\beta$ Results

After applying the cuts described in Section 8.1 no excess of events is observed in the $0\nu\beta\beta$ decay energy region and therefore a limit on the half-life is evaluated. Two methods are used to set a limit. The first, known as the "Helene" method [132], is a simple counting experiment which compares the number of observed events to the number of expected background events within a specific energy window containing the $0\nu\beta\beta$ peak and if no signal is seen a limit is set. The drawback of this method is that it is dependent on background fluctuations. The energy window selection is optimised

by using the the following expression:

$$\frac{\eta}{B+\sigma_B}, \tag{8.5.1}$$

where η is the efficiency of selecting the signal, B is the expected background to the signal (from MC) and σ_B is the error on the expected background to the signal. Maximum sensitivity is achieved when the expression reaches its maximum.

The second method is the CL_s method (described in Section 6.7.3). It is a more conservative and robust method, which is less dependent on background fluctuations and takes into account the shape of the energy spectrum. The final results are therefore presented using the CL_S method.

8.5.1 Neutrino Mass Mechanism

The neutrino mass mechanism, $\langle m_{\nu e} \rangle$, (Section 3.3.1) is the most discussed method for the production of $0\nu\beta\beta$ decay. The optimisation for the Helene energy window is carried out from a lower energy bound (starting at 2MeV) to an upper bound energy of 3.2, 3.1 and 3.0MeV, increasing in steps of 0.1MeV. Figure 8.11 shows the optimisation study for ^{100}Mo Composite Foils, Phase I data. In this case the energy window which maximises Expression 8.5.1 is $2.9 - 3.1$MeV. The CL_S method uses the full energy range of the $\beta\beta$ spectrum ($0.4 - 3.2$MeV, with 0.4MeV being a minimum energy requirement of the $2e^-$ sum energy to suppress low energy events). The evaluated $0\nu\beta\beta$ limits for each of the four data samples are summarised in Table 8.4 (using the Helene method) and Table 8.5 (using the CL_S method).

The four individual data samples are combined to obtain a limit for the total data sample using the method described in Section 8.4.1. A visual representation of the limit obtained with the CL_S method can be seen in Figure 8.12. The efficiency for observing $0\nu\beta\beta$ decay with the CL_S method is 12.5% and < 13.9 $0\nu\beta\beta$ events at 90%CL are excluded. The combined limit (calculated at the 90%CL) for the $0\nu\beta\beta$ decay of ^{100} Mo is

$$T^{0\nu}_{1/2} > 1.1 \times 10^{24} \text{ years}. \tag{8.5.2}$$

The limit is validated with the Helene method for an optimised energy window of $2.9 - 3.1$MeV, with 0 data events selected, 3.53 ± 0.38 background events expected and

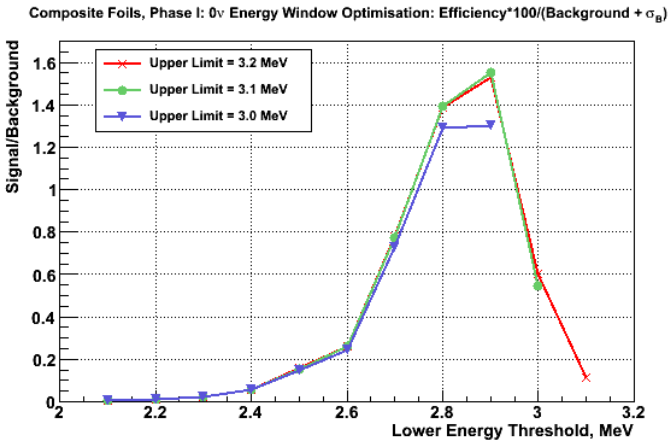

Figure 8.11: Optimisation of the energy window for the Helene method, using the optimisation variable $\eta/(B+\sigma_B)$. This example is for the ^{100}Mo Composite Foils, Phase I data.

Set	Helene Method					
	Energy Window (MeV)	Data	Bkg	Excluded Events	η	Limit (years)
CP I	2.9 -3.1	0	0.6 ± 1.0	< 2.3	2.5%	$> 1.9 \times 10^{23}$
CP II	2.9 -3.1	0	2.3 ± 1.3	< 2.3	2.2%	$> 5.6 \times 10^{23}$
MP I	2.8 -3.2	2	1.8 ± 0.9	< 4.0	6.0%	$> 1.4 \times 10^{23}$
MP II	2.8 -3.1	2	2.5 ± 0.8	< 3.7	5.6%	$> 4.9 \times 10^{23}$

Table 8.4: Summary of the limits obtained for the $0\nu\beta\beta$ mass mechanism mode for the four data samples, using the Helene method. The Energy window selected by optimisation, the number of selected data events, the number of expected background events, the number of excluded $0\nu\beta\beta$ events at a 90% CL, the efficiency (η) and the limit are shown.

Set	CL_S Method				
	Data	Bkg	Excluded Events	η	Limit (years)
CP I	88425	88376	< 11.8	13.6%	$> 2.0 \times 10^{23}$
CP II	257913	257881	< 11.9	12.3%	$> 5.9 \times 10^{23}$
MP I	51167	51148	< 8.3	12.6%	$> 1.5 \times 10^{23}$
MP II	159599	159570	< 7.1	12.4%	$> 5.6 \times 10^{23}$

Table 8.5: Summary of the limits obtained for the $0\nu\beta\beta$ mass mechanism mode for the four data samples, using the the CL_S method. The number of data events, the number of expected background events, the number of excluded $0\nu\beta\beta$ events at a 90% CL, the efficiency (η) and the limit are shown.

< 2.3 $0\nu\beta\beta$ events excluded at the 90% CL. The $0\nu\beta\beta$ efficiency is 2.5% and the limit obtained is $T^{0\nu}_{1/2} > 1.3 \times 10^{24}$ years at 90% CL.

8.5.2 Right-Handed Currents

The $\langle\lambda\rangle$ parameter from the right-handed currents $0\nu\beta\beta$ mechanism, described in Section 3.3.2, is investigated in this thesis as only the $\langle\lambda\rangle$ parameter was available in the GENBB generator used for NEMO3. The right-handed currents mode produces the same energy sum distribution as the mass mechanism $0\nu\beta\beta$ decay mode. The differences between the two mechanisms can be seen in the cosine of the angle between the two electrons and the single electron energy distributions. The expected angular distribution should follow $(1+\cos\theta)$, however due to the detector acceptance and efficiencies the angular distribution looks similar to the mass mechanism distribution, with a preference at smaller angles ($\cos\theta \sim 1$) for the $\langle\lambda\rangle$ process. The single electron energy distribution for the right-handed currents is asymmetrical. The asymmetry observed in the single electrons,

$$\text{Asymmetry} = \frac{E_1 - E_2}{E_1 + E_2}, \tag{8.5.3}$$

can be used to discriminate between the two $0\nu\beta\beta$ decay modes. Figure 8.13 shows the single electron energy (Figures 8.13(a) and 8.13(b)), angular (Figures 8.13(c) and

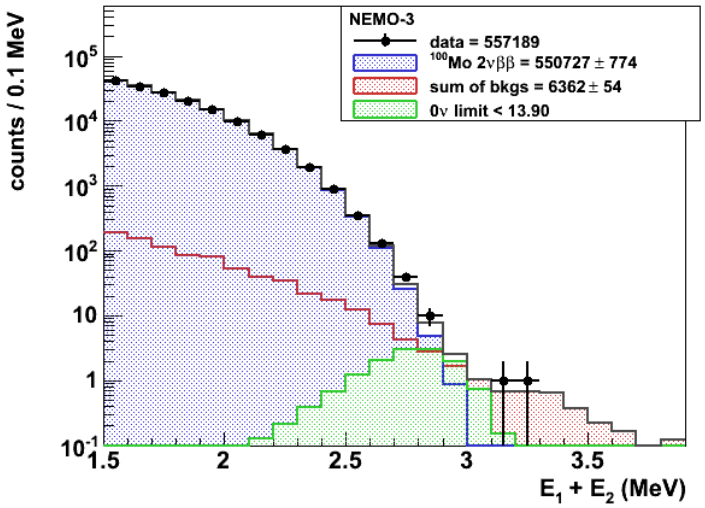

Figure 8.12: Two electron energy sum distribution (zoomed in to the 1.5 - 3.9MeV energy region for clarity) for the combined ^{100}Mo data set, showing the sum of the expected backgrounds, the $2\nu\beta\beta$ signal and the combined limit on the $0\nu\beta\beta$ mass mechanism at 90% CL obtained using the CL_S method.

8.13(d)) and asymmetry (Figures 8.13(e) and 8.13(f)) distributions seen in the $0\nu\beta\beta$ mass mechanism mode and in the right-handed currents $0\nu\beta\beta$ decay mode. The example shown is for ^{100}Mo Composite sample simulations.

If a positive $0\nu\beta\beta$ decay signal is observed with significant statistics then the asymmetry in the single electrons can be used to distinguish between the two decay mechanisms [128].

The limit obtained, using the CL_S method described in Section 6.7.3, for the $0\nu\beta\beta$ right-handed currents mechanism for the combined data set, at the 90%CL, is

$$T_{1/2}^{0\nu\lambda} > 5.5 \times 10^{23} \text{ years} \tag{8.5.4}$$

with an efficiency of 6.9% and an excluded number of 0ν events <14.5 at the 90% CL. A visual representation of the limit can be seen in Figure 8.14.

The limit is validated with the Helene method for an optimised energy window of $2.9-3.1$MeV, with 0 data events selected, 3.53 ± 0.38 background events expected and < 2.3 $0\nu\beta\beta$ events excluded at the 90% CL. The $0\nu\beta\beta$ efficiency is 1.3% and the limit obtained is $T_{1/2}^{0\nu\lambda} > 6.6 \times 10^{23}$ years at 90% CL.

As the two electron energy sum spectrum is the same for the mass and right-handed currents mechanisms one would expect the limit obtained to be similar. How-

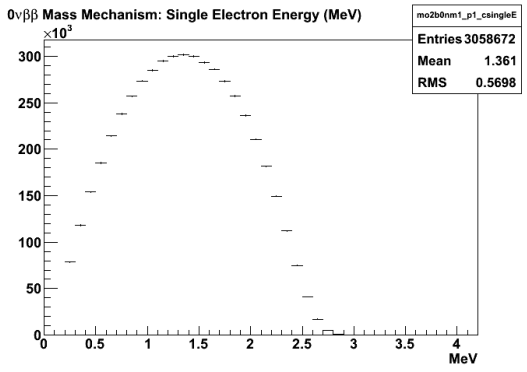

(a) MM: $2e^-$ Single electron energy

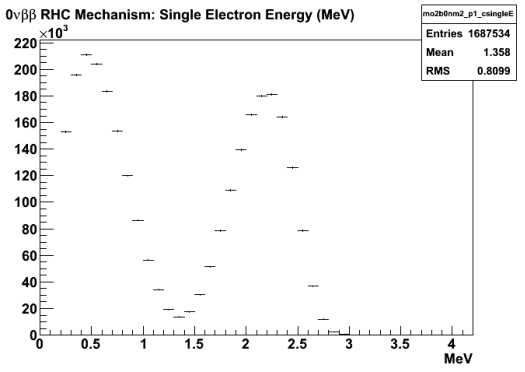

(b) RHC: Single electron energy

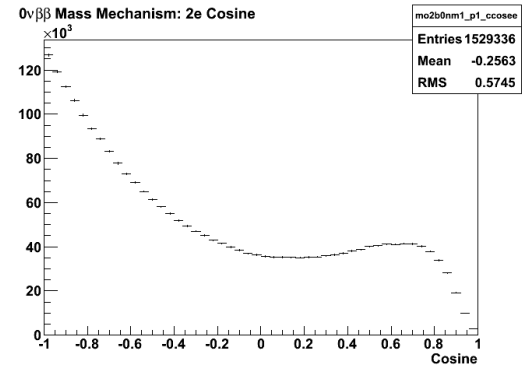

(c) MM: Angle between 2 electrons

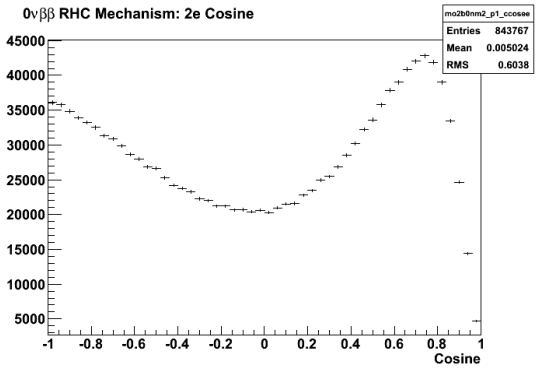

(d) RHC: Angle between 2 electrons

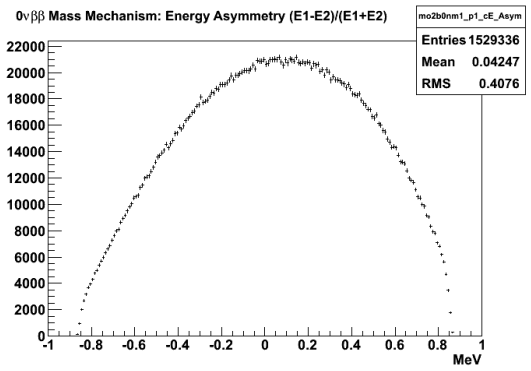

(e) MM: Asymmetry

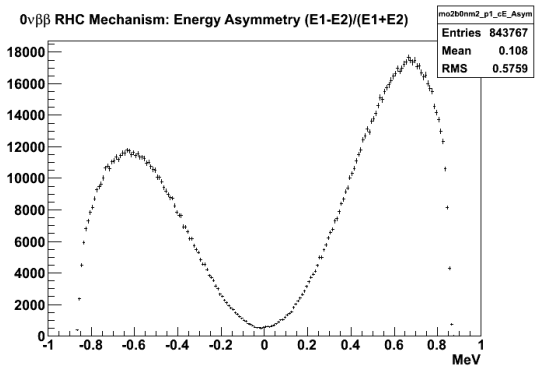

(f) RHC: Asymmetry

Figure 8.13: Distributions of the mass mechanism (MM) and the right-handed currents (RHC) $0\nu\beta\beta$ mechanism showing (a) + (b) the single electron energy, E_e, (c) + (d) the cosine of the angle between the two electrons and (e) + (f) the asymmetry, $\frac{E_1-E_2}{E_1+E_2}$, for the ^{100}Mo Composite sample simulations.

ever, due to the detector acceptance the efficiency for the right-handed currents angular and single electron distributions is decreased (as described at the beginning of this section), lowering the $\langle\lambda\rangle$ limit.

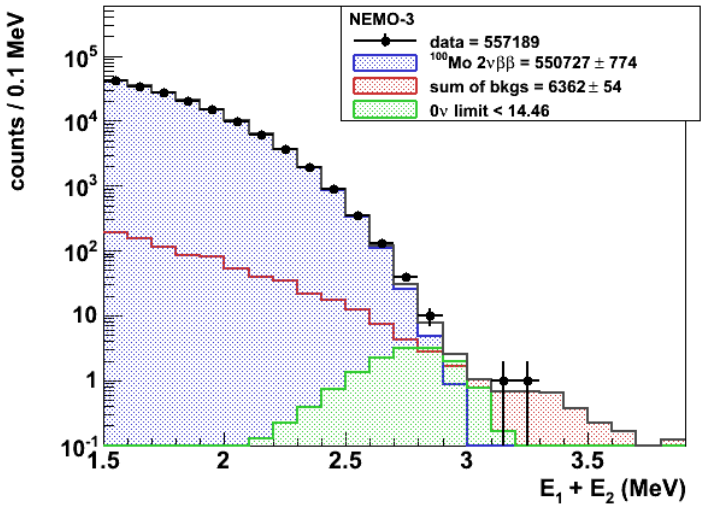

Figure 8.14: Two electron energy sum distribution (zoomed in to the 1.5 - 3.9MeV energy region for clarity) for the combined ^{100}Mo data set, showing the sum of the expected backgrounds, the $2\nu\beta\beta$ signal and the combined limit on the $0\nu\beta\beta$ right-handed currents mechanism at 90% CL obtained using the CL_S method.

8.5.3 Majoron Particle Emission

The 'Majoron' $0\nu\beta\beta$ mechanism involves the emission of one or two Majoron particles, described in Section 3.3.3, and produces a continuous energy spectrum (similar to that of $2\nu\beta\beta$). The Majoron mode studied in this thesis is the spectral index $n = 1$ mode as nuclear matrix element (NME) calculations currently only exist for this mode and therefore it is the only one that leads to an extraction of the Majoron to neutrino coupling physics parameter.

The limit obtained, using the CL_S method described in Section 6.7.3 on the full spectrum, for the $n = 1$ Majoron emission mechanism ($\langle g_{\chi^0}\rangle$), which is the most discussed Majoron mode, for the combined data set, at the 90% CL, is

$$T_{1/2}^{0\nu\chi^0} > 5.3 \times 10^{22} \text{ years} \tag{8.5.5}$$

with an efficiency of 9.0% and an excluded number of 0ν events < 196.8 at the 90% CL for an energy window of 0.4 - 3.2MeV. A visual representation of the limit for the $n = 1$

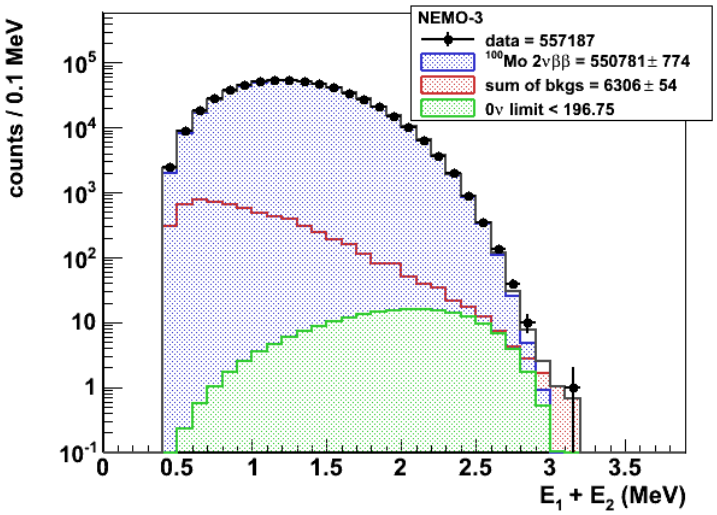

Figure 8.15: Two electron energy sum distribution for the combined ^{100}Mo data set, showing the sum of the expected backgrounds, the $2\nu\beta\beta$ signal and the combined limit on the $0\nu\beta\beta$ Majoron mechanism ($n = 1$ mode) at 90% CL obtained using the CL_S method.

Majoron emission mechanism can be seen in Figure 8.15. The NEMO3 experiment is the most sensitive in the world to the $0\nu\beta\beta$ Majoron mechanism due to the mode's continuous energy spectrum and NEMO3's ability to identify backgrounds using the calorimeter-tracker technique for event topology. For a continuous energy spectrum topological background suppression becomes much more important than background suppression achieved with energy resolution. The continuous energy spectrum also means that the Majoron emission mechanisms limits are weaker than the mass and right-currents mechanisms due to a larger background contribution.

8.6 Discussion

8.6.1 $2\nu\beta\beta$ Nuclear Matrix Element

There is a some uncertainty in the calculation of the $0\nu\beta\beta$ nuclear matrix element (NME), $M^{0\nu}$, which introduces the largest uncertainty into the extraction of the effective Majorana neutrino mass (and other $0\nu\beta\beta$ decay mode physics parameters). Although the NMEs $M^{0\nu}$ ($0\nu\beta\beta$) and $M^{2\nu}$ ($2\nu\beta\beta$) are different a more precise knowledge of $M^{2\nu}$ can inform the $M^{0\nu}$ calculations. As within the QRPA model NMEs have a strong dependence on the g_{pp} parameter (Section 3.4.2) it has been suggested [66, 133] to fix the g_{pp} parameter to the experimentally extracted value of $M^{2\nu}$ for calculations of

$M^{0\nu}$. This makes the different calculations of $M^{0\nu}$ within the QRPA model converge. The experimental value of $M^{2\nu}$ can be extracted from the measured value of the ^{100}Mo half-life (Equation 8.4.1), using Equation 3.2.3, reiterated here:

$$[T^{2\nu}_{1/2}]^{-1} = G^{2\nu}|M^{2\nu}|^2,$$

where $G^{2\nu} = 8.9 \times 10^{-18}$ yr^{-1} and is the precisely calculable phase space factor evaluated for $g_A = 1.25$ [67]. The obtained $M^{2\nu}$, scaled by the electron rest mass, is

$$M^{2\nu} = 0.126 \pm 0.004. \tag{8.6.1}$$

This value can be compared with the PHFB (Section 3.4.3) theoretical calculation, where $M^{2\nu} = 0.104$ [134]. This is the world's most precise measurement of $M^{2\nu}$ for ^{100}Mo and can be compared to the previous result of $M^{2\nu} = 0.118 \pm 0.005$, based on a combination of several previous measurements [131].

8.6.2 The Effective Neutrino Mass

An upper bound on the effective Majorana neutrino mass ($\langle m_{\nu e}\rangle$) is extracted from the limit on the $0\nu\beta\beta$ half-life (Equation 8.5.2), using Equation 3.3.3, reiterated here:

$$[T^{0\nu}_{1/2}]^{-1} = G^{0\nu}|M^{0\nu}|^2 \left(\frac{\langle m_{\nu e}\rangle}{m_e}\right)^2,$$

where $G^{0\nu} = 4.57 \times 10^{-14}$ yr^{-1} is the precisely calculable phase space factor evaluated for $g_A = 1.25$ [111, 135]. Table 8.6 shows the obtained limits on the effective Majorana neutrino mass as a function of g_A and g_{pp} using the NMEs, $M'^{0\nu}$, computed for the QRPA, R(QRPA), PHFB and IBM-2 models (referenced in the table), where

$$M'^{0\nu} = \left(\frac{g_A}{1.25}\right)^2 M^{0\nu}, \tag{8.6.2}$$

allowing the phase space evaluated for $g_A = 1.25$ to be used for all calculations. Including all NME uncertainties, the limit (at 90% CL) on the effective Majorana neutrino mass is

$$\langle m_{\nu e}\rangle < 0.3 - 1.0 \text{ eV}. \tag{8.6.3}$$

This is one of the world's most stringent constraints on the effective neutrino Majorana mass and is comparable to the limit of $\langle m_{\nu_e}\rangle$ < 0.3 - 0.7eV obtained with the

Model	g_A	g_{pp}	$M'^{0\nu}$	$\langle m_{\nu e}\rangle$ (eV)	$\langle g_{\chi^0}\rangle$ ($\times 10^{-4}$)	Ref.
QRPA	1.00	1.07	-3.103 - 2.257	0.75 - 1.03	0.49 - 0.67	[136]
QRPA	1.25	1.09	-3.931 - 2.737	0.59 - 0.85	0.38 - 0.55	[136]
R(QRPA)	1.25	$2\nu\beta\beta$	2.685 - 2.875	0.81 - 0.87	0.53 - 0.56	[66]
R(QRPA)	1.00	$2\nu\beta\beta$	2.28 - 2.40	0.97 - 1.02	0.63 - 0.66	[66]
R(QRPA)	1.25	$2\nu\beta\beta$	2.22 - 2.77	0.84 - 1.04	0.55 - 0.68	[133]
R(QRPA)	1.00	$2\nu\beta\beta$	3.53 - 4.58	0.51 - 0.60	0.33 - 0.43	[133]
PHFB	1.25	-	6.72 - 7.72	0.30 - 0.35	0.20 - 0.23	[137]
PHFB	1.00	-	4.71 - 5.45	0.43 - 0.50	0.28 - 0.32	[137]
IBM-2	1.25	-	3.73 - 4.22	0.55 - 0.63	0.34 - 0.41	[77]

Table 8.6: 90% CL upper limits on effective Majorana neutrino mass, $\langle m_{\nu e}\rangle$, and the Majoron to neutrino coupling, $\langle g_{\chi^0}\rangle$, as a function of g_A and g_{pp} using NMEs calculated in the QRPA, R(QRPA), PHFB and IBM-2 models.

CUORICINO detector for a total exposure of 19.8kg·yr of ^{130}Te [88] and Klapdor's claim of $\langle m_{\nu_e}\rangle < 0.2$-0.6eV (with a "best fit" of 0.4eV, which is starting to be excluded with the result present here) obtained with the Heidelberg-Moscow experiment [47].

8.6.3 The Majoron Neutrino Coupling Factor

An upper bound on the Majoron to neutrino coupling ($\langle g_{\chi^0}\rangle$) is extracted from the limit on the Majoron $0\nu\beta\beta$ half-life (Equation 8.5.5) for the most discussed $n = 1$ Majoron mode, using Equation 3.3.7, reiterated here:

$$[T^{0\nu\chi^0}_{1/2}]^{-1} = G^{0\nu\chi^0}|M^{0\nu}|^2\langle g_{\chi^0}\rangle^2,$$

where $G^{0\nu\chi^o} = 8.23 \times 10^{-16}$ yr^{-1} and is the precisely calculable phase space factor evaluated for $g_A = 1.25$ [67]. The NMEs, $M^{0\nu}$, for the Majoron to neutrino coupling are identical to those for the mass mechanism. Table 8.6 shows the obtained limits on the Majoron to neutrino coupling. Including all NME uncertainties, the limit (at 90% CL) on the Majoron to neutrino coupling is

$$\langle g_{\chi^0}\rangle < (0.2 - 0.7) \times 10^{-4}. \tag{8.6.4}$$

This is the world's most stringent bound on the Majoron coupling constant, which has been improved by a factor of ~ 2 compared to the previous world's best result obtained with NEMO3 ($\langle g_{\chi^0} \rangle < (0.4 - 0.8) \times 10^{-4}$) [138] and by a factor of ~ 4 compared to other experiments (for example, $\langle g_{\chi^0} \rangle < (0.8 - 2.3) \times 10^{-4}$ obtained with the Heidelberg-Moscow experiment [79]). The differences in the range of $\langle g_{\chi^0} \rangle$ presented here and the range of previous results is due to the range of the NMEs used to extract the parameter, chosen by the authors, with a more conservative NME range used for the result presented in this thesis.

8.6.4 The Right-Handed Currents Coupling Parameter

An upper bound on the right-handed currents coupling parameter $\langle \lambda \rangle$ (describing the coupling between the right-handed leptonic current and right-handed quark current (Section 3.3.2)) is extracted from the limit on the right-handed current $0\nu\beta\beta$ half-life (Equation 8.5.4) using Equation 3.3.4, reiterated here:

$$[T^{0\nu\lambda}_{1/2}]^{-1} = G^{0\nu\lambda}|M^{0\nu\lambda}|^2\langle\lambda\rangle^2,$$

where $G^{0\nu\lambda}$ is phase space factor. For the right-handed currents $0\nu\beta\beta$ decay mode it is more difficult to separate the $M^{0\nu\lambda}$ and $G^{0\nu\lambda}$, therefore to extract a limit on $\langle\lambda\rangle$ a coefficient, $C^0_{\lambda\lambda}$, is used, which is a convolution of $G^{0\nu\lambda}$ and $M^{0\nu\lambda}$ [139]. Equation 3.3.4 then becomes:

$$[T^{0\nu\lambda}_{1/2}]^{-1} = C^0_{\lambda\lambda}\langle\lambda\rangle^2, \tag{8.6.5}$$

where $C^0_{\lambda\lambda} = 9.66 \times 10^{-13}$ [139]. The limit on the right-handed currents coupling parameter $\langle\lambda\rangle$ is then

$$\langle\lambda\rangle < 1.4 \times 10^{-6}. \tag{8.6.6}$$

This is one of the most stringent constraints on the right-handed currents admixture parameter $\langle\lambda\rangle$ and is comparable to $\langle\lambda\rangle < 1.1 \times 10^{-6}$ obtained with ^{76}Ge experiments [140] and to Klapdor's claim of $\langle\lambda\rangle < (0.6 - 1.6) \times 10^{-6}$ (when taking into account different NMEs) [140].

Chapter 9

The SuperNEMO Experiment and Detector

The SuperNEMO experiment is based on the technology and success of the NEMO3 experiment, using a tracker-calorimeter detection technique for particle and energy identification. It uses the same technology as that of NEMO3, with thin source foils at the centre of a detector module, surrounded by drift cells operating in Geiger mode (providing particle identification) and enclosed by calorimeter walls (providing energy measurements). The detector will hold ~ 100kg of double beta decay source isotope to reach a projected sensitivity of 10^{26} years ($50 - 100$meV effective Majorana neutrino mass). An underground location is required for the experiment in order to screen it from muons, as for NEMO3 and any low background experiment.

SuperNEMO underwent a three year R&D study in order to utilise and improve the technique and technology used in the NEMO3 experiment, with five main areas of focus: source foil production, tracker development, calorimeter development, ultra-low background materials production and measurement and software development. The construction of the experiment has now started.

9.1 The SuperNEMO Detector

The SuperNEMO detector will contain 100kg of double beta decay source foil (^{82}Se is the first choice isotope to be used, with ^{150}Nd and ^{48}Ca being considered depending on enrichment possibilities), providing a sensitivity of 10^{26} years (corresponding to $50 - 100$meV effective Majorana neutrino mass). The detector is of a modular design with two possible calorimeter designs: the 'Baseline (or 'Block')' design (Section 9.2.1)

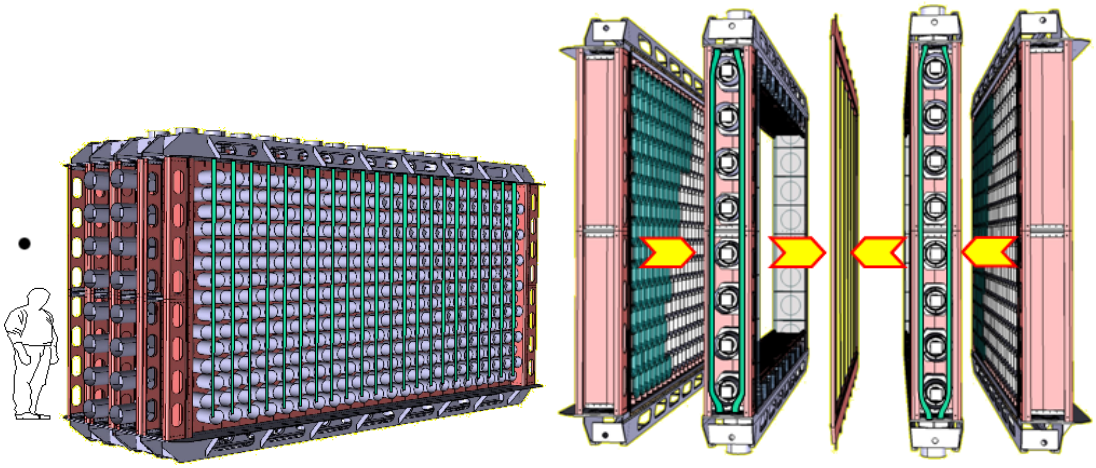

Figure 9.1: Views of a SuperNEMO baseline module: an enclosed module ($\sim$ 4m (height) x 6m (length) x 2m (width)) on the left and a view of the module's components: (from left to right) calorimeter wall, tracker, source foil, tracker and calorimeter wall (on the right).

and the 'Bar' design (Section 9.2.2). Each module is an independent, fully operational detector able to start data taking as soon as it is built.

The baseline design (Figure 9.1) consists of 20 modules ($\sim$ 4m (height) x 6m (length) x 2m (width)), each containing 5kg of vertically suspended thin ($\sim$ 40mg/cm^2) isotope source foil (providing a total of 100kg), surrounded by $\sim$ 2000 Geiger mode drift cells and enclosed by the calorimeter walls (containing $\sim$ 550 8" PMTs), composed of square scintillator blocks. The advantages of the baseline design are the size of the modules, providing flexibility in the location of the detector (as one underground laboratory space may not be large enough to house all of the modules) and a faster commissioning time, allowing for data to be taken sooner. Other main advantages (and disadvantages) are considered in the calorimeter design (Section 9.2.1).

The bar design (Figure 9.2) consists of 7 modules (2.8m (height) x 6.65m (length) x 6.65m (width)), each containing 12.5kg of vertically suspended thin ($\sim$ 40mg/cm^2) isotope source foil (providing a total of 105kg). The source foil is surrounded by Geiger mode drift cells, which then have a calorimeter wall composed of vertical 2m long scintillator bars (stacked up next to each other horizontally) on either side. This structure is repeated in a sandwich like design, containing 6 sheets of vertically suspended source foils and 7 vertical bar calorimeter walls in each module. The advantages of this layered bar design are more efficient γ tagging (helping to identify and reduce the

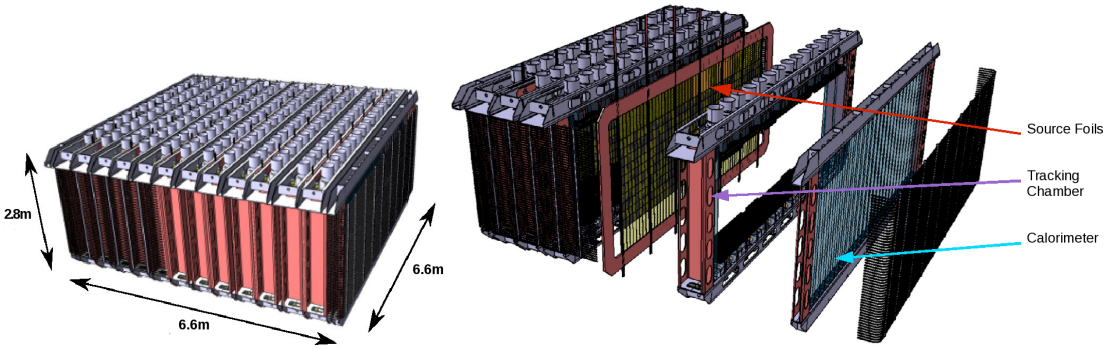

Figure 9.2: Views of a SuperNEMO bar module: one complete module of 2.8m height x 6.65m length x 6.65m width (on the left) and a cross-sectional view of a complete module, showing the source foil-scintillator wall layered structure (on the right).

backgrounds to the experiment), reduction in cost and improvement in radio-purity due to the calorimeter considerations (as discussed in Section 9.2.2).

In February 2010 the SuperNEMO collaboration made a decision to use the baseline design for the SuperNEMO detector after considering the advantages and disadvantages of each design. The discussion regarding the decision is presented in Section 12.4.

9.1.1 SuperNEMO Sensitivity

SuperNEMO's sensitivity has been studied by taking into account detector effects known from the experience with NEMO3 and by carrying out full detector simulations and taking into consideration parameters such as the source thickness (20 - 40mg/cm^2) and radio-purity, the absence and presence of a magnetic field, calorimeter energy resolution and design and exposure time. The calorimeter energy resolution is one of the dominant factors in achieving the required sensitivity (Section 9.2), with an innate detector energy resolution of $\sim 5\%$ [1] originating due to the smearing of the energy distribution caused by the electrons exiting the source foils (hence a source foil as thin as possible is preferable). Therefore an energy resolution better than this cannot be achieved. The target sensitivity of 10^{26} years ($50 - 100$ meV) has been confirmed with simulations, as demonstrated in Figure 9.3.

Sensitivity is shown as a function of energy resolution for three source purity mod-

[1] Hereafter the energy resolution is quoted for electrons as $\%$ full-width half-maximum (FWHM) at 1MeV, unless stated otherwise.

Parameters	SuperNEMO	NEMO3
Isotope	^{82}Se	^{100}Mo
Mass	100kg	7kg
$0\nu\beta\beta$ Detection Efficiency	30%	18%
Energy Resolution	$\frac{7-8\%}{\sqrt{E(MeV)}}$	$\frac{14-17\%}{\sqrt{E(MeV)}}$
^{214}Bi Purity	$< 10\mu$Bq/kg	$< 300\mu$Bq/kg
^{208}Tl Purity	$< 2\mu$Bq/kg	$< 20\mu$Bq/kg
Exposure	500 kg years	30 kg years
$T^{0\nu\beta\beta}_{1/2}$ Sensitivity	1×10^{26} years	1×10^{24} years
Effective Majorana Mass $\langle m_{\nu_e} \rangle$	$50 - 100$meV	$0.3 - 1.0$eV

Table 9.1: SuperNEMO R&D parameters and goals compared to those of NEMO3.

els ("2n2b": the absence of ^{214}Bi and ^{208}Tl, "SN_bgr": ^{214}Bi and ^{208}Tl at the target level of SuperNEMO and "N3_bgr":^{214}Bi and ^{208}Tl at the level of NEMO3), a foil thickness of 40mg/cm^2, with the magnetic field switched on (at 25G) and off, and a fixed exposure of 500kg years (Figure 9.3(a)). The sensitivity is also shown as a function of exposure (in kg years) for the three source purity models, a foil thickness of 40mg/cm^2, with the magnetic field switched on (at 25G) and off, and a fixed energy resolution of 7% FWHM at 1MeV for the baseline and bar designs (Figure 9.3(b)).

9.1.2 SuperNEMO R&D

The SuperNEMO R&D focuses on four main areas for both of the designs (source foil production, purification of materials, tracker development and software development) and looks at calorimeter development for each of the designs individually. The main goals of the SuperNEMO R&D, with comparison to NEMO3, are summarised in Table 9.1.

Source production and purification can be achieved using chemical and distillation methods, with enrichment possible through centrifuging. The radio-purity of the source foils is of utmost importance in order to achieve the desired sensitivity. A dedicated detector, known as the BiPo detector, has been designed and commissioned to measure the level of ^{214}Bi (^{208}Tl) contamination in the source foils from the ^{238}U (^{232}Th) ra-

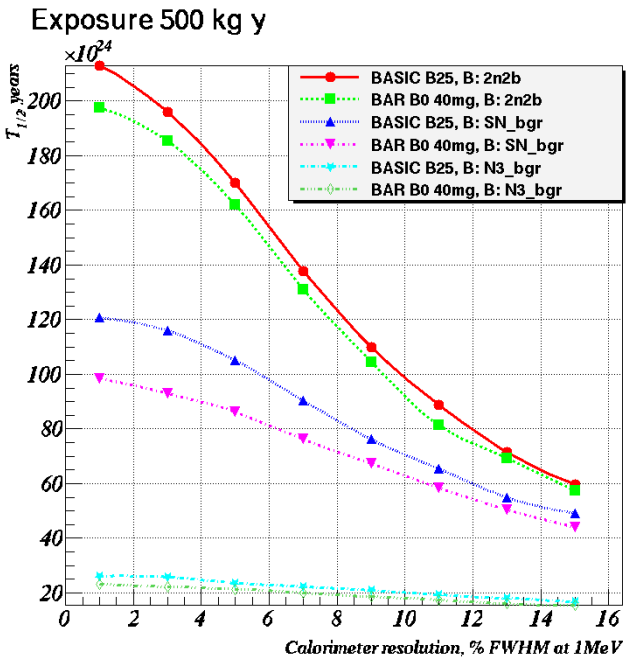

(a) Sensitivity as a function of energy resolution

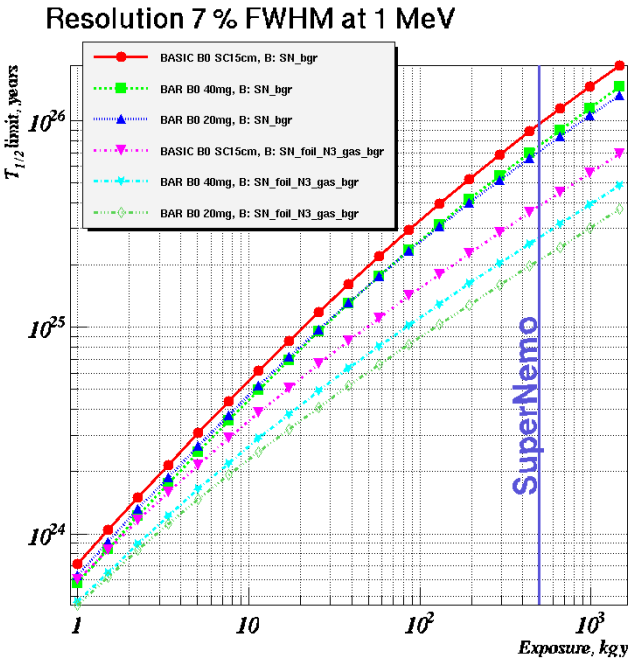

(b) Sensitivity as a function of exposure

Figure 9.3: SuperNEMO half-life sensitivity for the baseline (labelled as 'BASIC') and bar (labelled as 'BAR') designs as a function of (a) energy resolution with a fixed exposure of 500kg years and (b) exposure with a fixed energy resolution of 7% FWHM at 1 MeV for the baseline and bar designs. Three radio-purity models are considered (the absence of ^{214}Bi and ^{208}Tl, ^{214}Bi and ^{208}Tl at the level of SuperNEMO and ^{214}Bi and ^{208}Tl at the level of NEMO3) for a foil thickness of 40mg/cm^2 with the magnetic field switched on (at 25G) and off [141].

dioactivity chains to a sensitivity of 10μBq/kg (2μBq/kg) [142]. The detector principle is to place the source foils in between two scintillators, which will tag the electron emitted by the β-decay of ^{214}Bi (^{212}Bi) and subsequently the α emitted by the decay of ^{214}Po (^{212}Po).

Each SuperNEMO module (for the baseline design) contains ~ 2000 octagonal Geiger drift cells ($\sim 5 \times 10^5$ wires for the entire baseline detector). The tracker development focuses on optimising its operating parameters, such as the wire length, material, configuration, detector readout and end-cap design. Challenges include plasma initiation and propagation efficiency, crosstalk between the cells, and ageing and radiopurity of the cells. Due to the large number of wires a dedicated wiring robot is being developed for the mass production of the drift cells. A 90-cell tracker prototype has been commissioned and tested with cosmic muons. The tracking studies carried out show good plasma propagation and charge collection across 4m long anode wires and good resolution (ΔXY: 0.7mm and ΔZ: 1.3cm) [143].

The SuperNEMO software, including a full MC simulation, has been developed using C++, ROOT and GEANT-4.9 based on NEMO3 experience. New algorithms have improved performance of the reconstruction efficiency.

9.2 The SuperNEMO Calorimeter Design

The energy resolution of the calorimeter is of utmost importance to the success of SuperNEMO, as can be illustrated by the following half-life sensitivity formula:

$$T^{0\nu}_{1/2} > \frac{ln2 \cdot N_A}{A} \cdot \frac{\eta}{\kappa_{CL}} \cdot \sqrt{\frac{M \cdot t}{N_{bkg} \cdot \Delta E}} \text{ [144]}, \tag{9.2.1}$$

where the energy resolution ΔE (in keV at 1 σ) is as significant as the isotope mass M (in kg), the run time t (in years) and the expected number of background events N_{bkg} (in kg^{-1}keV^{-1}yr^{-1}). Factors N_A and A are Avogadro's number (6.022 $\times 10^{23}$ mol^{-1}) and the atomic mass (in gmol^{-1}) of the isotope respectively, η is the detector efficiency and κ_{CL} is the number of σs corresponding to the confidence level (usually 1.64σ for a 90% CL) of the $0\nu\beta\beta$ half-life sensitivity $T^{0\nu}_{1/2}$. One of the dominant backgrounds to $0\nu\beta\beta$ is the irreducible $2\nu\beta\beta$ tail, making the energy resolution one of the determining factors of the detector's sensitivity to $0\nu\beta\beta$. This is demonstrated in Figure 9.3 and can also be seen in Figure 9.4, where simulations carried out for ^{82}Se with a calorimeter energy

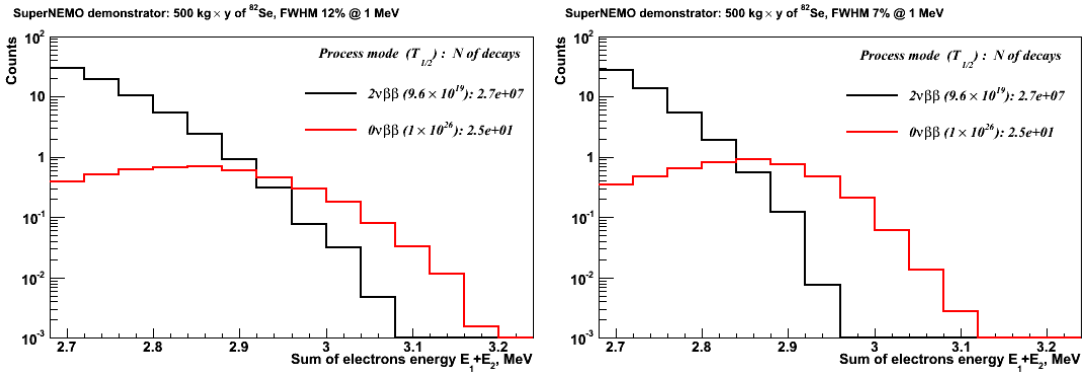

(a) 12% FWHM at 1 MeV (b) 7% FWHM at 1 MeV

Figure 9.4: Calorimeter energy resolution simulations for ^{82}Se for 500kg·yr, with the $0\nu\beta\beta$ half-life (red) normalised to 10^{26} years. 12% (a) and 7% (b) FWHM at 1 MeV energy resolutions are shown, illustrating the overlap of the $2\nu\beta\beta$ (black) tail.

resolution of 12% and 7% FWHM at 1MeV respectively and normalised to a 10^{26} year $0\nu\beta\beta$ half-life are shown. It can be seen that a much clearer separation between the $2\nu\beta\beta$ tail and the $0\nu\beta\beta$ peak is achieved with a 7% energy resolution.

SuperNEMO has a need for a robust calorimeter (using reliable and time withstanding technology) with ease of manufacturing and assembly, which provides the required energy resolution at a sensible cost. The calorimeter R&D for SuperNEMO consists of three main areas of study: energy and time resolution (Chapters 10 and 12), calibration and photomultiplier tube (PMT) radio-purity.

During five years of data taking the gain and stability of $\sim 11,000$ PMTs must be monitored at a 1% level. The detector response must be linear, and any non-linear effects must be monitored at a 1% level up to $3-4$MeV (the region of interest for $0\nu\beta\beta$). The absolute calibration system will use ^{207}Bi sources (providing conversion electrons with single energies of 482keV and 976keV) inserted into the detector on a monthly basis. A UV-LED based light injection system is being developed for gain and linearity monitoring. Using low activity alpha sources embedded into the scintillator to monitor the gain is an additional possibility being studied. ^{60}Co (providing two coincident γs of 1.1 and 1.3 MeV) will occasionally be used for absolute time caiblration.

Specific to low background counting experiments ultra-pure materials must be used throughout the detector. One of the main sources of contamination comes from

the PMTs, specifically from the photocathode glass, which is closest to the active volume of the detector. The PMT radiopurity requirements, depending on radon emanation from the PMT glass, are: ^{214}Bi < 0.05Bq/kg and ^{208}Tl < 0.004Bq/kg. These requirements for SuperNEMO have prompted development of low-background glass on a new scale and the collaboration is currently working closely with Hamamatsu to develop a radio-pure Barium salt free glass to reach the radio-purity requirements of the detector. Currently, the radioactivity limits reached with glass containing Barium salt are ^{40}K < 0.6Bq/kg, ^{214}Bi < 0.8Bq/kg and ^{208}Tl < 0.06Bq/kg. A PMT has been constructed and tested using this Barium salt glass. Radioactivity levels of an order of magnitude better have been reached with the silica Barium salt free glass being developed by Hamamatsu, however a PMT has not yet been built using this silica glass. There are plans to test this in the near future.

9.2.1 The Baseline Design Calorimeter

The baseline design is similar to that of NEMO3, however it uses polyvinyl-toluene (PVT) scintillator instead of polystyrene (PST) scintillator. It consists of 308mm^2 or 256mm^2 square PVT blocks with a hemispherical "cutout" directly coupled to 8" PMTs (Figure 9.6(a)). Different geometries of the blocks have been considered and previously it was thought that optical simulations [145] and test bench measurements have shown a hexagonal geometry (with a 28cm diameter and a 10cm minimum thickness) to give the best performance. However, recently simulations and test bench measurements have shown that normalising the area of a square block to the same area as that of a hexagonal block give very similar energy resolution results [146]. The final size of the square blocks will be decided by the end of 2011. An energy resolution of 7% FWHM at 1MeV has been reached with the blocks [147], with the big breakthrough being made by coupling the scintillator blocks directly to the hemispherical 8" without the use of a light-guide. Instead, the block has a hemispherical cutout to enable the face of the PMT to fit it directly.

The advantages of the baseline design are that a 7% FWHM at 1 MeV energy resolution has been reached, good time resolution (250ps σ at 1MeV [2]) and the use of well understood and proven technology of NEMO3. $11,000$ block + PMT units

[2]Hereafter the time resolution is quoted for electrons as σ at 1MeV, unless stated otherwise.

would be required for the full detector, which increases the cost of the experiment. The number of channels used could potentially increase the radioactivity within the active detector volume.

9.2.2 The Bar Design Calorimeter

The bar design consists of vertically placed 2m $\times 10$cm (with the ends tapered to 6.5cm at 45° angles in order to match the diameter of the bar to that of the $3"$ PMT) $\times 2.5$cm thick PVT bars with $3"$ PMTs at each end of the bar (Figure 9.6(b)). The advantages of the bar design are more efficient γ tagging (enabled by the layered design of the detector) and the reduction of the number of bar + PMT units to $5,000 - 7,000$ for the full detector, reducing the cost of the experiment and the radioactivity within the active volume of the detector. However, as the bar design is new unproved technology which is more difficult to extrapolate from NEMO3, test bench measurements and simulations must be carried out to see whether a sufficient energy resolution and time resolution can be reached with this design to achieve the desired SuperNEMO sensitivity. Other issues, such as uniformity and ageing of the bars, must also be considered.

The more efficienct γ tagging of the bar design could mean that the time of flight requirements for the detector could be relaxed. This would allow a smaller gap between the source foils and the scintillator walls, which has been shown to increase efficiency in simulations [148]. The bars also provide an increased impact resolution of $2 - 3$cm. As can be seen in Figure 9.5(a) simulations have shown that an energy resolution of 9% at 1MeV could be enough to achieve the desired sensitivity of $\sim 10^{26}$ years [141]. The sensitivity as a function of exposure for the bar design at an energy resolution of 9% can be seen in Figure 9.5(b).

The test bench measurements and results for the bar design are presented in this thesis.

9.3 The SuperNEMO Time Line

The construction of the SuperNEMO "demonstrator" module is currently underway. The idea of the demonstrator module is to have one (of twenty) fully operational stand alone SuperNEMO module containing 7kg of ^{82}Se, which can start taking data and testing the principles of the technology used for SuperNEMO as soon as it has been

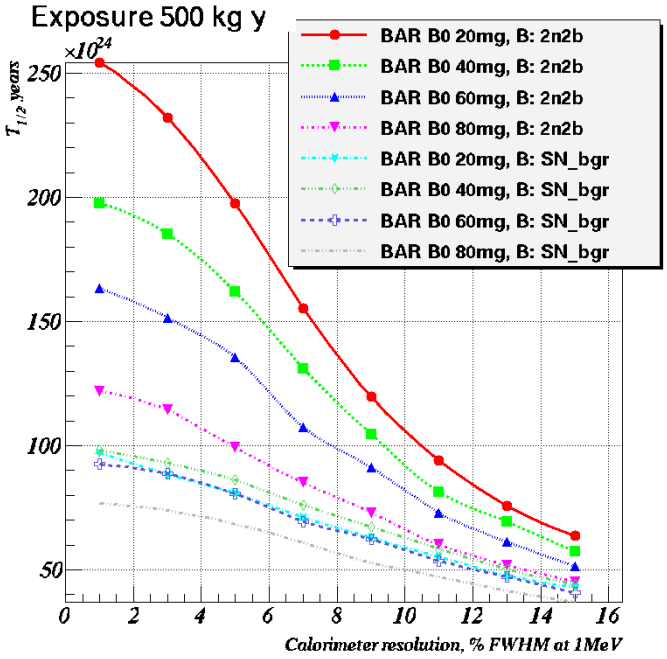

(a) Sensitivity as a function of energy resolution

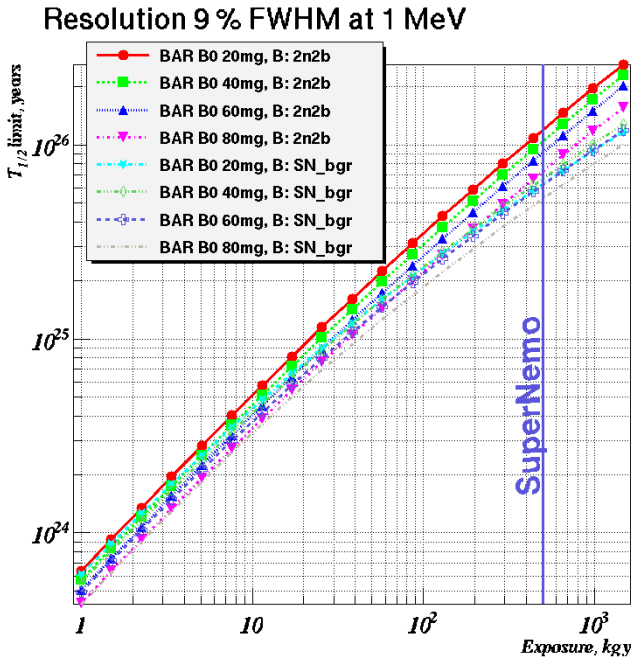

(b) Sensitivity as a function of exposure

Figure 9.5: SuperNEMO half-life sensitivity for the bar (labelled as 'BAR') design as a function of (a) energy resolution with a fixed exposure of 500kg years and (b) exposure with a fixed energy resolution of 9% FWHM at 1 MeV. Two radio-purity models (the absence of ^{214}Bi and ^{208}Tl and ^{214}Bi and ^{208}Tl at the level of SuperNEMO) and four foil thickness models (20mg/cm^2, 40mg/cm^2, 60mg/cm^2 and 80mg/cm^2) are considered [141].

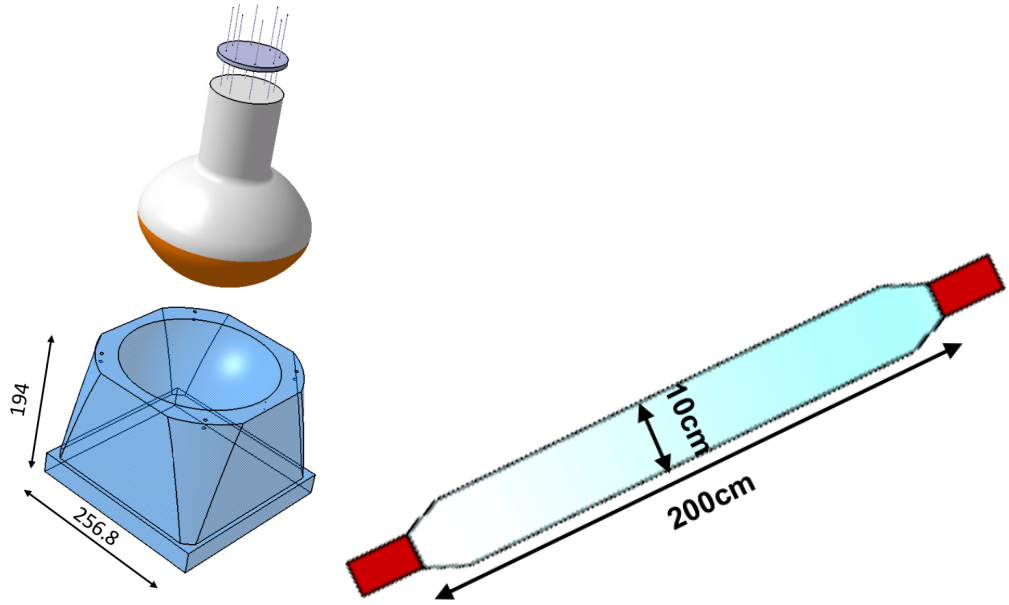

(a) Baseline design calorimeter unit

(b) Bar design calorimter unit

Figure 9.6: SuperNEMO (a) baseline (a 308mm^2 or 256mm^2 block coupled to an 8 ” PMT) and (b) bar (2m $\times$10cm $\times$2.5cm PVT bars coupled to 3$''$ PMTs at each end) calorimeter unit designs.

commissioned. The demonstrator will be installed and commissioned in the Laboratoire Soutterain de Modane (LSM) within 2013 and begin running at the end of 2013.

In parallel to the demonstrator running the rest of the SuperNEMO modules will start being constructed in 2014, with each module being commissioned and starting running as soon as it is ready, utilising the advantage of the modular design of SuperNEMO. By 2019 SuperNEMO hopes to reach its design sensitivity of $\langle m_{\nu_e} \rangle \sim$ 50-100meV.

Chapter 10

Parameters Influencing Energy Resolution

The energy resolution of the calorimeter is an important factor in achieving the desired SuperNEMO sensitivity, as described in Section 9.2. However, other calorimeter requirements must be considered, which can limit the methods used to achieve the desired energy resolution. The PMT considerations include the quantum efficiency, cathode to first dynode collection efficiency, uniformity, gain stability and linearity, and radio-purity. The scintillator material must be considered, requiring a low Z material in order to minimise back-scattering of external low energy electrons to maintain the detection efficiency. The radio-purity of the scintillator must also be taken into account. The calorimeter must be relatively easy to manufacture and assemble, at a sensible cost.

The general structure of a calorimeter unit consists of a scintillator bar wrapped in a reflective wrapper optically coupled via a gel to a 3" PMT at each end. Each of these four components and their influence on the energy resolution are considered in the sections that follow.

10.1 Energy Resolution

In order to achieve a sensitivity of 10^{26} years SuperNEMO's calorimeter requires an unprecedented energy resolution for plastic scintillator. The energy resolution, $\frac{\Delta E}{E}$, is dominated by stochastic photon fluctuations for scintillation detectors. For a high number of photo-electrons ($N_{pe} > 20$) the statistical error $\frac{1}{\sqrt{N_{pe}}}$ is reduced and leads to an optimisation of the energy resolution, which is expressed as:

$$\frac{\Delta E}{E} = \frac{2.35\sigma}{E} = \frac{2.35}{\sqrt{N_{pe}}}, \tag{10.1.1}$$

where N_{pe} is the number of photo-electrons and the factor of 2.35 converts 1σ to the full-width half-maximum (FWHM). The energy resolution can be shown as three experimental objectives:

$$\frac{N_{ph}}{E_e} \cdot \epsilon_{col}^{light} \cdot (QE^{PMT} \cdot \epsilon_{col}^{PMT}) = N_{pe}, \tag{10.1.2}$$

where $\frac{N_{ph}}{E_e}$ is the number of photons per unit energy and is determined by the scintillator light output (the number of detected photo-electrons). ϵ_{col}^{light} is the light collection efficiency and depends on the material, surface treatment and geometry of the scintillator, the reflector material and its efficiency and the optical coupling quality (gels, light guides etc). Intrinsic characteristics of the PMT include the quantum efficiency (QE) of the photo-cathode QE^{PMT}, the collection efficiency ϵ_{col}^{PMT} and, to a lesser extent, the gain of the first dynode.

10.2 Photomultiplier Tubes

The dominant factor in influencing energy resolution for PMTs is the quantum efficiency (QE) of the PMT's photo-cathode. There are three main manufacturer contenders for SuperNEMO PMTs: ETL (Electronic Tubes Limited), Hamamatsu and Photonis. Significant breakthroughs have been made with new bi-alkali photo-cathodes developed by Hamamatsu and Photonis, with a QE range of $35-43\%$ at the peak wavelength. ETL are currently in the R&D stage of their high QE development, however they produce very radio-pure PMTs and have therefore been considered in the study. The PMTs used for the study of the bar calorimeter design and their characteristics are given in Table 10.1.

10.2.1 ETL (Electron Tubes Limited)

Whilst ETL are still in the R&D phase for their high QE photo-cathode development, they are known for producing very radio-pure PMTs. Equation 9.2.1 shows that the number of background events (N_{bkg}) and the energy resolution (ΔE) have the same significance for the $0\nu\beta\beta$ decay sensitivity. Other PMT factors which affect the energy resolution, such as the first dynode collection efficiency and gain, are not explicitly

Type	Cathode ⌀(in.)	Quoted Max QE	QE at 400nm	Dynode Stages	Gain
ETL 9390KB	5”	28%	26%	10	$\sim 10^6$
Hamamatsu R6233-100	3”	35%	32%	8	2.3×10^5 [149]
Hamamatsu R6233-100-S	3”	43%	40%	8	2.3×10^5 [149]
Photonis XP5312	3”	43%	43% [150]	8	2.4×10^5
Photonis XP5302	3”	45%	45%	8	2.4×10^5

Table 10.1: SuperNEMO bar design calorimeter candidate PMTs and their characteristics. Independent measurements were carried out where referenced.

stated by manufacturers and therefore must be investigated. It is possible that these factors, combined with the radio-purity of the PMTs, may be enough to compensate for the lower QE of the tubes to maintain the SuperNEMO sensitivity.

Two $5"$ 9390KB ETL tubes with a peak QE of 28% were used for testing of the calorimeter bar design (the wavelength vs. QE of the tubes can be seen in Figure 10.1(a)). The photo-cathode of the tubes is bi-alkali and the PMT window is made of borosilicate glass.

10.2.2 Hamamatsu

Hamamatsu have developed high QE Super-Bialkali (SBA - R6233-100) and Ultra-Bialkali (UBA) photo-cathodes with peak efficiencies of 35% and 43% respectively. $3"$ UBA select tubes are not yet available for the market, however SuperNEMO was provided with proto-type ‘SBA-Select’ tubes (R6233-100-S) for testing, which are essentially UBA type tubes. Both SBA and SBA-Select tubes were used for testing of the calorimeter bar design. The wavelength vs. the QE of the tubes can be seen in Figure 10.1(b). The photo-cathode of the tubes is bi-alkali and the PMT window is made of borosilicate glass.

10.2.3 Photonis

Photonis have also developed high QE super bi-alkali photo-cathodes. The SuperNEMO collaboration and Photonis have closely worked on development of $8"$ bi-alkali PMTs for the baseline design to obtain impressive results and unprecedented en-

ergy resolution [147]. Prototype $3"$ PMTs are used by the SuperNEMO collaboration to test and develop the photo-cathode with Photonis, then applying the developments to the $8"$ tubes.

The two tubes used for testing of the calorimeter bar design were such $3"$ prototypes: XP5312 and XP5302, which have a peak QE of 43% and 45% respectively. The XP5312 and XP5302 tubes both have a super bi-alkali photo-cathode, but the XP5302 tube uses further improved technology to achieve a higher QE. A typical spectral response and measured QE vs. the wavelength of the XP5302 tube can be seen in Figures 10.1(c) and 10.1(d). The PMT windows are made of Lime glass.

During baseline design testing it was found that the Photonis $8"$ PMTs produce a better energy resolution ($\sim 6.5\%$ FWHM at 1MeV) than the Hamamatsu $8"$ tubes ($\sim 7.5\%$ FWHM at 1MeV) [151]. This difference seems to come from the collection efficiency of the tube. Unfortunately, Photonis have announced a full stop to their photo-multiplier R&D branch in 2009. The bars were still tested with the Photonis PMTs to produce a direct comparison of Hamamatsu and Photonis tubes. The collaboration has been working closely with Hamamatsu to improve the collection efficiency of their tubes. By changing the voltage divider of the tube and increasing the gain at the first and second dynodes (at the expense of the overall gain of the PMT) the collection efficiency has been improved, giving an improvement in the energy resolution of 0.5% obtained with the Hamamatsu tube [146].

10.3 Scintillators

Many types of scintillator are available on the market. Non-organic scintillators have an advantage of a high light yield but have slow timing, a high rate of electron back-scattering and can often be radio-polluted. However, two types of non-organic scintillator were considered for SuperNEMO to see whether the benefits could outweigh the disadvantages to achieve the required energy resolution. YSO scintillator (composed of Y_2SiO_5, doped with Ce) has suitable properties of fast timing and a high light yield, however the high electron back-scattering, bad radio-purity and high cost of YSO took it out of the running. The Phoswich scintillator is a hybrid consisting of two scintillators optically coupled to each other: CaF_2 scintillator doped with Eu and plastic scintillator. The plastic scintillator provides fast timing and the CaF_2 gives a high light yield. This

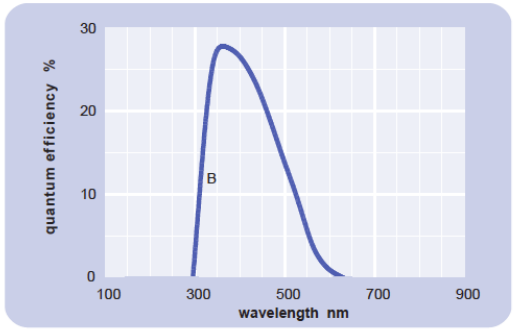

(a) ETL [152]

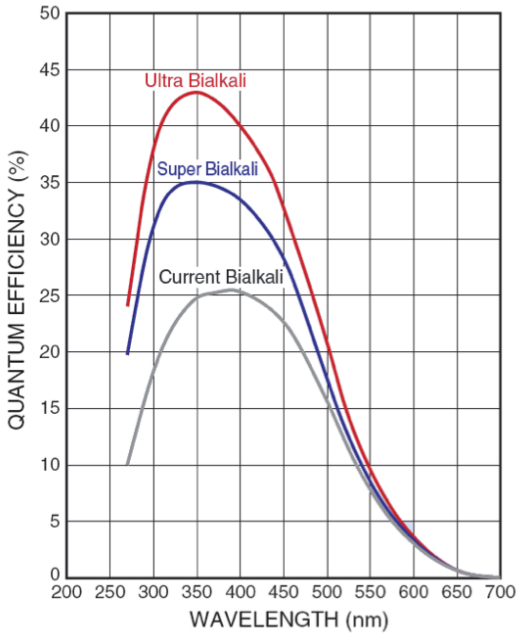

(b) Hamamatsu [153]

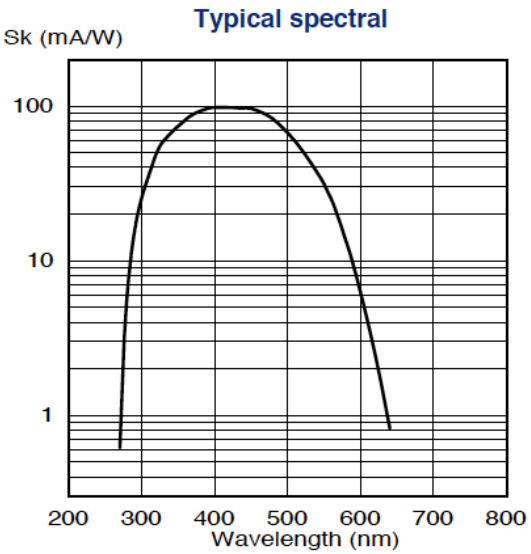

(c) Photonis Spectral Sensitivity [154]

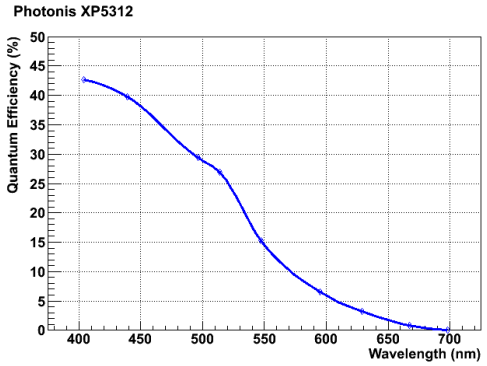

(d) Photonis Measured QE [150]

Figure 10.1: Wavelength vs. QE for (a) the ETL photo-cathode [152] and (b) the Hamamatsu photo-cathodes for the standard Bialkili (bottom curve), Super-Bialkili (middle curve) and Ultra-Bialkali (top curve) photo-cathodes [153]. Figure 10.1(c) shows a typical spectral sensitiviy (cathode radiant sensitivity vs. wavelength) [154] and (d) measured QE vs. wavelength for the Photonis XP5312 photo-cathode [150].

reduces the problem of back-scattering as electrons now enter the low Z medium of the plastic scintillator. However, the overall performance of the scintillator was not of a sufficient quality for the SuperNEMO detector.

Liquid (toluene based) organic scintillators (consisting of 0.5% of PPO (2,5-Diphenyloxazole) scintillating agent and 0.0025% of wavelength shifting POPOP) were considered for the SuperNEMO calorimeter as they have fast timing, low back-scattering, good uniformity and radio-purity. However, due to the difficulty of the mechanical design and the energy losses of external electrons in the entrance window of the liquid scintillator container, which reduces the energy resolution to lower than the requirement, liquid scintillator is not a suitable candidate for SuperNEMO.

This led to a choice of organic solid plastic scintillator, which has fast timing, low back-scattering and high radio-purity, is mechanically easy to manufacture compared to liquid scintillator and allows the scintillator bars for the bar design to be produced.

Electron back-scattering is proportional to Z^2 and reduces the detection efficiency. The scintillator material must therefore be a low Z one in order to minimise electron back-scattering as low energy electrons are being studied. For this reason high Z type scintillators, such as mineral oils, NaI (sodium iodide) and CsI (caesium iodide) scintillators, are not considered for the SuperNEMO calorimeter. The two main choices of low Z scintillator are PST (polystyrene), as used by NEMO3, and PVT (polyvinyl toluene). The scintillator is also required to have good coincidence time resolution (< 250ps σ at 1MeV) for accurate ToF information, which is a characteristic of both PST and PVT scintillators. Another consideration for the scintillator is the manufacturing process. Uniformity of the light yield can be problematic, in particular for large geometry scintillators such as the 2m long bars, as it is difficult to achieve uniform cooling during the manufacturing process, which directly affects the light yield uniformity. Scintillators that are cast rather than extruded are more uniform and are therefore preferred, but are more expensive to manufacture.

Both PST and PVT scintillators are relatively radio-pure. PST scintillators produce $\sim 7,000$ photon/1MeV e^-, compared to $\sim 10,000$ photons/1MeV e^- for PVT scintillators. PVT scintillators have a higher light yield than PST scintillators, therefore the focus of the calorimeter R&D has been on PVT scintillators, the results of which are presented in this thesis. However, there are some difficulties with using PVT

Type	Light Yield (ph/1MeV e^-)	Refractive Index	Decay Time (ns)	Attenuation Length (cm)	λ (nm)
PST	$\sim 7,000$	1.58	$\sim 2-3$	200	430
Bicron BC-408	$10,000$	1.58	2.1	380	425
ELJEN EJ-200	$10,000$	1.58	2.1	380	425

Table 10.2: SuperNEMO bar design calorimeter candidate scintillators and their characteristics, where λ is the wavelength of maximum emission (nm). The refractive index is quoted at a wavelength of 589.3nm.

scintillator, such as 'crazing' (or corroding) of the scintillator when it comes into contact with various common substances, including the natural oils on a person's fingers. This makes handling of the scintillator of utmost importance, requiring gloves to be worn whenever in contact with the PVT. Crazing is also caused when the PVT is exposed to sudden temperature fluctuations when using ethanol or methanol to clean the scintillator surface. After various testing it was found that isopropanol does not cause crazing as it evaporates more slowly and is therefore the preferred choice of cleaning solution for PVT scintillators. PVT is also more brittle than PST and can therefore crack if impacted, requiring a high level of care when handling. For these reasons PVT is more difficult to machine. Ageing is also a concern for PVT scintillators, especially of such a considerable size as the bar.

The characteristics of the two cast PVT scintillators used to study the calorimeter bar design are shown in Table 10.2, compared to typical characteristics of a PST scintillator. The Bicron BC-408 and ELJEN EJ-200 scintillators combine the properties of long optical attenuation length, fast timing, a high light output and have emission spectra (shown in Figure 10.2) well matched to that of common PMTs. This makes them good candidates for ToF systems using scintillators greater than one metre long, as in the case of the bars.

10.4 Optical Coupling Materials

Good optical coupling between the scintillator and the PMT is extremely important for uniform and complete light collection, therefore it is a strong factor in influencing

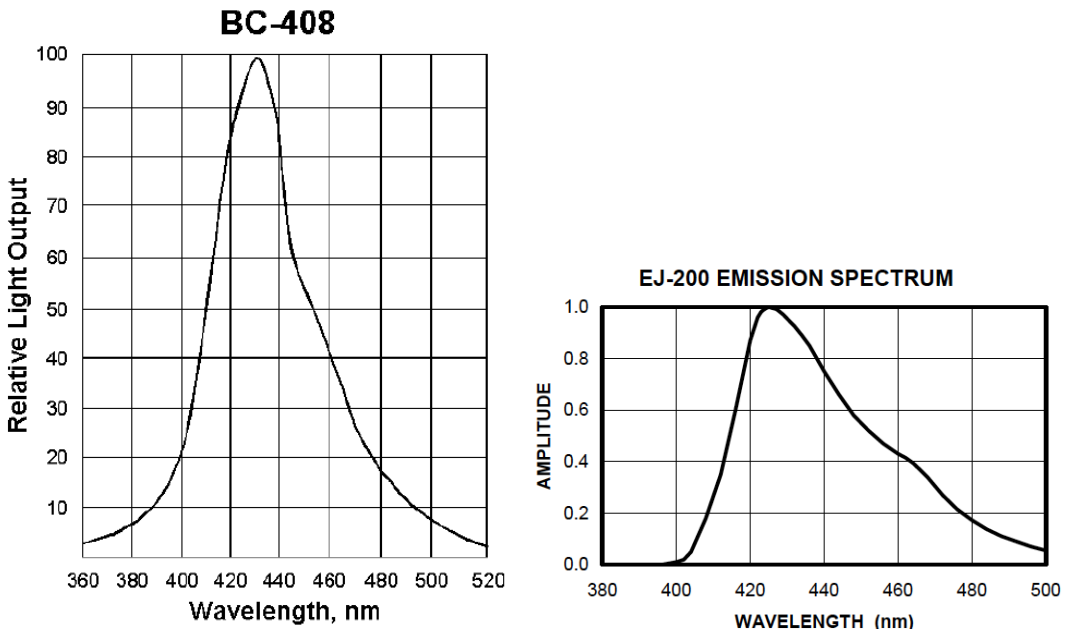

(a) Bicron BC-408 [155] (b) ELJEN EJ-200 [156]

Figure 10.2: Emission spectra of SuperNEMO scintillator candidates: (a) Bicron's BC-408 [155] and (b) ELJEN's EJ-200 [156].

the energy resolution. The refractive index, which should have a value between the refractive index of the scintillator and that of the PMT glass, and the transmittance of the coupling material are the dominant factors in getting good optical contact. It is important that the optical gel used does not corrode PVT scintillator, therefore crazing tests have been carried out in order to select appropriate gels. The viscosity of a gel is another consideration. A heavily viscous gel can pose a problem for large non-flat surfaces (such as coupling a hemispherical PMT to a scintillator, as for the baseline design) as it is difficult to entirely remove the air bubbles which obstruct the contact between the scintillator and the PMT. However, when working with small flat surfaces, such as the edge of a 2.5cm thick bar and a 3" PMT window, a viscous gel such as Bicron's BC-630 provides good optical contact without crazing PVT scintillator. BC-630 gel is composed of silicone (methyl phenyl polysiloxane) and its properties (summarised in Table 10.3) are a refractive index of 1.465 (compared to 1.491 for PMMA and 1.50 - 1.54 for Crown glass), a viscosity of $\sim 10^5$ (compared to 81 for olive oil and 2.5×10^5 for peanut butter), and a transmission of 95% at 280 - 700 nm. Due to BC-630's refractive index (1.465) being closely matched to that of the PVT

Type	Refractive Index	Viscosity (cP)	Transmission	Composition
Bicron BC-630	1.465	$\sim 10^5$	95% at 280nm - 700nm	Silicone (Methyl Phenyl Polysiloxane)

Table 10.3: Bicron BC-630 optical gel characteristics. The refractive index is given at a wavelength of 589.3nm. The dynamic (absolute) viscosity value is given in centi-Poise (cP) at 25°C.

scintillator (1.58) and the PMT borosilicate glass (1.470) and other suitable properties of the gel it is used for testing the bar calorimeter set up.

An optical epoxy grease (RTV 615 based), the same as was used for NEMO3, will be used to couple the PMTs and scintillators in the final construction of the SuperNEMO calorimeter in order to obtain good optical coupling.

10.5 Reflective Wrappings

The reflective material used in the SuperNEMO calorimeter must have a low Z (to minimise back-scattering), a high reflectivity, a low density and must be dimensionally thin. The reflector has to be thin and of a low density in order to reduce the electron energy loss as it passes through the material. A high reflectivity of the material is required in order to redirect any escaped light back towards the PMT photo-cathode. The reflector must also be as radio-pure as possible to reduce the number of background events within the active detector volume. The reflector types used for the study of the bar calorimeter design and their characteristics are given in Table 10.4.

Energy resolution can depend on whether the reflective material used is specular (reflecting the incident light at one angle) or diffusive (reflecting the incident light at many different angles). Optical simulations have shown that the impact of specular or diffusive reflector on energy resolution depends on the geometry of the scintillator [145, 151]. This is due to bulk absorption and surface effects contributing to the overall light collection of the calorimeter system. For example, scintillator blocks obtain a better energy resolution with diffusive reflection around the lateral sides, whereas scintillator bars work better with specular reflection due to their geometry.

Type	Thickness (μm)	Reflectance (%)	Density (mg/cm^2)	Density (g/cm^3)	S or D?
PFTE Ribbon	25	> 70	1.0	0.4	D
PFTE (3 layers)	75	> 80	3.0	0.4	D
Goodfellow Al-Mylar	6	~ 93	0.78 - 0.84	1.2	S
Goodfellow Al-Mylar	12	79 ± 4 [157]	1.6 - 1.7	1.2	S
Vikuiti ESR	65	> 98	7.8	1.2	S
ReflechTech ESR	100	94 ± 4 [157]	12	1.2	S

Table 10.4: SuperNEMO bar design calorimeter candidate reflective materials and their characteristics. Independent measurements were carried out where referenced. S and D indicate whether the reflector is specular (S) or diffusive (D).

10.5.1 PTFE (Teflon)

PFTE ribbon (or Teflon) is a type of diffusive reflector. When using the $\sim$ 1cm wide ribbon wrapping it around the scintillator in three layers produces a better energy resolution than with one layer. Due to the small width of the ribbon it is difficult to use in the manufacture of a full scale bar design calorimeter, however it is important to test its influence on the energy resolution as for certain geometry scintillators (such as the baseline design blocks) the energy resolution obtained is as good as that obtained with Mylar or, in some cases, ESR [147]. Special apparatus are required to collect the isotropically scattered light of the diffusive reflector to quantify the reflectance, therefore its measurement could not be carried out.

10.5.2 Enhanced Specular Reflector

ESR (enhanced specular reflector) is a relatively new polymer based product. It is composed of layers that form a gradient of refractive indices. The ESR works by refracting light with an incident angle $\theta_i < \theta_c$ (where θ_c is the critical angle) to the next layer until $\theta_i > \theta_c$. Reflectivity as a function of wavelength comparing ESR to aluminised Mylar can be seen in Figure 10.3.

Two companies produce the ESR: Vikuiti and ReflechTech. Vikuiti ESR is extremely expensive at $\sim$ 400 GBP for a $12" \times 12"$ sheet and is marketed as an aid to

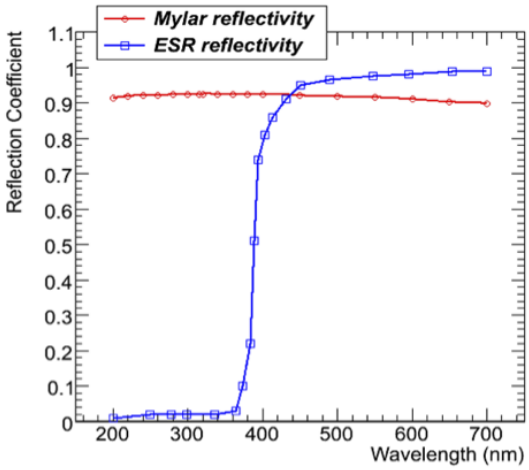

Figure 10.3: Reflectivity as a function of wavelength for aluminised Mylar and ESR [145].

back-lighting of LCDs (liquid crystal displays). Due to its expense an amount of Vikuiti ESR to wrap a 2m long bar in was unavailable (and not viable for a full scale calorimeter production) therefore it was not tested for the calorimeter bar design. ReflechTech ESR has a much more reasonable price of $\sim$ 120 USD for a 1m $\times$60m roll and is marketed for massive solar reflector applications. Despite the price difference measurements confirm that ReflechTech's ESR has a reflectance similar to that of Vikuiti. ReflechTech ESR was used for testing of the calorimeter bar design.

Chapter 11

The Calorimeter R&D Setup

The "bar" calorimeter test-bench has been designed to carry out energy and time resolution measurements of a full scintillator bar unit, with the possibility of testing the bar both horizontally and vertically (as it would be positioned in SuperNEMO). The energy and time resolution measurements are carried out by exciting the scintillator with a flux of monochromatic electrons of a known energy and fitting the resulting distributions. The monochromatic electron source approximates the delta function and any smearing of the distributions that is seen is due to the light collection properties of the calorimeter unit. PMT gain is characterised using the single photo-electron (1^{st}-PE) method [158, 159].

11.1 The Monochromatic Electron Source

Two different electron sources are used for resolution measurements. The first, and more discussed in this thesis, is a ^{207}Bi source, which is cheap and simple to implement in an experimental setup as the 976keV K-shell conversion electron (CE) is used. However, as the fitting function for ^{207}Bi needs to incorporate a convolution of X-rays, γs, L-shell and M-shell CEs the extraction of the energy resolution is complex. The second electron source is a ^{90}Sr β beam passed through a magnetic field to select monochromatic electrons of known energy. The spectrum obtained from the beam can easily be fitted with a Gaussian function, however is more difficult to set up, expensive and relatively large. Both methods have been used to cross check the energy resolution measurements acquired and have been found to be consistent (Section 12.2).

11.2 The Data Acquisition System

The data acquisition system (DAQ) uses two standards - the Nuclear Instrumentation Module (NIM) standard and the Computer Automated Measurement and Control (CAMAC) standard. The NIM standard is used for signal discrimination and logic electronics and the CAMAC standard is used for collection of the signals (with an Analog-to-Digital Converter (ADC) and a Time-to-Digital Converter (TDC)) and for computer communication.

Two modes of operation are used with the DAQ - one to obtain a measurement of the leakage currents of the PMTs and any background noise coming from the electronics, known as a pedestal run, and one to obtain the energy and time resolution measurements (collected simultaneously) of the scintillator bar unit. When collecting energy and time resolution measurements the two PMT signals are sent to a pre-amp to amplify the signal (with identical length LEMO cables for the two signals used throughout the DAQ to ensure there is no time difference between the two PMT signals introduced by the electronics) and then to a 50 Ω passive splitter, dividing the signal in two.

One half of the split signals goes to the charge integration ADC - a 2249W LeCroy 12 channel, 11-bit unit, with an input sensitivity of 0.25 pC (pico Coulombs) per count and a dynamic range of $\sim$ 500 pC (bins $>$ 1980 are overflow). This unit allows operation at wide gates (30 ns - 10 μs) and has been optimised for linearity and stability.

The other half of the split signal goes to a leading edge discriminator, creating pulses used to trigger the TDC and gated ADC (after passing through a further chain of electronics, described below) and for collection of signals by the time integration TDC. The TDC unit used, LeCroy 2228A (or 2228) is an 11 bit unit with 8 channels, each of which measures the time from a leading edge of a common start pulse to the leading edge of individual stop pulses. The TDC resolution is 55 ps (or 100 ps for the 2228 module), as confirmed by measurements. The two discriminator pulses have an equal delay on them (not delayed beyond the range of the TDC) and are used as the individual stops for the TDC.

The discriminator pulse used for the gate triggering has to be in coincidence with the "Not Busy" logic (generated by the Out Register once an event is read in). This then activates pulses from the coincidence unit. One of these is used to activate the gate generating unit (CAEN 2255A), which creates a pulse with a predefined width (tuned

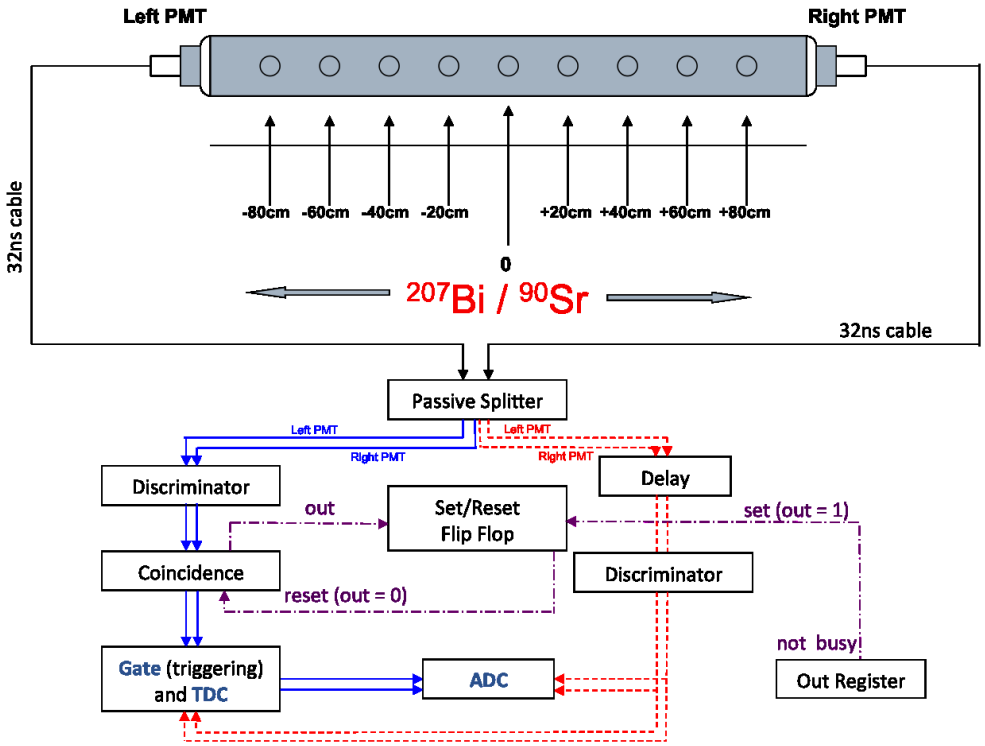

Figure 11.1: The data acquisition system (DAQ) for scintillator bars. The dashed red lines show the unaltered collected signal, the solid blue lines show the electronics logic and the dashed and dotted purple lines show the set-reset flip-flop loop.

to the TDC range) and is used as the integration gate for the TDC common start.

The other coincidence pulse is used to activate the ADC gate. A CERN N7337 set-reset flip-flop is used to interpret the "Busy" or "Not Busy" signals from the Out Register, which then provides the coincidence unit with the corresponding logic signal.

When a pedestal run is being obtained the triggering signal from a pulse generator is sent directly to the discriminator unit, after which the chain of events remains identical.

Block diagrams of the entire DAQ system and the TDC acquisition system can be seen in Figures 11.1 and 11.2 respectively.

11.3 The ^{207}Bi Technique

11.3.1 ^{207}Bi Decay Scheme

Using ^{207}Bi is a cheap and compact way to acquire energy and time resolution measurements of the scintillator bar unit. However, the fitting method for ^{207} Bi is complex

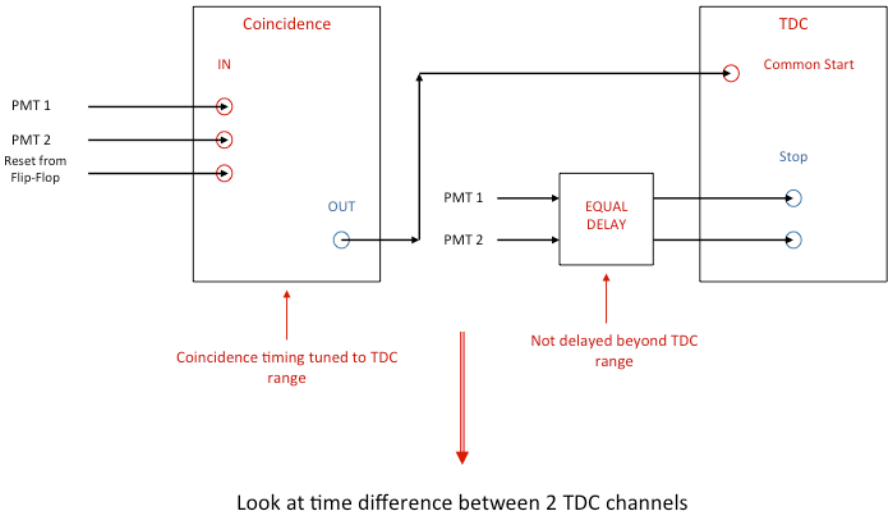

Figure 11.2: The TDC data acquisition system (DAQ) for scintillator bars.

due to its decay scheme (Figure 11.3).

When considering the ^{207}Bi decay chain, the ^{207}Bi captures one of its shell electrons and decays to an excited state of ^{207}Pb via a process known as electron capture (Section 3.1). The ^{207}Pb is left in an excited state. In order to get back to the ground state it de-excites via two γ emissions of 1064 and 570keV (which have a conversion efficiency of $\sim 7\%$). Due to the overlap of the electron and nucleus wave functions there is a small probability of the electron being found within the nucleus meaning the excited nucleus has some probability to transfer the energy to that electron. Therefore there is a chance that instead of a γ emission process the ^{207}Pb de-excites via a conversion electron process at 976keV (which produces the mono-chromatic 976keV K-shell conversion electron used as the source for testing). This process will almost always be accompanied by a $\sim$ 570keV γ (unless this also occurs via electron conversion, which has a small probability of happening). As this process is simultaneous the acquired bismuth spectrum gets broadened, therefore worsening the resolution. The large γ background, which is more noticeable in the long geometry of the bar, also contributes to worsening the resolution. At the same time, when the ^{207}Bi captures an electron to decay to ^{207}Pb, it is left with a "hole" in the atomic shell and its remaining electrons cascade down to lower orbits to fill it, emitting an X-ray of $\sim$ 15-30keV.

Therefore a "pile up" effect becomes apparent as the 976keV conversion electron is always accompanied by a 570keV γ and a 15-30keV X-ray. Due to the solid angle

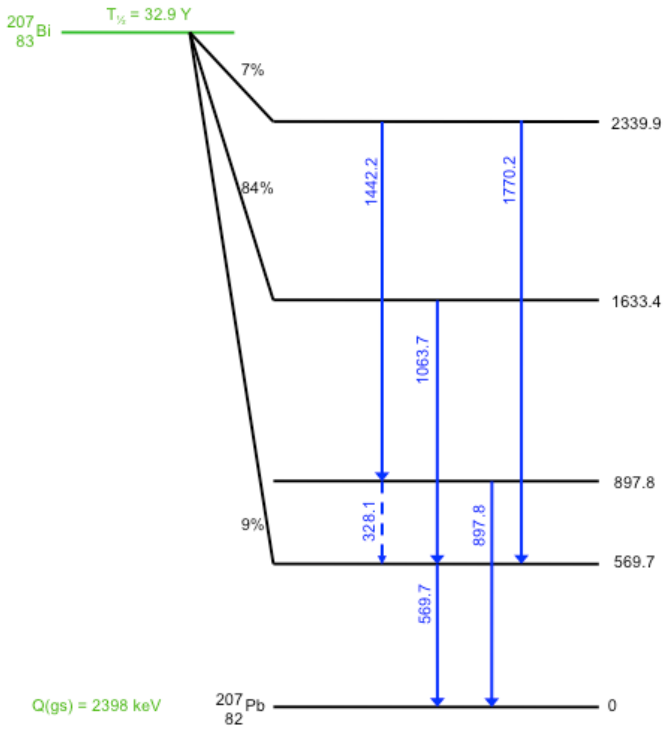

Figure 11.3: ^{207}Bi decay scheme, showing the excited states of ^{207}Pb and the corresponding de-excitation transitions. The γ transitions are indicated in blue.

in the geometry of the bar testing these γs and X-rays are more likely to be picked up by the scintillator. This means that the fitting method for ^{207}Bi has to take this into account with a convolution of K-shell, L-shell and M-shell conversion electrons, γs and X-rays (Section 11.3.3). The energy resolution is also worsened by electron energy loss through ionization in the air and the reflective material wrapped around the scintillator (according to the Landau distribution), which smears the energy spectrum. This must also be considered in the fitting method.

11.3.2 Acquiring the Data

To acquire the data for the scintillator bar characterisation the bar is placed (on metal supports, in order to avoid having the bar entirely lying down on a surface) inside a wooden light tight box. The box allows access for LEMO and High Voltage (HV) cables to the two PMTs and contains a support structure to hold the PMTs in place (Figures 11.4(a) and 11.4(b)).

The data are acquired in the following way. The ^{207}Bi source is placed directly onto the bar and scanned at up to nine points across it (-80cm, -60cm, -40cm, -20cm,

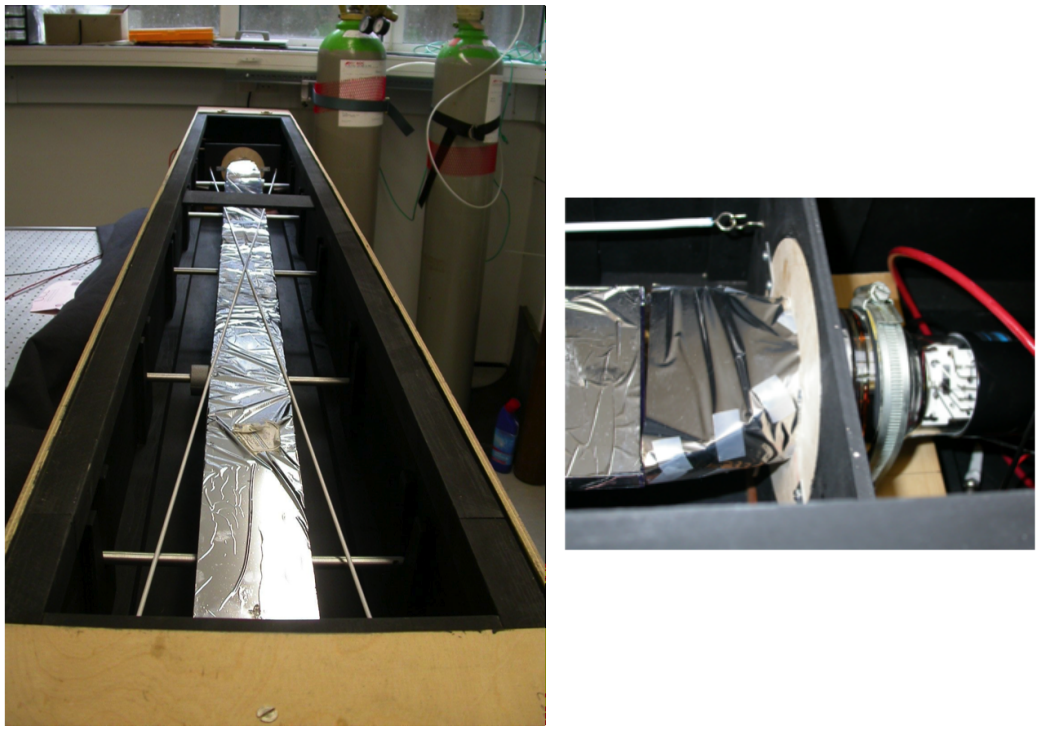

(a) The light tight box containing the scintillator bar setup (b) The PMT support structure inside the box

Figure 11.4: Scintillator bar setup, showing the light tight black box containing the scintillator bar setup (a), where you can see the support structure for the bar and the PMTs (using wires to ensure good optical contact between the PMTs and the scintillator) and the scintillator bar wrapped in Mylar. The PMT support structure can be seen in (b), with a light-guide connecting the PMT and the scintillator bar.

0cm, +20cm, +40cm, +60cm and +80cm, where 0cm marks the centre of the bar). Six runs are required to be taken at each point being measured. A background run is first carried out in order to subtract any cosmic muons, which could contribute to the energy resolution of the bar due to its large geometry (this problem would be avoided for SuperNEMO due to its location in an underground laboratory, shielding it from the muons). The second run is taken with the ^{207}Bi source to acquire a full ^{207}Bi spectrum. The third run is taken with a 2mm thick aluminium disk placed between the source and the scintillator, which filters the conversion electrons, producing a spectrum of only the γs of the ^{207}Bi. The full and γ spectra are required for the fit parametrisation. Before each of the three runs is taken a pedestal run must be taken to measure any electronics noise produced by the system (estimated by the σ of the pedestal run). The mean value

of the pedestal run is then subtracted from the relevant run. An example of the obtained ADC spectra can be seen in Figure 11.5, which shows the individual and summed PMT spectra with and without the filter for the ^{207}Bi runs and the spectra for the background run.

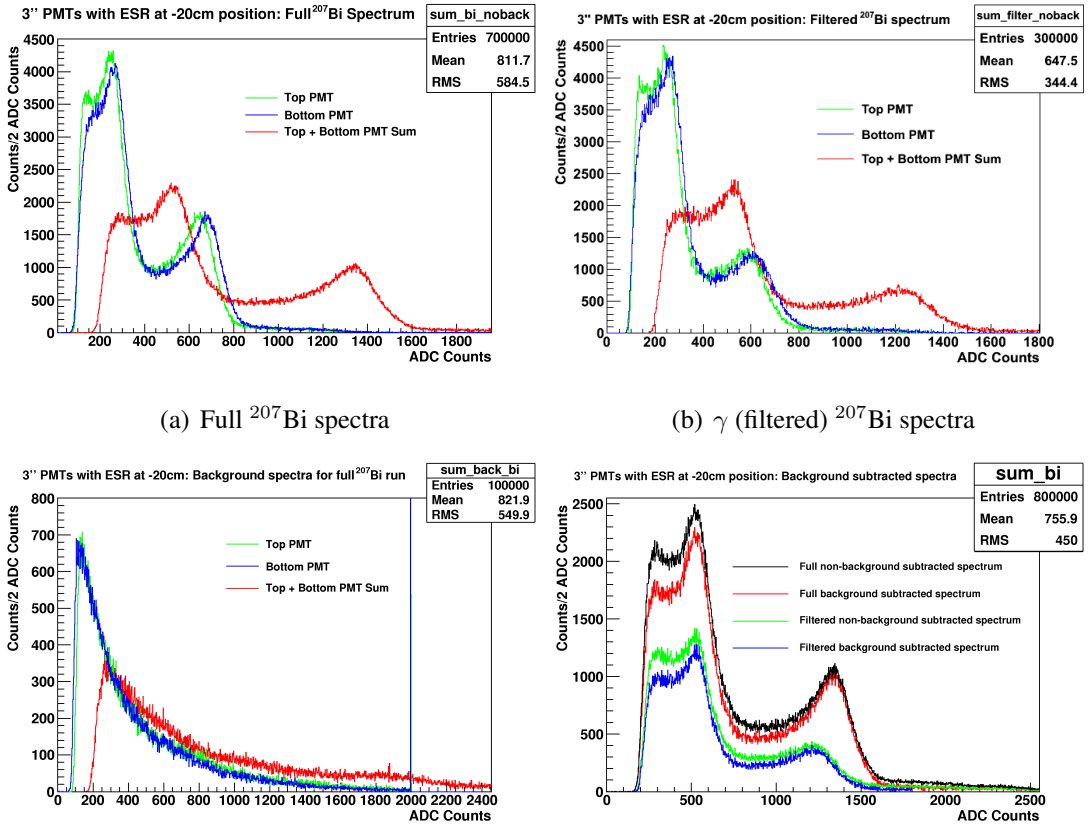

(a) Full ^{207}Bi spectra

(b) γ (filtered) ^{207}Bi spectra

(c) Background spectra

(d) Summed background subtracted spectra

Figure 11.5: ADC spectra obtained with ^{207}Bi for the scintillator bar setup, with the bar in a vertical position, wrapped in ESR and the ^{207}Bi source at the -20cm position. The individual PMT spectra (for the "top" and "bottom" PMTs) and the summed spectra are shown for (a) the full ^{207}Bi run, (b) the filtered ^{207}Bi run (showing γs only) and (c) the background run. The effect of background subtraction can be seen on the summed PMT spectra for the full and filtered runs in (d).

11.3.3 Analysis Procedure and Parametrisation of the ^{207}Bi Energy Spectrum

To increase the light collection and improve the resolution the data acquired from each PMT at the ends of the bar is summed. As it is possible that the two PMTs used have

slightly different gains, it is important to normalise the data before adding the spectra. This is done individually for the spectra of each PMT. The full and filtered (γ only) spectra are normalised to each other and background subtracted. The filtered spectrum is then subtracted from the full spectrum to obtain the ^{207}Bi conversion electron spectrum. The subtracted electron only spectrum can be used to obtain a cross check of the energy resolution measured. The main method, described below, uses the full and filtered spectra to obtain a fit to the data. However, a complicated analytical function (Equation 11.3.8) is required for this. The electron only spectrum can be fitted with a simpler triple Gaussian function of the K, L and M-shell electrons of the 976keV peak (Equation 11.3.6) to obtain the energy resolution.

Figure 11.6 show the normalised full and filtered spectrum together and the conversion electron spectrum after the subtraction. A deficit of events is seen in the subtracted spectrum at lower energies (at ADC bin $\sim$ 400, labelled (1) in Figure 11.6(b)). This deficit can also be seen in simulations (Section 11.3.4). A speculative explanation for this could be due to the conversion electron decay from the excited state of ^{207}Pb always being accompanied by a 570keV γ. As the scintillator bar used for testing is 1.25 - 2.5cm thick and has a low Z there is a large probability that this γ will not interact as there is not enough material. When an aluminium filter disk is introduced the γ from the source interacts with the aluminium, most likely by Compton scattering, producing a low energy electron which then interacts in the scintillator. The aluminium filter therefore acts as a γ to electron converter, creating a surplus of events when the filter is used. A surplus of events is seen in the subtracted spectrum at ADC bin $\sim$ 200 (labelled (2) in Figure 11.6(b)). This can be explained by the 15-30keV X-rays accompanying the ^{207}Bi electron capture. These X-rays are absorbed by the 2mm thick aluminium disk and are therefore not seen in the filtered spectrum.

Once the required data has been obtained and processed as described above it is ready to be used for the ^{207}Bi parametrisation, which is an analytical method where a function is fitted to the shape of the ^{207}Bi energy spectra. The fit works in the following way. At first the two γ lines (at 1.06MeV and 570keV) of the filtered ^{207}Bi are fitted with a Compton edge, which is the maximum energy the γ can transfer to an electron inside the scintillator before escaping, described by a variation of the Heaviside step function

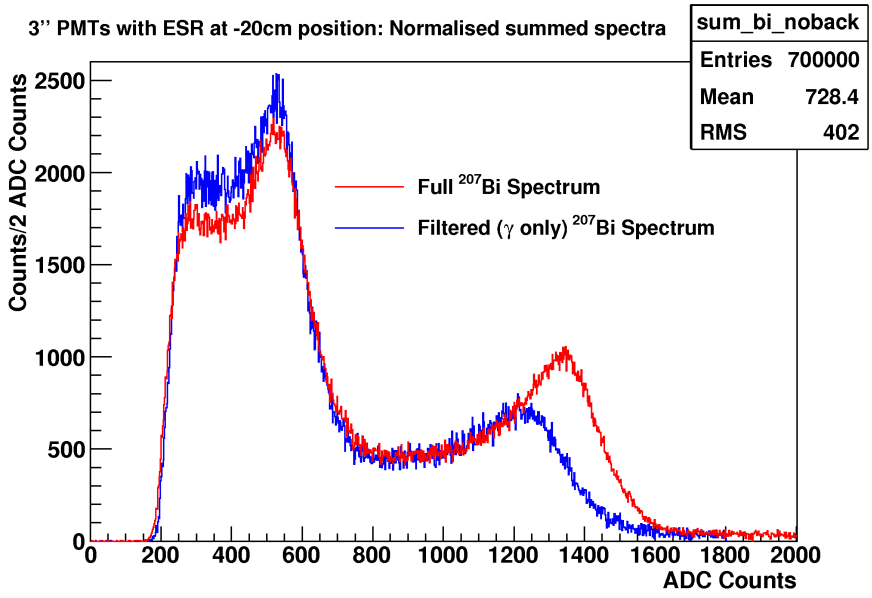

(a) Full and filtered (γ only) normalised ^{207}Bi spectra

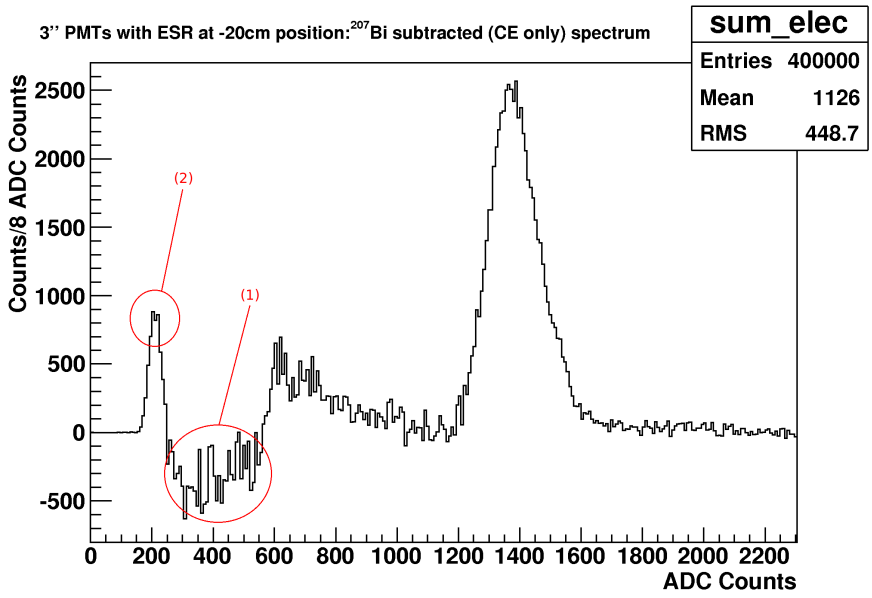

(b) Conversion electron only ^{207}Bi spectrum

Figure 11.6: Normalised full and filtered (γ only) ^{207}Bi spectra (shown in a) and subtracted ^{207}Bi spectrum, showing conversion electrons only (shown in b) for the bar in a vertical position, wrapped in ESR and with the source placed at the -20cm position. In (b) - (1) shows a deficit of events and (2) shows a surplus of events in the subtracted spectrum caused by the introduction of the aluminium filter to obtain a γ only run (see text for details).

$$\frac{1+e^{-C_1 x}}{1+e^{(C_2-x)/C_3}}, \tag{11.3.1}$$

where C_2 is the approximate energy of the Compton edge and x is the corresponding ADC bin number. C_1, C_2 and C_3 are free parameters of the function for each Compton edge. The parameters are obtained from the fit to the γ only spectrum and are then fixed for the fit to the full spectrum. The full ^{207}Bi spectrum is described by a combination of two triple Gaussian fits (for the K, L and M shell electrons of the 482keV and 976keV conversion electrons) and gamma lines. The conversion electrons are each described by a triple Gaussian distribution, where a Gaussian distribution is defined as

$$G(\mu,\sigma) \equiv \frac{1}{\sigma\sqrt{2\pi}} \cdot e^{\left(\frac{-(x-\mu)^2}{2\sigma^2}\right)}, \tag{11.3.2}$$

where μ is the mean of the distribution, σ is the σ of the Gaussian distribution and x is the corresponding ADC bin number. The L and M-shell Gaussian functions are set to be dependent on the K-shell parameters in order to reduce the number of free parameters in the fit. The number of photo-electrons, N_{pe}, can be approximated by

$$N_{pe} \approx \left(\frac{\mu}{\sigma}\right)^2, \tag{11.3.3}$$

assuming $N_{pe} > 20$. From this it can be seen that energy (and time) resolution changes as a function of square root. Therefore,

$$\sigma^{'} = \sigma\sqrt{1+\frac{E\alpha}{\mu}}, \tag{11.3.4}$$

can be used to express the resolution of the K, L and M-shell electrons, where α is the ADC calibration constant,

$$\alpha = \frac{\text{976keV peak position in ADC - 482keV peak position in ADC}}{976\text{keV} - 482\text{keV}}. \tag{11.3.5}$$

The triple Gaussian of the K, L and M-shell electrons is then given by

Transition	Shell	Relative Intensity (%)
482keV	K-shell	1.52
554keV	L-shell	0.44
566keV	M-shell	0.15
976keV	K-shell	7.03
1048keV	L-shell	1.84
1060keV	M-shell	0.54

Table 11.1: Relative intensities of the 482keV and 976keV conversion electron transitions [124].

$$I_1 G(\mu_K, \sigma_K) + I_2 G\left(\mu_K + E_{KL}\alpha, \sigma_K\sqrt{1+\frac{E_{KL}\alpha}{\mu_K}}\right) + I_3 G\left(\mu_K + E_{KM}\alpha, \sigma_K\sqrt{1+\frac{E_{KM}\alpha}{\mu_K}}\right), \quad (11.3.6)$$

where I_1, I_2 and I_3 are the known K, L and M-shell transition intensities for the 482keV and 976keV conversion electrons, shown in Table 11.1. The μ_K, σ_K and α factors are free parameters of the fit and x is the corresponding ADC bin number; μ_K and σ_K are the mean and σ of the K-shell conversion electron; E_{KL} and E_{KM} are the known energy differences between the K-L and K-M shells [124].

As an example the function of the 976keV conversion electron is

$$7.03 \cdot G(\mu_K, \sigma_K) + 1.84 \cdot G\left(\mu_K + 72.1\alpha, \sigma_K\sqrt{1+\frac{72.1\alpha}{\mu_K}}\right) + 0.545 \cdot G\left(\mu_K + 84.1\alpha, \sigma_K\sqrt{1+\frac{84.1\alpha}{\mu_K}}\right) \quad (11.3.7)$$

To summarise, the analytical description of ^{207}Bi is achieved with two Compton edges at 1.06MeV and 0.57MeV and two triple Gaussians for the conversion electrons at 482keV and 976keV:

$$GC(570keV) + CE(482keV) + GC(1060keV) + GE(976keV), \quad (11.3.8)$$

where GC(keV) is the function described in Equation 11.3.1 and CE(keV) is the function described in Equation 11.3.6.

An example of the fitting procedure for the γ only spectrum and the full ^{207}Bi spectrum can be seen in Figure 11.7.

The energy resolution is then extracted from the μ and σ returned by the fit, using Equation 10.1.1.

11.3.4 Validation of the ^{207}Bi Fit

In order to test the validity of the fitting method the fitting procedure is applied to simulated ^{207}Bi spectra. ^{207}Bi events are generated with GEANT-3.21 [115] used for the geometry description of the calorimeter and GENBB [114] used for the ^{207}Bi decay kinematics description. Parameters such as the geometry of the scintillator and the distance between the source and the scintillator are user defined. The energy resolution for which the simulation is run is also user defined, by providing the number of photo-electrons that the PMT sees (using Equation 10.1.1 to convert the number of photo-electrons into energy resolution). Effects such as gamma interaction rates, pile up, Landau energy losses of the electrons and edge effects (when an electron passing through the edge of the scintillator only deposits part of its energy) are taken into account in the physics description of the decay, therefore by fitting the simulated MC with the analytical ^{207}Bi function an estimate of these effects can be obtained by comparing the obtained energy resolution with the user defined MC truth.

In order to see how much pile up (and other effects) affects the scintillator bar geometry compared to that of a small scintillator block (which better tests the analytical fit function due to its smaller surface area, reducing γ interaction rates and pile up) two geometries were studied: a scintillator bar (2m x 10cm x 1.25cm) with the source placed directly on the bar and a small scintillator block (5cm x 5cm x 2cm) with a 6cm air gap between the source and the block. As the fit used on the data fits the filtered γ only spectrum and then applies the obtained parameters to the full spectrum the 2mm aluminium disk must also be included in the simulations, and two simulated "runs" must be acquired - with and without the electron filter. The simulations were run for four different light outputs: 1000, 800, 600 and 400 photo-electrons. Figure 11.8 shows the spectra obtained for the block and the bar setups with and without the aluminium

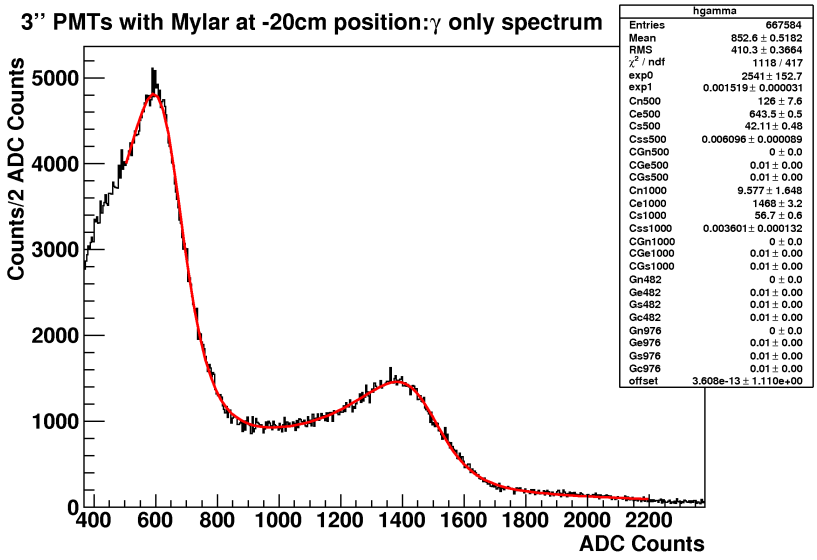

(a) Filtered (γ only) ^{207}Bi spectrum fit

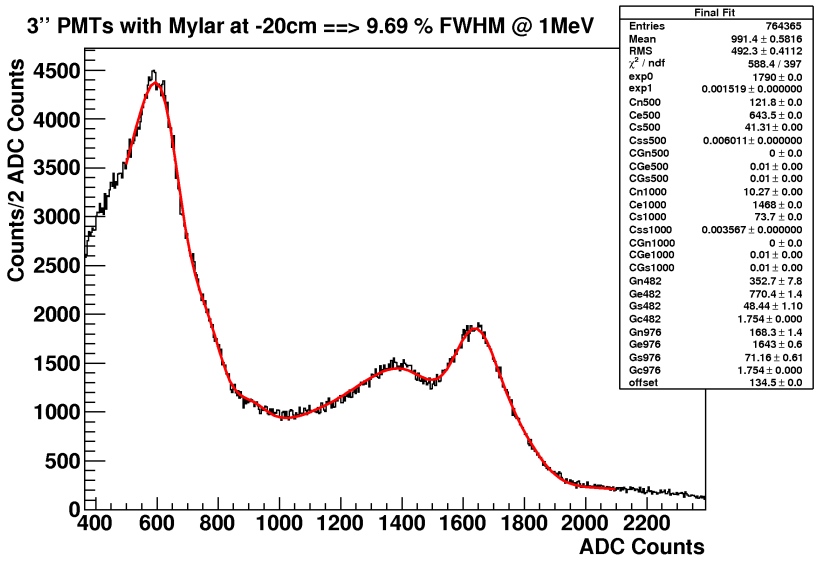

(b) Full ^{207}Bi spectrum fit

Figure 11.7: An example of the fitting procedure used for ^{207}Bi, for the bar in a vertical position, wrapped in Mylar and with the source at the -20 cm position, with the γ only spectrum fit (a) and the full ^{207}Bi fit (b) shown. The parameters obtained from the fit are $\mu = 623.2$ and $\sigma = 311.2$, giving an energy resolution of 9.9% at 1MeV.

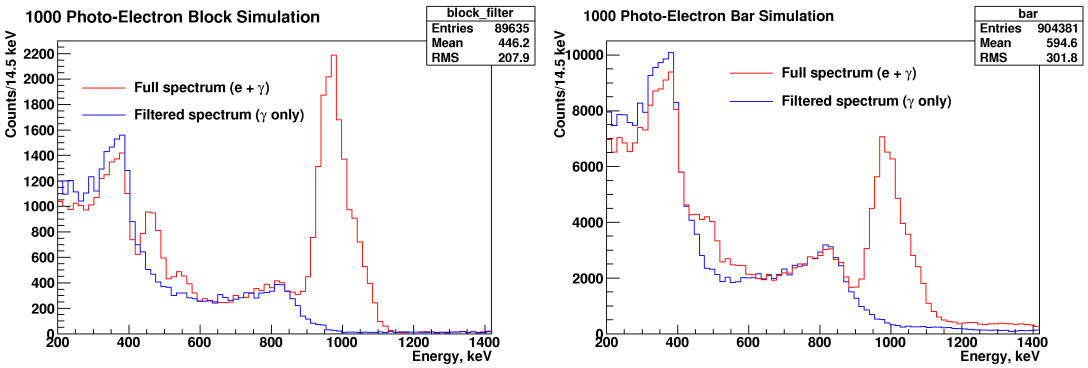

(a) 5cm x 5cm x 2cm Block

(b) 2m x 10cm x 1.25 cm Bar

Figure 11.8: Simulated MC truth of 7.3% FWHM at 1MeV for a 5cm x 5cm x 2cm block (a) and a 2m x 10cm x 1.25cm bar (b) showing the full and filtered ^{207}Bi spectra.

disk filter for a 1000 photo-electron output (corresponding to an energy resolution of 7.3% FWHM at 1MeV). It can be seen that the peak in the bar simulations is more smeared than in the block simulations, showing that the pile up effect is greater for the bar setup than for a block, as expected.

The results obtained for the light outputs tested can be seen in Table 11.2, showing the differences between the simulated and reconstructed energy resolutions for the block and the bar setups. For photo-electron outputs of 1000, 800 and 600 the block setup resolution remains a $\sim$ constant 0.3% away from MC truth, whilst the bar setup resolution is a $\sim$ constant 0.6% away from MC truth. For a lower light output of 400 photo-electrons the difference between the energy resolution returned by the fit and the MC truth increases, showing the effect is larger for lower light outputs.

A systematic error on the measured energy resolution is estimated by varying the initial parameters (and their limits) provided for the ^{207}Bi fit. This contributes $\pm 0.4\%$ to the systematic error. Another measurement of the systematic error was made by acquiring multiple measurements of the same point on the bar made under identical conditions for various setups. The measured resolution for these points was consistent with the systematic error of $\pm 0.4\%$. A further contribution is estimated by looking at differences between MC truth set in simulations and the energy resolution measured by the fit, as described above. Simulations were carried out for a 2m x 10cm x 2.54cm bar (more widely used in the calorimeter unit tests) for a range of energy resolutions (8 - 12%) relevant to the results obtained with the scintillator bar setup. Table 11.3

Light Output (N_{pe})	MC Truth $\frac{\Delta E}{E}$ (%)	Block Reconstructed $\frac{\Delta E}{E}$ (%)	Diff.	Bar Reconstructed $\frac{\Delta E}{E}$ (%)	Diff.
1000	7.3	7.6	-0.3	7.9	-0.6
800	8.2	8.5	-0.3	8.7	-0.5
600	9.5	9.8	-0.3	10.1	-0.6
400	11.6	12.3	-0.7	12.5	-0.9

Table 11.2: Comparison of the simulated energy resolution (FWHM at 1MeV) to the energy resolution extracted with the analytical ^{207}Bi fit extrapolated to 1MeV, for a 5cm x 5cm x 2cm block geometry and a 2m x 10cm x 1.25cm bar geometry.

shows the differences between the simulated and measured energy resolutions, with an average systematic of -1.1%, which is implemented into the measurement as a correction to the acquired energy resolutions.

For a discussion on optimising the ^{207}Bi fit see Section 11.6 below.

11.3.5 TDC Analysis

To analyse the TDC data the time difference between the two TDC channels is looked at. The γs from ^{207}Bi contribute to the width of the TDC distribution, therefore in order to look at the true time resolution of the scintillator bar unit some of the background γs are excluded from the fit. This is achieved by selecting TDC events that fall within ± 5 ADC counts of the 976keV conversion electron peak ADC distribution as mostly electrons contribute to this peak, reducing the γ background. The difference between the two TDC channels (for the summed spectra) is then obtained and a simple Gaussian fit is used to extract the time energy resolution, σ_{time},

$$\sigma_{time} = \sigma_{fit} \cdot \text{TDC resolution (55 or 100 ps)}, \tag{11.3.9}$$

where σ_{fit} is the σ returned by the fit and is multiplied by the TDC resolution, or scale, (55 ps for the 2228A module and 100 ps for the 2228 module) depending on the TDC module used. The coincidence time resolution (CTR) is then

$$\text{CTR} = \frac{\sigma_{time}}{\sqrt{2}} \tag{11.3.10}$$

MC Truth $\frac{\Delta E}{E}$ (%)	Bar Reconstructed $\frac{\Delta E}{E}$ (%)	Difference
8.0	8.7	-0.7
9.0	10.3	-1.3
9.5	10.8	-1.3
10.0	11.1	-1.1
10.5	11.5	-1.0
11.0	12.1	-1.1
11.5	12.7	-1.2
12.0	13.1	-1.1

Table 11.3: Comparison of the simulated energy resolution (FWHM at 1MeV) to the energy resolution extracted with the analytical ^{207}Bi fit extrapolated to 1MeV, for a 2m x 10cm x 2.54cm bar geometry.

Figure 11.9 shows an example of an ADC selected TDC time difference spectrum with a Gaussian fit.

11.4 The ^{90}Sr Technique

SuperNEMO collaborators at CENBG (Centre d'Etudes Nucláires de Bordeaux Gradignan) focus on R&D using Photonis PMTs (Section 10.2) with a mono-chromatic electron test beam of ^{90}Sr. The beam is produced by a spectrometer, which uses the momentum created by a magnetic field to select the βs from the continuous ^{90}Sr energy spectrum. The test beam has a range of 0.4 - 2.0MeV, allowing the user to select the energy of the beam to be supplied to the calorimeter unit. The injection energy precision of the beam is $\pm 1\%$, determined by the physical diameter of the beam aperture and the resolution of the silicon detector used for the calibration.

The data acquisition and analysis pre-processing when using a ^{90}Sr source are identical to those used for ^{207}Bi. Instead of using a complex fit such as for ^{207}Bi the ^{90}Sr spectrum requires a simple Gaussian fit, greatly reducing the complexity of the parametrisation.

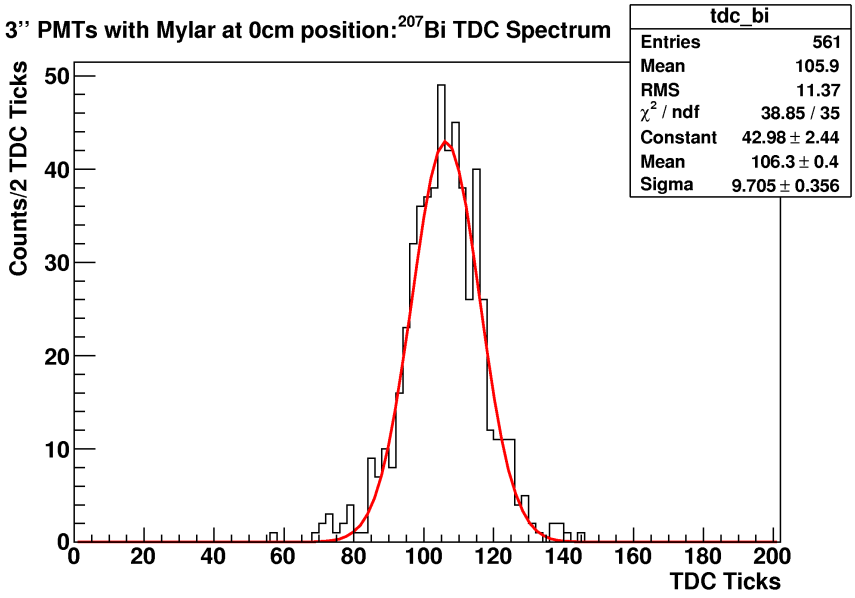

Figure 11.9: An example of an ADC selected (within ± 5 of the 976keV peak) TDC time difference spectrum for ^{207}Bi with a Gaussian fit, with a time resolution (σ_{time}) of 534 ps and a coincidence time resolution of 378 ps, for the bar in a vertical position, wrapped in Mylar and with the source at the 0cm position.

11.5 PMT Gain Measurement

In order to obtain accurate results for energy and time resolution measurements, the two PMTs used to obtain the measurements must be run with the same gain, requiring them to be gain calibrated. The 1^{st}-PE method [158, 159] is used to measure the gain of the 3" Hamamatsu R6223-100S PMTs.

The gain, g_i, between two dynodes, d_i and d_{i-1}, is proportional to the difference in the voltage applied to them multiplied by the secondary emission coefficient, δ_i:

$$g_i = \epsilon_{i-1}\delta_i\epsilon_i V_i^{\alpha}, \tag{11.5.1}$$

where ϵ_i and ϵ_{i-1} are the collection efficiencies of the dynodes d_i and d_{i-1} and α is a constant usually in the range 0.6 - 0.8.

The absolute gain of the PMT, G_{PMT}, is extracted with the pedestal-subtracted first photo-electron peak position, 1PE_{ADC}, in ADC bins:

$$G_{PMT} = (1\text{PE} - \text{pedestal})_{ADC} \left(\frac{\text{ADC}_{LSB}(C)}{e^-_{charge}(C)} \right), \tag{11.5.2}$$

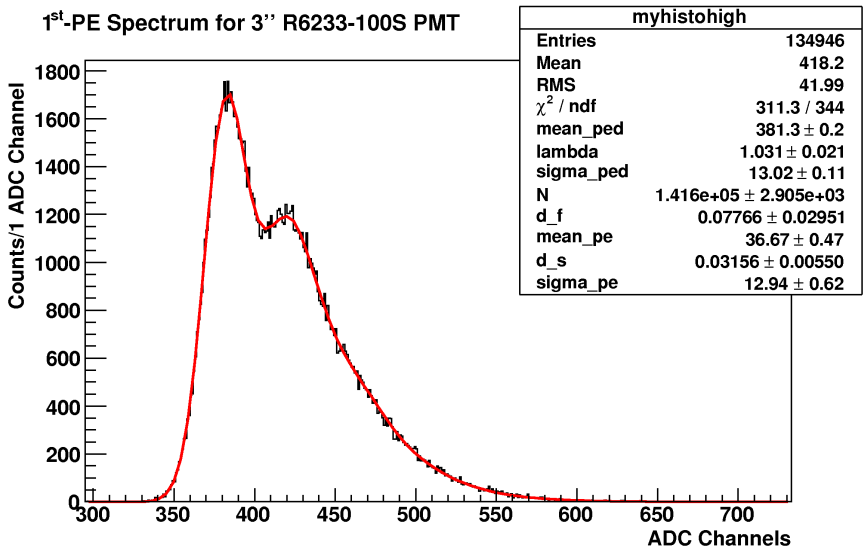

Figure 11.10: An example of a 1^{st}-PE spectrum for a 3" Hamamatsu R6223-100S PMT at 1400V with the fit to the data shown.

where pedestal$_{ADC}$ is the value of the pedestal position in ADC counts and ADC$_{LSB}$ (the least significant bit of the ADC = 0.25fC) is the value required to transform the ADC bin value into a charge.

The data for the gain measurement is acquired by shining a light emitting diode (LED) directly onto the PMT. Once the 1^{st}-PE spectrum is obtained it is then fit with the analytical function described in [158]. An example of a 1^{st}-PE spectrum and its fit is shown in Figure 11.10 for a 3" Hamamatsu R6223-100S PMT. The first peak corresponds to the pedestal at bin 381, the second peak is that of the 1^{st}-PE at bin 420 and the tail of the distribution is the sum of the higher-order overlapping photo-electron peaks.

A number of measurements are carried out at different HVs and the gain is then extracted from the data using Equation 11.5.2, producing a characteristic gain curve of the PMT. Figure 11.11 shows the gain curves obtained for the two 3" Hamamatsu R6223-100S PMTs used for scintillator bar testing, tested up to 1500V (the maximum voltage that can be applied to the PMTs). The measured curves are consistent with Hamamatsu's expectation of $\sim 2.3 \times 10^5$ (Table 10.1) and can be used to gain equalise the two PMTs used.

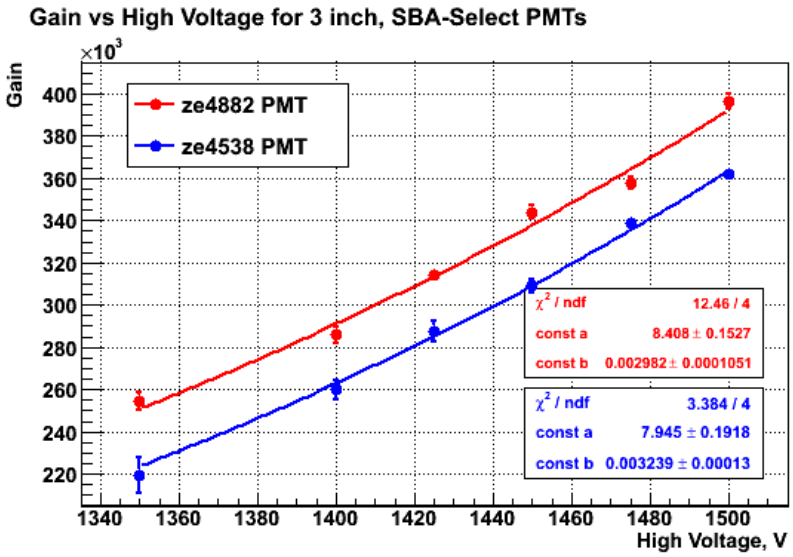

Figure 11.11: Gain curves for the 3" Hamamatsu R6223-100S PMTs at 1350 - 1500 volts.

11.6 Discussion

It is difficult to parametrise the effects of pile up and multi-Compton scattering, which are of particular concern to the scintillator bar setup due to the bar's large geometry, in the function used to fit the ^{207}Bi. There are a number of possible solutions to the pile up problem, some of which have been investigated.

The source could be lifted from the bar to create an air gap between the source and the scintillator so that the 570keV γ has more of a chance of escaping and not interacting in the bar. However, this was not found to improve the energy resolution and greatly worsened the time resolution (due to the large solid angle illuminated by the source, created when the source is lifted, contributing to the width of the TDC distribution, Section 12.2).

Using some sort of lead shielding to stop the γs could be considered, however this would be heavy, bulky and difficult to implement in the setup as there is limited space available inside the black box that contains the bar setup.

The most logical solution is to create a "look up table" by running simulations for the bar setup at energy resolutions of 0.1% intervals to reproduce all possible resolutions that can be obtained with the bar setup. However, before this can be done a more accurate description of the bar setup needs to be implemented into the simulations, in particular the physics of the pile-up caused by the 570keV γ and 15-30keV X-rays must

be well described. Once the simulations with the full physics descriptions have been carried out the data spectrum can then be fitted to the generated MC spectra from the look up table, using a Kolmogorov-Smirnov (K-S) test [160] or similar to determine the goodness of the fit and find the best simulated resolution to match the data. As the pile up effects wuld be included in the simulations this would mean that it would no longer affect the energy resolution measurements, allowing a more accurate measurement of the energy resolution of the setup to be made. Another advantage of this method is that the data would only have to be acquired with the full ^{207}Bi spectrum, reducing the time required to collect data and minimising any human error introduced when replacing the source with the filter.

Chapter 12

Energy and Time Resolution Measurements

Many different configurations of the bar calorimeter unit were considered and tested, with the parameters of the configurations tested summarised in Table 12.1.

Parameter	Options Tested	
Photo-multipliers	ETL, Hamamatsu and Photonis	Table 10.1
Scintillators	Bicron (BC-408) and Eljen (EJ-200)	Table 10.2
Scintillator shapes	1 of 200cm x 10cm x 1.25cm, 2 of 200cm x 10cm x 2.54cm (with ends tapered to 6.5cm at 45° angle) and 1 of 200cm x 10cm x 10cm (with ends tapered to a 6.8cm ⌀ circle at 70° angle)	
Optical couplings	Bicron BC-630 gel	Table 10.3
Reflective wrappings	PTFE, Al-Mylar and ESR	Table 10.4
Light-guides	With light-guide, without light-guide	

Table 12.1: Parameters of the tested bar scintillator configurations.

The measurements of the possible configurations of the scintillator bar unit are organised (by scintillator shape) into three groups:

- **Configuration 1**: Tests are carried out on the 200cm x 10cm x 1.25cm BC-408 bar. 3" PMTs are the ideal choice for a calorimeter bar design, however due to

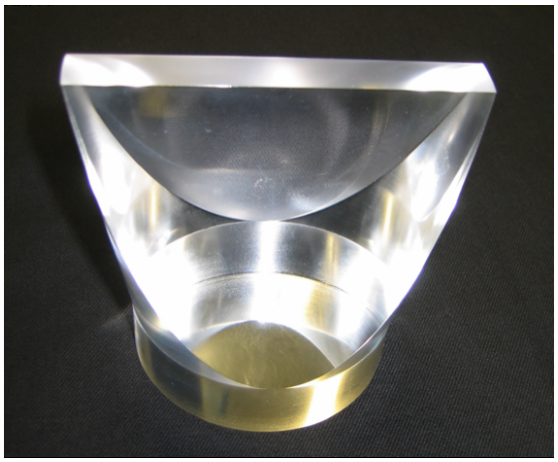

Figure 12.1: The polished PMMA light-guide used to couple a 10cm width bar to a 3" PMT.

the size of this bar when using a 3" PMT the width of the scintillator is greater than the diameter of the photo-cathode, therefore two PMMA light-guides were designed to direct the collected light from the ends of the scintillator bar to the PMTs. The light-guides (Figure 12.1) were polished by hand and coupled to the scintillator and PMT joints using optical grease in order to achieve the highest possible light collection. 5" PMTs were also tested in order to collect all of the light from the scintillator bar without using a light-guide.

- **Configuration 2**: Tests are carried out on the two 200cm x 10cm (with ends tapered to 6.5cm at 45° angles) x 2.54cm EJ-200 bars. Due to multiple optical coupling layers introduced by the light-guide the energy resolution measured in Configuration 1 is relatively poor compared to that of other setups, therefore instead of using a light-guide the scintillator bar was tapered to fit the 3" photo-cathode profile fully without any overlap.

- **Configuration 3**: Tests are carried out on the 200cm x 10cm x 10cm (with ends tapered to a 6.8cm ⌀ circle at 70° angles to fit the 3" PMT photo-cathode diameter fully without any overlap) EJ-200 bar. With a 2.54cm thick bar multiple layers of the calorimeter in a module can be used to tag the γs. However, the meausrement of internal and external backgrounds becomes very convoluted due to the layered design of the calorimeter and the small thickness of the bars, making background varification and the search of $0\nu\beta\beta$ decay to excited states complex.

PMT Size & Make	Light-guide?	Reflector	$\frac{\Delta E}{E}(\%)$	Comments
3" Ham. R6223-100S	Yes	Al-Mylar	13.5	(1)*
3" Ham. R6233-100S	No	Al-Mylar	12.7	(2)*
3" Ham. R6233-100S	No	ESR	12.9	(2)*
5" ETL 9390KB	No	ESR	13.5	

Table 12.2: Results of measurements obtained with Configuration 1. The energy resolution measurement (FWHM at 1MeV) is obtained from the sum of the PMTs. The -1.1% offset from simulations is not included and the energy resolution has a $\pm 0.4\%$ error on it (Section 11.3.4). Any comments regarding measurements can be found below in Section 12.1.

Using a 10cm thick bar would be using a geometry closer to that of the blocks used in NEMO3 (which also have a thickness of 10cm), which is tested technology for γ-tagging. Therefore a 10cm thick bar was tested to see whether a good enough energy resolution could be achieved with this setup, whilst being able to use previous experience gained from NEMO3.

12.1 Configuration 1

A summary of the measurements obtained with Configuration 1 is shown in Table 12.2, showing the parameters used in the setup (excluding the size of the scintillator, which is constant for each configuration), the results obtained and any comments on the setup and results of the tests. The BC-408 200cm x 10cm x 1.25cm scintillator bar was the first bar available for testing. All tests were carried out with the BC-630 optical gel. The TDC setup was not yet implemented at the time of these tests, therefore no TDC data are available for Configuration 1.

Optical simulations carried out with GEANT4 show that the best energy resolution should be achieved with the source positioned at the ends of the bar [161], where one of the PMTs is getting most light, whilst the worst resolution should be in the central position of the bar. The energy resolution is not expected to vary by more than $\pm \sim 0.5\%$ across the length of the bar. When analysing the spectra of the individual PMTs the energy resolution should be highest at the end where the source is placed and lowest at the end farthest away from the source. The resolutions obtained for the 5" 9390KB

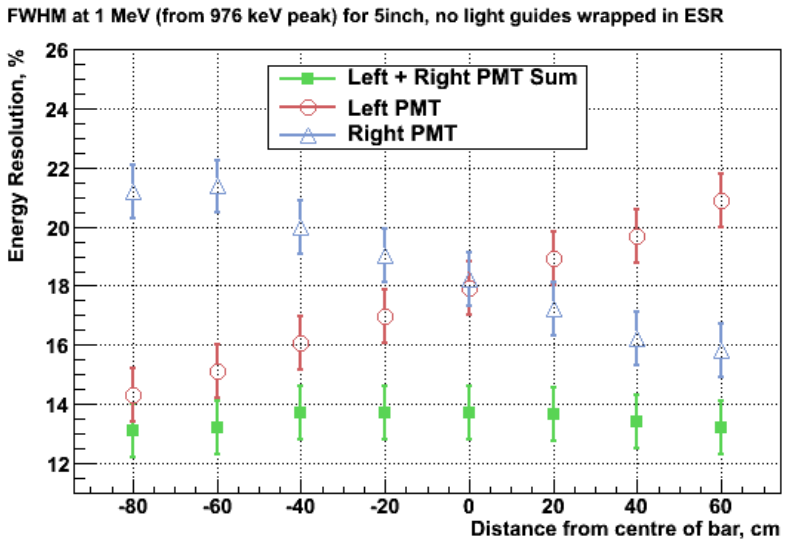

Figure 12.2: Individual and summed energy resolutions obtained for the 5" PMTs, no light-guides, ESR setup.

ETL PMTs, no light-guides, wrapped in ESR setup can be seen in Figure 12.2. The trend expected from the individual PMTs can be seen, with the resolutions being similar at the 0cm position on the bar ($\sim 18\%$ FWHM at 1MeV). The trend for the summed PMT resolution is also as expected, with the best energy resolution achieved at the -80cm and 60cm positions on the bar. The errors shown on the plot are systematic errors obtained from the fit to the generated MC. The average summed energy resolution obtained is $13.5\%^{-0.4\%}_{+0.2\%}$ FWHM at 1MeV, with the errors taken from the best (13.1% FWHM at 1MeV) and worst (13.7% FWHM at 1MeV) energy resolutions obtained.

Comment (1)*: For all of the measurements in Table 12.2 a small aluminium box was placed around the source when collecting data, to filter any electrons being emitted into the northern hemisphere of the setup, which could contribute to the energy resolution width by making false deposits in the scintillator. The aluminium box was not used for the first setup (3" Hamamatsu R6233-100S PMTs, with light-guides, with the scintillator wrapped in Al-Mylar). To estimate whether the aluminium box shield improved the energy resolution a measurement was carried out at the 60cm position on the bar using identical setups with and without the box. The energy resolution with using the box was measured to be 12.6% FWHM at 1MeV, and the energy resolution without using the box 13.0%. Some improvement is seen in the energy resolution, however only one point was tested due to time constraints, therefore a more accurate

estimate cannot be made.

Comment (2)*: As ESR has a higher reflectivity coefficient than Al-Mylar it is expected that a setup using ESR wrapping would give improved energy resolution results compared to a setup using Al-Mylar. In order to investigate this the light outputs of the Al-Mylar and ESR in identical setups (3" Hamamatsu PMTs without light-guides) were looked at. Figure 12.3 shows the 976keV peak position in ADC counts for the Al-Mylar and ESR setups. The light output of the Mylar setup increases at the far (80cm) end of the bar, whilst the ESR setup light output decreases at that end. A possible explanation for this is that at the far end of the bar the Al-Mylar wrapping was less tight than at the near (-80cm) end, creating an air gap between the Al-Mylar and the scintillator. Optical simulations show that a small air gap between the scintillator and the reflective material increases the light collection [145], which could be the effect seen here. However, for the ESR setup case the far end of the setup was dirty with optical grease (due to limited time available to create the setup), attracting dust and other dirt, which could worsen the light collection. At certain points, such as at -80cm, the light output of the ESR setup is $\sim 50\%$ higher than that of the Al-Mylar setup, which is expected to be seen translated into energy resolution. In order to create a uniform air gap between the bar and the reflective wrapper to exclude such uncertainties the bar setup later incorporated an "ESR Pipe" (Section 12.2) to go around the scintillator bar, keeping a constant distance between the reflective material and the scintillator throughout the length of the bar.

The best energy resolution of 12.7% FWHM at 1MeV obtained for Configuration 1 is with the 3" Hamamatsu R6233-100S PMTs, without light-guides, with the scintillator wrapped in Al-Mylar setup. Although some of the light is being lost by the PMT due to the width of the bar being larger than the diameter of the PMT this setup still provides better results than using light-guides. This is due to the amount of optical couplings introduced into the system when using the light-guides. For this reason no light-guides were used in any future setups.

12.2 Configuration 2

A summary of the measurements obtained with Configuration 2 is shown in Table 12.3, showing the parameters used in the setup, the results obtained and any comments on the

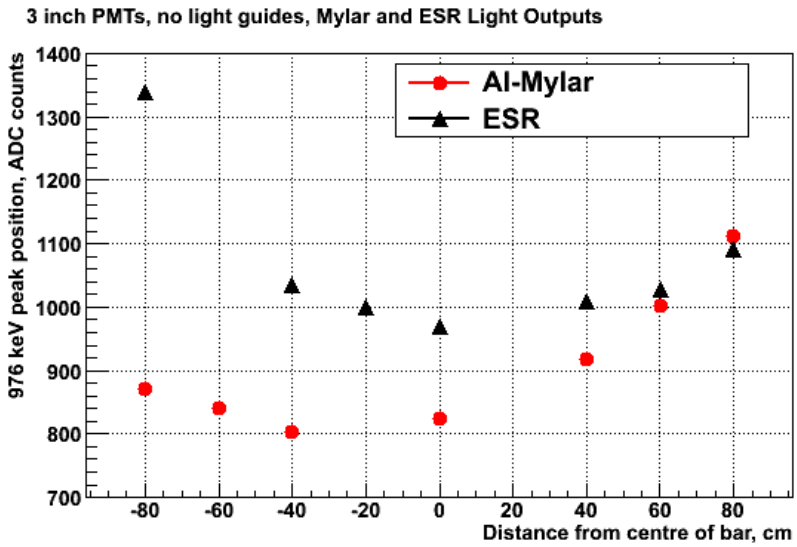

Figure 12.3: Al-Mylar vs. ESR: light outputs for the 976keV peak in ADC counts for identical setup conditions (3" PMTs, no light-guides).

setup and results of the tests. Two EJ-200 200cm x 10cm (tapered to 6.5cm) x 2.54cm bars were available for testing, referred to as Bar 1 and Bar 2. All tests were carried out with the BC-630 optical optical gel.

Comment (3)*: Using scintillator bars tapered to fit the photo-cathode of the high QE 3" PMTs is an optimised design of the scintillator bar calorimeter, as the scintillator bar fits the PMTs without any overlap. Optical simulations have shown that creating an air gap between the scintillator bar and the reflective wrapping material improves the energy resolution of the system [145] by minimising the number of surface absorptions along the bar. The larger the gap the less reflections of the light from the reflective material. In order to provide a uniform gap between the scintillator and the reflective material an "ESR Pipe" (shown in Figure 12.4) is introduced into the setup, with the scintillator centred inside a 150mm diameter plastic pipe lined with ReflechTech 100μm thick ESR (with an estimated 15-20keV energy loss through the ESR). The ESR pipe contains nine holes to allow the source access to the bar (with an air gap of $\sim$ 8.8cm). The bar is placed in a vertical orientation to test the resolution with the alignment that SuperNEMO would actually use. Aluminium face plates are introduced into the design to align the bar with the PMTs, causing some light to be reflected away from the PMTs.

Comment (4)*: The bar was brought down into a horizontal position to remove

PMT Size & Make	Bar	Source	Refl.	ESR Pipe?	$\frac{\Delta E}{E}(\%)$	CTR	C
3" H. R6223-100S	1,V	^{207}Bi	ESR	Yes	10.1	-	(3)*
3" H. R6223-100S	1,H	^{207}Bi	ESR	Yes	11.2	850 ps	(4)*
3" H. R6223-100S	1,H	^{207}Bi	PFTE	No	12.6	410 ps	(5)*
3" H. R6223-100S	1,H	^{207}Bi	-	No	13.1	523 ps	
3" H. R6223-100S	1,H	^{207}Bi	PFTE	No	12.3	431 ps	(6)*
3" H. R6223-100S	1,H	^{207}Bi	PFTE	No	12.4	417 ps	(6)*
3" H. R6233-100S	1,H	^{90}Sr	PFTE	No	11.1	464 ps	
& 3" H. R6233-100							
3" Ph. XP5312	1,H	^{90}Sr	Mylar	No	11.3	520 ps	
& 3" Ph. XP5302							
3" H. R6233-100S	1,H	^{90}Sr	Mylar	No	10.7	463 ps	(11)*
& 3" H. R6233-100							
3" H. R6233-100S	1,H	^{90}Sr	ESR	No	11.0	500 ps	
& 3" H. R6233-100							
3" H. R6233-100S	2,H	^{90}Sr	Mylar	No	9.7	448 ps	
& 3" H. R6233-100							
3" H. R6233-100S	2,H	^{207}Bi	Mylar	No	11.3	448 ps	
& 3" H. R6233-100							
3" H. R6233-100S	2,V	^{207}Bi	Mylar	No	10.3	424 ps	
& 3" H. R6233-100							

Table 12.3: Results of measurements obtained with Configuration 2. The orientation of the bar (horizontal (H) or vertical (V)) and whether Bar 1 or Bar 2 is used is indicated. The energy resolution measurement (FWHM at 1MeV) is obtained from the sum of the PMTs. The -1.1% offset from simulations is not included and the energy resolution has a $\pm 0.4\%$ error on it (Section 11.3.4). The coincidence time resolution (CTR) measurement is shown. Any comments (C) regarding measurements can be found below in Section 12.2.

(a) The “top” end (b) The “bottom” end

Figure 12.4: The 150mm ⌀ “ESR Pipe”, creating a uniform gap between the ESR and the scintillator bar, in a vertical orientation.

the face plates obstructing light in the vertical design. The average energy resolution obtained with the horizontal orientation, 11.3% FWHM at 1MeV, is $\sim 1.1\%$ worse than with the vertical orientation. This could have been caused by a problem with the optical contact in the setup. In the vertical orientation gravity helps to obtain good optical contact. To test this the scintillator and PMTs were re-gelled and put back together and two points along the bar were measured again. At -80cm the re-gelling provided an energy resolution of 11.0% (cf. 10.9% before re-gelling) and at 60cm the re-gelling provided an energy resolution of 10.4% (cf. 12.9% before re-gelling), showing that optical contact could have been the cause of the degradation. The 2228 TDC module (with 100ps resolution) was used to acquire the TDC data.

12.2.1 Time Resolution Measurements Investigation

The CTR resolution of NEMO3 is 250ps σ at 1MeV. A time resolution similar to that is desirable for the SuperNEMO calorimeter. Initial tests of the scintillator bar calorimeter unit indicated a CTR of 850ps. An in depth investigation, summarised below and in Table 12.4, was carried out in order to improve and understand what is contributing to the width of the TDC distribution. The best CTR achieved with the scintillator bar unit after optimising the setup was $\sim$ 400ps.

Comment (5)*: When using the ESR pipe an air gap of $\sim$ 8.8cm is created between the source and the scintillator bar. This creates a large solid angle illuminated by the source, contributing to the width of the TDC distribution. The source was brought down onto the bar to decrease the solid angle illuminated by the source and to decrease the path travelled by the light to improve the time resolution of the system. Nine points were tested across the bar with each point of measurement individually wrapped in Teflon (three layers thick and $\sim$ 6cm wide). A CTR of 410ps was achieved with this setup - a great improvement on the previous 850ps, however still far from the desired 250ps.

Comment(6)*: The 2228A TDC module, with a finer 55ps resolution, was introduced into the system to see whether this would improve the CTR measurement. A measurement was repeated with the two different TDC modules with identical setups ($3^{"}$ Hamamatsu PMTs, with the bar wrapped entirely in PFTE, at the 0cm position). The 2228 TDC module (100ps resolution) gave a result of 431ps CTR. The 2228A

TDC module (55ps resolution) gave a result of 417ps CTR. Whilst some improvement is seen the resolution of the TDC module is not what is causing the CTR to be greater than expected. From this point onwards only the finer resolution 2228A TDC module is used.

Comment (7)*: The discriminator used in the DAQ so far has been a leading edge discriminator (which uses the leading edge of the signal for triggering). In order to see how this effects the TDC width a constant fraction discriminator (CFD), which takes into account the pulse shape of the signal, was introduced into the DAQ instead. A measurement with identical setups (3" Hamamatsu PMTs, with the bar wrapped entirely in PFTE, at the 0cm position) was carried out. The leading edge discriminator gave a result of 417ps CTR, and the CFD gave a result of 548ps CTR. In order to investigate why using the CFD gives a worse CTR than using the leading edge discriminator the contribution of the electronics with the CFD in the chain was looked at. This was done by splitting the signal from one PMT and passing it through an identical chain of electronics. A narrow peak was obtained with this test, indicating that the electronics behaved reasonably. The threshold of the CFD was varied (set to minimum, achieving a CTR of 585ps and set to maximum, achieving a CTR of 598ps), which did not improve the CTR. In conclusion, the leading edge discriminator gives a better CTR result. This is thought to be due to the pulse shapes of the signals being different, in which case a CFD gives a worse result. When using the leading edge discriminator and cutting on the ADC spectra to select TDC data (Section 11.3.5) this is effectively doing the job of a CFD.

Comment (8)*: The next part of the investigation involved looking at whether the coincidence unit contributes to the measurement of the TDC width. The TDC trigger was changed to not use the coincidence for triggering. Instead, the TDC "start" came directly from the PMT1 discriminated signal. The TDC "stop" came from the PMT2 discrimated signal delayed by ~ 24ns (a slightly longer time than that which the signal takes to travel across the entire bar), to ensure the "stop" always comes after the "start" (Figure 12.5). No improvement was seen in the CTR result, concluding that the coincidence unit does not contribute to the width of the TDC distribution.

Comment (9)*: In order to see the contribution to the TDC width coming from the length of the scintillator bar the test was carried out with a "short" bar. A block

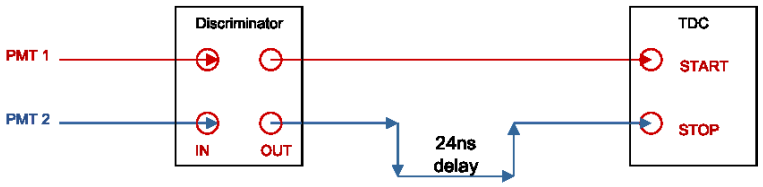

Figure 12.5: The TDC data acquisition system (DAQ) for scintillator bars with the coincidence unit taken out of triggering.

of BC-408 PVT scintillator (15cm x 15cm x 2cm) was used, coupled to the two 3" Hamamatsu tubes. The block had no reflective wrapping in order to degrade the light output to make it similar to that of the bar (the energy resolution obtained was 11.5%, similar to that of the bar setup wrapped in PFTE). The CTR achieved was 306ps - an improvement from the best (individual point) CTR of 395ps achieved for the bar setup. However, a CTR of $\sim$ 250ps is expected to be seen for a block this size.

Comment (10)*: After many variations of the DAQ and setup and no great improvement in the TDC width measurement it was decided to test the intrinsic time resolution of the 3" Hamamatsu tubes. At this point one of the tubes developed a crack (possibly due to an HV spike), causing the photo-cathode to evaporate entirely. A 3" Hamamatsu R6233-100 tube (Table 10.1) with a QE of $\sim 35\%$ at 350nm was used to replace this. Despite the R6233-100-S tube having an 8% higher QE than the R6233-100 tube both PMTs show a similar performance [147]. The EJ-200 and BC-408 scintillators have suppressed light emmissions below 400nm, therefore the shift of the QE profile of the R6233-100-S to lower wavelengths (Figure 10.1(b)) could explain the similar performance of the tubes. To test the intrinsic time resolution of the PMTs the two tubes were placed side by side with a UV LED, pulsed at 2.23V to give an ADC peak position similar to that of ^{207}Bi, suspended centrally above them. The CTR of the 3" Hamamatsu tubes was found to be 258ps (compared to 306ps measured with the "short" bar). Therefore a sizeable contribution to time resolution comes from the intrinsic time resolution of the 3" Hamamatsu tubes (258ps compared to an average measurement of 460ps for the EJ-200 Bar 1). The time transition spread (TTS), which is the spread of the time that the electron avalanche takes to go through the dynode chain, for the 3" Hamamatsu R6233-100-S tube is 14ns ($\sim$ 3 times worse than for an 8" tube, which has a TTS of 4ns). A flat cathode window, as in the 3" Hamamatsu

Scint. Size & Make	Refl.	Setup Details	CTR	C
EJ-200 Bar 1	PFTE	Source brought down onto bar	410	(5)*
EJ-200 Bar 1	PFTE	2226 TDC module used (100ps resolution)	431	(6)*
EJ-200 Bar 1	PTFE	2228 TDC Module used (55ps resolution)	417	(6)*
EJ-200 Bar 1	PFTE	Constant Fraction Discriminator used	548	(7)*
EJ-200 Bar 1	PFTE	Remove coincidence unit from triggering	613	(8)*
BC-408: 15cm x 15cm x 2cm	-	"Short" bar tested	306	(9)*
-	-	Intrinsic time resolution of 3" R6233-100-S and and R6233-100 PMTs	258	(10)*

Table 12.4: Summary of the time resolution investigation measurements. The scintillator and reflector used and the coincidence time resolution (CTR), in ps, obtained are shown. All tests were carried out with the 3" Hamamatsu R6233-100-S PMTs and with a ^{207}Bi source. Any comments (C) regarding measurements can be found in Section 12.2.1.

R6233-100-S tube, generally leads to a poor time resolution due to the variation of the drift time from the cathode to the 1^{st}-dynode. After discussions with Hamamatsu it was discovered that they have a "plano-concave" tube with a flat window on the outside but a concave photocathode on the inside, which reduces the TTS to 4ns (designed for another experiment). Although there is no one-to-one correspondence between the TTS and the time resolution it is expected that reducing the TTS and introducing a concave photocathode would help to improve the time resolution of the system. The tubes are available to purchase, however due to time and money constraints the tubes were not acquired.

12.2.2 ^{90}Sr Measurements

The scintillator bar setup was taken to CENBG to be tested with the ^{90}Sr to cross check the energy and time resolution measurements with those obtained at UCL. Using ^{90}Sr removes many complications associated with the ^{207}Bi fit. As an additional cross check the scintillator bar setup was tested with the UCL DAQ and the DAQ used at CENBG for consistency.

The bulk attenuation length of the EJ-200 scintillator bar was measured as part of the testing. The peak of the ^{90}Sr Gaussian distribution in ADC counts for the individual PMTs is plotted as a function of the source location (its distance from the centre of the bar) and is fitted with an exponential function:

$$y = Ae^{bx}, \tag{12.2.1}$$

where A and b are the constant and the slope of the distribution, y is the value of the ^{90}Sr peak in ADC counts and x is the position of the source on the bar in cm. The attenuation length is then $\frac{1}{b}$. An example of an attenuation length fit can be seen in Figure 12.6, obtained for the EJ-200 Bar 1 setup, wrapped in PFTE with 3" Hamamatsu PMTs. The attenuation length measured with the R6233-100 tube (referred to as the "left" tube) was measured to be 154cm and the attenuation length measured with the R6233-100-S tube (referred to as the "right" tube) was measured to be 171cm. On average the attenuation length was measured to be 158cm with the R6233-100 PMT and 165cm with the R6233-100-S PMT.

Comment (11)*: When using scintillator bars for the SuperNEMO calorimeter design it is important to be able to identify the position of an event on the bar and the precision to which this can be done. To acquire a measurement of this the ^{90}Sr spectrometer was moved to a "mystery" point on the bar unknown to me (for the EJ-200 Bar 1 wrapped in Al-Mylar with the 3" Hamamatsu PMTs). The mean of the TDC distribution ($t_2 - t_1$) plotted as a function of position of the source (obtained from earlier measurements of bar scanning), shown in Figure 12.7(a), was then fitted with a straight line equation:

$$y = mx + c, \tag{12.2.2}$$

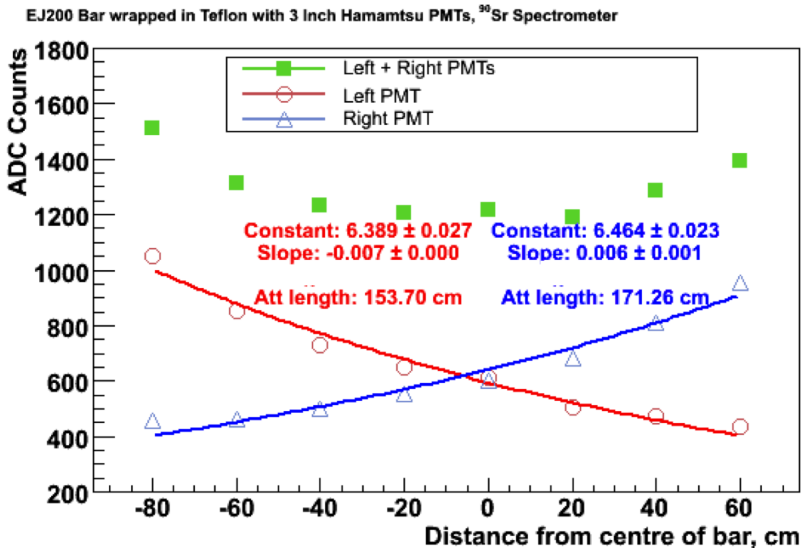

Figure 12.6: An example of obtaining the attenuation length of the calorimeter unit with ^{90}Sr for a setup using the EJ-200 Bar 1 wrapped in PFTE with 3" Hamamatsu R6233-100 and R6233-100-S PMTs.

where m and c are the gradient and the constant of the line, y is the TDC mean (in TDC ticks) and x is the position of the source (in cm). The fit returned the values of $m = -3.479$ and $c = -126.09$. In order to get the position of the mystery point the mean of the TDC width distribution obtained for the mystery point (Figure 12.7(b)) was then converted to a position, using the values returned by the fit. The position was reconstructed at -33.4cm, with the actual location of the ^{90}Sr at -33.3cm.

To obtain the error on the mystery point position the straight line equation obtained from the TDC mean as a function of position is used to convert the TDC width distribution from TDC ticks to position in cm. The error is then the width (σ) of this Gaussian distribution (Figure 12.8). The mystery point position was measured to be -33.4cm $\pm$ 3.7cm. The average σ obtained for all of the measurements with the EJ-200 Bar 1 wrapped in Al-Mylar with 3" Hamamatsu PMTs setup is 3.6, translating to an error of $\pm$ 3.6cm. Therefore the location of an event on the scintillator bar can be found to within $\pm$ 3.6cm.

The spectrometer is able to produce a monochromatic source of electrons from ^{90}Sr from 0.4 to 2.0MeV (Section 11.4). When testing the energy and time resolution of the scintillator bar calorimeter unit a dependence inversely proportional to the square root of the energy ($\sqrt{E}$) is expected to be seen. The EJ-200 Bar 1 wrapped in Al-Mylar

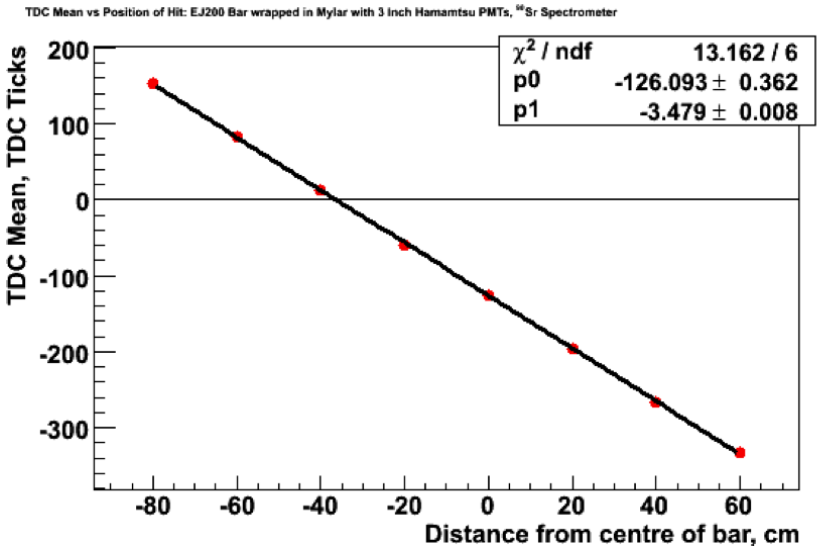

(a) TDC mean as a function of position of the source

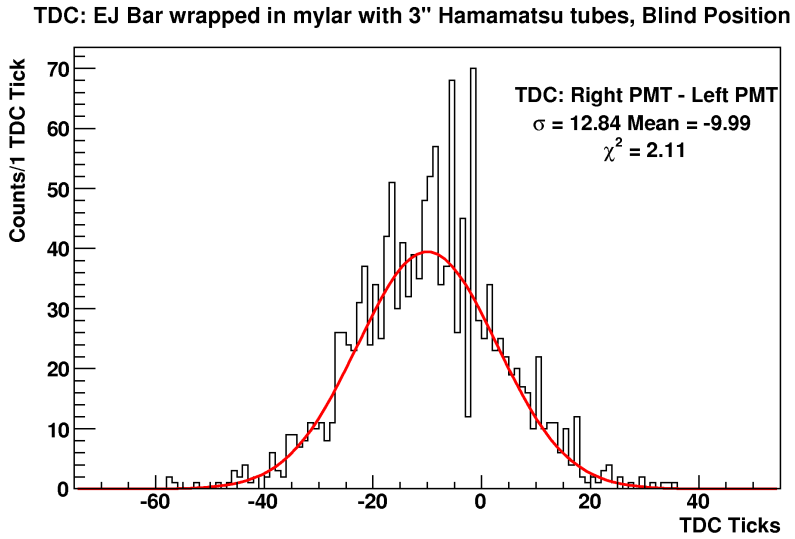

(b) TDC distribution for the "mystery" point

Figure 12.7: The distributions used to obtain the location of the ^{90}Sr at a "mystery" point for the EJ-200 Bar 1 wrapped in Al-Mylar with 3" Hamamatsu PMTs setup.

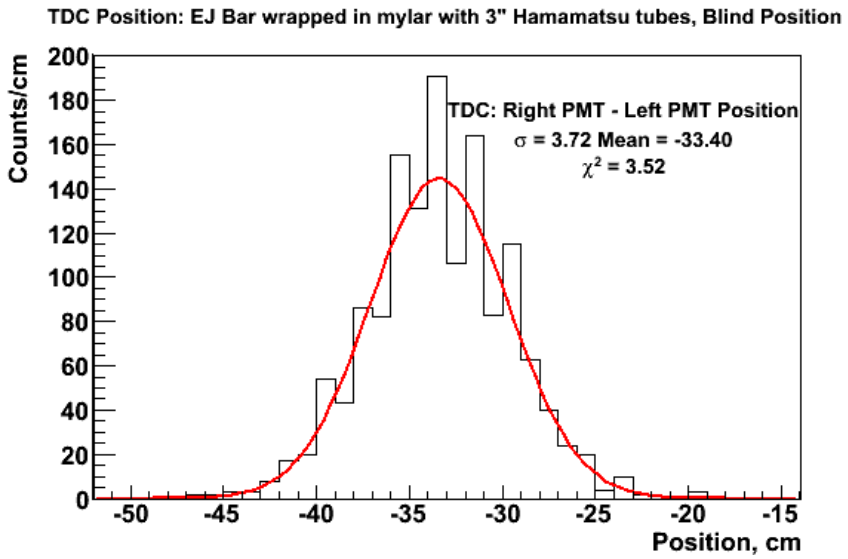

Figure 12.8: An example of the TDC distribution converted to position to obtain the error on position for a setup using the EJ-200 Bar 1 wrapped in PFTE with 3" Hamamatsu R6233-100 and R6233-100-S PMTs.

with 3 Hamamatsu PMTs setup was tested for five different energies (between 0.4 and 1.6MeV) with the ^{90}Sr spectrometer placed at the 0cm position on the bar. Both the energy resolution (Figure 12.9(a)) and the time resolution (Figure 12.9(b)) were found to have a good $\sqrt{E}$ dependence.

12.2.3 Configuration 2 Conclusion

The best energy resolution obtained with Configuration 2 is 10.1% FWHM at 1MeV with the EJ-200 Bar 1 wrapped in ESR with the 3" Hamamatsu PMTs (in the vertical orientation) using ^{207}Bi and 9.7% FWHM at 1MeV with the EJ-200 Bar 2 wrapped in Al-Mylar with the 3" Hamamatsu PMTs using ^{90}Sr. These results show that the UCL (^{207}Bi) and CENBG (^{90}Sr) methods produce consistent results, therefore the ^{207}Bi analytical function used to fit the collected data works well. The results obtained with the UCL DAQ and the CENBG DAQ were also found to be consistent.

12.3 Configuration 3

The schematics and picture of the EJ-200 200cm x 10cm x 10cm (with the ends tapered to a 6.8cm ⌀ circle at 70° angles) bar, referred to as the "square" bar, can be seen in Figure 12.10. The weight of the bar is ∼ 25kg, therefore there is some doubt as to whether the 3" PMT can withstand the weight of the bar when it is in a vertical

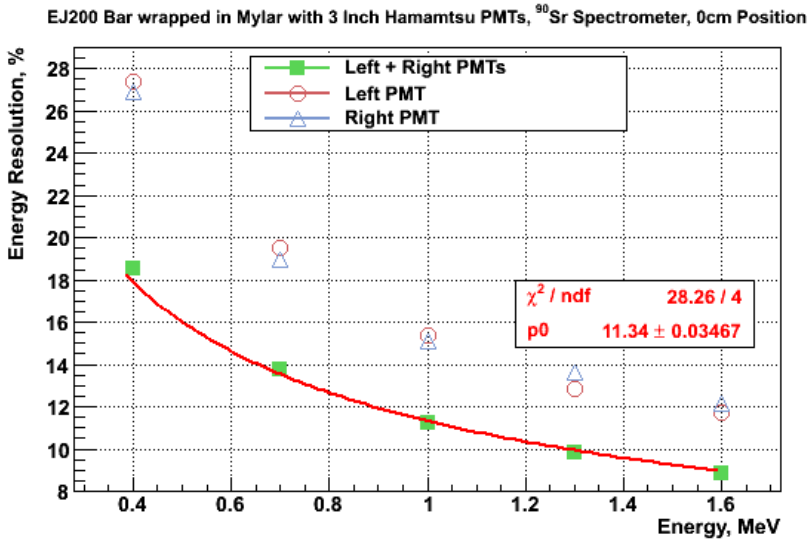

(a) Energy resolution as a function of ^{90}Sr energy

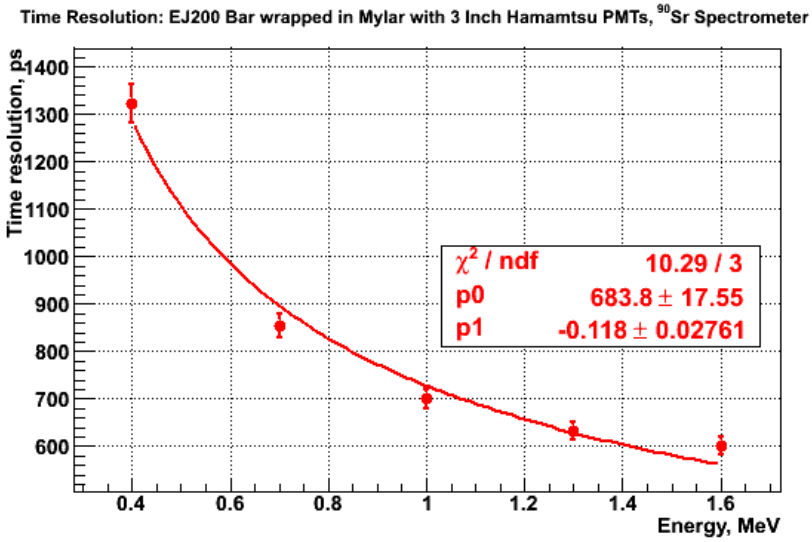

(b) Time resolution as a function of ^{90}Sr energy

Figure 12.9: Energy (a) and time (b) resolution as a function of ^{90}Sr energy for the EJ-200 Bar 1 wrapped in Al-Mylar with 3" Hamamatsu PMTs setup, showing a $\sqrt{E}$ dependence.

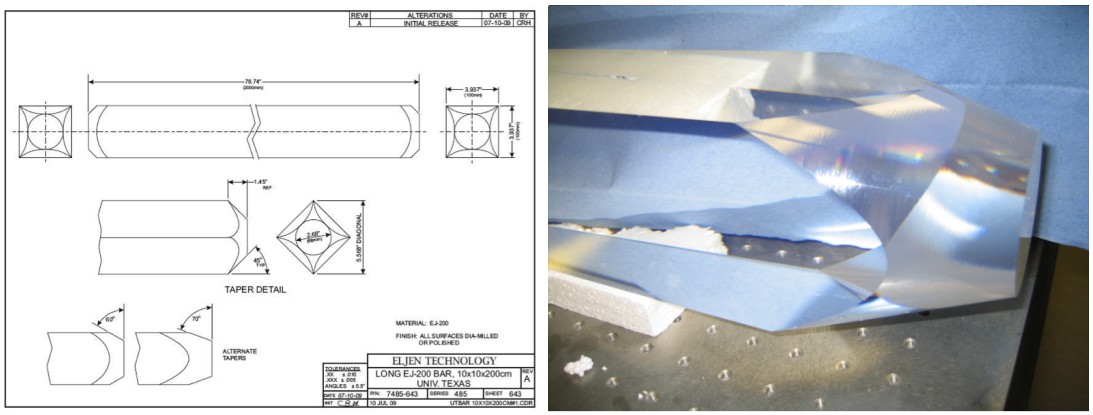

Figure 12.10: The EJ-200 "Square" bar schematics (a) and physical appearance (b).

orientation. Hamamatsu were planning to do a "pressure" test, with their concern being that the stem area at the bottom side of the PMT may be broken by the applied pressure. An additional support mechanism was suggested to be implemented by Hamamatsu to reduce the burden on the PMT. However, due to time constraints the EJ-200 square bar tests were carried out in the horizontal orientation.

The square bar tests were carried out with the 3" Hamamatsu PMTs, with the bar wrapped in Al-Mylar and with the BC-630 optical gel used for coupling. Due to the large thickness of the bar the γ background picked up by the calorimeter unit is extremely large. Figure 12.11 shows the full and filtered ^{207}Bi spectra obtained with the EJ-200 square bar, at the 0cm position. The thickness of the bar means that there is a higher probability of γ interaction within the bar, therefore the 1.7MeV Compton shoulder at 1300 ADC counts starts to become visible. Too much γ background is introduced for the full analytical ^{207}Bi fit (described in Section 11.3.3) to be used. Instead, a less robust but simpler triple Gaussian fit (Equation 11.3.6) is used on the the subtracted, or electron only, spectrum (obtained with the procedure described in Section 11.3.3) to obtain the energy resolution. Figure 12.11 shows the subtracted spectrum for the 0cm position, where a "false" peak can be seen at $\sim$ 1800 ADC counts. When subtracting the spectra, the normalisation is done to the 976keV peak and Compton shoulder therefore this false peak becomes visible in the subtracted spectrum due to the 1.7MeV Compton shoulder picked up by the scintillator bar. The energy resolution obtained for the 0cm position is 12.5% FWHM at 1MeV.

Simulations with GEANT-3.21 for the EJ-200 square bar (200cm x 10cm x 10cm,

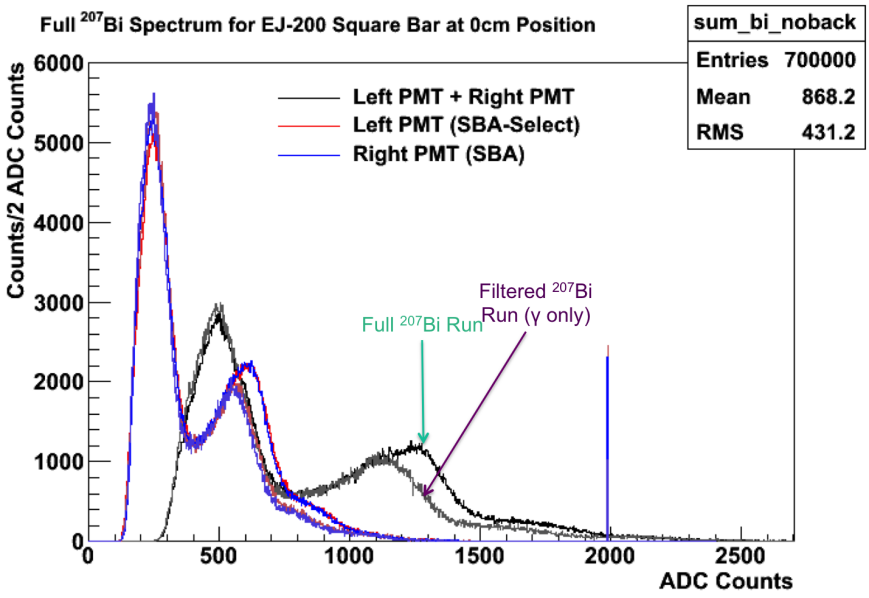

(a) Full and filtered (γ only) ^{207}Bi spectra

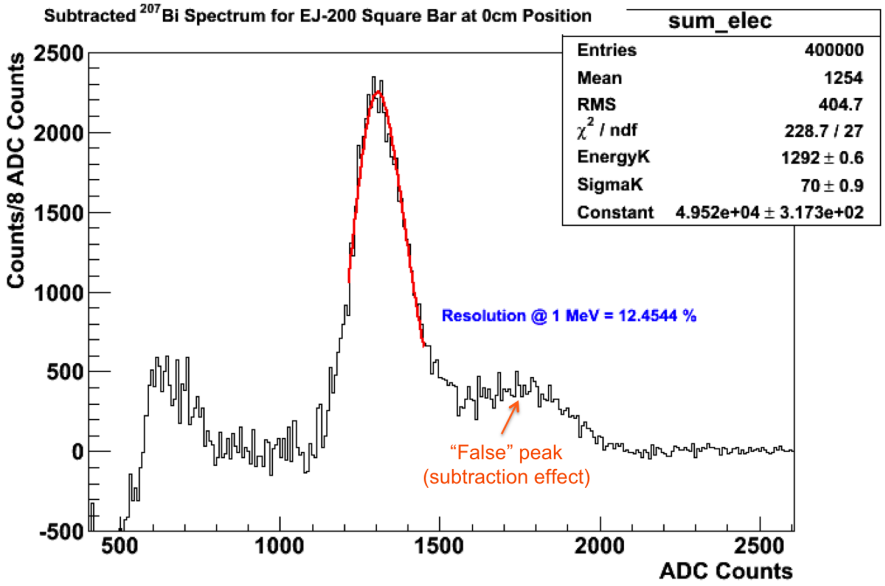

(b) Conversion electron only ^{207}Bi spectrum

Figure 12.11: ADC spectra obtained with ^{207}Bi for the EJ-200 "Square" bar at the 0cm position, with the bar wrapped in Al-Mylar, using 3" Hamamatsu PMTs. The full and filtered spectra for the individual and summed PMTs are shown in (a) and the subtracted (electron) only spectrum for the summed PMTs is show in (b). An energy resolution of 12.5% FWHM at 1MeV is obtained.

without the taper) were carried out for the 0cm position for an MC truth of 12.5% to confirm the large γ background seen in the data. Figure 12.12 shows the full and filtered spectra for the summed PMTs obtained with the data and with the simulations for the 0cm position. The simulations confirm what is seen in the data - the 976keV conversion electron peak and Compton shoulder become more merged and difficult to distinguish. The 1.7MeV Compton shoulder is also seen to appear in the simulations at $\sim$ 1300 ADC counts.

Some non-uniformity across the length of the bar was seen when the measurements were carried out, with one side of the bar giving a better performance (with an energy resolution of 12.8$\%$ FWHM at 1MeV) than the other (with an energy resolution of 14.3$\%$ FWHM at 1MeV). In order to explore the non-uniformity of the bar further three "faces" (out of four) of the bar were tested. Every paremeter was kept constant (meaning no re-gelling of the PMTs was done between measurements of different faces) with the ^{207}Bi source placed on top of Face 1 and suspended by the sides of the bar and centralised for Face 2 and Face 3 measurements.

A summary of the measurements obtained for the three different faces of the bar is shown in Table 12.5. Some non-uniformity is seen from one face of the bar to another. This could be explained by the large size of the bar or something going wrong during the production of the bar (several unsuccessful attempts were made to produce the bar). The energy resolution obtained with the thick square bar is 12.1 - 13.1$\%$ FWHM at 1 MeV, up to 3$\%$ worse than for the 2.54cm thick EJ-200 bars. If used for the SuperNEMO calorimeter, this energy resolution would not achieve the required sensitivity for the $0\nu\beta\beta$ half-life of 10^{26} years therefore the 10cm thick bar is not an option.

12.4 Summary and Conclusions

Many different parameters were varied and tested for the scintillator bar calorimeter unit. The best setup was found to be using a 200cm x 10cm (with ends tapered to 6.5cm at 45° angles) x 2.54cm EJ-200 scintillator, wrapped in ESR or Al-Mylar, with 3" Hamamatsu R6233-100-S PMTs giving an energy resolution of $\sim$ 10$\%$ FWHM at 1MeV and a CTR of $\sim$ 450ps (σ at 1MeV). This energy resolution result is unprecedented for a scintillator of such a large size. The result was validated with two independent methods (using ^{207}Bi and ^{90}Sr) and was found to be consistent, proving

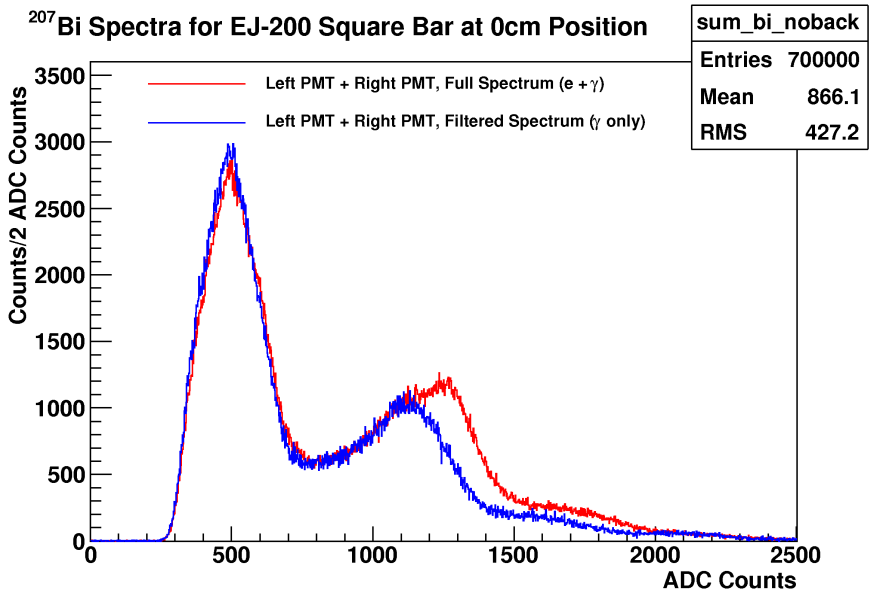

(a) Data

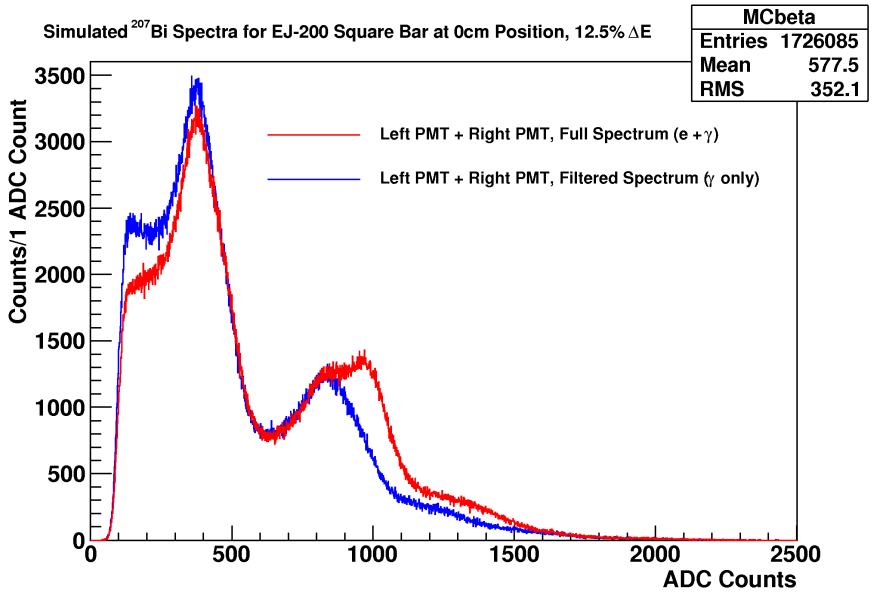

(b) MC

Figure 12.12: ADC spectra obtained with ^{207}Bi for data (a) and MC (b) simulations for an MC truth of 12.5% FWHM at 1 MeV for the EJ-200 "Square" bar at the 0cm position.

PMT Size & Make	Reflector	Bar Face	$\frac{\Delta E}{E}(\%)$	CTR (ps)
3" H. R6233-100 & 3" H. R6233-100-S	Al-Mylar	1	13.1	646
3" H. R6233-100 & 3" H. R6233-100-S	Al-Mylar	2	12.9	640
3" H. R6233-100 & 3" H. R6233-100-S	Al-Mylar	3	12.1	636

Table 12.5: Results of measurements obtained with Configuration 3. The energy resolution measurement (FWHM at 1MeV) is obtained from the sum of the PMTs. The -1.1% offset from simulations is not included and the energy resolution has a $\pm 0.4\%$ error on it (Section 11.3.4).

the method used is robust and reliable. It should be noted that this energy resolution is a conservative estimate as the -1.1% systematic shift (Section 11.3.4) found with simulations has not been included in this final result. When including the shift a potential energy resolution of $\sim 9\%$ FWHM at 1 MeV is achievable for the scintillator bar unit.

In February 2010 a decision regarding the SuperNEMO calorimeter design for the demonstrator module was made by the collaboration. An unprecedented energy resolution of 7% FWHM at 1MeV has been obtained with the block design, which corresponds to the target resolution of the SuperNEMO calorimeter of 4% FWHM at 3MeV [147]. Following a discussion, focusing on the sensitivity, risks and costs of the designs, it was agreed that the block calorimeter design would be used. It was decided that the current information available on the bar calorimeter design does not give sufficient advantages to be chosen over the block design, even when considering the saving in cost and reduction of background introduced by the PMTs using the bar design would provide. The main disadvantage of the bar design was that a fully functional demonstrator module could not be built using scintillator bars. The prerequisite of the demonstartor module was to have a stand alone fully functional SuperNEMO module. With one module of the bar design containing 12.5kg of ^{82}Se this was too expensive an option to consider. Other issues of concern were the inexperience of the bar design. Concerns regarding the time calibration of the bars, accurate measurement of external and internal backgrounds (especially for ^{208}Tl) and the bars' design sensi-

tivity for the analysis to the excited states of ^{82}Se due to the layered structure of the design were raised. If the target backgrounds for SuperNEMO can be reached with the SuperNEMO demonstrator module the block calorimeter design would ultimately give a 50% better sensitivity than the bar design. However, if the demonstrator finds that the dominating problem in reaching the target sensitivity is caused by the emanation of radon from the PMTs then the bar design remains as a "back up" option.

A low level R&D programme will continue for the scintillator bars, such as further optimisation of the energy and time resolutions of the calorimeter unit, looking at the ageing effects of the bars (for example, by measuring energy and time resolutions in identical setups as a function of time) and full detector simulations.

Chapter 13

Conclusion

Neutrinoless double beta decay ($0\nu\beta\beta$) is a lepton number violating process, forbidden in the Standard Model of particle physics. If it is observed it identifies the neutrino to be that of a Majorana nature, with the neutrino being its own anti-particle. It is also one of the most sensitive processes to ascertain the effective mass of the neutrino and has access to the neutrino mass hierarchy (complimentary to oscillation experiments). It will therefore have large implications for the fields of particle and nuclear physics, cosmology and astrophysics. Studying two neutrino double beta decay ($2\nu\beta\beta$) provides insight into the nuclear models used to calculate nuclear matrix elements for $0\nu\beta\beta$, which are required for the extraction of the corresponding physics parameters, such as the effective neutrino Majorana mass, $\langle m_{\nu e} \rangle$. $2\nu\beta\beta$ decay is also an irreducible background to $0\nu\beta\beta$ decay (with the two having the same event topology) and must therefore be studied in great depth before a $0\nu\beta\beta$ decay search can be carried out.

The NEMO3 detector, located in the Laboratoire Souterrain de Modane (which provides a rock overburden of 4850 metres water equivalent to shield the detector from cosmic rays), collected data from February 2003 to January 2011 from 10kg of seven different double beta decay isotopes. The NEMO3 collaboration has produced some of the world's most competitive results for the $2\nu\beta\beta$ and $0\nu\beta\beta$ decay isotopes used, including the ^{100}Mo (which is NEMO3's main isotope at 6.9kg) result presented here.

The thesis gives a detailed description of the main NEMO3 components - the tracking chamber, calorimeter, source foils, calibration, radon purification facility and passive shielding. NEMO3's main distinguishing feature from other experiments is the topological identification of events, which allows identification of electrons, positrons (using NEMO3's magnetic field), γs and αs. This means that the only backgrounds

to $\beta\beta$ decay are $2e^-$ events, which mimic $2\nu\beta\beta$ and $0\nu\beta\beta$ decay. Topological background suppression is particularly important for a continuous energy spectrum, such as produced by $2\nu\beta\beta$ decay and some of the $0\nu\beta\beta$ decay modes, making NEMO3 the most sensitive experiment for these searches. The internal and external background models used for ^{100}Mo are described.

The validity of the cuts applied to the data and the Monte Carlo simulations is tested and presented and the methods used to extract $2\nu\beta\beta$ and $0\nu\beta\beta$ decay half-lives, limits and corresponding parameters are given. The $2\nu\beta\beta$ decay half-life measured is

$$T_{1/2}^{2\nu} = [7.02 \pm 0.01(stat) \pm 0.46(syst)] \times 10^{18}\text{years},$$

for 6.9kg of ^{100}Mo collected over 1471 days (obtained from February 2003 to December 2009, for which laser energy corrections are available). The nuclear matrix element is then extracted from the half-life and is

$$M^{2\nu} = 0.126 \pm 0.004.$$

This is the world's most precise measurement for ^{100}Mo to date and helps to provide constraints on future $0\nu\beta\beta$ nuclear matrix element calculations.

No excess of events are observed in the $0\nu\beta\beta$ region of interest and the limit found on the Majorana neutrino mass mechanism of $0\nu\beta\beta$ decay [1] is

$$T_{1/2}^{0\nu} > 1.1 \times 10^{24} \text{ years},$$

corresponding to an effective Majorana neutrino mass of

$$\langle m_{\nu e} \rangle < 0.3 - 1.0 \text{ eV},$$

which is one of the world's most stringent constraints on $\langle m_{\nu e} \rangle$, comparable to the limit of $\langle m_{\nu_e} \rangle$ < 0.3 - 0.7eV obtained with the CUORICINO [88] and Klapdor's claim of $\langle m_{\nu_e} \rangle$ < 0.2-0.6eV (with a "best fit" of 0.4eV, which is starting to be excluded with the result present here) obtained with the Heidelberg-Moscow experiment [47].

A half-life limit of

[1] Hereafter all the limits stated are given at a confidence level (CL) of 90%.

$$T_{1/2}^{0\nu\lambda} > 5.5 \times 10^{23} \text{ years},$$

is obtained for the $0\nu\beta\beta$ right-handed currents decay mode, corresponding to a right-handed currents admixture parameter of

$$\langle\lambda\rangle < 1.4 \times 10^{-6}.$$

This is one of the most stringent constraints obtained on the right-handed currents admixture parameter $\langle\lambda\rangle$.

A half-life limit of

$$T_{1/2}^{0\nu\chi^0} > 5.3 \times 10^{22} \text{ years}$$

is set for the main Majoron particle emission mode (with spectral index n = 1), corresponding to a Majoron coupling constant of

$$\langle g_{\chi^0}\rangle < (0.2 - 0.7) \times 10^{-4}.$$

These is the world's most stringent bound on $\langle g_{\chi^0}\rangle$ and has been improved by a factor of ~ 2 compared to the previous world's best result obtained with NEMO3 [138].

SuperNEMO is a next generation double beta decay experiment based on the successful tracker-calorimeter technique used in NEMO3, with the "demonstrator" module currently under construction. The detector will hold $\sim$ 100kg of ^{82}Se to reach a sensitivity of 10^{26} years for $0\nu\beta\beta$ decay, corresponding to an effective neutrino mass of $\langle m_{\nu e}\rangle$ < 50 - 100meV, providing access to the inverted neutrino mass hierarchy. A detector description and R&D activities are presented in the thesis, covering source foil production, purification of materials used to construct the detector, tracker, calorimeter and software development. The main focus of the work presented in the thesis is R&D of an alternative calorimeter design for SuperNEMO, known as the "bar" design. The advantages and disadvantages of both the calorimeter baseline (or "block") and bar design are given. An overview of parameters influencing energy resolution of a calorimeter system is described and considered in the test bench measurements of a bar calorimeter unit. Many different configurations of scintillators, photomultiplier

tubes (PMTs) and reflective wrappings were considered and tested and the results are presented in this thesis.

An energy resolution of 10% FWHM at 1MeV and a coincidence time resolution of 450ps (σ at 1MeV) have been obtained for the calorimeter bar setup. The result advocates the advantages of using PVT based scintillator and high quantum efficiency PMTs. Whilst this is an unprecedented energy resolution for a scintillator of this size it does not meet the requirements of the 7% FWHM at 1MeV for the SuperNEMO baseline design calorimeter, which has been met with a block calorimeter setup. In February 2010 the SuperNEMO collaboration reached the decision to use the block design for the SuperNEMO demonstrator module, with the advantages of the block design outweighing those of the bar design, described in the thesis. This decision could not have been made in a properly informed manner without the detailed study of the bar design presented here. The bar design remains a "back up" option for the SuperNEMO detector depending on the findings of the demonstrator. If the target backgrounds for the detector can be achieved with the SuperNEMO demonstrator then the baseline design will give a 50% better sensitivity than the bar design due to the better energy resolution of the baseline design. However, if it is found that radon emanation from the PMTs is limiting the sensitivity then the bar design may be the way forward. A low level R&D programme will continue to run for the bar design.

Bibliography

[1] A. Barabash et al. Testing the Pauli Exclusion Principle with the NEMO2 detector. *Nucl. Phys. B*, Proc. Suppl.(87):510–511, 2000.

[2] G. Bellini et al. New experimental limits on the Pauli-forbidden transitions in ^{12}C nuclei obtained with 482 days Borexino data. *Nucl. Phys.*, C(81):034317, 2010.

[3] W. Pauli. Dear radioactive ladies and gentlemen. *Phys. Today*, 31N9:27, 1978.

[4] F.L. Wilson. Fermi's theory of beta decay. *Amer. Journ. of Phys.*, 36(12):1150 – 1160, 1968.

[5] F. Reines and C.L. Cowan Jr. Detection of the free neutrino. *Phys. Rev.*, 92(3):830–831, 1953.

[6] F. Reines and C.L. Cowan Jr. Free antineutrino absorption cross section and measurement of the free antineutrino absorption cross section by protons. *Phys. Rev.*, 113(1):273–239, 1959.

[7] M. Goldhaber, L. Grodzins, and A.W. Sunyar. Helicity of neutrinos. *Phys. Rev.*, 109:1015–1017, 1958.

[8] B. Pontecorvo. Mesonium and Antimesoneum. *J. Exptl. Theoret. Phys.*, 33:549, 1957.

[9] B. Pontecorvo. Inverse beta processes and nonconservation of lepton charge. *J. Exptl. Theoret. Phys.*, 34:247, 1958.

[10] Z. Maki, M. Nakagawa, and S. Sakata. Remarks on the unified model of elementary particles. *Prog. Theor. Phys.*, 28(5):870–880, 1962.

[11] G. Danby et al. Observation of high-energy neutrino reactions and the existence of two kinds of neutrino. *Phys. Rev. Lett.*, 9(1):36 – 44, 1962.

[12] K. Kodama et al. Observation of tau-neutrino interactions. *Phys. Lett. B*, 504:218–224, 2001.

[13] R. Davis, D.S. Hamer, and K.C. Hoffman. Search for neutrinos from the sun. *Phys. Rev. Lett.*, 20:1205–1209, 1968.

[14] Q.R. Ahmad et al. Measurement of the rate of $\nu_e + d \rightarrow p + p + e^-$ interactions produced by ^{8}B solar neutrinos at the Sudbury Neutrino Observatory. *Phys. Rev. Lett.*, 87(7):071301, 2001.

[15] Y. Fukuda et al. Evidence for oscillation of atmospheric neutrinos. *Phys. Rev. Lett.*, 81(8):1562 – 1567, 1998.

[16] K. Nakamura et al. Status of K2K. *Nucl. Phys. Proc. Suppl.*, 91:203, 2001.

[17] D.G. Michael at al. Observation of muon neutrino disappearance with the MINOS detectors in the NuMI neutrino beam. *Phys. Rev. Lett.*, 97:191801, 2006.

[18] B. Aharmim et al. An independent measurement of the total active ^{8}B solar neutrino flux using an array of ^{3}He proportional counters at the Sudbury Neutrino Observatory. *Phys. Rev. Lett.*, 101:111301, 2008, nucl-ex/0806.0989.

[19] G. Prior. Results from the Sudbury Neutrino Observatory phase III. *Nucl. Phys. Proc. Suppl.*, 188:96 – 100, 2009.

[20] Y. Ashie et al. A measurement of atmospheric neutrino parameters by Super-Kamiokande I. *Phys. Rev. D*, 71:112005, 2005, hep-ex/0501064.

[21] K. Okumura. Recent status of Super-Kamiokande. *AIP Conf. Proc.*, 981:139–141, 2008.

[22] M. Apollonio et al. Search for neutrino oscillations on a long base-line at the CHOOZ nuclear power station. *Eur. Phys. J. C*, 27:331–374, 2003, hep-ex/0301017.

[23] S. Abe et al. Precision measurement of neutrino oscillation parameters with KamLAND. *Phys. Rev. Lett.*, 100:221803, 2008, hep-ex/0801.4589.

[24] I. Shimizu. KamLAND results. *Nucl. Phys. Proc. Suppl.*, 188:84–89, 2009.

[25] M.H. Ahn et al. Measurement of neutrino oscillation by the K2K experiment. *Phys. Rev. D*, 74:072003, 2006, hep-ex/0606032.

[26] R. Terri. Results of the K2K oscillation analysis. *AIP Conf. Proc.*, 981:169–171, 2008.

[27] P. Adamson et al. Measurement of neutrino oscillations with the MINOS detectors in the NuMI beam. *Phys. Rev. Lett.*, 101:131802, 2008, hep-ex/0806.2237.

[28] B. Aharmin et al. Low-energy-threshold analysis of the Phase I and Phase II data sets of the Sudbury Neutrino Observatory. *Phys. Rev. C*, 81:055504, 2010.

[29] Y. Takeuchi. Contributed to XXIV international conference on neutrino physics and astrophysics (Neutrino 2010), Athens, Greece, 14-19 June. 2010.

[30] P. Adamson et al. Measurement of the neutrino mass splitting and flavour mixing by MINOS. *Phys. Rev. Lett.*, 106:181801, 2011.

[31] K. Abe et al. Indication of electron neutrino appearance from an accelarator-produced off-axis muon neutrino beam. *Phys. Rev. Lett.*, 107(4):041801, 2011.

[32] P. Adamson et al. Improved search for muon-neutrino to electron-neutrino oscillations in MINOS. 2011, arXiv:1108.0015[hep-ex].

[33] T. Schwetz, M. Tortola, and J.W.F. Valle. Where we are on θ_{13}: addendum to 'Global neutrino data and recent reactor fluxes: status of three-flavour oscillation parameters'. 2011, arXiv:1108.1376 [hep-ph].

[34] Y. Itow et al. Indication of electron neutrino appearance from an accelerator-produced-off-axis muon neutrino beam. *Phys. Rev. Lett.*, 107:041801, 2011.

[35] D.S. Ayres et al. NOνA proposal to build a 30-kiloton off-axis detector to study neutrino oscillations in the Fermilab NuMI beamline. 2004, hep-ex/0503053.

[36] H.R. Band et al. Acrylic target vessels for a high-precision measurement of θ_{13} with the Daya Bay antineutrino detectors. 2012, arXiv:1202.2000v2 [physics.ins-det].

[37] Y. Abe et al. Indication for the disappearance of reactor $\overline{\nu_e}$ in the Double Chooz experiment. 2012, arXiv:1112.6353v2[hep-ph].

[38] G.L. Fogli et al. Evidence of $\theta_{13} > 0$ from global neutrino data analysis. *Phys. Rev. D*, 84:053007, 2011.

[39] C. Giunti and Ch.W. Kim. Fundamentals of neutrino physics and astrophysics: Massive Neutrinos. *Oxford, UK*, Univ. Pr.:710, 2007, ISBN: 978-0-19-850871-7.

[40] E. Majorana. Theory of the symmetry of electrons and positrons. *Nuovo Cim.*, 14:171–184, 1937.

[41] E.W. Otten and C. Weinheimer. Neutrino mass limit from tritium beta decay. *Rept. Prog. Phys.*, 71:086201, 2008, hep-ex/0909.2104.

[42] Ch. Kraus et al. Final results from phase II of the Mainz neutrino mass search in Tritium β decay. *Eur. Phys. J. C*, 40:447 – 468, 2005, hep-ex/0412056.

[43] U. Seljak et al. Cosmological parameter analysis including SDSS Ly-α forest and galaxy bias: Constraints on the primordial spectrum of fluctuations, neutrino mass and dark energy. *Phys. Rev. D*, 71:103515, 2005, astro-ph/0407372.

[44] A.M. Malinovsky, A.A. Voevodkin, V.N. Lukash, E.V Mikheeva, and A.A. Vikhlinin. Cosmological constraints on the neutrino mass from CMB anisotropy and large-scale structure of the universe. *Astron. Lett.*, 34:445–450, 2008.

[45] Yu.G. Zdesenko, F.A. Danevich, and V.I. Tretyak. Has neutrinoless double beta decay of ^{76}Ge been really observed? *Phys. Lett. B*, 546:206–215, 2002.

[46] M. Beck et al. The KATRIN experiment. *J. Phys. Conf. Ser.*, 203:012097, 2010.

[47] H.V. Klapdor-Kleingrothaus et al. First evidence for neutrinoless double beta decay and world status of double beta decay experiments. *Nucl. Phys. B Proc. Suppl. S*, 143:229, 2005.

[48] F. Fergulio, A. Strumia, and F Vissani. Neutrino oscillation signals in β and $0\nu\beta\beta$ experiments. *Nucl. Phys. B*, 637:345, 2002.

[49] C.F.V. Weizsacker. Zur Theorie der Kernmassen. *Z. Phys.*, 96:431–458, 1935.

[50] M. Goeppert-Mayer. Double beta-disintegration. *Phys. Rev.*, 48:512–516, 1935.

[51] G. Racah. On pair production through charged particle collisions. *Nuovo Cim.*, 14:93–113, 1937.

[52] W.H. Furry. On transition probabilities in double beta-disintegration. *Phys. Rev.*, 56:1184–1193, 1939.

[53] S.T. Petcov, H. Sugiyama, and Y. Takanishi. Neutrinoless double beta decay and $H^{\pm\pm} \to l'^{\pm} l^{\pm}$ decays in the Higgs triplet model. *Phys. Rev. D*, 80:015005, 2009, hep-ph/0904.0759.

[54] M. Hirsch, H.V. Klapdor-Kleingrothaus, and S.G. Kovalenko. Supersymmetry and neutrinoless double beta decay. *Phys. Rev. D*, 53:1329 – 1348, 1996, hep-ph/9502385.

[55] M. Doi, T. Kotani, and E. Takasugi. Double beta decay and Majorana neutrino. *Prog. Theor. Phys. Suppl.*, 83:1, 1985.

[56] K. Zuber. Neutrino physics. *Institute of Physics Publishing*, 2004.

[57] J. Schechter and J. Valle. Neutrinoless double beta decay in SU(2)×SU(1) theories. *Phys. Rev. D*, 25:774, 1982.

[58] R. Mohapatra and P. Pal. Massive neutrinos in physics and astrophysics. *World Sci. Lect. Note Phys.*, 60:1, 2003.

[59] C. Amsler et al. Review of particle physics. *Phys. Lett. B*, 667:1, 2008.

[60] M. Hirsch et al. On the observability of Majoron emitting double beta decays. *arXiv:hep-ph/9511227*, 1995.

[61] Z.G. Berezhiani, A.Yu. Smirnov, and J.W.F. Valle. Observable Majoron emission in neutrinoless double beta decay. *Phys. Lett. B*, 291:99–105, 1992, hep-ph/9207209.

[62] R.N. Mohapatra, A. Perez-Lorenzana, and C.A. Pires. Neutrino mass, bulk Majoron and neutrinoless double beta decay. *Phys. Lett. B*, 491:143–147, 2000, hep-ph/0008158.

[63] P. Bamert, C.P. Burgess, and R.N. Mohapatra. Multi-Majoron modes for neutrinoless double beta decay. *449*, Nucl. Phys. B:25–48, 1995, hep-ph/9412365.

[64] R.N. Mohapatra and E. Takasugi. Neutrinoless double beta decay with double Majoron emission. *Phys. Lett. B*, 211:192, 1988.

[65] N. Fatemi-Ghomi. Measurement of the double beta decay half-life of ^{150}Nd and search for neutrinoless decay modes with NEMO-3 detector. *Thesis*, University of Manchester, UK, 2009, hep-ex/0905.0822.

[66] V.A. Rodin, A. Faessler, F. Simkovic, and P. Vogel. Assessment of uncertainties in QRPA neutrinoless double beta decay nuclear matrix elements. *Nucl. Phys.*, A(766):107–131, 2006, nucl-th/0706.4304 and erratum.

[67] J. Suhonen and O. Civitarese. Weak-interaction and nuclear-structure aspects of nuclear double beta decay. *Phys. Rept.*, 300:123 – 214, 1998.

[68] A. Faessler and F. Simkovic. Double beta decay. *J. Phys. G*, 24:2139 – 2178, 1998, hep-ph/9901215.

[69] F.T. Avignone, S.R. Elliott, and J. Engel. Double beta decay, majorana neutrinos and neutrino mass. *Rev. Mod. Phys.*, 80:481 – 516, 2008, nucl-ex/0708.1033.

[70] J. Menendez, A. Poves, E. Caurier, and F. Nowacki. Disassembling the nuclear matrix elements of the neutrinoless double beta decay. *Nucl. Phys. A*, 818:139–151, 2009, nucl-th/0801.3760.

[71] J. Menendez, A. Poves, E. Caurier, and F. Nowacki. Deformation and the nuclear matrix elements of the neutrinoless double beta decay. 2008, nucl-th/0809.2183.

[72] M. Kortelainen and J. Suhonen. Nuclear matrix elements of neutrinoless double beta decay with improved short-range correlations. *Phys. Rev. C*, 76:024315, 2007, nucl-th/0708.0115.

[73] R. Chandra, P.K. Chaturvedi, K. Rath, P.K. Raina, and J.G. Hirsch. Multipolar correlations and deformation effect on nuclear transition matrix elements of double beta decay. 2009, nucl-th/0902.0658v3.

[74] R. Chandra, P.K. Chaturvedi, K. Rath, P.K. Raina, and J.G. Hirsch. Nuclear deformation and neutrinoless double beta decay of ^{94}Zr, ^{96}Zr, ^{98}Mo, ^{100}Mo, ^{104}Ru, ^{110}Pd, ^{128}Te, ^{130}Te and ^{150}Nd nuclei with a mechanism involving neutrino mass. *Phys. Rev. C*, 78:054302, 2008.

[75] E. Caurrier, J. Menendez, F. Nowacki, and A. Poves. Influence of pairing on the nuclear matrix elements of the neutrinoless $\beta\beta$ decays. *Phys. Rev. Lett.*, 100:052503, 2008.

[76] F. Simkovic, G. Pantis, J.D. Vergados, and A. Faessler. Additional nucleon current contributions to neutrinoless double beta decay. *Phys. Rev. C*, 60:055502, 1999.

[77] J. Barea and F. Iachello. Neutrinoless double beta decay in the microscopic interacting boson model. *Phys. Rev.*, C(79):044301, 2009.

[78] R. Flack et al. NEMO-3 and SuperNEMO: A search for zero neutrino double beta decay. *Nucl. Phys. B Proc. Suppl.*, 217(1):53–55, 2011.

[79] H.V. Klapdor-Kleingrothaus et al. Latest results from the Heidelberg-Moscow double beta decay experiment. *Eur. Phys. J. A*, 12:147–154, 2001, hep-pu/0103062.

[80] R. Arnold et al. First results of the search for neutrinoless double beta decay with the NEMO3 detector. *Phys. Rev. Lett.*, 95:182302, 2005.

[81] J. Argyriades et al. Measurement of the two neutrino double beta decay half-life of Zr-96 with the NEMO-3 detector. *Nucl. Phys. A*, 847(3-4):168–179, 2010.

[82] R. Arnold et al. Measurement of $\beta\beta$ decay half-life of ^{130}Te with the NEMO-3 detector. *Phys. Rev. Lett.*, 107(6):062504, 2011.

[83] J. Argyriades et al. Measurement of the double-β decay half-life of ^{150}Nd and search for neutrinoless decay modes with the NEMO-3 detector. *Phys. Rev. C*, 80(3):032501, hep-ex/0810.0248.

[84] N. Ackerman et al. Observation of two-neutrino double-beta decay in ^{136}Xe with EX0-200. 2011, arXiv:1108.4193v1[nucl-ex].

[85] S. Umehara et al. Neutrino-less double beta decay of ^{48}Ca by CaF-2(Eu) scintillators. *Phys. Rev. C*, 78:058501, 2008, nucl-ex/0810.4746.

[86] C.E. Aalseth et al. The IGEX ^{76}Ge neutrinoless double-beta decay experiment: Prospects for next generation experiments. *Phys. Rev. D*, 65:092007, 2002.

[87] V.I. Tretyak. Workshop on calculation of double-beta-decay matrix elements (MEDEX '11): The NEMO-3 results after completion of data taking. *AIP Conf. Proc.*, 1417, 2011.

[88] E. Andreotti et al. ^{130}Te neutrinoless double-beta decay with CUORICINO. *Astroparticle Phys.*, 34:822–831, 2011.

[89] J. Janicsko-Csathy. Satus of the GERDA experiment. *Nucl. Phys. Proc. Suppl.*, 188:68–70, 2009.

[90] V.E. Guiseppe et al. The Majorana neutrinoless double-beta decay experiment. *IEEE Nucl. Sci. Symp. Conf. Rec.*, 2008:1793–1798, 2008, arXiv:0811.2446[nucl-ex].

[91] I.C. Bandac et al. Search for neutrinoless double beta decay with the CUORE detector. *J. Phys. Conf. Ser.*, 110:082001, 2008.

[92] S. Umehara et al. CANDLES for double beta decay of ^{48}Ca. *J. Phys. Conf. Ser.*, 39:356–358, 2006.

[93] K. Zuber. Nd double beta decay search with SNO+. *AIP Conf. Proc.*, 942:101–104, 2007.

[94] A. Gando et al. Measurement of the double-beta decay half-life of ^{136}Xe in KamLAND-Zen. 2012, arXiv:1201.4664v1 [hep-ex].

[95] R. Gornea. Double beta decay in liquid xenon. *J. Phys. Conf. Ser.*, 179:012004, 2009.

[96] R. Saakyan. Topological detection of double beta decay with NEMO3 and SuperNEMO. *J. Phys. Conf. Ser.*, 179:012006, 2009.

[97] J.R. Wilson. The COBRA experiment. *J. Phys. Conf. Ser.*, 120:052048, 2008.

[98] Y. Hirano et al. Study of double beta decay of ^{48}Ca with CANDLES. *J. Phys. Conf. Ser.*, 120:052053, 2008.

[99] M. Danilov et al. Detection of very small neutrino masses in double beta decay using laser tagging. *Phys. Lett. B*, 480:12, 2000.

[100] J.J. Gomez Cadenas, J. Martin-Albo, J. Munoz Vidal, and M. Sorel. The NEXT generation of neutrinoless double beta decay experiments. *J. Phys. Conf. Ser.*, 171:012068, 2009.

[101] N. Ishihara et al. DCBA experiment for searching for neutrinoless double beta decay (II). *J. Phys. Conf. Ser.*, 120:052062, 2008.

[102] H. Ejiri. The MOON project and DBD matrix elements. *J. Phys. Conf. Ser.*, 173:012009, 2009.

[103] A. Staudt, K. Muto, and H.V. Klapdor-Kleingrothaus. Calculation of 2nu and 0nu double-beta decay rates. *Europhys. Lett.*, 13:31–36, 1990.

[104] C.E. Aalseth et al. The IGEX experiment revisited: a response to the critique of Klapdor-Kleingrothaus, Dietz and Krivosheina. *Phys. Rev. D*, 70:078302, 2004, nucl-ex/0404036.

[105] S. Pirro et al. The final results of the Mi-Beta cryogenic experiment twoards the CUORICINO experiment. *AIP Conf. Proc.*, 605:449–552, 2002.

[106] S. Pirro et al. Present status of MI-BETA cryogenic experiment and preliminary results for CUORICINO. *Nucl. Instrum. Meth. A*, 444:71–76, 2000.

[107] R. Arnold. Technical design and performance of the NEMO 3 detector. *Nucl. Instrum. Meth. A*, 536(1-2):79 – 122, 2005.

[108] C. Augier et al. Technical performance of the NEMO 3 detector: Advantages and limitations, 2005. `http://hal.in2p3.fr/in2p3-00025761`.

[109] N. Takaoka, Y. Motomura, and K. Nagao. Half-life of ^{130}Te 2β-decay measured with geologically qualified samples. *Phys. Rev. C*, 53(4):1557–1561, 1996.

[110] T. Bernatowicz, J. Brannon, R. Brazzle, R. Cowsik, C. Hohenberg, and F. Podosek. Precise determination of relative and absolute 2β-decay rates of ^{128}Te and ^{130}Te. *Phys. Rev. C*, 47(2):806–825, 1993.

[111] F. Boehm and P. Vogel. Physics of Massive Neutrinos, 2nd 67 ed. *Cambridge University Press*, Cambridge, 1992.

[112] Y. Takeuchi et al. Measurement of radon concentrations at Super-Kamiokande. *Phys. Lett. B*, 452(3-4):418 – 424, 1999.

[113] J. Argyriades et al. Measurement of the background in the NEMO 3 double beta decay experiment. *Nucl. Instrum. Meth. A*, 606(3):449 – 465, 2009.

[114] O. A. Ponkratenko, V. I. Tretyak, and Yu. G. Zdesenko. Event generator DECAY4 for simulating double-beta processes and decays of radioactive nuclei. *Phys. Atom. Nucl.*, 63(7):1282 – 1287, 2000.

[115] R. Brun, F. Bruyant, M. Maire, A. C. McPherson, and P. Zanarini. GEANT3, 1987. CERN-DD-EE-84-1.

[116] V. Kovalenko. Radon level estimation. *NEMO3 Internal Note*, NemoDocDB-doc-619-v1, 2009.

[117] V. Vasiliev. Measurement of ^{130}Te $\beta\beta^{2\nu}$ decay with the NEMO3 detector. *NEMO3 Internal Note*, NemoDocDB-doc-126-v3, 2008.

[118] O. Helene. Upper limit of peak area. *Nucl. Instrum. Meth.*, 212(1-3):319 – 322, 1983.

[119] G. J. Feldman and R. D. Cousins. Unified approach to the classical statistical analysis of small signals. *Phys. Rev. D*, 57(7):3873–3889, 1998.

[120] T. Junk. Confidence level computation for combining searches with small statistics. *Nucl. Instrum. Meth. A*, 434(2-3):435 – 443, 1999.

[121] A. L. Read. Presentation of search results: The CLs technique. *J. Phys.*, G(28):2693 – 2704, 2002.

[122] W. Fisher. COLLIE: A confidence level limit evaluator, 2008. D0 Internal Note: 005818.

[123] P. Pagelkopf and J. Porstendrfer. Neutralisation rate and the fraction of the positive ^{218}Po-clusters in air. *Atmospheric Environment*, 37(8):1057 – 1064, 2003.

[124] R.B. Firestone and V.S. Shirley. Table of isotopes. *John Wiley and Sons*, 8th ed., NY, 1999.

[125] V Kovalenko. ^{100}Mo double beta decay analysis with the NEMO3 experiment. *Thesis*, 2006, Joint Institute for Nuclear Research, Russia.

[126] V. Kovalenko. ^{100}Mo Internal Background Model. *NEMO3 Internal Note*, NemoDocDB-doc-416-v1, 2008.

[127] V. Tretyak. Private communications.

[128] R. Arnold et al. Probing new physics models of neutrinoless double beta decay with SuperNEMO. *Eur. Phys. J*, 70:927–943, 2010.

[129] F. Simkovic, P. Domin, and S.V. Semenov. The single state dominance hypothesis and the two-neutrino double beta decay of ^{100}Mo. *J. Phys. G: Nucl. Part. Phys.*, 27:2233–2240, 2001.

[130] on behalf of the NEMO3 F. Mauger and SuperNEMO collaboration. Searching for leptonic number non-conservation with NEMO3 and SuperNEMO. *Journ. of Phys.: Conf. Seri.*, 203:012065, 2010.

[131] V.D. Ashitkov et al. Double beta decay of ^{100}Mo. *JETP Lett.*, 74(11):529–531, 2001.

[132] O. Helene. Determination of the upper limit of a peak area. *Nucl. Instrum. Meth. A*, 300(1):132 – 136, 1991.

[133] F. Simkovic et al. Anatomy of nuclear matrix elements for neutrinoless double beta decay. *Phys. Rev.*, C(77):045503, 2008, nucl-th/0710.2055.

[134] R. Chandra, J. Singh, and P.K. Rath. Two neutrino double β decay of $94 \leq A \leq 110$ nuclei for $0^+ \rightarrow 0^+$ transition. *Eur. Phys. J.*, A(23):223–234, 2005, nucl-th/0405074.

[135] A. Barabash. Private communications.

[136] O. Civitarese and J. Suhonen. Nuclear matrix elements for double beta decay in the QRPA approach: A Critical Review. *J. Phys. Conf. Ser.*, 173(012012), 2009.

[137] P.K. Rath, R. Chandra, K. Chaturvedi, P.K. Raina, and J.G. Hirsch. Uncertainties in nuclear transition matrix elements for neutrinoless double beta decay within the projected-Hartee-Fock-Bogoluibov model. *Phys. Rev.*, C(82):064310, 2010.

[138] R. Arnold et al. Limits on different majoron decay modes for ^{100}Mo and ^{82}Se for neutrinoless double beta decays in the NEMO3 experiment. *Nucl. Phys. A.*, 765(3-4):483–494, 2006.

[139] J. Suhonen. Opening of the Z=40 subshell gap and the double-beta decay of ^{100}Mo. *Nucl. Phys.*, A(700):649 – 665, 2002.

[140] K. Nakamura et al. Particle Data Group. *J. Phys. G*, 37:075021, 2010.

[141] Yu. Shitov. SuperNEMO sensitivity studies. *NEMO3 Internal Note*, NemoDocDB-doc-930-v2, 2009.

[142] J. Argyriades et al. Results of the BiPo-1 prototype for radiopurity measurements for the SuperNEMO double beta decay source foils. *Nucl. Instrum. Meth. A*, 622(1):120 – 128, 2010.

[143] S. Snow. Efficiency and resolution of the SuperNEMO 90-cell tracker prototype. *NEMO3 Internal Note*, NemoDocDB-doc-787-v1, 2009.

[144] F.T. Avignone III, G. S. King, and Yu. G. Zdesenko. Next generation double-beta decay experiments: Metrics for their evaluation. *New J. Phys.*, 7(6), 2005.

[145] B. Pahlka et al. Spectral modelling of the scintillator for the NEMO-3 and SuperNEMO detectors. *Nucl. Instrum. Meth. A*, 625:20, 2011.

[146] E. Chauveau. Development of high performance and low background scintillation counters for the calorimeter of the SuperNEMO experiment. *Thesis*, 2010, L'Université Bordeaux 1.

[147] M. B. Kauer. Search for the double beta decay of ^{96}Zr with NEMO-3 and calorimeter development for the SuperNEMO experiment. *Thesis*, 2010, University College London.

[148] A. Basharina-Freshville. Tracking efficiency studies for SuperNEMO. *NEMO3 Internal Note*, NemoDocDB-doc-458-v1, 2008.

[149] A. Basharina-Freshville. Gain measurement of the R6233-100 and R6233-100-S Hamamatsu PMTs. *NEMO3 Internal Note*, NemoDocDB-doc-2068-v1, 2008.

[150] E. Chauveau. Photonis PMT Characterisation. *NEMO3 Internal Note*, NemoDocDB-doc-407-v1, 2008.

[151] E. Chauveau. Baseline energy resolution measurements with Photonis and Hamamatsu PMTs. *NEMO3 Internal Note*, NemoDocDB-doc-544-v1, 2010.

[152] ET Enterprises Electron Tubes (www.electrontubes.com). 130mm (5") Photomultiplier 9390B Series Data Sheet. *DS-9390B Issue 7*, 2009.

[153] Hamamatsu Photonics (www.hamamatsu.com). UBA and SBA Photomultiplier Tube Series. *TPMH1305E06*, 2010.

[154] Photonis (www.photonis.com). Photomultiplier 8-stage 76mm (3"), Round Tube Data Sheet. 2006.

[155] Saint-Gobain Crystals (www.detectors.saint-gobain.com). BC-408 Premium Plastic Scntillator Data Sheet. 2008.

[156] Eljen Technology (www.eljentechnology.com). EJ-200 Plastic Scintillator Data Sheet. 2009.

[157] B. Anderson. Reflectivity measurements. *NEMO3 Internal Note*, NemoDocDB-doc-509-v1, 2009.

[158] I. Chirikov-Zorin et al. Method for precise analysis of the metal package photomultiplier single pohotelectron spectra. *Nucl. Instrum. Meth. A*, 456:310 – 324, 2001.

[159] T. Asch et al. Single photoelectron resolution for the calibration of photomultiplier systems. *Nuclear Science Symposium Conference Record, 2005 IEEE*, 2:887–890, 2005.

[160] I.M. Chakravarti, R.G. Laha, and J. Roy. Handbook of methods of applied statistics. *John Wukey and Sons*, 1:392–394, 1967.

[161] D. Waters. Bar resolution simulation studies. *NEMO3 Internal Note*, NemoDocDB-doc-821-v1, 2009.